Technical University of Denmark

DTU

Development of Hydrogen Electrodes for Alkaline Water Electrolysis

Kjartansdóttir, Cecilía Kristín; Møller, Per

Publication date:
2014

Link back to DTU Orbit

DTU Library
Technical Information Center of Denmark

Preface

This thesis is submitted as partial fulfilment of the requirement for the PhD degree at The Technical University of Denmark (DTU). The work has been carried out at the Department of Mechanical Engineering, section of Materials and Surface Engineering, in the time interval of Nov. 2009 – Dec. 2013, including 10 months of maternity leave. The PhD study was made under the supervision of Professor Per Møller with financial support from the Energy Technology Development and Demonstration Program in Denmark (EUDP) (project number: 63011-0200).

Kgs. Lyngby, 3 December 2013

Cecilía K. Kjartansdóttir

Abstract

The share of renewable energy worldwide is expected to increase by 38% in the period between 2011 and 2035. Consequently, the share of energy from fluctuating energy sources, such as wind, sun and hydro, will escalate and new alternatives for energy conversion, energy storage and load management will be needed. Producing hydrogen via water electrolysis using surplus, low cost, power from renewables offers the possibility of increased production capacity and load management with no greenhouse emissions.

Hydrogen is a valuable energy carrier, which is able to contribute to various forms of energy, such as, production of electricity via fuel cells, fuel for internal combustion engines or gas turbines, or as a raw material for the production of synthetic fuels via Sabatier or Fischer - Tropsch process. In some situations it may be suitable to simply inject hydrogen into the existing natural gas based infrastructure.

Alkaline water electrolysis (AWE) is the current standard (stat of the art) for industrial large-scale water electrolysis systems. One of the main criteria for industrial AWE is efficient and durable electrodes. The aim of the present PhD study was to develop electrode materials for hydrogen production in order to improve the efficiency and durability, and decrease the costs associated with industrial AWE. The primary effort was reserved to the hydrogen electrodes. Additionally, a new test setup for efficiency and durability measurements was to be designed and constructed.

During the present PhD study, new hydrogen electrodes with large electrocatalytic active surface area were developed. The electrodes were produced by physical vapour deposition (PVD) of about 20 μm of aluminium onto a nickel substrate followed by thermo-chemical diffusion and selective aluminium leaching. The obtained electrode surfaces were found to be highly porous; both at micro- and nano-scale, and surface roughness factors of up to 2300 times that of polished nickel were measured. The electrocatalytic surfaces were characterized to have unique adhesion to the substrate, which is a critical criterion for industrial applications. High Resolution Scanning Electron Microscope (HR-SEM) images reveal highly skeletal structure with pores down to a few nanometres. Half-cell potentiodynamic polarisation curves, recorded at 25°C, 200 mA/cm^2, show the electrodes to have 385 mV lower hydrogen overpotential and 50 mV lower oxygen overpotential, when compared to polished nickel.

Durability test was carried out in an industrial sized bipolar, non-zero gap AWE stack where the developed electrodes were applied both as anode and cathode. The stack was operated with 30 wt.% KOH electrolyte at a maximum temperature of 80°C and a pressure of 22 bar. The duration of the test was about 2 years where the stack was operated for approximately 9000 hours. Comparison of data captured from the first month of operation to data captured after the durability testing period indicates no significant deactivation/deterioration in performance of the electrodes during the whole operation period. The stack efficiency was measured to be 81% (HHV), after the test period, at 200 mA/cm^2 and 80 °C. It is noted that

the electrolysis test stack was in the development stage and some losses were expected in the stack itself due to stray currents.

Durability measurements were also carried out in a non-zero gap, single cell electrolysis setup with 50 wt.% KOH electrolyte, at 120°C and 200 mA/cm^2 for 1600 hours. The developed electrodes were applied both as cathode and anode. The cell efficiency was measured to be 88 % (HHV) during the first two hours of operation. After about 100 hours, the efficiency had decreased to 84% and was thereafter constant throughout the remaining test period. The reason for the efficiency drop is proposed to be degradation of the electrodes, caused by gas-erosion corrosion, together with formation of nickel hydrides in electrode metal lattice. The material degradation was considerably more severe at the anode compared to the cathode. The durability single-cell measurements indicate no deactivation of electrodes after shut-downs.

Microstructure investigations on the PVD Al-Ni diffusion couples at 610°C indicate the diffusion mechanism to be dominated by grain boundary diffusion of nickel-rich phases into the aluminium-rich PVD structure. The first intermetallic phase formed is determined to be $AlNi_3$. The phase is observed as small particles in the columnar grain boundaries of the aluminium structure, after only a few minutes of heat treatment. Due to the high mobility of aluminium at the annealing temperature, finding nickel and nickel-rich species to be the most mobile during the heat treatment is highly unexpected and is in contrast with what is stated in the current scientific literature. Together with the $AlNi_3$ particles observed in the aluminium residue, only Al_3Ni and Al_3Ni_2 are present in the diffusion layer for up to 30 minutes of heat treatment. Over 30 minutes of heat treatment results in depletion of the aluminium and formation of highly porous γ-Al_2O_3 phase at the top surface. After 2 hours, of heat treatment only Al_3Ni_2 and thin layers of AlNi and $AlNi_3$ are observed in the diffusion zone, with no traces of the $AlNi_3$ phase. Heat treatments performed for longer than 2 hour result in gradual thickening of the AlNi, $AlNi_3$ and γ-Al_2O_3 diffusion layers and grain growth in the Al_2Ni_3 phase. The diffusion mechanism can be the key to good properties of the developed PVD Al/Ni electrodes.

Electrodes produced with shorter time of diffusion, 10-30 minutes, are found to be more prone to alkaline aluminium leaching and only 4-5 wt.% of aluminium residue is found in the leached skeletal nickel structure. For the electrodes heat treated for 24 hours, up to 15 wt.% aluminium residue is observed in the skeletal nickel structure. However, leaching of the PVD Al-Ni structure, after short periods of diffusion, results in formation of cracks perpendicular to the Ni substrate. The cracks reduce/affect the mechanical strength of the treated coatings. Electrodes heat treated for short times are found not to be stable under OER. However, selective aluminium leaching of electrodes heat treated for 24 hours results in dense, crack free and more mechanically stable/stronger structure. Electrochemical characterisation on the effect of surface area of the developed electrodes, indicate that the electrocatalytic activity increases in proportion to the porous layer up to the whole 20 µm investigated.

With the aim of reducing the production costs associated with the electrode manufacturing, four process techniques and combinations of these were screened. These were; (1) hot dip

aluminising of nickel followed by thermo-chemical diffusion, (2) direct thermo-chemical diffusion of aluminium and nickel sheets, (3) aluminium ionic liquid electroplating on a nickel plate followed by thermo-chemical diffusion and (4) physical vapour deposition of aluminium onto electroplated sulfamate nickel substrate followed by thermo-chemical diffusion. Due to the high affinity of aluminium towards hydrogen and oxygen, producing oxide free AlNi alloy coatings in an inexpensive and simple manner was found to be challenging. Only the direct diffusion between aluminium and nickel sheets in argon atmosphere and the PVD Al onto electroplated sulfamate nickel were found to give promising coatings.

Resumé

Andelen af vedvarende energi på verdensplan forventes at stige med 38% i perioden mellem 2011 og 2035. Derfor vil andelen af energi fra fluktuerende energikilder, såsom vind, sol og vandkraft eskalere, og der vil blive behov for nye alternativer til energi konvertering, energilagring og load management. Produktion af hydrogen via elektrolyse fra overskydende elproduktion fra vedvarende energi giver mulighed for øget produktionskapacitet og load management uden drivhusgasser.

Hydrogen er en værdifuld energibærer, der på mange måder er i stand til at bidrage til forskellige former for energikilder såsom; produktion af el via brændselsceller, brændstof til forbrændingsmotorer eller gasturbiner, eller som råstof til fremstilling af syntetiske brændstoffer via Sabatier eller Fischer–Tropsch processen. I nogle situationer kan det accepteres blot at injiceres hydrogen i den eksisterende naturgas infrastruktur.

Alkalisk elektrolyse (AWE) er den nuværende standard (state of the art) for store industrielle vand elektrolyse -systemer. Et af de vigtigste kriterier for industriel AWE er effektive og holdbare elektroder. Formålet med nærværende Ph.d.-projekt var således at udvikle elektrode materialer til brintproduktion med henblik på at forbedre effektiviteten og holdbarheden, samt mindske omkostningerne, der er forbundet med industriel AWE. I forlængelse heraf blev der udviklet nye test setups for evaluering af effektivitet og holdbarhedstests.

I forbindelse med nærværende ph.d.-projekt blev nye brint elektroder med stor elektrokatalytisk aktiv udviklet. Elektroderne blev fremstillet ved (PVD) deponering af 20 µm aluminium på et nikkel substrat efterfulgt af termokemisk diffusion og selektiv fjernelse af aluminium via ætsning. Det nye elektrodemateriale var særdeles porøst på såvel mikro som nanoskala, og opnåede en aktiv overflade op til 2300 gange større end en poleret nikkel overflade.

De elektrokatalytiske overflader udviste unik adhæsion til substratet, som er afgørende for en efterfølgende industriel anvendelse. High Resolution Scanning Electron Microscope (HR-SEM) billeder bekræftede en robust skelet-struktur med porer ned til nogle få nanometer. Halv-celle potentiodynamisk recordede polarisationskurver ved 25°C og 200 mA/cm^2 viste at elektroderne havde 385 mV lavere brintoverspændings potentiale og 50 mV lavere ilt overspændings potentiale sammenlignet med poleret nikkel.

Elektrodernes stabilitets test blev udført i en industriel bipolar, ikke zero-gap AWE stak hvor elektroderne blev anvendt både som anode og katode. Stakken var forsynet med 30 vægt % KOH elektrolyt og havde en maksimal drifts temperatur på 80°C ved et gas tryk på 22 bar. Varigheden af testen var omkring 2 år, hvor stakken var i drift over 9000 timer. Sammenligning af driftsdata registreret fra første måneds drift til data registreret efter 9000 timer viser ingen signifikant deaktivering af elektrodernes katalytiske aktivitet. Stakkens effektivitet blev målt til at være 81% (HHV) efter perioden test på 200 mA/cm^2 ved 80°C

Det bemærkes, at elektrolyse test stakken var i udviklingsfasen, og nogen effektivitets tab var at forvente i stakken grundet fejl-strømme.

Elektrodetest målinger blev ligeledes udført i en ikke zero-gap, enkelt celle elektrolyse setup med 50 vægtprocent % KOH elektrolyt, ved 120°C og 200 mA/cm^2 i 1600 timer. De udviklede elektroder blev anvendt både som katode og anode. Cellens effektivitet blev målt til at være 88% (HHV) i løbet af de første to timers drift. Efter omkring 100 timer var effektiviteten faldet til 84% og effektiviteten var efterfølgende konstant i den resterende del af testperioden. Årsagen til reduktionen i effektivitet tillægges nedbrydning af elektroderne, forårsaget af gaserosion eller korrosion, sammen med en mulig dannelse af nikkel hydrider, hvad angår katoden. Materialet nedbrydningen var mere omfattende ved anoden i end ved katoden. Single celle målinger indikerede ingen deaktivering af elektroder under pauser - uden elektrolyse.

Mikrostruktur undersøgelser af PVD Al-Ni diffusion ved 610°C indikerer at diffusion mekanismen er domineret af en korn grænse diffusion af nikkel-rige faser i den PVD deponerede aluminium fase. Den første intermetalliske fase der dannes er fastslået til at være AlNi3. Denne optræder i de søjleformede korngrænser af aluminium strukturen efter kun nogle minutters varmebehandling. Det er særdeles overraskende og uventet at konstatere at nikkel og nikkelholdige faser er de mest mobile faser under diffusionsglødningen af den PVD deponerede aluminium på et nikkel basismateriale. Iagttagelserne er i kontrast til hvad der fremgår af den videnskabelige litteratur.

Udover at der er AlNi$_3$i korngrænserne af aluminium strukturen, observeres der Al$_3$Ni og Al$_3$Ni$_2$ i diffusionslaget efter op til 30 minutters varmebehandling. Efter 2 timers varmebehandling kan dannelsen af en meget porøs γ - Al$_2$O$_3$ fase ved den øverste overflade iagttages. Kun Al$_3$Ni$_2$ og tynde lag af AlNi og AlNi$_3$ observeres i diffusionszone, mendens AlNi$_3$ fase ikke kan identificeres. Varmebehandlinger længere end 2 timer resulterer i langsom opbygning af AlNi, AlNi$_3$ og γ - Al$_2$O$_3$ fase samt kornvækst i Al$_2$Ni$_3$ fasen. Den noget særprægede diffusionsmekanisme kan vise sig at være årsagen til de gode egenskaber af den udviklede PVD Al/Ni elektrode. Elektroder fremstillet med korte diffusions tider, 10-30 minutter, er konstateret at være lettere at ætse selektivt i alkalisk miljø med et rest aluminium indhold på 4-5 vægt% i den udætsede skeletal struktur.

For elektroder der varmebehandles i 24 timer, kan der observeres op til 15 vægt % rest aluminium i det resterende nikkel struktur. Selektiv udætsning af PVD Al-Ni struktur efter kort tids diffusion, resulterer i dannelse af revner vinkelret på nikkel substratet. Revnerne formindsker den mekaniske styrke af belægninger. Elektroder varmebehandlet i korte tid viser sig ikke at være stabile under OER. Selektiv ætsning af aluminium fra elektroder varmebehandlet i 24 timer viser resulterer derimod i tætte, krakfrie og mere mekanisk stabile strukturer. Elektrokemisk karakterisering af overfladearealets for de nye udviklede elektroder viser, at den elektrokatalytiske aktivitet stiger proportional til det porøse lags tykkere, op til 20 μm.

Med henblik på at reducere produktionsomkostningerne i forbindelse med fremstilling af elektroder, blev fire mulige procesteknologier, foruden den allerede undersøgte afprøvet.

Disse var: (1) varmaluminering af nikkel, efterfulgt af termo- kemisk diffusion, (2) direkte termo- kemisk diffusion af aluminium folie med nikkel plader, (3) elektrolytisk deponering af aluminium belægninger fra ioniske væsker på et nikkelsubstrat efterfulgt af termo- kemisk diffusion og slutteligt (4) PVD belægninger af aluminium på en elektrolytisk deponeret sulfamate nikkeloverflade efterfulgt af termo- kemisk diffusion.

På grund af den høje affinitet af oxygen til aluminium og dermed også smeltet aluminiums høje affinitet til vand og den efterfølgende høje opløsning af hydrogen i smeltet aluminium kan fremstilling af AlNi legeringer for elektroder betragtes som en udfordring. Det blev hurtigt klart at termokemisk diffusion, henholdsvis mellem en aluminium folie og nikkel i en argon atmosfære og en PVD deponeret aluminium belægning på en elektropletteret sulfamate nikkel var blandt de mest lovende procesteknologier til fremstilling af skeletal nikkel.

Acknowledgements

First and foremost, I would like to thank my supervisor, Professor Per Møller, for his valuable supervision, inspiring ideas, enthusiasm and support throughout the whole project. His unlimited engagement and passion for science and, moreover, for bridging the gap between research and industry has been a great motivation for me.

I wish to thank the scientists at Siemens A/S (Scion) for welcoming me to their laboratory facilities. I particularly want to thank Sune Egelund and Michael Caspersen for their help with experiments, invaluable discussions and collaboration. I also want to thank Melany Roeefzaad for introducing me to the cyclic voltammetry technique and for her help and support during optimisation of the measurement setup. Martin Kalmar Hansen is gratefully acknowledged for his detailed comments on an earlier draft on this thesis. Kasper Bondo Hansen is thanked for his contribution to the ionic liquid electroplating experiments.

Jørgen Jensen, Alexander Dierking from the company GreenHydrogen.dk and Lars Yde from Aarhus University are gratefully acknowledged for making the durability testing of the electrodes in an electrolysis stack, possible.

I am thankful to all my colleagues in the Section of Materials and Surface Engineering for their assistance during my PhD, and for making work a pleasant place. Especially I wish to thank Alexander Elmkvist Barington for his preparation work on the hot dip aluminising specimens and Malene Kaab for the various cooperation and assistance. Special thanks go to my great office-mates Svava Daviðsdóttir, Visweswara Chakravarthy Gudla and Rameez Ud Din, for all the interesting and valuable scientific discussions, support and good company.

In particular I want to thank my dear colleague, Trine Nybo Lomholt, for the thorough proofreading of the thesis, all the encouraging words and all the help when I needed it the most. Thank you so much Trine.

Last but not least, my deepest thanks go to my beloved Ole for his endless support and patience during the whole PhD journey. I especially want to thank him for taking such a good care of our sweet daughter and our home in my abundant absence during the last several months.

List of Publications

I.   C. K. Kjartansdóttir, L. P. Nielsen, and P. Møller, "**Development of durable and efficient electrodes for large-scale alkaline water electrolysis**," International Journal of Hydrogen Energy, vol. 38, no. 20, pp. 8221–8231, Jul. 2013.

II.   C. K. Kjartansdóttir, M. Caspersen, S. Egelund and P. Møller, "**Electrochemical investigation of surface area effects on PVD Al-Ni as electrocatalyst for alkaline water electrolysis,**" Manuscript to be submitted to Electrochimica Acta.

III.   C. K. Kjartansdóttir, A. Hossein, T. Kasama and P. Møller, "**Investigations of the diffusion mechanism of PVD Al and Ni couples at 610°C**," Manuscript to be submitted.

IV.   M. Flyvbjerg, C.K. Kjartansdóttir, M. Caspersen and P. Møller, "**Unveiling the secrets of the Standard Hydrogen Electrode - An inspiration for the on-going development of hydrogen electrocatalyst**," Manuscript submitted to Journal of the American Chemical Society, Dec. 2013.

List of Participating Activities

I.   C. K. Kjartansdóttir , L.P. Nielsen and P. Møller, **"2nd Generation Alkaline Electrolysis for Hydrogen Production,"** Presentation. Danish Metallurgical Society Symposium, Roskilde, Denmark, 2011.

II.   C. K. Kjartansdóttir , L.P. Nielsen and P. Møller, **"Electrodes with good durability for alkaline water electrolysis,"** Poster presentation, World Hydrogen Energy Conference 2012, Toronto, Canada, 2012.

III.   C. K. Kjartandsóttir and P. Møller, **"Development of hydrogen electrodes for industrial scale alkaline water electrolysis,"** Danish Metallurgical Society Symposium, Lyngby, Damark, 2013.

IV.   L. Yde, C. K. Kjartansdóttir, F. Allebrod, M. B. Mogensen, P. Møller, L. R. Hilbert, P. T. Nielsen, T. Mathiesen, J. Jensen, L. Andersen, and A. Dierking, **"2nd Generation Alkaline Electrolysis,"** Århus University Business and Social Science – Centre for Energy Technologies, Danmark, 2013.

V.   A. B. G. S. W, **"Ny produktionsmetode muliggør "stinkende billig" brint,"** Ingeniøren, 2010. [Online]. Available: http://ing.dk/artikel/ny-produktionsmetode-muliggor-stinkende-billig-brint-114709. [Accessed: 16-Nov-2013].

Abbreviations

AWE	Alkaline water electrolysis
BSE	Back-scatter electron
CAD	Computer-aided design (CAD)
CE	Counter electrode
CV	Cyclic voltammetry
EBSD	Electron backscatter diffraction
EDS	Energy-dispersive X-ray spectroscopy
EIS	Electrochemical Impedance Spectroscopy
EUDP	The Energy Technology Development and Demonstration Program in Denmark
GI	Grazing incidence
HER	Hydrogen evolution reaction
HHV	Higher heating value
HR-SEM	High resolution scanning electron microscope
HTAWE	High temp alkaline water electrolysis
ICCI	Ion channelling contrast imaging
IR	Ohmic resistance
KOH	Potassium hydroxide
LOM	Light optical microscope
MEA	Membrane electrode assembly
OCP	Open circuit potential
OER	Oxygen evolution reaction
PEEK	Polyether ether ketone
PEM	Polymer electrolyte membrane
PTFE	Polytetrafluoroethylene
PVD	Physical vapour deposition
RE	Reference electrode
SE	Secondary electron
SEM	Scanning electron microscope
SHE	Standard hydrogen electrode
SOEC	Solid oxide electrolysis cell
SOEC	Solid oxide fuel cell
SPE	Solid polymer electrolysis
STP	Standard temperature and pressure
TS	Thermal spraying
WE	Working electrode
XPS	X-Ray photoelectron spectroscopy
XRD	X-Ray diffraction

Contents

Appended papers

I.   Development of durable and efficient electrodes for large-scale alkaline water electrolysis

II.   Electrochemical investigation of surface area effects on PVD Al-Ni as electrocatalyst for alkaline water electrolysis

III.   Investigations of the diffusion mechanism of PVD Al and Ni couples at 610°C

IV.   Unveiling the secrets of the Standard Hydrogen Electrode - An inspiration for the on-going development of hydrogen electrocatalyst

Appendix

List of Figures

List of Tables

1 Introduction

1.1 Background

According to the World Meteorological Organization (WMO), the concentration of greenhouse gases in the atmosphere rose in 2012 to the highest ever recorded [1]. Carbon dioxide, mainly from fossil fuel related emissions, is responsible for about 80% of the warming effect from greenhouse gases. The increase in carbon dioxide in the atmosphere from 2011 to 2012 was measured to be higher than the average growth rate for the past ten years. This happens despite the plentiful goals and policies towards reduction in CO_2 emission worldwide counting, for instance;

- The target of limiting the long – term global temperature increase to 2°C as agreed at the United Nations Framework Convention on Climate Change Conference, Mexico 2010 [2].

- The energy and climate change objectives for 2020 accepted at the European Council in 2007 with the aim of 20% reduction in greenhouse emission and 20% increase in the share of renewable energy together with commitment of 80-95% reduction in greenhouse emission by 2050 [3].

Additionally, according to the World Energy Outlook released in November 2013 [4], the worldwide energy demand will increase by one-third from 2011 to 2035. Accordingly, in order to meet the ever increasing energy demand and diminish the risk of dramatic climate change in the coming years, rapid shift in the global energy trend away from coal is necessary.

Renewable energy is commonly recognised to be the answer for a more secure, reliable and sustainable future. The share of renewables in primary energy worldwide is expected to increase by 38% from 2011 to 2035 [4]. This implies that a larger share of the energy will come from fluctuating energy sources such as wind, sun and hydro. Hence, developing new efficient alternatives for energy conversion, energy storage and load management is essential.

Combining production of hydrogen via water electrolysis with renewable energy sources offers the possibility of increased production capacity and load management with no greenhouse emissions. Hydrogen as an energy carrier comprises the advantage of flexibility, being able to contribute to various kinds of energy sources. Fig. 1 shows possible routes for hydrogen produced by water electrolysis. The most obvious route is the production of hydrogen with excessive power from fluctuating renewables followed by storage and later production of electricity via fuel cells, combustion engines or gas turbines, when needed. The hydrogen can also be used as a raw material for production of synthetic fuels, such as

methane by the Sabatier process [153], liquid fuels by the Fischer–Tropsch synthesis [154] or simply injected into the existing natural gas infrastructure [155].
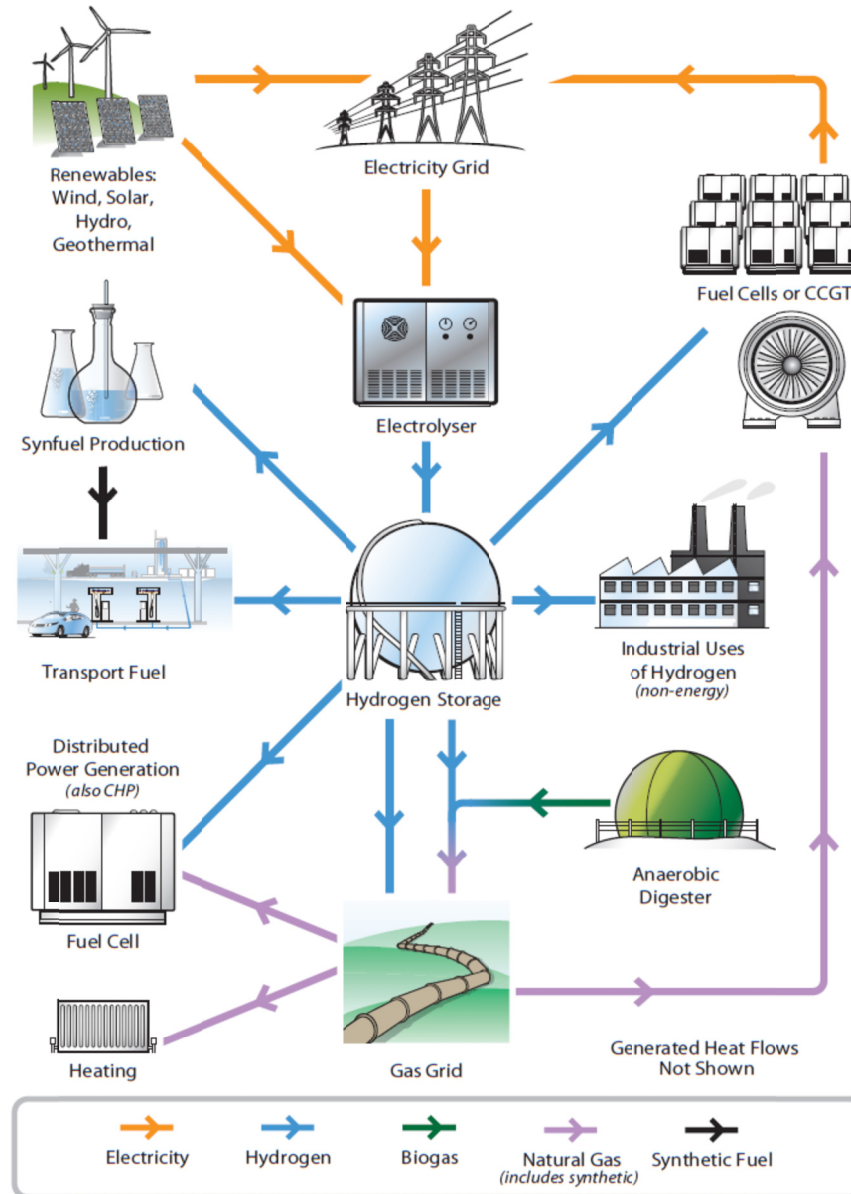
Fig. 1: Illustration of possible routes for hydrogen produced by water electrolysis [5].

A variety of water electrolysis systems have been proposed developed and constructed over the years. Among the commercially available water electrolysis systems, alkaline water electrolysis (AWE) comprises by far the highest production rate and the lowest production cost, making the technique the current standard for large-scale water electrolysis systems [10,15]. However, finding low cost electrode materials that are both efficient and have long term stability is one of the remaining challenges within the field of AWE.

1.2   Objectives of the present study and structure of the thesis

The present PhD study is a part of a research, industrial, development and demonstration program called 2nd Generation Alkaline Electrolysis. The project was initiated in 2008 and the project participants were Århus University Business and Social Science – Centre for Energy Technologies (CET (former HIRC)), Technical University of Denmark – Mechanical Engineering (DTU-MEK), Technical University of Denmark – Energy Conversion (DTU-EC), FORCE Technology and GreenHydrogen.dk. The project was supported by EUDP.

Expected results from the project were as follows:

A generation of alkaline electrolysers characterized by:
- Increased electrode efficiency to more than 88% (HHV) at a current density of 200 mA /cm^2.
- Increased operation temperature to more than 100°C
- Operation pressure of more than 30 bar
- Improved stack architecture that will decrease the price of the stack with at least 50%.
- A modular design that makes it easy to customize plants in the size from 20 to 200 kW.
- Demonstration of a 20 kW 2nd generation stack at H2-College at the campus of Århus University in Herning.

The overall purpose is research, development and demonstration of the emerging renewable energy concept based on hydrogen as a renewable energy carrier, produced from water and wind power. The methodology of the project was to be implemented through 8 different work packages one of these being improvement of electrodes.

There are two ways to increase the efficiency of an electrode. Increase the electrocatalytic properties of the electrode surface or increasing the specific surface area of the electrode. Both of these results in a reduction of the necessary voltage to draw the current applied. The work package will deal with both, through literary studies and laboratory tests in order to find and specify for production the optimal electrode solution regarding efficiency, durability and price.

The objective of the present PhD study was to identify electrode materials for hydrogen production in order to improve the efficiency and durability and decrease the costs associated with alkaline water electrolysis. New materials were to be designed for the electrodes containing no precious metals. The primary focus of the study was reserved to the hydrogen electrodes (the cathodes). Additionally, new test setup for efficiency and durability measurements was to be developed and constructed.

The thesis is divided in to 9 chapters and 4 appended papers.

Chapter 1 is a short introduction of the drive for producing hydrogen via water electrolysis together with the objectives of the PhD study and structure of the thesis.

Chapter 2 encloses the fundamentals of water electrolysis including the main principle, the thermodynamics and an overview of the main cause for an efficiency loss in an electrolysis cell. The main principle behind the kinetics of a hydrogen electrode is introduced in a subchapter called Electrocatalysis.

Chapter 3 gives an overview of the current main types of water electrolysis technologies. The chapter will be focused on the current status and research trends of alkaline electrolysis.

In **Chapter 4** the methodology for testing and characterisation of the developed electrodes surfaces is covered. The thesis is written with the intentions of assisting the next generation of researchers in the field of alkaline water electrolysis electrocatalysts. Well reported principles behind the measurements and analytic methods used will therefore not be described. Instead, the emphasis will be on experimental challenges and principles, encountered during the PhD study, that are not found to be well covered in the literature.

In **Chapter 5** the development process of the electrolysis test setups constructed during the present project will be presented.

In **Chapter 6** the practice for material selection and structure modification for developing a new hydrogen electrocatalyst for alkaline electrolysis is introduced.

In **Chapter 7** a screening of process techniques and combination of these for producing high surface area nickel electrodes for alkaline electrolysis will be described and the main results reported.

In **Chapter 8** results from electrochemical and durability tests prepared on the most promising electrocatalytic surface from the screening in chapter 7 are reported.

Overall conclusions of the findings reported in the thesis and the appended papers, are given in **Chapter 9**.

Appended papers:
Three of the appended papers are first-authored by the candidate and for the fourth paper the candidate is a co-author.

P-1: Development of durable and efficient electrodes for large-scale alkaline water electrolysis.
In this paper, studies on the electrode developed in this PhD study are reported. Structural characterisation of the electrodes is performed by high-resolution scanning electron microscope. The electrocatalytic activity of the developed electrodes is studied with steady-

state electrochemical measurements and cyclic voltammetry. Durability tests are carried out in an industrial scale-electrolysis stack.

P-2: Electrochemical investigation of surface area effects on PVD Al-Ni as electrocatalyst for alkaline water electrolysis.
In this paper, the influence of the actual surface area on the electrocatalytic activity of the developed electrocatalyst is investigated. The structure and composition of the developed electrodes is characterised by the means of a scanning electron microscope and X-ray diffraction. The electrocatalytic activity and actual surface area are studied with potentiodynamic polarisation, cyclic voltammetry and electrochemical impedance spectroscopy.

P-3: Investigations of the diffusion mechanism of PVD Al and Ni couples at 610°C.
In this paper, investigation on the diffusion mechanisms of the developed electrocatalyst is reported. PVD Al-Ni diffusion couples, heat treated at 610°C for few minutes up to 24 hours, are investigated by the means of, high resolution scanning electron microscope, energy dispersive X-ray spectroscopy, X-ray diffractometry, electron backscatter diffraction, ion channelling contrast imaging and transmission electron microscopy.

P-4: Unveiling the secrets of the Standard Hydrogen Electrode - An inspiration for the on-going development of hydrogen electrocatalyst.
In this paper, a new perspective on electrode design and electrodeposition of the platinum black electrode are presented.

2 Fundamentals of Water Electrolysis

2.1 The Principle

Water electrolysis is a process where electricity is used to decompose water into its components - gaseous hydrogen and oxygen according to.

$$H_2O \rightarrow H_2 + \frac{1}{2}O_2 \qquad (1)$$

A typical water electrolysis cell consists of two electrodes, a diaphragm, an electrolyte and a power supply. The most common type of water electrolysis cell, the alkaline electrolysis cell, is illustrated in Fig. 2.
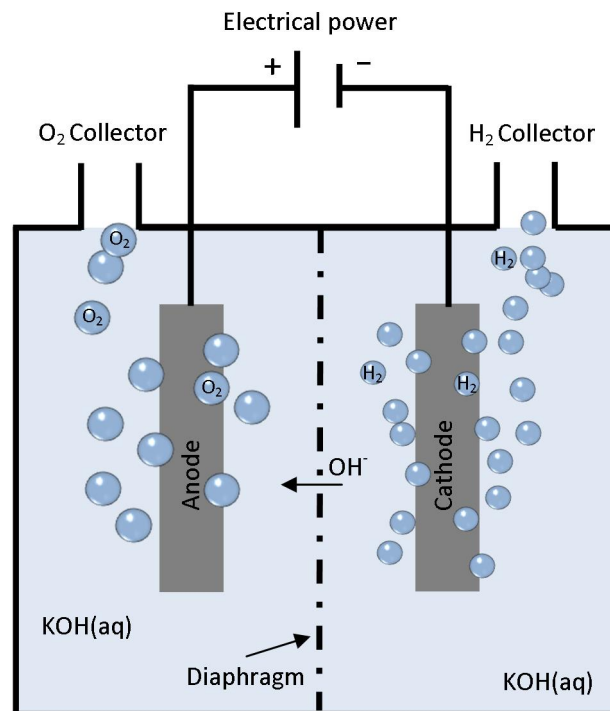
Fig. 2: Outline of the operating principles of an alkaline water electrolysis cell.

When current is applied to the system, hydrogen gas is formed at the cathode and oxygen gas at the anode. The diaphragm is a membrane that hinders the mixing of gasses developed at the two electrodes and allows the ions to pass. The gas produced can be captured in their pure form when drifting up from the electrolyte. The reactions taking place at the electrodes, i.e. the half-cell reactions, differ between the types of water electrolysis techniques applied. These mechanisms are introduced in chapter 3.

2.2   Thermodynamics

As indicated by the power supply in Fig. 2, the decomposition of water into hydrogen and oxygen is not thermodynamically favourable, i.e. the decomposition process is energy consuming. The total energy needed for decomposing one mole of water into oxygen and hydrogen corresponds to the enthalpy change (ΔH) for the reaction, which is 285.9 kJ at standard conditions [6]. At low temperatures the majority of this energy is required to be in the form of electrical energy and the rest can be applied as thermal energy. The energy needed for the decomposition of water can be expressed from the enthalpy changes for the reaction as follows:

$$\Delta H = \Delta G + T\Delta S \tag{2}$$

Where ΔG is the Gibbs free energy change for the reaction, ΔS is the entropy change and T is the temperature of the reaction in Kelvin. The Gibbs free energy can be regarded as the minimum amount of the electric energy that has to be applied to the system for the reaction to take place. ΔG can be calculated from the reversible voltage (E_{rev}) (also called the equilibrium voltage (E_{eq})) according to:

$$\Delta G = nFE_{rev} \tag{3}$$

Where n is the number of moles of electrons transferred in the reaction (here 2) and F is the Faradays constant (9.64853399×10^4 C/mol). E_{rev} is the absolute minimum voltages needed in order to produce hydrogen and oxygen via water splitting. $E_{rev,}$ thus equals the sum of the reversible voltage (E_{rev}) of the anodic and cathodic reaction in the system to:

$$E_{rev} = E_{rev\,oxygen} + E_{rev\,hydrogen} \tag{4}$$

At standard conditions the reversible voltage of oxygen and hydrogen are 1.229 V and 0.000 V, respectively, resulting in E_{rev} = 1.229 V [7]. Accordingly, for the following reaction in eq. (1) to take place in a water electrolysis cell, 1.229 volts must be applied between the anode and cathode. When inserting the reversible voltage into eq. (3) the Gibbs free energy of the reaction can be calculated giving ΔG = 237.2 kJ/mol. The electrical potential needed for decomposition of water for conditions varying from the standard conditions can be derived directly from the Nernst equation according to [8]:

$$E_{T,P} = E_{rev} + \frac{RT}{nF}\ln\left(\frac{P_{H_2}P_{O_2}^{\frac{1}{2}}}{P_{H_2O}}\right) \tag{5}$$

Where R is the gas constant (8.3144621 J/ mol K), P_{H2} the partial pressure of hydrogen, P_{O2} the partial pressure of oxygen and P_{H2O} the partial pressure of water. Assuming the same partial pressure over the whole system, eq. (5) can be written as:

$$E_{rev,T,P} = E_{rev} + \frac{RT}{nF}\ln(P^{\frac{1}{2}}) \tag{6}$$

Consequently, if the system is pressurised, $E_{rev,T,P} > E_{rev}$, then more electrical energy is required for the reaction in eq. (1) to take place. The increase in voltage is, however, minor at low temperatures. If, as an example, an electrolysis cell is pressurised to 200 atm. at 80°C, the increase in E_{rev} is only 0.04 V. Furthermore, it has been shown that pressurising the system can help in reducing the ionic resistivity in the cell, see concentration overpotential in section 2.3. When knowing the Gibbs free energy and the enthalpy for the system the energy that can be applied to the reaction in the form of heat can be calculated from eq. (2). At standard conditions the thermal energy is:

$$285.9 \text{ kJ/mol} - 237.2 \text{ kJ/mol} = 48.7 \text{ kJ/mol} \tag{7}$$

However, if this amount of heat cannot be integrated into the process, the shortage of energy has to come from the electrical source, i.e. more than $E_{rev} = 1.229$ volt difference is required between the anode and cathode for the water splitting reaction to take place. The total electrical energy required for maintaining an electrochemical reaction without generation or absorption of heat, at a specific temperature, is called the total thermo neutral voltage (E_{th}). The minimum amount of energy needed for the reaction is equal to the enthalpy of the thermo-neutral voltage and can be defined as:

$$E_{th} \equiv \frac{\Delta H}{nF} = \frac{\Delta G}{nF} + \frac{T\Delta S}{nF} \tag{8}$$

At standard temperature and pressure (STP) the E_{th} is calculated to be 1.481 V [9]. Fig. 3 illustrates the thermo-neutral voltage and the reversible voltage for hydrogen production via water electrolysis as a function of temperature.
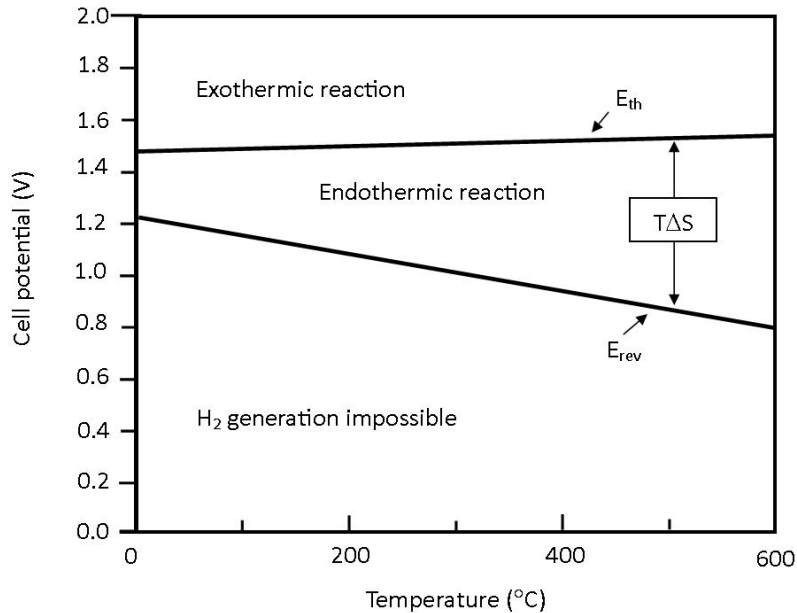
Fig. 3: The thermoneutral voltage (E_{th}) and reversible voltage (E_{rev}) for the production of hydrogen in a water electrolysis cell. The system is calculated for water in liquid phase. The image is a redraw from [10].

If an electrolysis cell is operated above the E_{th} conditions, the system generates heat (exothermic). If, on the other hand, operated below E_{th} the system absorbs heat (endothermic). Operating below the E_{rev} voltage the decomposition of water is thermodynamically impossible.

In Fig. 3 the benefits of producing at elevated temperatures is evident. By increasing the temperature, a larger amount of the energy needed for the process to occur can be applied in the form of thermal energy. Therefore, if low cost thermal energy is available the cost associated with the production of hydrogen via water electrolysis can be minimised. In fact, at temperatures above 2000°C water can be decomposed directly via thermochemical processes [11]. Nevertheless, with direct heating alone, without the use of catalysts, much higher temperatures are required. According to the thermodynamics, temperatures above 4100°C are needed for the splitting process to be thermodynamically favourable. In [7] Rand et al. writes that only ~1vol% of water is decomposed at 2000°C. Whereas in [12] Isao Abe reports that 5000 K direct heating is needed for full decomposition of water and 2500 K for partial decomposition.

2.3   The resistance in the electrolysis cell

Apart from the theoretical energy consumption during electrolysis, there are a number of additional electrical barriers that needs to be overcome for the electrolysis process to occur. Thus, the cell voltage during electrolysis is always higher than E_{th} derived from the thermodynamics. The additional voltage needed to overcome these barriers is often called overpotential or overvoltage. The overpotentials in an electrolysis cell can be divided into three categories [13].

- Resistance overpotential (η_{res})
- Concentration overpotential (η_{con})
- Activation overpotential (η_{act})

The *resistance overpotential* represents the electrical resistance in the cell from external wiring, electrical connections to the electrodes and the resistance in the electrodes themselves. This type of overpotential can usually be minimised by selecting good electrically conducting materials for the wires and connections and by assuring sufficient cross sections of those. The resistance in the electrodes themselves can become considerably large. This can for example be the case for electrodes containing passivated oxides or isolating impurities, thus, this should be avoided.

The *concentration overpotential* is caused by the resistance in the ionic transfer in the electrolyte located between the anode and cathode. The concentration overpotential depends on the ionic conductivity of the electrolyte, the distance between the anode and cathode, the conductivity of the diaphragm and the presence of gas bubbles in the electrolyte. The conductivity of the electrolyte and the cell configuration for AWE cells are discussed in more detail in section 3.1.

During water electrolysis hydrogen and oxygen gas is formed on the electrode surfaces. The gas bubbles formed are small and do not have the required volume to drift away from the electrode surfaces immediately. Only after sufficient coalescence the gas bubbles get large enough to drift away from the electrode surfaces into the electrolyte. The bubble coverage on the electrode surfaces and the bubble dispersion in the electrolyte are often referred to as the bubble phenomenon in AWE. The gas bubbles attached to the surfaces block some part of the active electrode area and thereby hinder the electrochemical reaction to take place. The gas bubbles in the electrolyte itself evidently increase the ionic resistivity of the electrolyte. These two effects cause a high ohmic drop during operation and are responsible for the largest amount of the concentration overpotential in AWE cells [14]. Pressurising the electrolysis stacks, assuring good convection in the electrolyte and the use of zero gap cell configuration (see section 3.1.2.2) can be applied for minimising this type of overpotential.

The *activation overpotential* represents the activation energies of the electrochemical reactions taking place on the anode and cathode which increase logarithmically with the current density [15]. The concentration overpotential together with the activation overpotential is responsible for the greatest deal of the overpotentials during electrolysis. The activation overpotentials for the oxygen and hydrogen evolution reaction are discussed in detail in section 2.5.

The overall cell voltage for a water electrolysis cell (under adiabatic conditions) can then be written as:

$$E_{cell} = E_{th} + E_{res} + E_{act} + E_{con} \tag{9}$$

Both the concentration overpotential and the resistance overpotential cause heat generation in the system. Some of the generated heat can, in well isolated electrolysis system, be used for heating up the electrolyte. In that way the efficiency loss from the overpotentials can be minimised.

For the ease of identifying every single overpotential source in an electrolysis cell, the overall cell resistance can be expressed by the electrical circuit analogy as displayed in Fig. 4. Here R_E represents the electrical resistance from wiring and connections to the electrodes. R_{anode} and $R_{cathode}$ are the overpotentials required to overcome the activation energies of the oxygen and hydrogen formation, respectively. R_{O2} and R_{H2} is the resistance from the oxygen and hydrogen bubbles in the electrolyte and on the electrodes surfaces. R_{ions} represents the resistance in the electrolyte and $R_{diaphragm}$ is the diaphragm resistance.
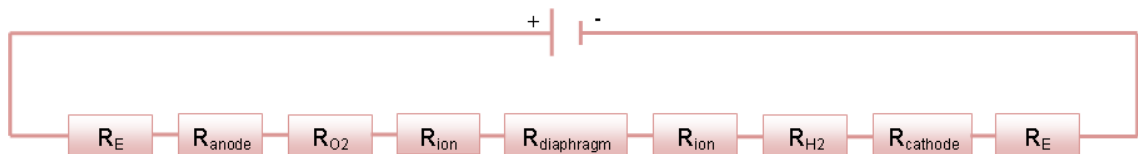
Fig. 4: The electrical circuit analogy of the resistances within a water electrolysis cell.

2.4   Efficiency

The efficiency of the water electrolysis process can be expressed in many different ways, depending on how the electrolysis system is assessed and compared. As a result, this sometimes introduces some confusions and misunderstandings in the literature. The cell efficiency is the most essential for electrode development. The cell efficiency (η) is calculated by comparing the measured cell voltage either to the reversible or the thermo neutral voltage as shown in eq. (10) and (11):

$$\eta_{rev} = \frac{E_{rev}}{E_{cell}} \tag{10}$$

$$\eta_{th} = \frac{E_{th}}{E_{cell}} \tag{11}$$

If, for instance, an electrolysis cell is operated at STP at cell potentials of E_{cell} =1.48 V, the efficiency is calculated to be 100% according to eq. (11). If on the other hand eq. (10) is used the efficiency is calculated to be only 83%. Thus, when reporting electrolysis efficiency it is important to inform about how the efficiency is calculated. If not, the reported value is of no use for the reader. E_{th} is also known as the higher heating value (HHV). Thus, in the literature η_{th} is commonly referred to the efficiency according to the HHV. The η_{rev} is always less than 1, because hydrogen cannot be produced if the potential is less than E_{rev} applied to the system. In contrast, η_{th} can be higher than 1. This is because some of the heat needed for the reaction can be absorbed from the environment.

Another way to calculate the efficiency is by comparing the energy input to electrolysis system with the hydrogen production rate [10]. This can be done according to:

$$\eta_{\text{H2 production rate}} = \frac{V(m^3 h^{-1})}{Uit\ (kJ)} \tag{12}$$

Where V is the hydrogen production rate at a unit volume of an electrolysis cell, U is the cell voltage, i is the current and t is the time.

For commercial electrolysis systems the efficiency is typically calculated from the total energy consumption for each cubic meter of hydrogen produced. According to the HHV, 100% efficiency is reached with 3.54 kWh/Nm^3. Thus, ideally, 39 kWh of electricity and 8.9 liters of water are required to produce about 11000 litres or 1 kg of hydrogen at STP [16]. However, the current most efficient commercial electrolysis systems only have a maximum efficiency of 82% corresponding to 4.3 kWh/Nm^3. Performance data for electrolysers from the leading current electrolyser manufactures is gathered in Table 1 in chapter 3.

2.5 Electrocatalysis

An electrocatalyst is a material which can provide low activation pathways for a specific electrochemical reaction and permit the reactions to occur at high current densities. The catalytic activity of an electrocatalyst depends on the electron configuration of the catalyst material (the intrinsic properties) and the structure and geometry (the actual surface area) of the catalyst. The activity can be measured from the activation overpotential of the catalyst towards the reaction. The activation overpotential is caused by the resistance against the reaction itself at the electrode-electrolyte interface. That is, for any chemical or electrochemical reaction there is an energy barrier, a minimum energy above the average, which the reactants must possess for the reaction to proceed [13]. The rate determining step can be either ion or electron transfer across the interface, or it can also be some kind of conversion of a species involved in the reaction. At a sufficient overpotential and in the absence of mass transfer limitations the relationship between the current density (i) and the activation overpotential (η_{act}) is given by the Tafel equation eq. (13). [17]:

$$\log \pm i = \log i_0 \pm \frac{\alpha nF}{2.3RT} \eta_{act} \tag{13}$$

where α is the transfer coefficient and is determined by the shape of the energy barrier that must be overcome. The plus sign stands for anodic reactions and the minus sign for cathodic reactions. i_0 is the exchange current density, that is the current density at the reversible voltage (E_{rev}) (at ($\eta=0$)). This potential is often called equilibrium potential and can be found in tables in most electrochemistry related books. The Tafel equation is commonly used to find the so-called Tafel slope ($b = \pm \frac{\alpha nF}{2.3RT}$) and the exchange current density for comparing the activity of the electrocatalyst. Obviously, a good electrocatalyst has a high exchange current density and low Tafel slope.

Equation (13) shows that the activation overpotential increases logarithmically with the current density (A/cm^2). Therefore, if a catalyst has a large actual surface area, is rough and porous, the less current is actually applied to each location resulting in lower activation energy. If, for example, 1 A current is applied between anode and cathode in an electrolysis cell with highly polished electrodes having visual surface area of 25 cm^2, the actual current density on the electrodes will be 0.04 A/cm^2. If however the same current is applied to a surfaces with the same visual surface area but much larger actual surface area, for example with roughness factor of 1000. The actual current density becomes 1000 times smaller than for the previous case or $4e^{-5}$ A/cm^2. In that way the electrolysis cell can be operated with low overpotentials at much higher current densities than before.

The hydrogen reaction in an alkaline media is widely accepted to be a combination of the Volmer-Heyrovsky-Tafel mechanism [18]. The activation energy for the mechanism depends of the rate of each step. The slowest step is therefore called the rate determining step. The first discharge step where hydrogen is adsorbed at the electrode surface is known as the Volmer reaction and the second step where hydrogen molecules are formed is known as the Heyrovsky reaction. The recombination of two adsorbed hydrogen atoms is known as Tafel reactions. Both Volmer and Heyrovsky reactions are electrochemical reactions whereas

the Tafel reaction is solely a chemical reaction. In Fig. 5 the reaction steps for the hydrogen evolution reaction (HER) as they take place in alkaline solutions are schematically illustrated.
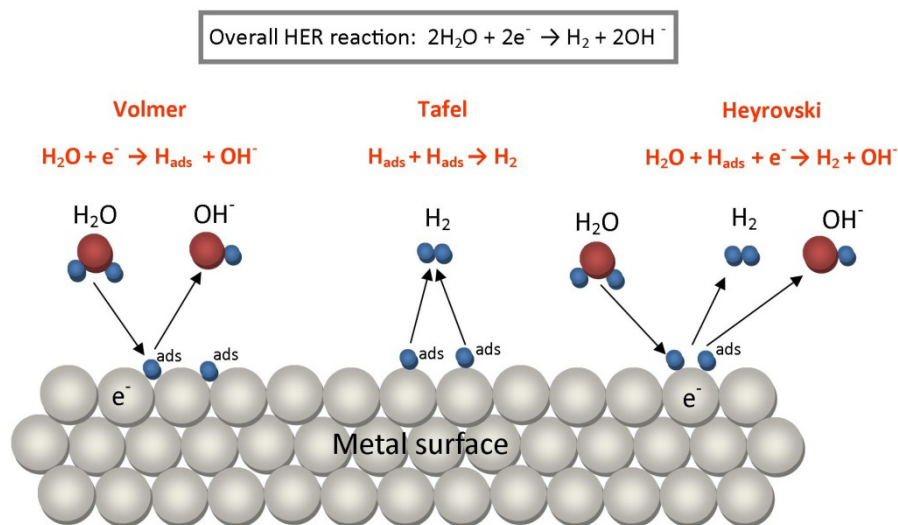
Fig. 5: Elementary reaction steps of HER in alkaline media.

Due to the high population of reactants, that is water, HER does typically not have any diffusion limitations [18]. Most theories state that the adsorbed hydrogen atoms combine into hydrogen molecules either by reacting with further discharging H_2O or by recombining with another adsorbed hydrogen atom. That is either by Volmer –Heyrovsky or Volmer – Tafel pathways. The two discharging steps occur simultaneously and the slower step determines the HER rate.

From the previous it is clear that the ability of a catalyst to adsorb hydrogen atoms plays a key role in the mechanism and kinetics of hydrogen electrodes [19]. The ability to absorb hydrogen depends on the ability of the surface to bond with hydrogen, i.e. the metal hydrogen bond strength (H-M). First of all the absorbed hydrogen changes the free energy of the Volmer step by the amount equal to the free energy of formation of the M-H bond. This means that the Volmer reaction can occur at potential that is $-\Delta G_{ads}$ more positive to the equilibrium potential of the reaction [19]. Secondly, the absorbed hydrogen makes the two other reaction steps possible.

The activation energy of HER (η_{act}) obviously decreases with increased adsorption energy (M–H bond strength), while increased adsorption energy means increase in terms of H_{ads} coverage on the electrode surface. Therefore if the M-H bond energy is too strong for the Tafel reaction to take place, the H_{ads} will occupy the available surface sites and inhibit the second step of the total reaction. Thus the best hydrogen electrode should be the one having an intermediate M–H bond energy (or free energy of hydrogen adsorption ($-\Delta G_{ads}$)), as stated in the Sabatier principle [36]. When plotting the electrocatalytic activity (exchange current density for HER) versus the M–H bond strength for different metals, a so-called volcano plot is formed. The volcano plot in Fig. 6 supports Sabatier's theory and shows clearly that platinum should be the most active metal for hydrogen evolution.
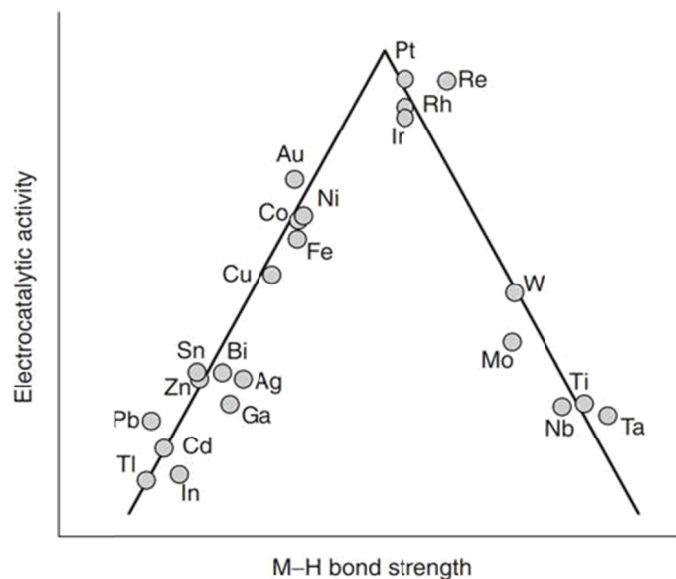
Fig. 6: The dependence of the electrocatalytic activity for HER on the metal – hydrogen bond formed [18]

A more modern way to define the volcano curve principle is based on the electronic configuration of the atoms within the lattice of the catalyst material [20]–[23] or the so-called hypo- hyper-d theory. Here metals on the left side of the volcano plot are called hypo-d-electronic metals because they have empty or half-filled vacant d-orbitals and the metals on the right side of the volcano plot is called hyper-d- electronic elements because they have internally pared d-electrons which are not available for bonding in pure metals. The optimum (best catalyst, the catalyst at the top of the volcano plot) is either defined to be at d^8 or d^5 [24]. It has been shown that by combining hypo-d-electronic metals with hyper-d-electronic metals synergetic electrocatalytic effect resulting in higher activity for HER is reached [24]–[29] NiMo being the most popular composition.

As mentioned before the actual electrocatalytic effect does not only depend on the electron configuration. The structure and topography of the catalyst also has a great influence on the apparent electrocatalytic efficiency and many authors have published an increase in electrocatalytic activity towards the HER by selectively leaching one or more elements from metal alloys [28], [30]–[37]. In addition the rate of the reaction is affected by the crystal orientation and the interaction between the neighbouring species. Also, lattice defects such as dislocations, kinks, vacancies and stacking faults are often recognised as active sides for the HER [38].

The mechanism for the oxygen evolution reaction (OER) is more complex than the hydrogen evolution reaction. Several pathways have been suggested were the most commonly accepted for alkaline water electrolysis are [10]:

$$OH_{ads}^- \rightarrow OH_{ads} + e^- \tag{14}$$

$$OH^- + OH_{ads}^- \rightarrow O_{ads} + H_2O + e^- \tag{15}$$

$$O_{ads} + O_{ads} \rightarrow O_2 \tag{16}$$
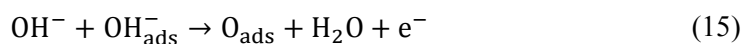
Where one of the charge transfer steps is the rate determining step. The overpotential of the most common OER electrocatalysts is listed in Table 4 in section 3.1.1.2.

The rate of an electrocatalytic reaction, such as the HER, depends not only on the activity of the electrocatalyst. The rate is also determined by the composition of the electrolyte closest to the catalyst. The area is called the double layer and is not taken into consideration in the derivation of the Tafel equation [39]. The electrocatalytic double layer is found on the transition zone where the charge transport changes from being an electron transport to ion transport [40]. The density of electrons closest to the electrode surface depends on the potential of the electrode. In the case of the cathode for HER this means that the amount of OH^- and K^+ closest to the electrolyte is dependent of the electrode potential. Therefore, relatively to the electrolyte the metal layer is seen as negatively or positively charged depending of which ion is dominant. The double layer acts as a capacitor to the electrode reaction due to the charging and discharging of the electrode layer closest to the electrolyte and the change in the electron density of the metal phase. Hence, the double layer phenomenon should therefore be taken into account for kinetic evaluations of electrocatalysts. Thorough explanation of the double layer phenomenon can be found in various textbooks such as [19], [41]–[43].

3 Water Electrolysis Technologies

The water electrolysis technique is not at all a new invention. The technique was developed over two centuries ago by the two companions Nicholson and Carlisle [44]. Today there are three main types of water electrolysis technologies available; these are alkaline electrolysis, polymer electrolyte membrane (PEM) electrolysis (also named solid polymer electrolysis (SPE)) and solid oxide electrolysis cell (SOEC). Alkaline and PEM electrolysis have both reached commercialisation while SOECs are still in the development stage. Commercial alkaline and PEM electrolysers are typically operated at temperatures below 100°C while SOECs are operated at gas phase conditions at temperatures in the range of 800-1,000°C [6]. The advantage of the high operation temperature is a significant reduction in the electrical energy demand for hydrogen production. Consequently, developers of water electrolysis systems are increasingly looking in the direction of higher operation temperatures. The drawbacks of working at elevated temperatures are however greater challenges regarding the decomposition of materials, which often causes corrosion of metals and the degradation of polymers used for sealing and etc., which in fact are the main reasons for the SOECs still being at the R&D stage.

For the commercially available electrolysers, PEM electrolysers display the best efficiencies at higher current densities. The investment cost for PEMs is, nevertheless, at least 10 times larger than for their alkaline counterparties. The capital cost for commercial electrolysers are estimated to be less than $1,000/kW for the largest alkaline systems compared to more than $10,000/kW for small PEM electrolysers [16]. Additionally, the durability of the materials for PEM is much less than for alkaline electrolysis. The lifetime of commercial alkaline electrolysers is said to be about 100,000 hours compared to 10-50,000 hours for PEM electrolysers [45].   The performance data for the main commercial PEM and alkaline electrolysers are listed in Table 1.

Manufacturer	Technology	Production rate (Nm³/h)	Power (kW)	Energy consumption (kWh/Nm³)	Efficiency[a]	Max, pressure (bar)	H₂ purity (vol.%)	Location
AccaGen	Alkaline (bipolar)	1-100	6.7-487	6.7-4.87[b]	52.8-72.7	10 (optional 30) (200[c])	99.9 (99.999[d])	Switzerland
Avalence	Alkaline (monopolar)	0.4-4.6 (139[c])	2-25 (750[c])	5.43-5	65.2-70.8	448	n.a.	USA
Cland	Alkaline (bipolar)	0.5-30	n.a.	n.a.	n.a.	15	99.7 (99.999[d])	
ELT	Alkaline (bipolar)	3-330	13.8-1518	4.6-4.3	76.9-82.3	Atm.	99.8-99.9	Germany
ELT	Alkaline (bipolar)	100-760	465-3584	4.65-4.3	76.1-82.3	30	99.8-99.9	Germany
Erredue	Alkaline (bipolar)	0.6-21.3	3.6-108	6-5.1[b]	59-69.8	2.5-4	99.3-99.8 (99.999[d])	Italy
Giner	PEM (bipolar)	3.7	20	5.4[e]	65.5	85	n.a.	USA
Hydrogen Technologies, division of Statoil	Alkaline (bipolar)	10-500	43-2150	4.3	82.3	Atm.	99.9	Norway
Hydrogenics	Alkaline (bipolar)	10-60	54-312	5.4-5.2[b]	65.5-68.1	10 (optional 25)	99.9 (99.999[d])	Canada
Hydrogenics	PEM (bipolar)	1	7.2	7.2[b]	49.2	7.9	99.99	Canada
H2 Logic	Alkaline (bipolar)	0.66-42.62	3.6-213	5.45-5[b]	64.9-70.8	4 (optional 12)	99.3-99.8 (99.999[d])	Denmark
Idroenergy	Alkaline (bipolar)	0.4-80	3-377	7.5-4.71	47.2-75.2	1.8-8	99.5	Italy
Industrie HauteTechnologie	Alkaline (bipolar)	110-760	511.5-3534	4.65-4.3	76.1-82.3	32	99.8-99.9	Switzerland
Linde	Alkaline (bipolar)	5-250	n.a.	n.a.	n.a.	25	99.9 (99.998[d])	Germany
PIEL, division of ILT Technology	Alkaline (bipolar)	0.4-16	2.8-80	7.5[b]	50.6-70.8	1.8-18	99.5	Italy
Proton OnSite	PEM (bipolar)	0.265-30	1.8-174	7.3-5.8	48.5-61	13.8-15 (optional 30)	99.999	USA
Sagim	Alkaline (monopolar)	1-5	5-25	5	70.8	10	99.999	France
Teledyne Energy	Alkaline (bipolar)	2.8-56	n.a.	n.a.	n.a.	10	99.999	USA
System Treadwell Corporation	PEM (bipolar)	1.2-10.2	n.a.	n.a.	n.a.	75.7	n.a.	USA

Table 1: An overview of the main current electrolyser manufacturers, their product and performance data. The table is adopted from [46].

n.a: information not available
[a] Calculated according to the HHV of hydrogen (3.54 kWh/Nm³)
[b] Based on the global hydrogen production system
[c] In development
[d] With an additional purification system
[e] Only based on the electrolysis process

As seen from the table, alkaline electrolysers have by far the largest power capacity and are available up to the 3.5 MW range, compared to the maximum of 175 kW for PEM. The low power consumption and, thus, low production rate for PEM electrolysers makes alkaline electrolysis the current standard for large-scale hydrogen production among water decomposition techniques.

In the following chapter the three main types of water electrolysis technologies, alkaline, PEM and SOEC, will be introduced. Due to the nature of the thesis, a more detailed overview will be fashioned for the alkaline electrolysis technique compared to the other two.

3.1 Alkaline Water Electrolysis

Alkaline water electrolysis is the most mature water electrolysis technology and already in 1920s several MW plants had been produced worldwide [47]. The technique is considered to be simple and durable and lifetime up to 90-100.000 operation hours have been reported [45],[48]. Typical efficiency for commercial alkaline electrolysers is 60-75% and 80-85% for the best small scale systems [7]. Commercial alkaline electrolysers are typically operated in a liquid electrolyte containing 25-40% potassium hydroxide at a temperature ranging from 60-90°C [7],[10],[49]. The largest cell efficiency losses for alkaline electrolysis originates from the activation energies for hydrogen and oxygen, gas bubbles in the electrolyte and gas bubble coverage on the electrode surfaces. All of these overpotentials are related to the current density. Accordingly, the ohmic drop in an electrolysis cell increases dramatically with increased current density. Hence, in order to maintain moderate efficiencies of up to 82% HHV, the current density has to be kept relatively low or in the range of 100-400 mA/cm^2 [16]. The electrolysers are typically operated at 1-30 bar, depending on their application. High pressure operation can reduce the ionic resistance caused by gas bubbles in the electrolyte, due to shrinkages of bubbles, and save the cost of compressing hydrogen after production.

The electrolysis cell consists of two electrodes; an anode and a cathode, separated by an ionic conducting diaphragm. The diaphragm further serves as a gas separator to prevent mixing of hydrogen and oxygen gases during operation. The operational principle for AWE is illustrated in Fig. 2 (in chapter 2). When current is applied between the two electrodes, water molecules surrounding the cathode are decomposed into hydrogen (H_2) and hydroxyl ions (OH^-). The hydroxyl ions, which are negatively charged, migrate through the diaphragm to the positively charged anode, where water and oxygen are formed. The half-cell reactions and the charge carriers for the three main water electrolysis processes are listed in Table 2.

Technology	Cathode (HER)	Anode (OER)	Charge carrier
Alkaline	$H_2O + 2e^- \rightarrow H_2 + 2OH^-$	$2OH^- \rightarrow \frac{1}{2}O_2 + H_2O + 2e^-$	OH^-
PEM	$2H^+ + 2e^- \rightarrow H_2$	$H_2O \rightarrow \frac{1}{2}O_2 + 2H^+ + 2e^-$	H^+
SOEC	$H_2O + 2e^- \rightarrow H_2 + O^{2-}$	$O^{2-} \rightarrow \frac{1}{2}O_2 + 2e^-$	O^{2-}

Table 2: Half-cell reactions and charge carriers for the three main types of water electrolysis [49]

3.1.1 Cell components

3.1.1.1 The diaphragm

The purpose of the diaphragm is to keep the produced gases in each cell compartment to prevent recombination and contamination.

The criteria for the diaphragms are:

- Permeable for hydroxide ions and water
- Impermeable for gases
- Mechanical and chemical resistance to the electrolysis media
- Low ohmic resistance

Diaphragms typically have higher ionic resistivity compared to the electrolyte. In order to minimize the potential drop over the diaphragm, the diaphragms are produced as thin as possible. There is, nonetheless, a trade-off between reduction of thickness of the diaphragm and its mechanical stability.

Earlier the diaphragms for alkaline water electrolysers were made of asbestos. Now asbestos is prohibited due to its toxicity. Composite materials based on micro porous polymers or ceramics such as polyphenylene sulfide (Ryton®) [50] and polysulfone bonded ZrO_2 (Zirfon®) [51], have gradually substituted asbestos in the newer generations of alkaline electrolysers [52]. Scanning electron micrographs of a Zirfon® Perl 500 UTP diaphragm applied in this study is shown in Fig. 7. The white particles in the figure are ZrO_2 powder and the grey mesh is the polysulfone matrix.
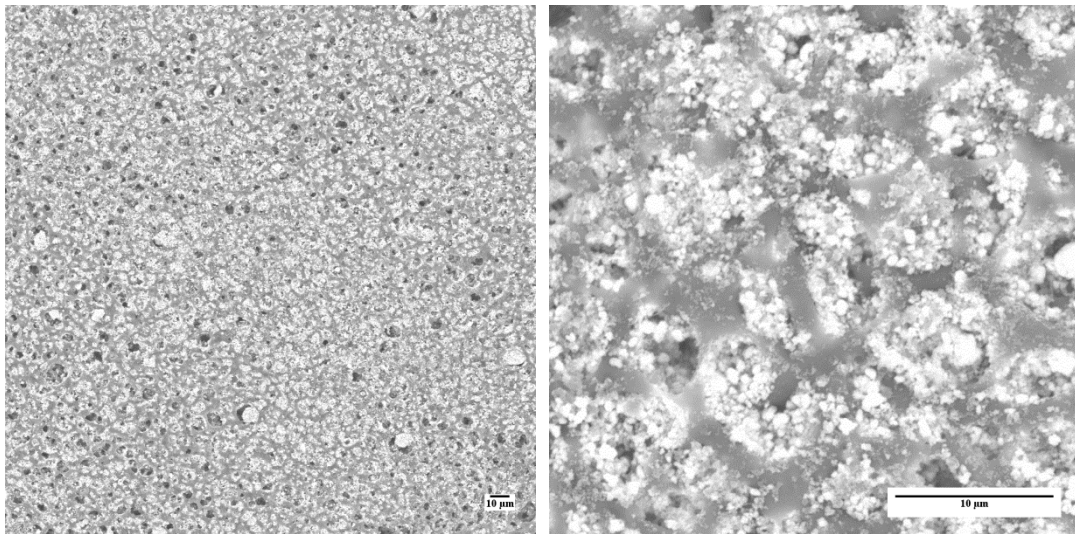
Fig. 7: Scanning electron micrograph of a Zirfon® Perl 500 UTP diaphragm utilised in this study. The white particles are ZrO_2 powder and the grey mesh is polysulfone.

3.1.1.2   The electrodes

The two electrodes, anode and cathode, at each side of the diaphragm must to be stable in the electrochemical cell, i.e. they should not corrode, and at the same time be a good catalyst for the electrochemical reaction taking place at their surfaces. Platinum is stable in alkaline environment and is known to be the best electrocatalyst for water electrolysis, especially for the hydrogen formation [18]. However, due to its high price, other less expensive materials have replaced platinum electrodes in AWE systems.

Among un-noble metals, nickel is one of the most stable in strong alkaline solutions [53], [54]. Nickel is also a relatively good catalyst for hydrogen and oxygen formation. Nickel or nickel plated substrates are therefore typically the core material used in electrodes for AWE systems [6],[10][45]. The nickel electrodes are typically activated by adding sulphur to the coatings or by producing a so-called Raney nickel structure on the surface. The method of sulphur activation of nickel electrodes dates back to at least 1923 with a Germanic patent thereof [55]. More recently, in 1978, Norsk Hydro (now NEL Hydrogen) patented a sulphurising process presented to give more mechanically stable cathodes than the former patent [56]. The effect of adding sulphur to the nickel coating is not fully known. It has been suggested that it is the formation of strongly absorbed hydrogen in the Ni-S structure being the reason for the increase in catalytic efficiency, compared to pure nickel electrodes [57].

In 1961 Justi and Winsel [58] discovered that Raney nickel (originally developed as a catalyst for hydrogenation of vegetable oils) was an effective hydrogen electrocatalyst for alkaline electrolysis. The principle behind Raney nickel catalysts is that aluminium or zinc is selectively leached from a NiAl or NiZn alloy. Lattice vacancies formed when leaching result in a large surface area and a high density of lattice defects, which are active sites for the electrocatalytic reaction to take place [38]. Since then, increasing the surface area and altering the electrocatalytic configuration of an electrocatalyst by selectively leaching one or more element from the metal alloys has widely been used to promote the activity of hydrogen electrocatalysts [15],[28], [32], [34], [37], [59], [60]- [63].

Beside the Raney nickel and nickel sulphide activation, attempts have been made to increase the electrocatalytic performance of nickel cathodes by doping with active substances such as Fe, Co and Mo [59],[63]–[66]. The stability of the dopants during operation is, however, questionable and the deactivation of Ni-Mo electrocatalyst over time has been reported [66], [67]. An overview of the hydrogen overpotential for different hydrogen electrocatalysts found in the literature is shown in Table 3.

Mixed oxides such as $LaNiO_3$, $NiCo_2O_4$ and Co_3O_4 as well as Raney nickel and Raney Co all display a high activity as oxygen electrocatalysts for AWE [68]-[75]. The literature implies that despite of the large amount of work directed towards finding the optimal oxygen electrode, few of the developed electrocatalysts have the sufficient durability or a low enough price to be feasible for industrial electrolysers [6]. An overview of the oxygen overpotential for different oxygen electrocatalysts found in the literature is shown in Table 4.

Composition	Preparation method	Working temp. (°C)	Electrolyte	Current density (mA cm^{-2})	$\eta_{hydrogen}$ (mV)	Publication year and [ref.]
Ni–Fe–Mo–Zn	Co-deposition	80	6M KOH	135	83	2004 [59]
Ni–S–Co	Electro-deposition	80	28 wt.% NaOH	150	70	2003 [76]
Ni50%–Zn	Electro-deposition	N/A	6.25 M NaOH	100	168	2002 [60]
MnNi$_{3.6}$Co$_{0.75}$Mn$_{0.4}$Al$_{0.27}$	Arc melting	70	30 wt.% KOH	100	39	2000 [61]
Ti$_2$Ni	Arc melting	70	30 wt.% KOH	100	16	1998 [77]
Ni50%Al	Melting	25	1 M NaOH	100	114	1993 [62]
Ni75%Mo25%	Co-deposition	80	6 M KOH	300	185	1993 [63]
Ni80%Fe18%	Co-deposition	80	6 M KOH	300	270	1993 [63]
Ni73%W25%	Co-deposition	80	6 M KOH	300	280	1993 [63]
Ni60%Zn40%	Co-deposition	80	6 M KOH	300	225	1993 [63]
Ni90%Cr10%	Co-deposition	80	6 M KOH	300	445	1993 [63]
Raney-nickel	Plasma-spray of Al/Ni alloy	160	30 wt.% KOH*	1000	150	1987 [15]
NiS-PTFE NiCoS-PTFE	Emulsion-paint of sulphide and PTFE, annealing at 300°C	90	30 wt.% KOH*	1000	100	1987 [15]
Sinter-nickel	Sintering of carbonyl-nickel	120	30 wt.% KOH*	1000	160	1987 [15]
NiS-reduced	Cathodic deposition of rough Ni/NiS-mixture activation of deposit in situ	120	30 wt.% KOH*	1000	150	1987 [15]
Raney Ni	Cathodic deposition of Zn/Ni,	90	30 wt.% KOH*	1000	250	1987 [15]
Raney Ni/Co-NiS	Cathodic deposition Zn/Ni/Co and Ni	90	30 wt.% KOH*	1000	150	1987 [15]
NiS	Electro-deposition	60	1M NaOH	100	97	1984 [57]
Skeleton nickel	Thermal arc spraying	25	1M NaOH	10	240	2007 [32]
Nickel-titanium	Thermal arc spraying	80	1M NaOH	100	240	2007 [32][33]
Ni$_2$Al$_3$	Pressed and heated	25	1 M KOH	250	280	2004 [28]
Ni$_2$Al$_3$Mo$_{0.306}$	Pressed and heated	25	1 M KOH	250	160	2004 [28]
Ni$_2$Al$_5$	Pressed and heated	25	1 M KOH	250	253	2004 [28]
Ni$_2$Al$_5$Mo$_{0.233}$	Pressed and heated	25	1 M KOH	250	60	2004 [28]
NiAl3	Pressed and heated	25	1 M KOH	250	136	2004 [28]
NiAl$_3$Mo$_{0.306}$	Pressed and heated	25	1 M KOH	250	57	2004 [28]
NiAl$_{5.95}$Mo$_{0.66}$	Plasma sprayed	25	1 M KOH	250	67	2004 [28]
Ni-Mo nanopowder	Synthesised	25	2 M KOH	20	70	2013 [27]
Cu/Ni	Electro-deposition	25	1 M KOH	100	350	2011 [78]
Cu/NiCoZn	Electro-deposition	25	1 M KOH	100	140	2011 [78]
Cu/NiCoZn–Ag	Electro-deposition	25	1 M KOH	100	100	2011 [78]
Cu/NiCoZn–Pd	Electro-deposition	25	1 M KOH	100	104	2011 [78]
Cu/NiCoZn–Pt	Electro-deposition	25	1 M KOH	100	96	2011 [78]
C/NiMn	Electro-deposition	25	1 M KOH	100	141	2013 [79]
C/NiMnZn	Electro-deposition	25	1 M KOH	100	127	2013 [79]
C/NiMnZ-PtPd	Electro-deposition	25	1 M KOH	100	121	2013 [79]
C/NiMnZ-PtRu	Electro-deposition	25	1 M KOH	100	118	2013 [79]

Table 3: An overview of the hydrogen overpotential for some electrocatalysts for AWE found in the literature.
* The author states that the electrolyte giving the highest conductivity at the working temperature is used (compatibly with material corrosion). It is however indicated in the text that most of the electrodes are measured at 30 wt.% KOH.

Composition	Preparation method	Working temp. (°C)	Electrolyte	Current density (mA cm-2)	$\eta_{hydrogen}$ (mV)	Publication year and [ref.]
LaNiO$_3$	co-precipitation	25	1 M KOH	100	315	1982 [80]
La$_{0.5}$Sr$_{0.5}$CoO$_3$	Spray-sinter	90	50 wt.% KOH	100	250	1989 [74]
Ni$_{0.2}$Co$_{0.8}$LaO$_3$	Plasma jet projection	90	50 wt.% KOH	100	270	1989 [74]
Raney Ni	Electro-deposition of Ni-Zn, heat treated f. 12 h. @400 °C	90	50 wt.%	100	280	1989 [74]
Raney-Co	Spray-sinter	90	50 wt.% KOH	100	230	1989 [74]
Co$_3$O$_4$	Spray -sinter	90	50 wt.% KOH	100	240	1989 [74]
Ni-Ir	Electro-deposition	25	5 M KOH	20	270	1990 [72]
Ni-Ru	Electro-deposition	25	5 M KOH	20	280	1990 [72]
Li 10% doped Co$_3$O$_4$	Spray pyrolysis	Room temp.	1 M KOH	1	550	2004 [81]
Ni + Spinel type Co$_3$O$_4$	Thermo-decomposition	25	1 M KOH	100	235±7	2007 [82]
Ni +La doped Co$_3$O$_4$	Thermo-decomposition	25	1 M KOH	100	224±7	2007 [82]
MnOx modified Au	Electro-deposition	25	0.5 KOH	10	300	2007 [83]
NiCo Aerogel	Epoxide addition process	25	1 M KOH	100	184	2011 [84]
NiFe(OH)$_2$	Electro-deposition	80	1 M NaOH	500	265	2011 [85]

Table 4: An overview of the oxygen overpotential for some electrocatalysts for AWE found in the literature.

As the present section indicates, a great deal of work has been devoted to the development of electrodes for AWE during the past 90 years. The state-of-the-art electrodes have, however, not changed much during the years. Among the newly developed electrocatalysts, durability measurements are usually lacking and few of the published electrocatalysts have actually been tested in real electrolysis systems and at current densities appropriate for them. One of the best electrolysis cell performances measured in an electrolysis stack originate from two different R&D hydrogen programs carried out in the 1980s and 1990s [86],[87]. In the earlier work, carried out at the Belgian Nuclear Research Centre (S.C.K,/C.E.N.), a cell voltage of 1.6 V measured at 90°C and 0.2 A/cm^2 is reported. The electrodes are described as perforated nickel, coated with Ni-S at the cathode and spinel oxides containing Ni and/or Co at the anode. In the latter research program, carried out at the German Aerospace Center (DLR), vacuum plasma sprayed electrodes were used. The cathode was made of Mo containing Raney nickel and the anode of spinel oxides of Raney Ni/Co. They published cell voltages ranging from 1.6 to 1.65 measured at 80°C and 0.3 A/cm^2. Both of the research programs used a zero-gap cell structure, as described in section 3.1.2.2.

As mentioned above, the literature implies that the state-of-the-art electrodes used for industrial electrolysers today, both anode and cathode, is sulphur or Raney activated nickel or nickel coated steel [6],[10]. By combining the development work published on

electrolysers and electrocatalysts, rough ideas about the state-of-the-art electrodes used in the industry today can be made. The exact structure and configuration of the electrodes is, nevertheless, kept confidential.

3.1.1.3   The electrolyte

The good conductivity, compared to other bases, and the less corrosive properties, compared to acids, makes potassium hydroxide (KOH) the most commonly used electrolyte for water electrolysis systems [47]. The conductivity of the KOH electrolyte depends on the temperature and concentration. In order to minimize the electrolyte resistivity in an electrolysis system, it is essential to find the concentration which gives the highest conductivity at the operating temperature. In 1997 See and White presented a thorough study of the conductivity of aqueous KOH in the temperature range of -15 to 100°C for concentrations of 15-45 wt.% [88]. More recently, Gilliam et. al. used the available conductivity data for KOH to develop an equation for calculating the conductivity of KOH in the range of 0-12 M and 0-100°C [89]. Using their results, Allebrod et. al. redrew a 3D plot of the conductivity of aqueous KOH as a function of temperature and concentration, see Fig. 8.
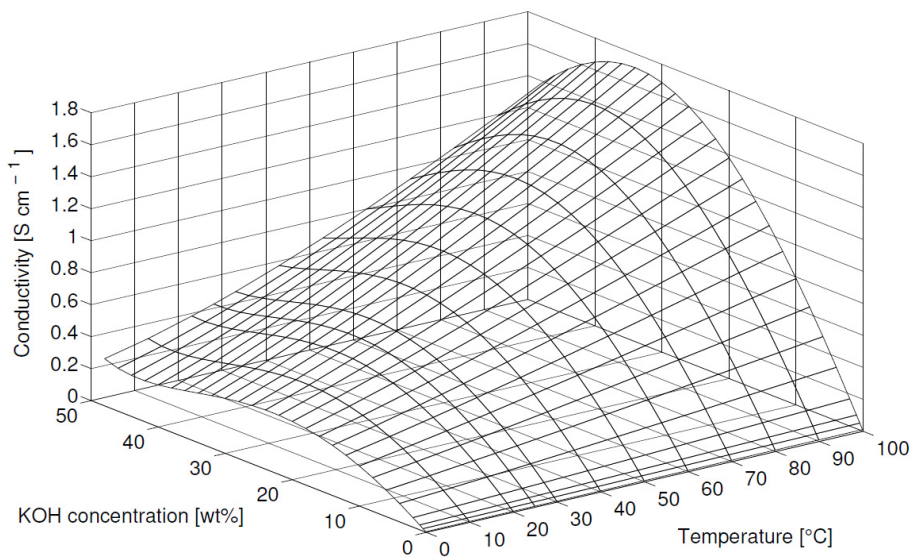
Fig. 8: 3D plot of the conductivity of aqueous KOH as a function of temperature and concentration [90]. Courtesy of Frank Allebrod.

As seen from the figure, the highest conductivity for aqueous KOH in the range of 80-100°C is reached between 30 and 40 wt.% KOH. The pH of the electrolyte rises in proportion to the amount of hydroxide ions in the solution according to [91]:

$$pH = 14 - pOH^- \tag{17}$$

where:

$$pOH = -log[OH^-] \tag{18}$$

which for a strong base such as KOH can be written as:

$$pOH = -log[KOH] \qquad (19)$$

Increasing the amount of KOH leads to higher pH and therefore a more aggressive alkaline environment for the components of the electrolysers. Higher temperature has an increasing effect on the corrosion rate as well. As a result, operating with KOH concentration and temperatures slightly lower than where the optimum can be necessary for increasing the lifetime of the electrolysis components, especially electrodes and diaphragm.

During the past three decades researchers in the field of AWE have become more aware of the large energy losses caused by gas bubbles in the electrolyte. Thus, more effort has been put in analysing and finding solutions for the so-called bubble phenomena [14], [92]–[96]. Already few solutions are in place for decreasing the ohmic drop caused by the gas bubbles. Firstly, an electrolyte flow is usually applied to endorse bubble separation from the electrode surfaces during operation. Secondly, the electrolysis cells are pressurised in order to reduce the gas bubble volume and, thirdly, zero gap configurations, as described in section 3.1.2.2, are used to minimise the amount of gas bubbles in the electrolyte between electrodes and diaphragms. These solutions do, nonetheless, only eliminate the high ohmic resistance caused by the bubble phenomena to a limited extent [14]. More recently many authors have reported a dramatic reduction in the ohmic drop by applying an external field such as magnetic, ultrasonic and super gravity to the electrolysis cell [94], [97]–[100]. The external fields promote the detachment of bubbles from the electrode surface during electrolysis. As a consequence the current density is increased since more active sites are available for the processes to proceed.

Another relatively new field in AWE is to apply ionic activators to the electrolyte to lower the anodic and cathodic activation energies. The process is typically based on in-situ metal deposition on the electrode surfaces, which are said to exhibit better catalytic activity than ex-situ processes. For the hydrogen reaction these can be ethylenediamine-based metal chloride complex ([M(en)$_3$]Clx, M=Co, Ni, etc.) together with Na$_2$MoO$_4$ or Na$_2$WO$_4$ [66], [101]–[103]. Nikolic et al. [101] reported energy savings of up to 15% for electrodes activated in situ with [Co(en)$_3$]Cl$_3$ and Na$_2$WO$_4$, compared to non-activated electrodes. The acceleration in electrochemical activity was explained by an increase in the actual surface area of the hydrogen electrodes. Tasic et al. [104] propose that the enhanced catalytic activity when applying Na$_2$MoO$_4$ and [Ni(en)$_3$]Cl$_2$ ionic activators in situ, is caused by the synergetic effect of increased true surface area and improved intrinsic catalytic effect.

Compared to the amount of research work available for electrodes and diaphragms, an extremely small amount of work is accessible in the field of electrolyte development. The research field of electrolytes for AWE systems is, therefore, still unexplored and yet new discoveries are to be expected. Surfactants that influence the wettability of the electrodes and makes them more hydrophobic could, for instance, be beneficial for minimising the amount of gas bubbles attached to the electrode surfaces during operation.

3.1.2   Cell configuration

3.1.2.1   Bipolar vs. monopolar

Until now only the components and configurations of the AWE unit cell have been discussed. But in fact, industrial electrolysers are composed of multiple electrolysis cells connected in parallel or in series. There are two primary electrolysis configurations available, commonly known as monopolar and bipolar [46], see Fig. 9 and 10.
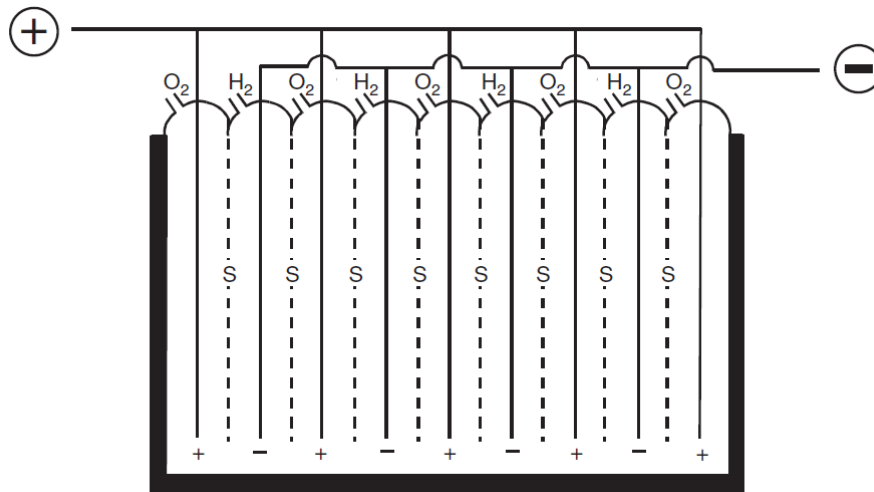
Fig. 9: Illustration of a monopolar stack configuration. S stands for the diaphragm separator [7].
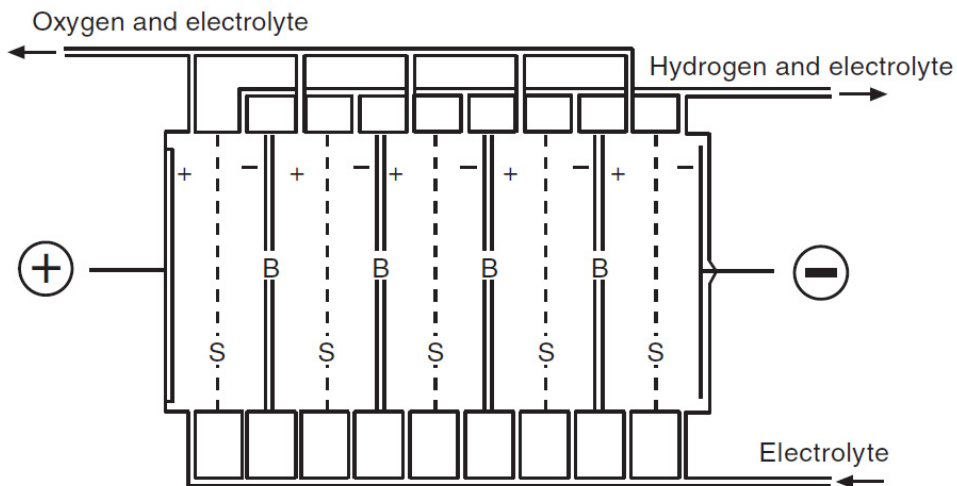
Fig 10: Illustration of a bipolar stack configuration. S stands for the diaphragm separator and B for bipolar electrode [7].

In a monopolar electrolyser each individual electrode is fed with a current from the outside and has a single polarity (monopolar), i.e. it is either a cathode or an anode. In an electrolysis stack the cells are connected in parallel. The voltage across the whole stack is the same as the voltage across any individual cell irrespective to the number of electrode pairs in the tank [16]. In a bipolar electrolyser, each electrode is an anode on the one side and a cathode on the other (bipolar). Thus, every two neighbouring electrodes form a unit cell. The cells are

connected in series and current is fed only to the end electrodes in the stack. The voltage across the whole stack of n cells is equal to n times the voltage of an individual cell [46].

Monopolar electrolysers have a simple and robust structure made of relatively inexpensive parts. Individual cells are easily isolated for maintenance. The essential drawback of the monopolar electrolysers is their large surface area which makes them more space requiring, unable to operate at high temperatures because of heat losses and increases the risk for potential drop in the cell hardware.

The bipolar electrolysers are more compact and generally more efficient which makes them more common in industrial applications. They can work at higher current densities and at higher pressure and temperature. This nevertheless introduces more challenging design issues for preventing electrolyte and gas leakage between cells [10].

For both the bipolar and the monopolar construction it is important to minimise the space between the electrodes and the diaphragm, in order to reduce the portion of cell overpotential from the electrolyte resistance. If, however, the space between the electrodes and the diaphragm is too small the flow of electrolyte, which determines the mass transport in the electrolyte, can be limited.

3.1.2.2   Zero-gap and non-zero-gap design

The electrodes and the diaphragm can be assembled in two ways, namely, non-zero-gap and zero-gap configurations, see Fig. 11.
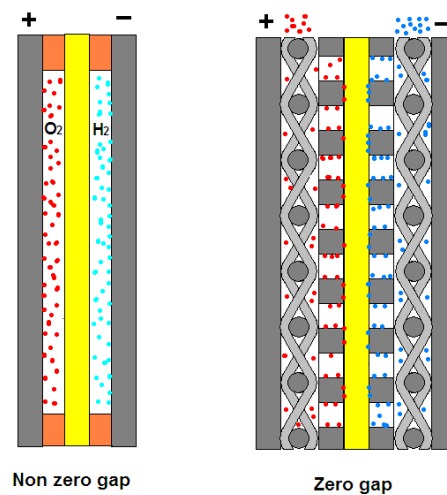
Fig. 11: Illustration of non-zero-gap and zer-gap configuration for AWE systems. Courtesy of GreenHydrogen.dk.

For the non-zero gap structure, solid electrodes are placed a few millimetres away from the diaphragm. The gases produced evolve from the electrodes and drift up in the space between the electrodes and the diaphragms. This means that during electrolysis the electrolyte between the electrode and diaphragm will be filled with gas bubbles resulting in a major increase in the ohmic loss from the electrolyte. The zero-gap configuration was designed in

order to minimize this problem [105]. For the zero-gap structure the diaphragm and electrodes are closely packed. The electrodes are perforated, so the electrolyte and gases can flow away from the electrode/diaphragm interface and evolve on the "back" of the electrodes.

3.2 High temperature alkaline water electrolysis (HTAWE)

By increasing the operation temperature for AWE the efficiency can be significantly increased. A great deal of research and development work has been dedicated to the development of AWE techniques at temperatures above 120°C [106]–[109]. Recently Allebrod et. al. [110] reported results from an alkaline electrolysis cell operated at temperatures up to 250°C at 42 bar. The cell was measured to operate at only 1.5 and 1.75 V potential, at current densities of 1 A/cm^2 and 2 A/cm^2, respectively. This corresponds to 85-99% efficiency according to the HHV, which is much larger than earlier reported for alkaline systems at high current densities. For comparison, H. Vandenborre et. al. reported a cell voltage of 1.6 V at 90°C and 1.5 V at 120°C for an alkaline electrolyser operated at 0.2 A/cm^2 current density [86]. Increasing the current density to 1 A/cm^2 resulted in a cell voltage of 1.9 V and 1.8 V for 90 and 120°C respectively. However, it is important to remember that the energy needed in order to heat and pressurise the cell is not taken into account for the efficiency measurements made by Allebrod et.al. The developers for such techniques usually assume availability of low cost heat sources when and if used in practise.

As for the SOECs, the HTAWEs are still in the R&D stage, where the drawbacks in the development of the HTAWE are mainly the low stability of the materials at the elevated temperatures. The big question is, therefore, if the efficiency benefit made by the high temperature is sufficient to compensate for the research, development and material cost associated with the HTAWE systems. The author is not aware of any published data for long time durability measurements of such systems. This indicates that the R&D is still at an early stage.

3.3 Polymer Electrolyte Membrane (PEM) electrolysis

PEM electrolysis is constructed in a similar way as the alkaline electrolysis. Fig. 12. shows the outline of a PEM electrolysis cell.
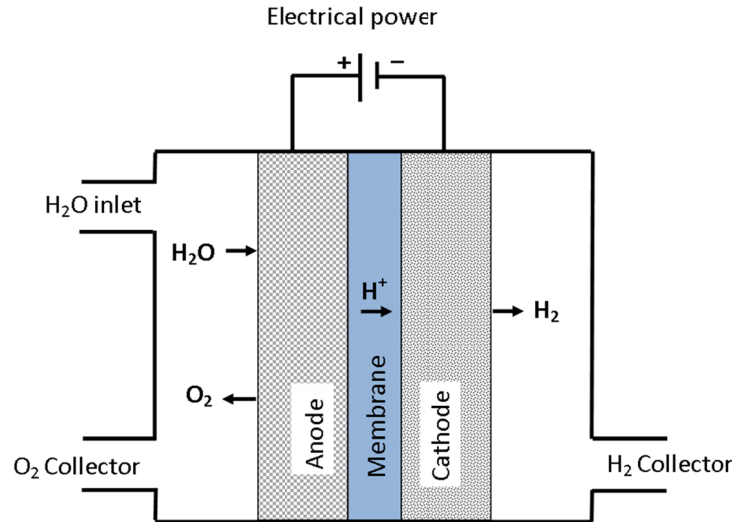
Fig. 12: Outline of the operating principle of a PEM electrolysis cell.

The main difference between the AWE and the PEM electrolysis is that an acidic solid membrane, typically Nafion, is used as an alternative to the alkaline liquid electrolyte. The membrane also acts as a gas separator for the production. When current is applied across the cell the deionised water present at the anode decomposes into oxygen and hydrogen ions (protons). Due to the presence of the sulfonic acid ($-SO_3H$) groups in the membrane the protons formed at the anode are able to migrate to the cathode and form hydrogen [111]. See half-cell reactions in Table 2 in section 3.1.

PEM electrolysers are operated under similar conditions as alkaline electrolysers. However, in contrast to the alkaline system, PEM electrolysis can operate at current densities up to 2.000 mA/cm^2 without diminishing the cell efficiency extensively [48]. This is due to the tightly packed structure of the electrodes and the membrane, often called membrane electrode assembly (MEA), and the thin (< 0.2 mm) and highly conductive polymer membrane that assures particularly low cell resistance. PEM electrolysers are most often produced according to the bipolar cell concept for proper evacuation of the gases.

The acidic environment makes the development of non-noble metal catalyst for the system extremely challenging. Thus, the electrodes typically consist of noble metals such as platinum or iridium, owing their share in the high price of the electrolysers. Currently PEM electrolysers only exist in small scales with maximum hydrogen productivity of 30 Nm^3/h. The small and compact structure of the electrolysers enables the electrolysers to be pressurised easily [16].

3.4 Solid Oxide Electrolysis Cell (SOEC)

As the name succests, the electrolyte for SOECs is made of a solid ceramic material that conducts oxygen ions. High operating temperatures are necessary for attaining acceptable ionic conductivity in the ceramic membrane. Equally to the PEM, meanwhile being the ionic conductor for the system, the membrane also acts as a gas separator. As mentioned before, SOECs operate at the vapour-phase, in the range of 800-1000C°, allowing a greater portion of the required energy to come from heat instead of electricity [6]. The high operating temperature calls for the use of expensive materials and fabrication methods. The electrolysis cell typically consists of an electrolyte of yttria stabilized zirconia (YSZ), a cathode made of nickel and YSZ containing cermet and an anode composite consisting of strontium-doped YSZ and perovskites such as $LaMnO_3$, $LaFo_3$, or $LaCoO_3$ [112], [113]. The operating principles for SOECs are schematically illustrated in Fig. 13.
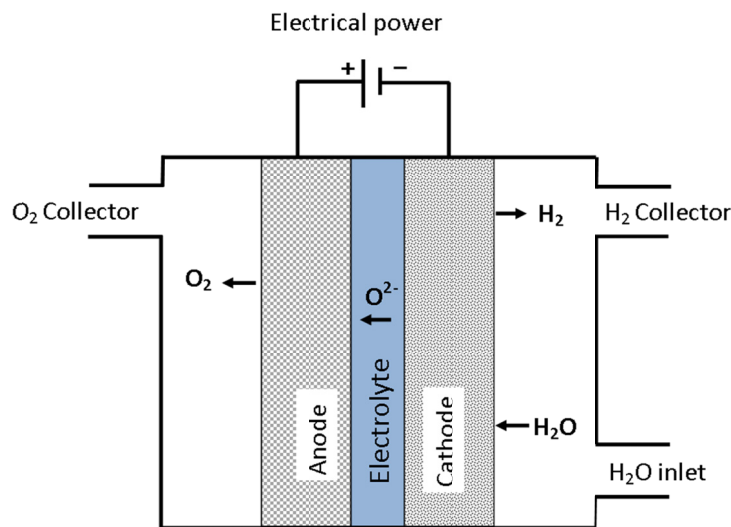
Fig. 13: Outline of the operating principle of a SOEC.

During operation water steam is fed to the cathode, where water is reduced to hydrogen gas (H_2) and the oxide ion (O^{2-}). The anions migrate through the porous solid oxide leading to formation of oxygen gas and release of electrons at the anode. The half-cell reactions are shown in Table 2 in section 3.1.

The SEOC technology was adopted from the solid oxide fuel cell (SOFC) technology in the 1980s [114], yet the solid oxide electrolysers are still in the research and development phase. When disregarding the energy needed to heat up the electrolysis cell its efficiency can reach 90%, but when including the efficiency loss from low price heating, the overall efficiency can only reach 60% [10].

4 Methodology for Testing and Characterisation

4.1 Structure and morphology

Numerous electrode surfaces have been developed and manufactured in the present PhD study. The structure and morphology of the produced surfaces were investigated by the means of light optical microscope (LOM) and scanning electron microscope (SEM). For the purpose of fast initial screening of the developed structures LOM or low magnification SEMs were used. Selected specimens were investigated in high magnification SEMs where further local microstructure investigations such as electron backscatter diffraction (EBSD) and ion channelling contrast imaging (ICCI) could be performed.

The light optical microscope used was an Olympus GX41 with an ALTRA 20 soft imaging system camera attached. TM 3000 Tabletop scanning electron microscope from Hitachi, with an integrated energy-dispersive X-ray spectroscopy (EDS), or JEOL JSM 5900 scanning electron microscope, with and integrated energy-dispersive X-ray spectroscopy from Oxford Instruments, were used for all low resolution SEM investigations. For high resolution (HR) SEM investigations a FEI Quanta 200 ESEM FEG and FEI Helios EBS3 were utilised. For EBSD and ICCI investigations a FEI Helios EBS3 was used.

For cross section investigation the specimens were prepared as follows:

- Hot-mounting in resin (more delicate specimens where cold mounted in epoxy via vacuum impregnation)
- Grinding down to 4000 grit
- Polished with 3 μm and 1 μm diamond
- Selected specimens were mechanical/chemical polished with 0.04 μm colloidal silica for increasing the contrast between grains
- The mounted specimens were carbon coated prior to the SEM investigations

For EBSD and ICCI investigations the specimens were prepared as follows:

- Mounted in a custom made sample holder where the specimen could be demounted after preparation
- Grinding down to 4000 grit
- 3, 1 and 0.25 μm diamond polishing
- Mechanical/chemical polishing with 0.04 μm colloidal silica

4.2   Composition and phase analysis

The EDS instruments attached to the SEMs used were utilised for elemental analyses of the specimens. Phase analyses base on crystallography were performed via X-ray diffraction (XRD) on a Bruker AXS, D8-Discover instrument with Cu K_α radiation.

4.3   Efficiency and durability measurements

In order to evaluate the electrocatalytic activity and durability of the developed electrodes, various electrochemical measurements were performed. The following techniques were used:

- Potentiodynamic polarisation
- Cyclic voltammetry (CV)
- Electrochemical Impedance Spectroscopy (EIS)
- Electrolysis cell measurements
- Electrolysis stack measurements

The potentiodynamic, CV, EIS and electrolysis tests were carried out in specially designed electrochemical half-and whole cells, whereas the stack measurements were performed in a commercially available AWE bipolar stack. The construction of the test setups are presented in chapter 5.

4.4   Pre-electrolysis

During long term durability measurements, a degradation of the electrode activity is often seen. Fig. 14 shows a degradation trend for a high surface nickel electrode developed in this study. The measurements are carried out in 1 M KOH, 25°C at fixed cathodic potential of -1256 mV vs. the standard hydrogen electrode (SHE) for 93 hours. The resistances from the electrolyte and gas evolution were not compensated. Hence, the noise is due to the formation of hydrogen gas at the operating potential.
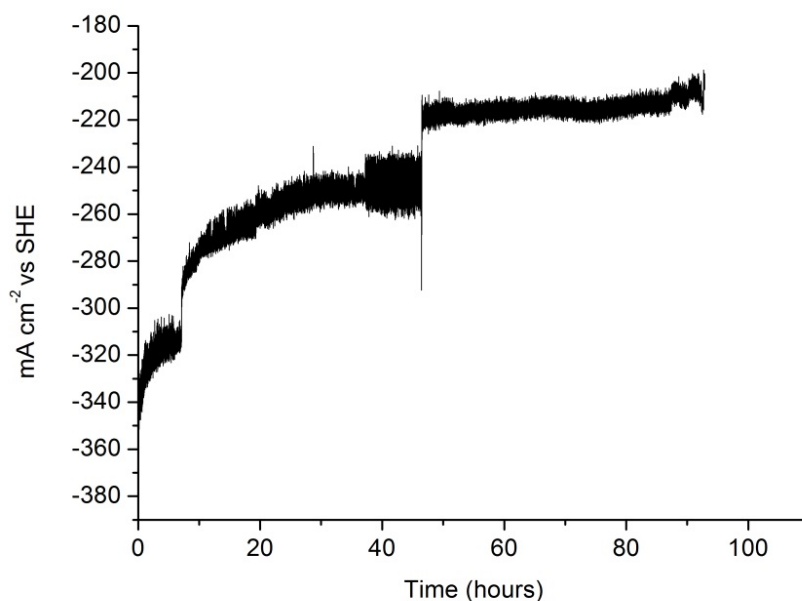
Fig. 14: Degradation of a high surface area nickel cathode during 93 hours of testing at -1256 mV fixed potential.

The reason for the deactivation is changes in the electron configuration of the electrodes making the electrodes less active hydrogen electrocatalysts. This can be due to the formation of nickel hydride phases inside the electrode lattice, corrosion or deactivating contaminants on the electrode surfaces.

Several authors have described deactivation of nickel cathodes during hydrogen evolution by hydrogen absorption and subsequent formation of nickel hydride in the metal lattice [115]–[118]. The same authors have shown that nickel electrodes can be reactivated by adding dissolved vanadium oxide (V_2O_5) to the electrolyte. Using vanadium oxide in industrial electrolysers is, however, not desired due to its high toxicity to living organisms and the environment.

The cause of the degradation can also be contaminants from the electrolyte that are reduced or absorbed on the electrode surface. This is especially the case for the cathode because at the HER potential many metals can be reduced. One could think that selecting analytically clean chemicals, such as KOH, would eliminate this problem. Nevertheless, even the cleanest chemicals commercially available contain some traces of other substances. For the experiment performed in Fig. 14 analytically clean KOH from Merck KGaA was used. The fabricant reports the following contaminants, among others, in the specifications for the chemical.

Contaminant specie	[%]
Ca	< 0.001
Cu	< 0.002
Fe	< 0.0005
Pb	< 0.0005
Zn	< 0.0025
Heavy metals	< 0.0005

Table 5: Contaminant residues in analytical clean KOH from Merck that could influence the electrocatalitic activity of the electrode during testing.

To investigate if some of the impurities were absorbed or deposited on the cathode used in the durability experiment in Fig. 14, elemental analyses were made by means of X-ray photoelectron spectroscopy (XPS). For comparison one un-activated electrode (not been immersed in KOH of leaching of Al) and one activated electrode that had been used for two potentiodynamic measurements followed by conditioning at -456 mV vs. SHE for 10 minutes were examined. The conditioning of the activated electrode was performed in order to dissolve impurities that possibly have been deposited on the electrode during polarisation and the potential was selected to be below the potential where NiO is formed. The external residues found on the surface of the electrodes are listed in Table 6.

[At.%]	El1 (Un-activated electrode)	El2 (Activated, polarised and conditioned electrode)	El3(Electrode used from cathodic durability test for 93 hours at -1256 mV vs. SHE)
C	12.38	3.22	3.73
Fe		0.89	10.80
K			3.56
Pb			0.24
Mg		0.60	1.92
Ti			0.66
Ca		0.25	0.81

Table 6: External residues found with XPS measurements performed on high surface nickel electrodes with three different pre-treatments.

The measuring range for the XPS analyses is about 1-10 nm. From the results listed in Table 6 it is clear that the electrode cathodically treated for 93 hours (El3) contained much more external residues compared to the two reference electrodes. This indicates that although highly pure analytic KOH is used, impurities are deposited onto the electrode at cathodic potentials.

It is interesting that 10 at.% of Fe is found on the surface of El3 compared to only 0.89 at% for El2, even though the producer of the KOH reports only < 0.0005% content of Fe. Deposition of Fe on the electrode surface is, on the other hand, not expected to be the main cause of the deactivation of the electrode. Fe has low hydrogen overpotential, see volcano plot in section 2.5, and during electrolysis the Fe deposits are often seen as dendrites, which can increase the actual surface area of the electrodes. Fe is also believed to prevent nickel hydride formation on nickel electrodes and, thus, result in less deactivation of hydrogen electrodes [119]. These experiments have, however, only been reported on smooth surfaces. One could therefore argue that if Fe is deposited on high surface area nickel some of the

most active sides for HER will be covered with Fe. Fe has slightly higher hydrogen overpotential compared to nickel, therefore this could result in slight deactivation.

The findings of lead on the El3 surface are interesting due to the fact that the metal is known to have high hydrogen overpotential, see volcano plot in section 2.5. Therefore, even a partial coverage of the surface or a few atom layers could deactivate the electrode material.

The XPS measurements strongly indicate that contaminants in the electrolyte become deposited on the cathode surface during electrolysis. Therefore, in order to eliminate the risk of deactivation of the hydrogen electrodes during electrolysis or electrochemical measurements, electrolyte cleaning (pre-electrolysis) should be performed at all times. Unfortunately, the importance of the purity of the electrolyte is often overlooked for electrocatalytic testing. In present work the electrolyte applied was always pre-electrolysed prior to the experiments. This was done by the means of inserting two nickel plates to the prepared electrolyte and applying about 2 V current between the electrodes for at least 48 hours.

4.5 The three electrode- electrochemical cell and IR-drop

Electrochemical measurements are typically performed in a three-electrode electrochemical cell. This is also the case in the present study. A typical three-electrode electrochemical cell is schematically illustrated in Fig. 15.
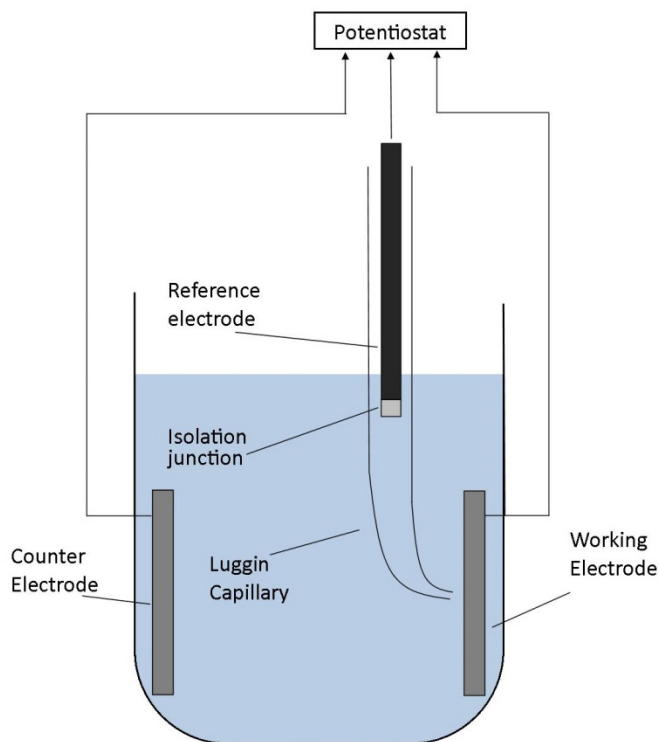
Fig. 15: Schematic illustration of a three-electrode electrochemical cell.

The principle behind the setup is to measure the potential of the working electrode with respect to the non-polarised reference electrode while current is flowing between the working electrode and the counter electrode. A simplified electric equivalent circuit for such a setup is shown in Fig. 16 to the left, where CE is the counter electrode, RE the reference electrode and WE the working electrode. R_Ω stand for the ohmic drop between CE and RE and R_p is the polarisation resistance.
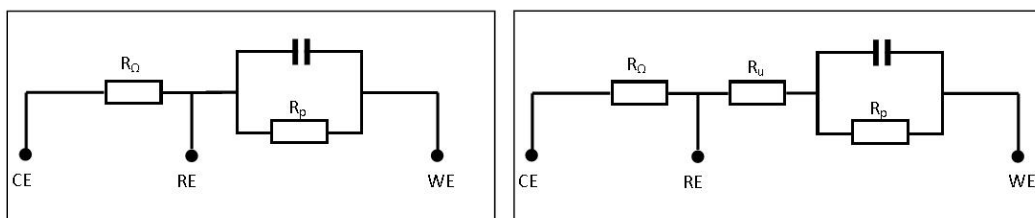
Fig. 16: A simplified version of the electric equivalent circuit for the an ideal three- electrode electrochemical cell setup, to the left, and a real three- electrode electrochemical cell setup, to the right.

However in real applications there is an ohmic drop (R_u) between the RE and the WE which means the potential of the measured WE has an error of $V=IR_u$, where I is the current applied to the cell. This is often called the uncompensated potential drop. R_u can be minimised by using a high ionic conducting electrolyte and by reducing the distance between WE and RE. This is typically done by using a luggin capillary. Hence, if this is done the potential drop between the RE and the WE can be neglected at low current densities. The problem of the R_u can also be solved by measuring the resistance between RE and WE before the electrochemical measurements are performed and compensate the measured data with the calculated resistance.

When performing electrochemical measurements where gas evolution takes place, such as for the HER or the oxygen evolution reaction (OER), special care must be taken. The reason is that the gas bubbles formed during the measurement result in dramatic increase of the R_u. Furthermore, the R_u is not a constant and depends on the amount and behaviour of the gas evolution. In this case, the potential drop between RE and WE changes from one second to another, depending of the placement, and amount of the gas bubbles in the electrolyte. Here measuring R_u in the beginning of the measurement is not enough. Ideally, the R_u should be measured prior to each and every potential measurement and subtracted from the R_Ω measured. This is actually what is done with the current interrupt technique. By this method the potentiostat interrupts the current prior to each measurement point and measures the voltage immediately before and after the current has been interrupted. When the current is interrupted the resistance drops immediately by the amount of R_u, but R_p drops slowly due to the capacitor. Therefore $R_{before}-R_{after} = R_u$ and IR_u can be subtracted from the next potential measurement point. The drastic difference between potentiodynamic measurements performed on polished nickel without compensating for the IR drop and with current interrupt IR compensation is shown in Fig. 17.
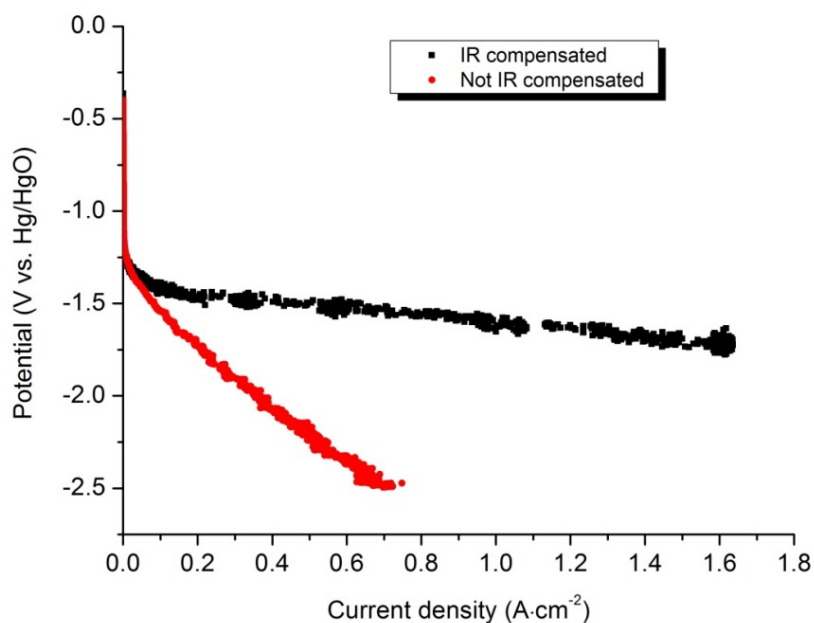
Fig. 17: Potentiodynamic measurements performed on a polished nickel with and without current interrupt IR compensation.

Unfortunately, the current interrupt IR compensation is very sensitive to noise. Using a Faraday cage to keep the external noise out can help diminishing the noise. What is more important is to use a low impedance reference electrode. Reference electrodes with high impedance can cause problems like overloads and potentiostat oscillation during measurements [120]. This problem escalates with a potentiostat designed for high performance and high speed. The impedance of a reference electrode is typically determined by the resistance in the junction, which separates the filling of the reference electrode from the electrolyte, as illustrated in Fig. 15. Slow flow of the filling solution through the junction is essential to minimise the impedance of the reference electrode. Unfortunately, this flow is often reduced in order not to alter the composition of the solution during measurements, resulting in increased resistance in the electrode.

For the present study, the reference electrode used was a Hg/HgO reference electrode from Radiometer. The electrode is filled with 1 M KOH and it has a fiber junction. The impedance of the reference electrode was measured to be about 100 kΩ. According to the application notes from the potentiostat manufacturer the impedance of the reference electrode applied during measurements should be less than 1 kΩ. When applying the Hg/HgO reference electrode during potentiodynamic measurements and current interrupt IR compensation, noisy outputs were attained. This problem escalated when measuring on highly active electrocatalytic surfaces.

In order to reduce the noise during measurements, a low impedance reference element, here nickel wire, was coupled to the reference electrode and a capacitor in-between, as illustrated in Fig. 18.
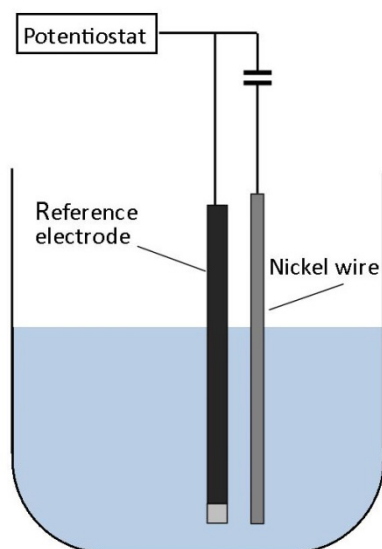
Fig. 18: Schematic illustration of the parallel connection of a low impedance nickel wire to the reference electrode in order to reduce noise during electrochemical measurements.

The capacitor ensures that the DC potential comes from reference electrode and the AC potential from the wire. The optimal size of the capacitor to be used was determined by trial and error and where 10 nF capacitor was selected. In Fig. 19 two potentiometric measurements prepared on high surface nickel electrodes were measured with the current interrupt IR compensation technique. One measurement was prepared with the nickel wire and another prepared without the nickel wire. Clearly, for the measurement where the nickel wire is used considerably less noise is observed.
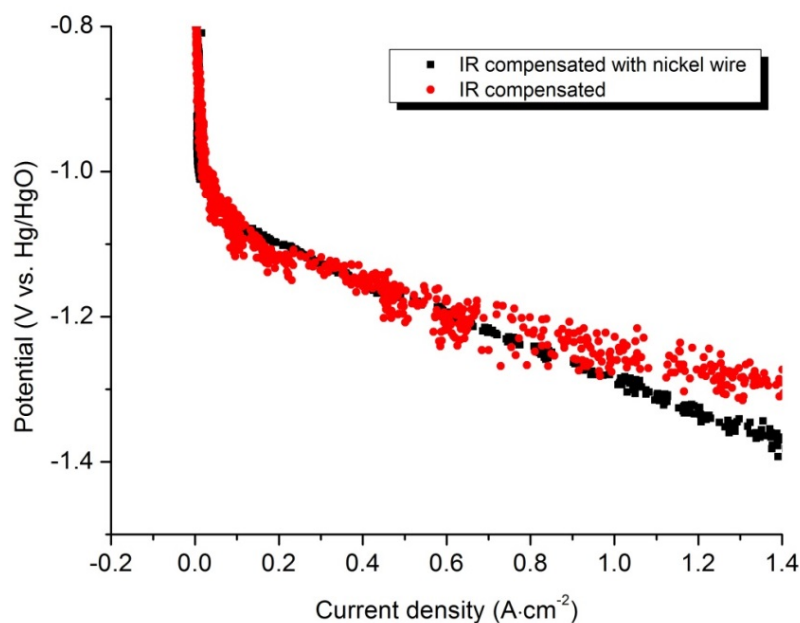
Fig. 19: Potentiodynamic measurements on a high surface are nickel electrode. One measurement is prepared with nickel wire coupled to the reference electrode as illustrated in Fig. 18 and one is measured with a standard three electrode cell setup.

4.6 Stability of electrodes

Although the corrosion stability of the electrodes or the electrocatalyst is one of the primary reasons for electrode development, this is usually not mentioned in the scientific publications. If the electrode material is not stable in the electrolyte during testing some or all of the Faradaic current goes to the corrosion process. Accordingly, the measured potential is not the potential for decomposition of water and cannot be used for evaluating the rate of the HER, OER or the overall electrolysis process. Assuring that an electrode designed for water electrolysis is stable in the experimental environment is essential for proper evaluation of the electrocatalytic behaviour.

4.7 Final remarks

Unfortunately, there are no standards for activity measurements of electrocatalysts for water electrolysis systems. The purity of the electrolyte, IR compensation and the quality of the potentiostat measurements are all factors that can have a large influence on the final experimental results. Furthermore, no general acceptance is in place for how the efficiency should be calculated. Accordingly, comparing and evaluating published results on electrocatalyst for water electrolysis can be challenging.

5 Development of the Test Setups

5.1 First generation test setup

No commercially available test setups for alkaline electrolysis systems are available. Thus, it was necessary to develop an electrolysis test setup before efficiency and durability testing of the designed electrodes could be done. In the early stage of the PhD study it was decided to design an electrolysis setup that was suitable for various types of measurements related to alkaline water electrolysis development. The criteria for the test setup were as follows:

- Adaptable both for whole and half-cell electrochemical measurements (meaning that the design has space for inserting of reference electrode close to one or both of the electrodes)

- Provides easy changing of electrodes and diaphragm

- Adjustable distances between electrodes and diaphragm

- Low electric resistance in connections and wiring to the electrodes

- Corrosion resistant in > 30% KOH and working temp of > 80°C

- The cell material must be isolating in order to avoid stray current during measurements

As mentioned before, distances between the electrodes and diaphragm, type of diaphragm and wiring all add extra ohmic losses to the electrolysis system. Therefore the idea with the first generation of the electrolysis test setup was to be able to adjust these parameters in order to optimise the setup for the future full size electrolysis stack.

The first challenge in the desig process was to find an isolating material that could resist the highly corrosive environment at elevated temperatures. Polyether ether ketone (PEEK) is known to be relatively resistant to alkaline environment [121] and it was easily available. As result, all components in the electrolysis test setup were made of PEEK. The electrolysis cell was made of two identical half-cell chambers which formed an electrolysis cell when mounted. The cell was made of stainless steel (316) and coated with Teflon (ACCOFAL P39) coating made by ACCOAT. Fig. 20 shows computer-aided design (CAD) drawings of the first generation cell design, whereas images of the final product can be seen in Fig. 21.

Space for diaphragm and gasket

Electrode

Electrode holder top part: To eliminate stray currents and to keep the electrode fixed

Electrode holder base part: Makes it possible to remove the holder, replace the specimen or adjust the distance without taking the structure apart
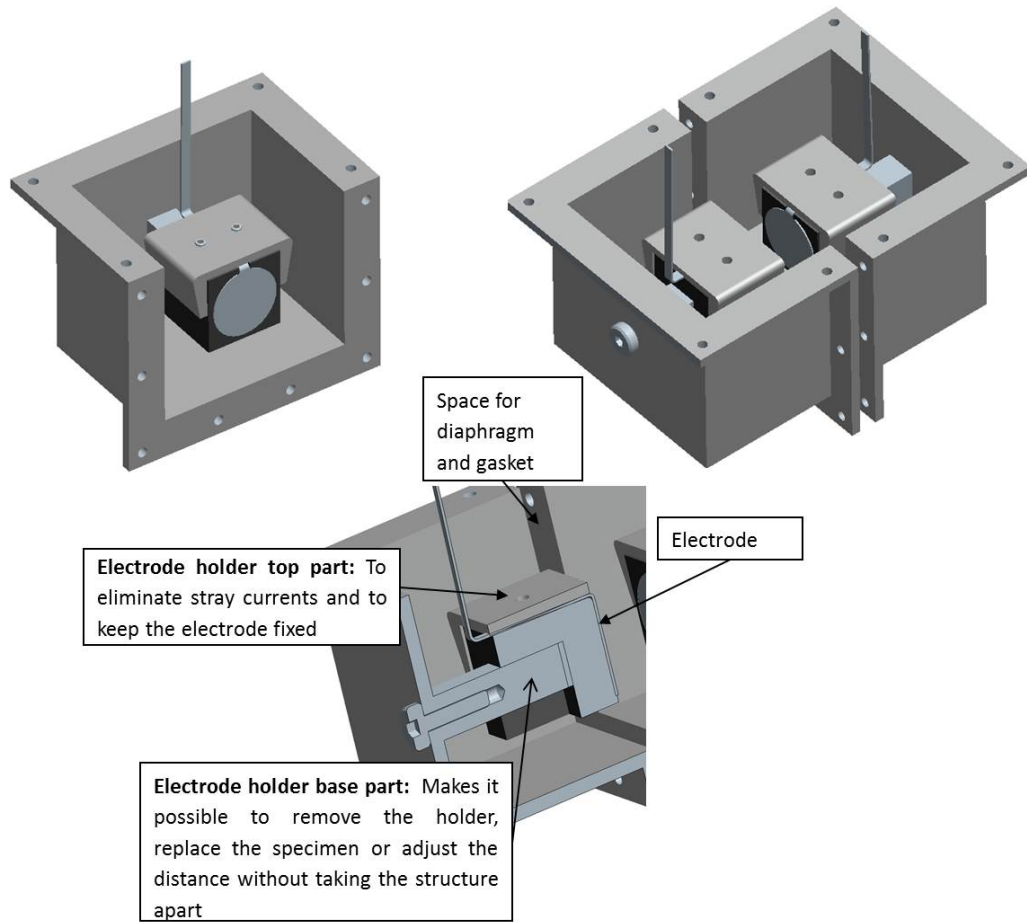
Fig. 20: CAD images of the first generation of the electrolysis test setup.
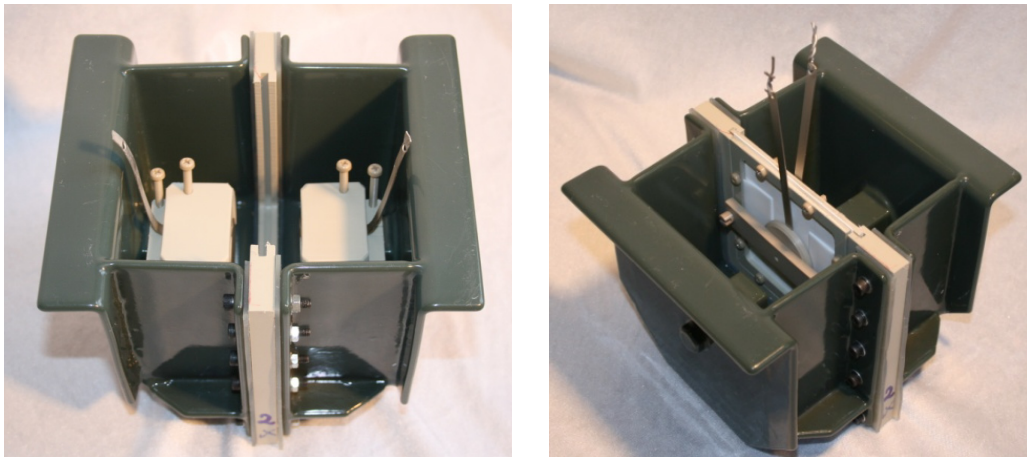
Fig. 21: The first generation electrolysis cell test setup. A) As designed. B) Modified

For assuring low ohmic drop from wiring, the electrodes were designed with a tail which reached above the electrolyte level during measurements. The tail could then be connected to the wires of the potentiostat with a crocodile clamp. The electrolyte in the cell was heated by placing the cell on a commercially available magnetic stirrer, connected to an electronic thermometer, which was placed inside the electrolysis cell for temperature control.

When using the as designed cell, see Fig. 21 A, precise adjustment of the distance between the electrodes and the diaphragm was challenging. Also the electrodes tended to tilt. Due to the fact that the electrolyte, together with the formed gas bobbles, is the major cause of the ohmic drop in the system, it is crucial to know the exact spacing between the electrodes in order to be able to compare two different measurements. Hence, even a small spacing error can lead to wrong interpretation of the measurements results.

An attempt was made to solve the spacing problem by making some minor modification to the cell, see Fig. 21 B. In the modified cell the electrodes are pressed towards the diaphragm, and polytetrafluoroethylene (PTFE) sheets with a known thickness are used as spacers. This setup proved to work quite fine for short periods of time. Long-time durability testing was, however, not possible due to leakage of the cell. Furthermore, the ACCOFAL coating was not resistant to the electrolyte. Blisters and detachment of the coating were observed after short time of operation.

5.2   Second generation electrolysis test setup

In the next generation electrolysis cell test setup, it was decided to focus mainly on the electrode part. It was not found necessary to be able to move or change electrodes or diaphragm without disassembling the cell. Two cell designs were made, one for whole-cell measurements and another for half-cell measurements. CAD drawings of the second generation whole-cell, electrolysis cell, are shown in Fig. 22.
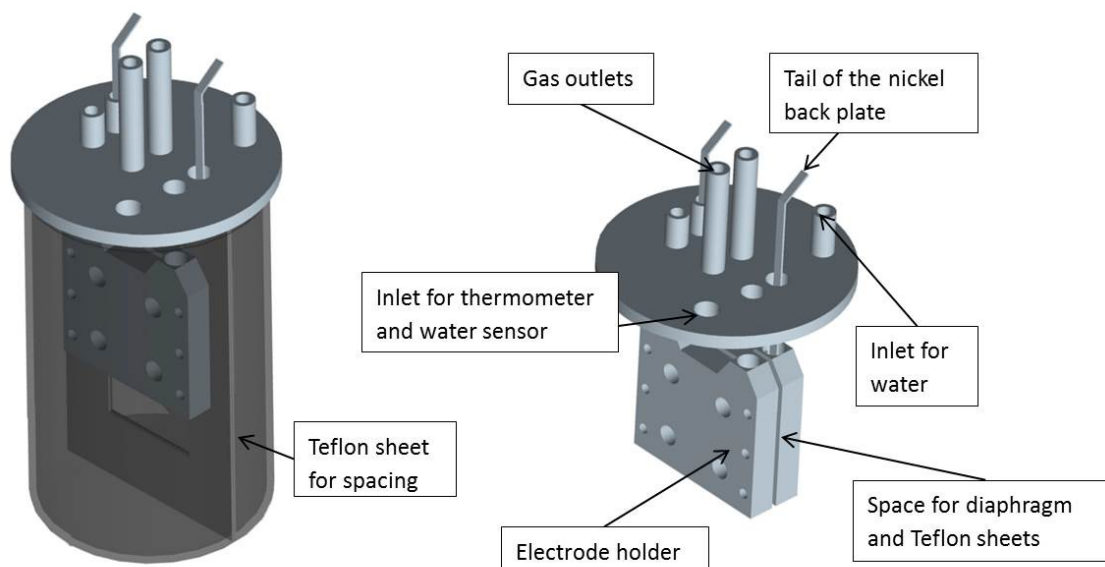
Fig. 22: CAD drawings of the second generation electrolysis test cell.

One of the main criteria for the second generation of electrolysis cell was high temperature resistance > 120°C in strong alkaline environment. PTFE is one of the most resistant polymers both for acidic and alkaline environment and is suitable for operations up to 150°C

in an aggressive environment. Thus, all components of the cell, including the beaker, were made of solid PTFE. Instead of having specially designed electrodes, the electrodes are placed on a nickel back plate that serves as a current collector. The nickel back plate has two tails, one for applying current to the cell and one for measuring potential difference between the anode and cathode.

The whole-cell setup is a closed system with a lid and an automatic water dosage system, making it possible to perform long-time durability tests in the cell without manual addition of water, due to evaporation of water during operation. The cell can be heated by applying heating mats from RS Components Ltd. The electrode holder is designed to fit electrodes with the size of 5x5 cm^2 where only 22 cm^2 of that area is exposed to the electrolyte. The purpose of the electrode holders, both in the first and second generation of the test setup, is to mask the connection wires and back and edges of the electrodes, so only the selected surface area of the electrodes is exposed to the electrolyte. The whole cell setup was used for durability testing carried out using an AE-PS-8080-60-T power supply coupled to a computer for data acquisition.

5.3   Second generation half-cell test setup

The second generation half-cell test setup was designed as a typical three electrode electrochemical cell with all components made of pure PTFE. Due to low current capabilities of measurement hardware, low surface area is generally an advantage for half-cell setups and, therefore, the openings for the electrodes, which is the exposed area of the electrodes, was selected to be 2 cm^2. The opening was circular in order to minimise "edge effects", i.e. higher current densities at the edges compared to other part of the surfaces. To assure low ohmic drop between the working electrode and the reference electrode a luggin capillary was used. The counter electrode was made of a nickel. The cell was placed in a Faraday cage for minimising external noise during measurements. Images of the half-cell test setup are shown in Fig. 23 and Fig. 24.
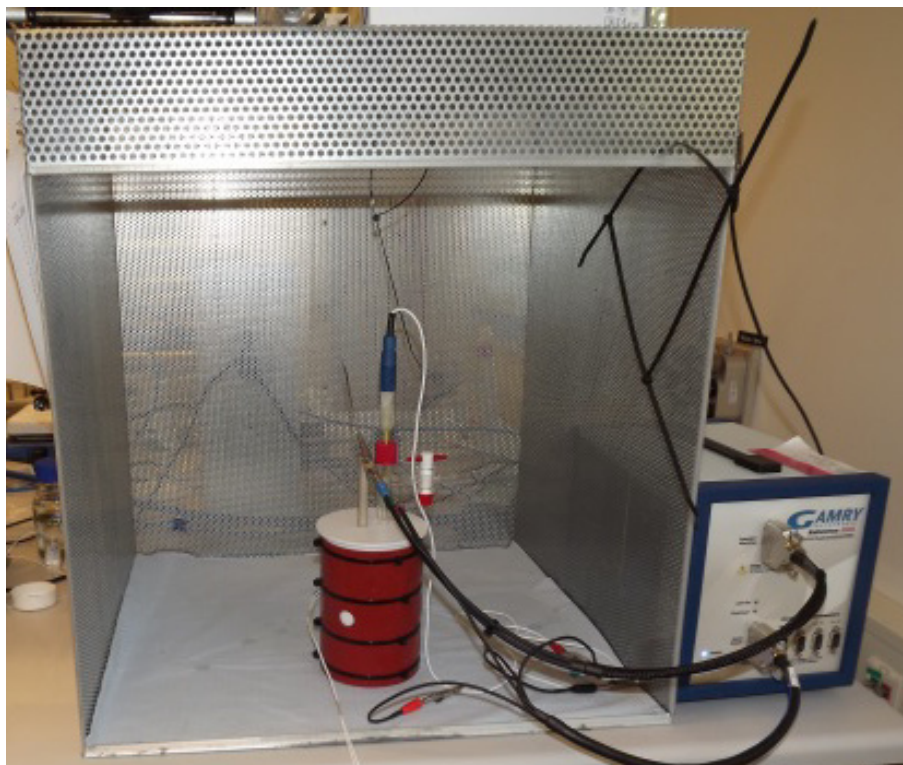
Fig. 23: The half-cell measurement setup as assembled and connected to the potentiostat.
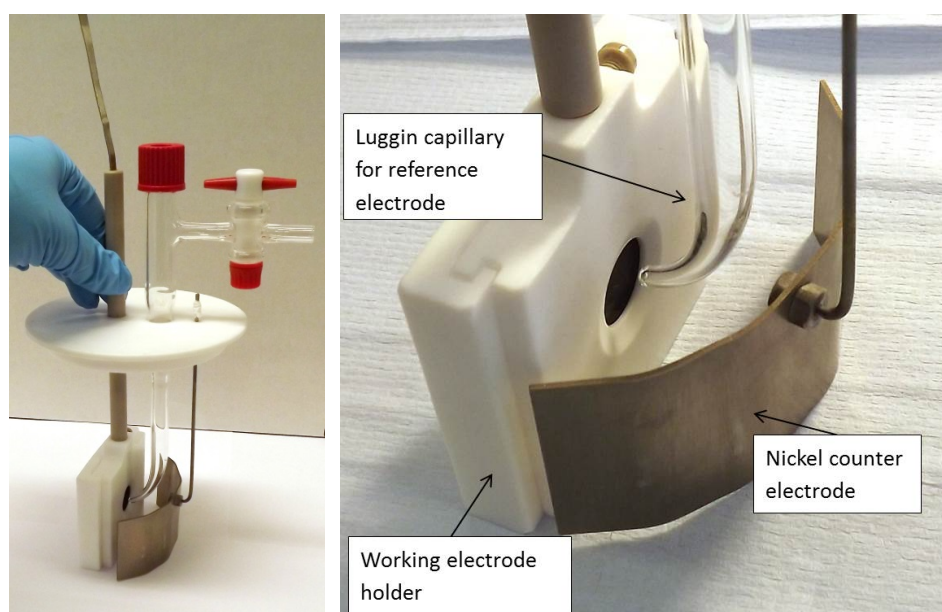
Fig. 24: The construction of the electrodes inside the PTFE beaker of the half-cell measurement setup.

The half-cell measurements were carried out with a Gamry Reference 3000 potentiostat/galvanostat coupled to a computer for data acquisition.

5.4   Industrial electrolysis stack

A durability test was carried out in a 17 cell bipolar, non-zero gap alkaline water electrolysis stack manufactured by GreenHydrogen.dk. An exploded view CAD image of the electrolysis stack is shown in Fig. 25. In Fig. 26 the stacking of the electrodes inside the electrolyser is illustrated. The electrodes in the stack measured 270 cm^2.
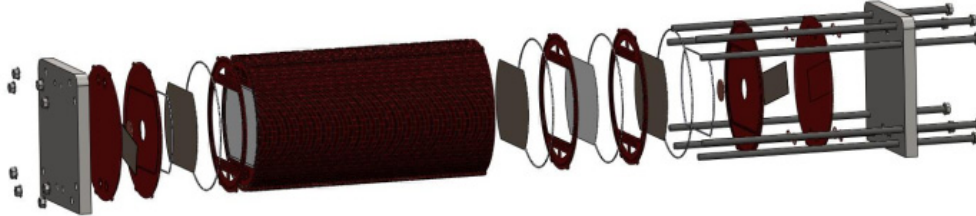
Fig. 25: CAD image of the construction of the electrolysis stack used for durability testing. Courtesy of GreenHydrogen.dk.
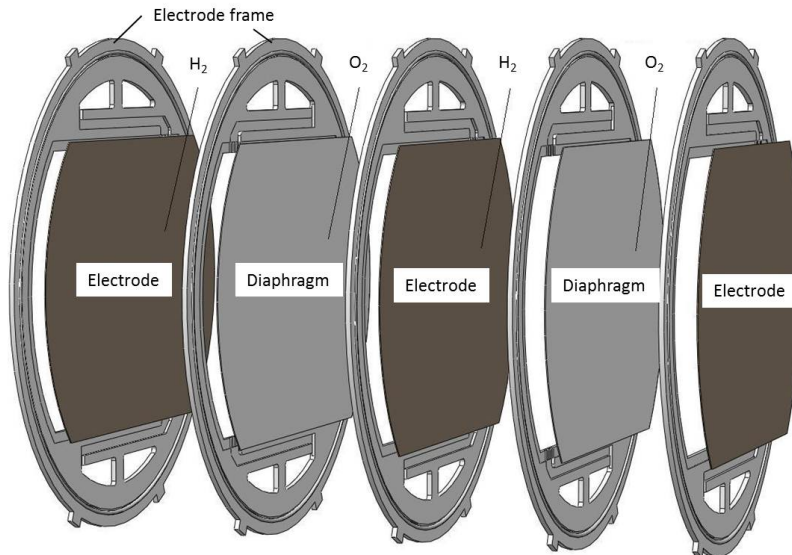
Fig. 26: The bipolar configuration of the electrolysis stack used for durability testing. Courtesy of GreenHydrogen.dk.

The durability test was performed in combination with a demonstration project named H2-College. In the project, 66 houses at the campus of Århus University in Herning were powered by hydrogen where surplus power from wind turbines was used to generate the electricity for the electrolysis process. Images of the electrolysis system and the hydrogen storage tank are shown in Fig. 27. Further information about the project can be found elsewhere [122], [123].

Fig. 27: Left: The electrolyser system used for H2-College. Right: The hydrogen storage tank from H2-College,

6 Preliminary Work for the Development of New Hydrogen Electrodes

When designing and developing a new electrocatalyst the three following criteria must be fulfilled:

- The catalyst needs to be corrosion resistant and possess long time stability during operation and shutdowns
- The catalyst material must possess good electrocatalytic properties (have low activation overpotential) towards the required reaction(s)
- The electrocatalyst needs to be electronically conductive

From the volcano plot for HER, see section 2.5, nickel, cobalt and iron are observed to be the best hydrogen catalysts among pure un-noble transition metals. Also, Co_3O_4, Raney-Cobalt and Raney-Nickel have been found as promising electrodes for the OER, see section 3.1.1.2. Accordingly, nickel, iron and cobalt are considered to be possible candidates as core material for the electrodes to be developed.

The next step for selecting a proper material for the electrode development is to assure that the material is stable under the harsh operating conditions in the alkaline media. When the right core metal has been selected, a method for increasing the activity of the selected electrode surface needs to be established. In this chapter the methodology for material selection and structure modification for the process of developing a new hydrogen electrode for AWE will be introduced.

6.1 Material selection

Pourbaix diagrams are commonly used in electrochemistry for identifying the thermochemical stable phases of an aqueous electrochemical system. Pourbaix diagrams are plotted with the pH of the electrolyte on the x-axis and the potential of the metal on the y-axis. The potential is defined according to the standard hydrogen electrode.
Fig 28-30 show Pourbaix diagrams for iron, nickel and cobalt at 80°C and 1 atm. pressure.
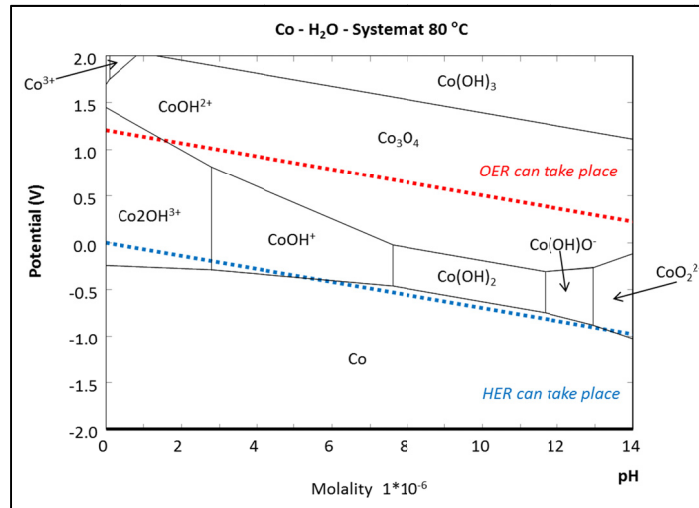
Fig 28: Pourbaix diagrams for cobalt in water at 80 °C.
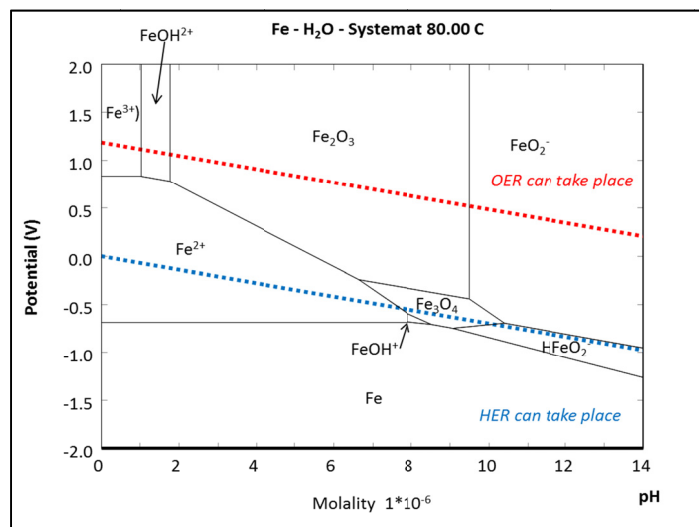
Fig 29: Pourbaix diagrams for iron in water at 80°C.
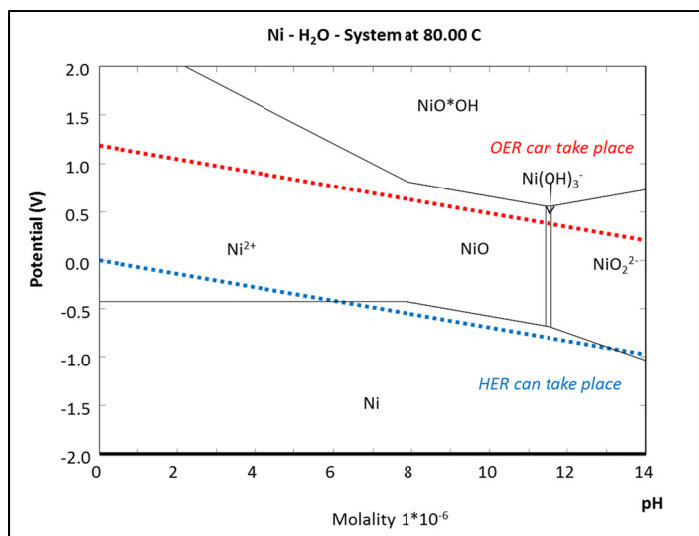
Fig. 30: Pourbaix diagrams for nickel in water at 80°C.

As the developed electrodes need to be stable in strong alkaline media (pH >14) and at intermediate temperature (> 80), looking at diagrams at pH 14 they give an indication of the corrosion resistivity of the metals under AWE conditions. Between the blue and the red lines in the diagrams water is stable. Above the red line oxygen is stable (oxygen evolution can take place) and below the blue lines hydrogen is stable (hydrogen evolution can take place). According to the diagrams, all of the suggested metals decompose at some point inside the potential range of AWE systems, between approximately -1 and 1 V vs SHE. Nevertheless, the thermodynamic calculations do not include information about the kinetics, i.e. the corrosion speed of the metals in the particular media. Hence, a corrosion investigation where the rate of corrosion is examined is necessary to evaluate the complete corrosion properties of the three metals.

In the beginning of the present PhD study, numerous initial electrolysis tests were carried out with cobalt and nickel electrodes. During this work an interesting observation was made. When high surface area cobalt specimen was stored in water for few days severe corrosion of the cobalt was observed, see Fig. 31.
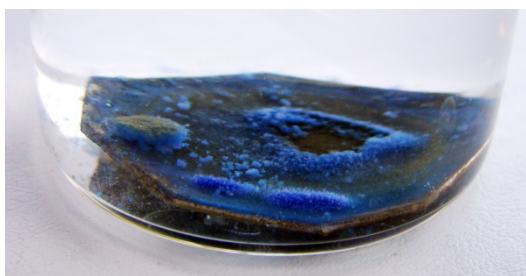
Fig. 31: Cobalt specimen after storage in water for a few days shows blue corrosion products on the surface.

As observed in the image, blue corrosion products are formed on the cobalt specimen. Additionally, the electrolysis experiments prepared with cobalt or cobalt containing electrodes all resulted in degradation of the cobalt. These findings coupled with the thermodynamic assessments indicate that cobalt is not stable in alkaline environment at zero potential. This means that if cobalt is selected as core material for the electrodes, the electrodes should not be stored in an electrolysis stack during shutdowns. This is obviously not feasible when working with full size electrolysis stacks. Cobalt was for that reason rejected as a core material for the electrode to be developed.

For the purpose of selecting the right material for the electrode development, corrosion measurements of iron and nickel where carried out in 30 wt.% KOH at 150°C and 5 bar hydrogen and oxygen pressure. The relatively high temperature was selected to accelerate the possible corrosion mechanisms. The corrosion experiments were twofold; one where oxygen gas was bubbled through the electrolyte and another where the gas was hydrogen. Five specimens of each metal were placed in the corrosion measurement tanks. The tanks were opened regularly and the test specimens weighed. The average weight change of the tested specimens during time of exposure is plotted in Fig. 32 and 33. Negative weight loss indicates weight gain.
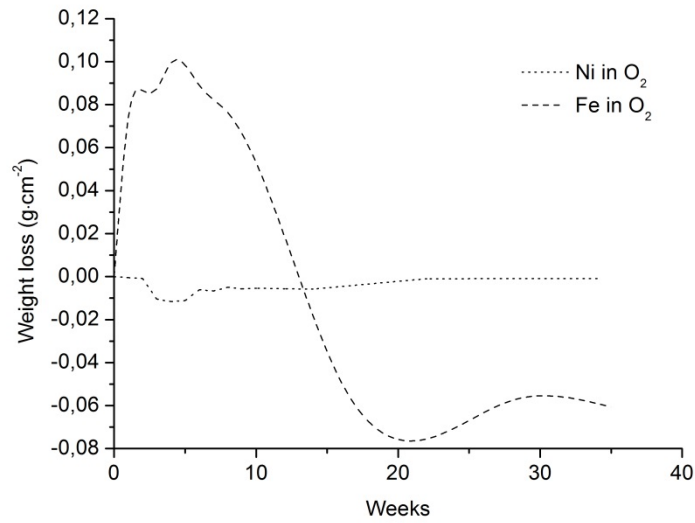
Fig. 32: Accumulated average weight loss of nickel and iron in 150°C 30 wt.% KOH at 5 bar O_2 pressure.
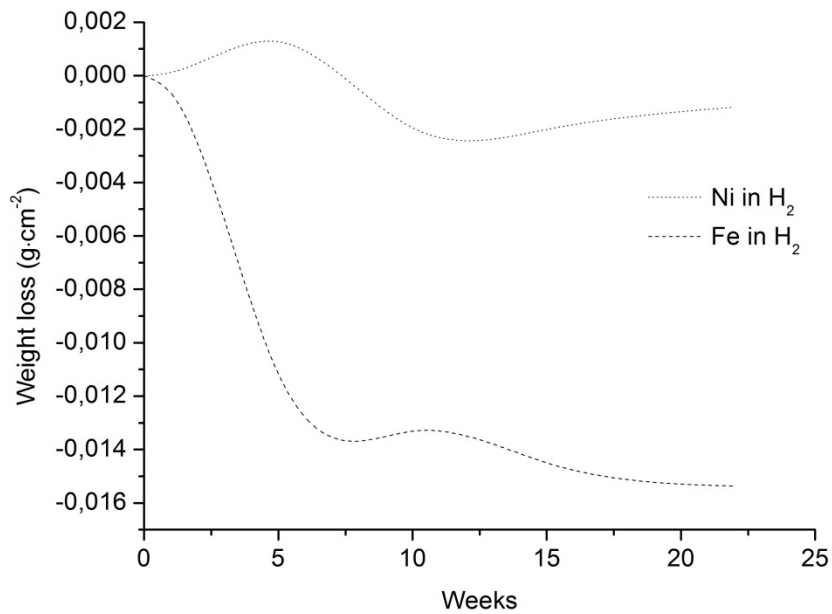
Fig. 33: Accumulated average weight loss of nickel and iron in 150°C 30 wt.% KOH at 5 bar H_2 pressure.

As seen from the plots, the weight of nickel does not change much during time, neither in the oxygen nor in the hydrogen tank. This is in contrast with the iron specimens where weight loss is observed during the first weeks of exposure in the oxygen tank, indicating material loss due to corrosion. After approximately 5 weeks of exposure in the oxygen tank the iron specimens start to gain weight. The weight gain originates from corrosion products formed on the iron surface during exposure. In the hydrogen tank, the iron specimens experience a weight gain only, indicating formation of corrosion products.

In Fig. 34 and Fig. 35 images of the test specimens before and after exposure are compared. For the iron specimens exposed to oxygen severe corrosion is observed. The nickel specimen seems, however, not to corrode in the oxygen environment and the weight gain apparently occurs due to formation of nickel oxide. For the hydrogen exposure the nickel specimen look identical to untreated specimen. This is not the case for the iron, where corrosion products are observed.
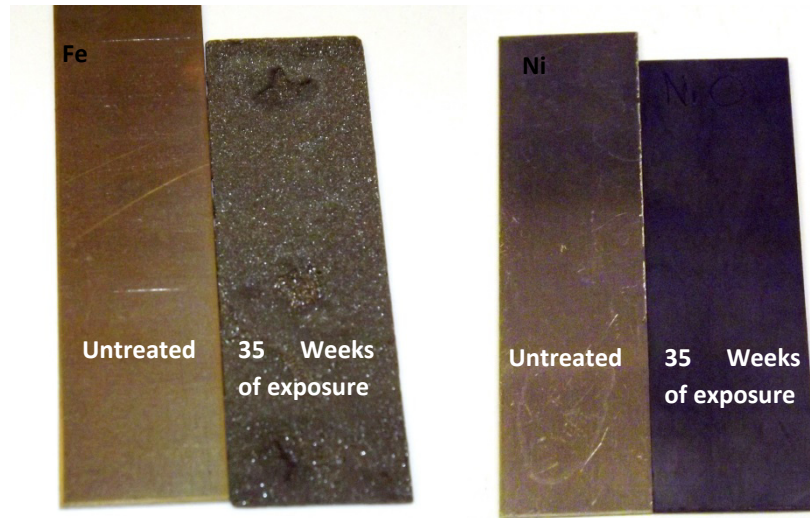
Fig. 34: Images of iron (to the left) and nickel (to the right) untreated and after 35 weeks of exposure in 150°C 30 wt% KOH at 5 bar O_2.
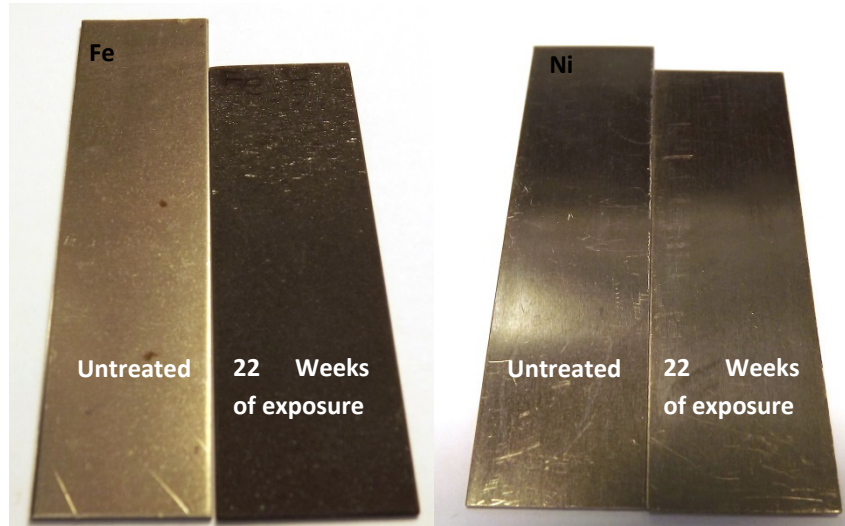
Fig. 35: Images of iron (to the left) and nickel (to the right) untreated and after 22 weeks of exposure in 150°C 30 wt% KOH at 5 bar H_2

The corrosion measurements strongly indicate that iron is not a good candidate as a core electrode material for AWE. The results show that nickel is the most stable metal in strong alkaline media, among active transition metals towards HER and OER. The fact that nickel is the state-of-the-art electrode material in commercial electrolysis systems supports these findings. For the aim of producing one solid electrode suitable for bipolar stack structure the material selected needs to be stable both in hydrogen and oxygen evolution environment as

well as at zero potential. For that purpose nickel is selected as the core material for the development of the new electrode.

6.2   Structural modifications

It has been mentioned various times before that the electrochemical activity of a catalyst does not only depend on the intrinsic properties of the catalyst. The structure and geometry of a catalyst also have an effect. Platinum black (or platinized platinum) is a good example of this. Platinum black is known to be the ultimately best hydrogen catalyst and has been measured to have 0.5 mV HER overpotential in 2 N sulphuric acid, whereas shiny platinum electrode is observed to have 150mV hydrogen overpotential [124]. The reason for the large difference in electrocatalytic activity is that platinum black has significantly larger surface area and additional surface defects compared to shiny platinum. Although, due to its price, platinum was not considered to be a candidate for the new electrolysis electrode its extremely good electrocatalytic properties was an inspiration for the development. In order to learn from the HER "master", platinum black surface was produced and its micro-structure inspected. The production method together with more thorough results and discussions of the platinum black electrode can be found in Appended paper III.

Fig. 36 shows the as plated platinum black surface. The platinum surface appears to be black (Black body) due to the high absorption of all incident electromagnetic radiation, regardless of frequency or angle of incidence.

Fig. 36: The as-plated platinum black surface.

Fig. 37 shows micrographs of the platinum surface captured in a high resolution SEM. The micrographs reveal the extreme large surface area of the coating characterised with a cauliflower structure. The large surface of the platinum black implies that the electrocatalytic activity of a surface can be largely increased by increasing the real surface area of the catalyst and the amount of crystal defects, where the HER is suggested to take place.
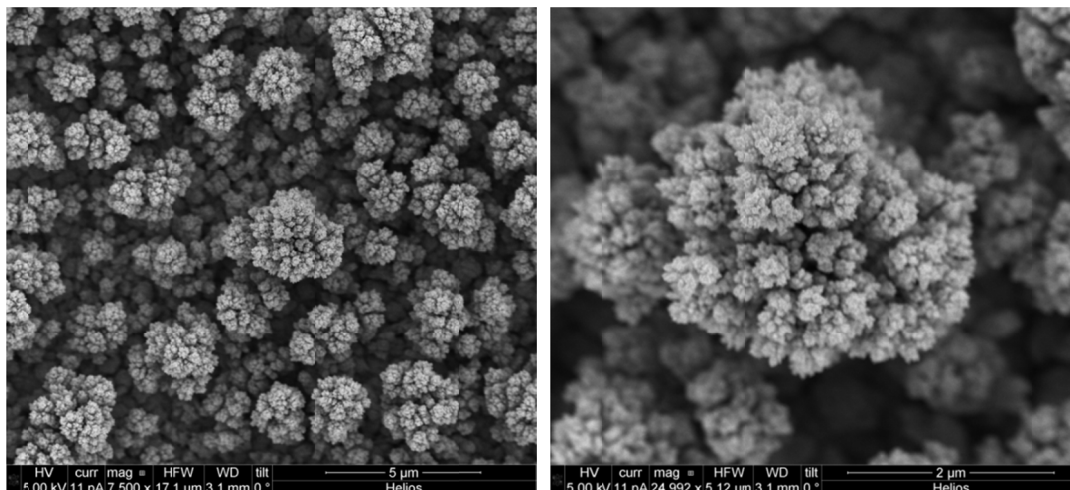
Fig. 37: High resolution scanning electron microscope images of platinum black surface.

Accordingly, the aim was to produce a nickel surface with a large real surface area and large amount of reactive crystal defects. A common method for preparing porous nickel catalysts is by selectively alkaline leaching of aluminium or zinc from a Ni-Al or a Ni-Zn alloy, respectively. Various techniques for producing the alloying surfaces have been reported:

- Electrodeposition of Ni-Al powder with Ni [125]–[129]
- Powder pressing of Ni-Al or Ni-Zn powders [62], [130]
- Electrodeposition of Ni–Zn alloys [60], [131], [132]
- Thermal spraying [28], [35], [36], [133]

When choosing the right process technique for the electrode development, the interlayer adhesion between the porous structure and the substrate as well as the purity of the final product must be taken into consideration. The highly alkaline electrolyte, the intermediate temperature (>80°C) and the oxygen and hydrogen gas evolution, all contribute in making the electrode media extremely corrosive. Proper adhesion between the electrocatalyst and the substrate is vital for the overall lifetime of electrodes for AWE. If the adhesion is not sufficient, the electrolyte can penetrate in-between the two layers resulting in gas evolution in the interphase, leading to gas erosion corrosion. The highly electrochemically active surface will then, partly or entirely, be "*blown-off*" diminishing the electrocatalytic efficiency of the electrode. Surely, similar gas erosion corrosion mechanism can take place between unattached layers in the electrode coating itself. Therefore, chemical bounding between the substrate and the electrocatalytic coating, instead of interlocking, is preferred.

Good electrical conductivity is another important factor, when producing electrocatalytic active surfaces. Insulating particles, such as oxides, increase the electrical resistance of the electrode and, consequently, decreases the efficiency of the electrolysis process. The brittle property of the oxides also increases the risk of gas erosion corrosion inside the porous structure. Hence, selecting the right process technique for producing the electrocatalyst is essential for the efficiency and durability of the developed electrocatalyst.

One of the most common ways to produce large surface nickel electrodes is by thermal spraying (TS) of Raney nickel powders (usually 50/50 wt.% Al/Ni) onto a nickel or a steel support [28], [30]–[34], [36], [134]. During spraying the Raney powder partly melts and a coating consisting of number of different Al/Ni phases is formed. This is followed by selectively leaching of aluminium from the alloy(s) and a skeletal nickel structure with a high surface area and large amount of crystal defects is formed.

In the case of the TS process, the coatings are characterized by a heterogeneous layered pancake-shape structure, containing voids and oxide inclusion as shown in the SEM micrograph and the corresponding illustration in Fig. 38.
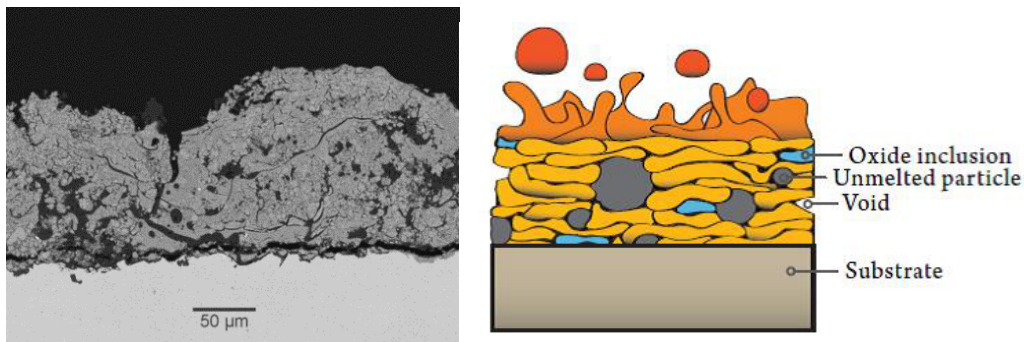
Fig. 38: Left: Cross section back scatter electron micrograph of a Raney nickel coating prepared by thermal spraying of Al/Ni powder onto a nickel substrate. Right: Schematic illustration of a thermally sprayed structure [42].

Because the TS structure contains no chemical bounding, between the substrate and coating, and it has oxides incorporated in the coatings, one can argue that this is not the ideal process technique for fabricating electrocatalytic surfaces for industrial AWE. Another drawback of the TS technique is that the coatings are relatively thick, typically over 100 μm, and rough, i.e. unlevelled, see Fig. 38. This type of surfaces gives problems when assembling the electrodes in an electrolysis stack.

Powder pressing is also a process where interlocking rather than chemical bounding is obtained. With the aim of finding a new cost efficient technology for producing electrocatalytic coatings with a large surface area and mechanical properties that can withstand the corrosion challenges in AWE, these process techniques were not selected for the present study. The process techniques selected for producing high surface area nickel electrodes are introduced in the next chapter.

7 Manufacturing of High Surface Area Nickel Coatings

The aim of the work, presented in this chapter, is to find a new cost efficient technology for producing electrocatalytic nickel coatings for industrial AWE applications. The coatings were required to have large actual surface area and mechanical properties that can withstand the corrosion challenges in industrial alkaline water electrolysers. The following processes and combination of processes were screened:

- Physical vapour deposition of aluminium onto an nickel plate followed by thermo-chemical diffusion
- Hot dip aluminising of nickel followed by thermo-chemical diffusion
- Direct thermo-chemical diffusion of aluminium and nickel sheets
- Aluminium ionic liquid electroplating on a nickel plate followed by thermo-chemical diffusion
- Physical vapour deposition of aluminium onto electroplated sulfamate nickel substrate followed by thermo-chemical diffusion

The best coatings attained from the screening where selectively aluminium leached in order to facilitate a porous nickel structure.

7.1 Physical vapour deposition of aluminium onto a nickel plate

7.1.1 Introduction

The first trial for producing high surface area nickel electrocatalytic surface was by physical vapour deposition (PVD) followed by thermo-chemical diffusion and alkaline leaching. The PVD technique was selected because of its superior interlayer adhesion and the possibility of high purity coatings. Moreover, the thickness of the coated layer can be controlled precisely assuring unique uniformity. The selected PVD techniqe was of the magnetron sputtering type, where material is ejected from a sputter target due to bombardment of ions to a substrate surface [42]. In the particular case very pure aluminium metal are sputtered to the electrode surface forming a thin film of aluminium.

7.1.2 Experimental procedure

Commercially available nickel plates with a thickness of 0.5 mm were used as electrode substrate. The purity of the nickel plates were determined by optical emission spectroscopy, detecting 99 wt.% Ni, 0.25 wt.% Mn, 0.14 wt.% Fe and 0.11 wt.% Al. Other residual elements were determined to be below 0.1%. The nickel specimens where coated with approximately 20 μm of aluminium by DC-magnetron sputtering using a CC800/9 SinOx coating unit from CemeCon AG. The aluminium source was an Al 1050 alloy target, run at

750 W, the RF bias on the substrate was set to 800 W and the start pressure in the chamber was 1mPa. The nickel substrates were cathodically degreased for two minutes prior to the PVD process. The substrates were heated and etched in situ by Ar sputtering, prior to the sputtering process, to remove nickel oxide (NiO) from the surface. The PVD aluminium coated nickel specimens were subsequently heat treated in an atmospheric furnace for 24 hours at 610°C followed by a selective aluminium leaching.

Among Al/Ni alloys, aluminium can only be alkaline leached from the Al_3Ni_2 and Al_3Ni phases [135]. Obviously, the Al_3Ni_2 phase contains more nickel and is therefore more mechanically stable compared to its Al_3Ni counterpart. The aim during the alloy formation procedure, i.e. the thermo-chemical diffusion process, was to obtain a relatively thick layer of the Al_3Ni_2 phase. The 24 hours of heat treatment was inspired from the calculated diffusion coefficients of the Ni-Al system in [136].

The first batch of the heat treated PVD Al/Ni specimens were leached as follows; 2 hours in 1 wt.% NaOH at room temperature followed by 20 hours in 10 wt.% NaOH at room temperature and 4 hours in 30 wt.% NaOH at 100°C. These specimens will be referred to as PVD Al/Ni 1. Batch two of the aluminium deposited specimens was leached in 30 wt.% KOH and 10% $KNaC_4H_4O_6 \times 4H_2O$ at 80°C with stirring for 24 hours. These specimens will be referred to as PVD Al/Ni 2. Images of a PVD aluminium deposited nickel plate as received, after heat treatment and after heat treatment and alkaline leaching are shown in Fig. 39.
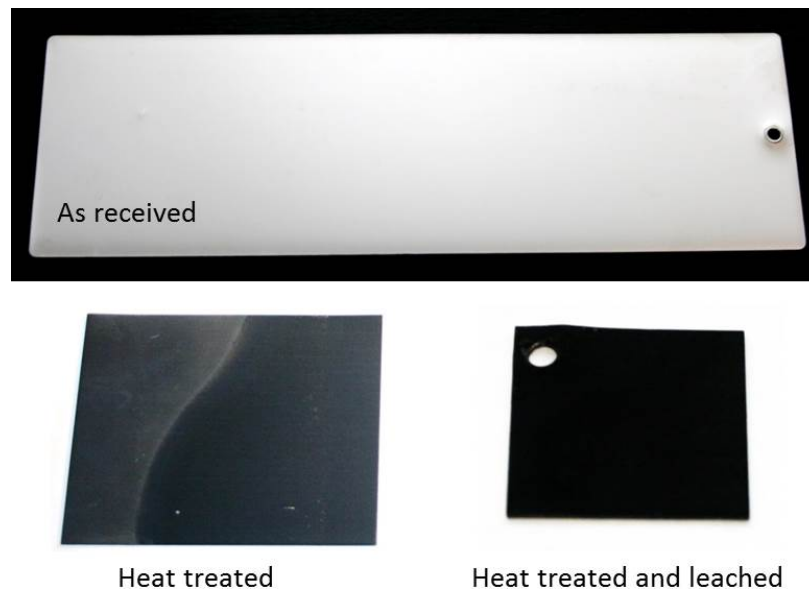
Fig. 39: PVD aluminium deposited nickel substrate, as received, heat treated and alkaline leached.

The appearance of the leached specimen is similar to platinum black. This indicates that a large surface area has been produced.

7.1.3 Results and discussions

Untreated nickel substrate and aluminium coating in the as-deposited state were examined in SEM. The back-scatter electron (BSE) micrographs in
Fig. 40 display parallel grooves on the nickel surface from the rolling process and large crystallites which characterise the annealed nickel substrate. The secondary electron (SE) surface images in Fig. 41 show how the PVD aluminium coating imitates the topography of the substrate, resulting in parallel grooves in the aluminium structure.
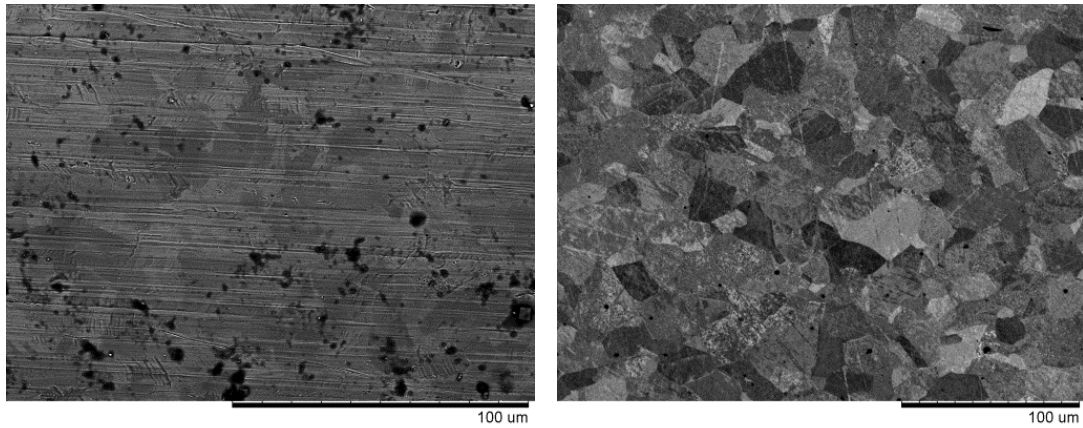
Fig. 40: BSE micrographs of nickel substrate, left: surface, right: cross section.
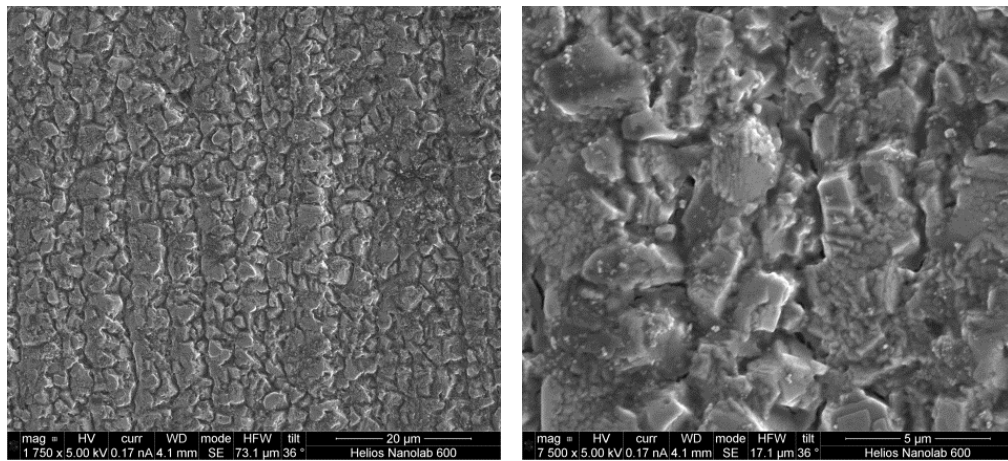
Fig. 41: SE micrograph of the PVD aluminium in as deposited state in different magnifications.

In Fig. 42 a cross section of a heat treated PVD Al/Ni electrode is shown together with the Ni-Al binary alloy phase diagram. Results from cross section elemental analyses are shown in Table 7.
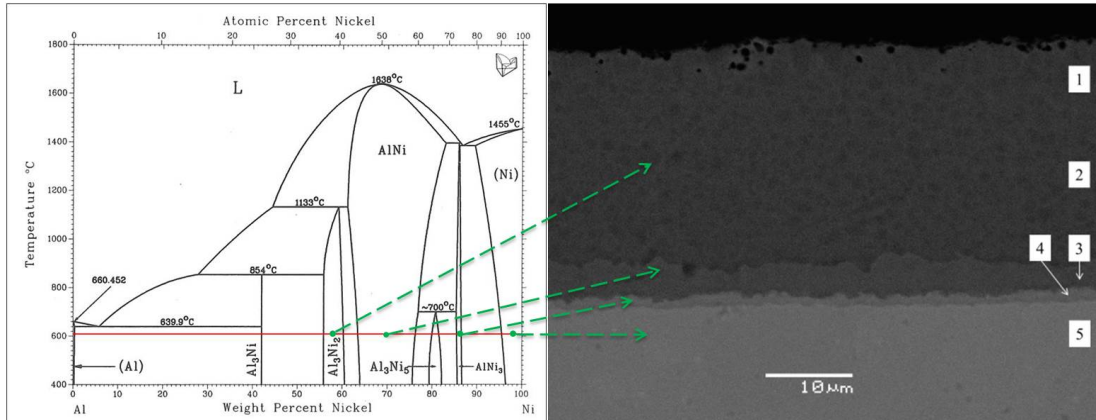
Fig. 42: Left: Ni-Al binary alloy phase diagram from [137]. The horizontal line indicates the thermo-chemical diffusion temperature (610°C). Right: Cross section of a PVD Al/Ni electrode after heat treatment at 610°C for 24h, prior to leaching. The arrows indicate the supposed intermetallic phase found in the cross section. The numbers refer to the EDS analysis in Table 7.

	Name of phase /original phase	Before leaching		Leached PVD Al/Ni 1			Leached PVD Al/Ni 2		
Phase nr.		Al [wt.%]	Ni [wt.%]	O [wt.%]	Al [wt.%]	Ni [wt.%]	O [wt.%]	Al [wt.%]	Ni [wt.%]
1	Ni_2Al_3	37	63	4	21	75	7	13	80
2	Ni_2Al_3	37	63		36	64	4	15	81
3	NiAl	30	70		30	70		29	71
4	Ni_3Al	13	87		13	87		14	86
5	Ni		100			100			100

Table 7: Results from the cross section EDS analysis on PVD Al/Ni electrodes before and after the first and the second leaching procedure. The phase numbers refer to the numbers in Fig. 42 and Fig. 43. All elements from the periodic table are analysed.

Comparing the EDS data with the Ni-Al phase diagram, it is supposed that the three following Al-Ni intermetallic phases are formed; Ni_2Al_3, NiAl and Ni_3Al, seen from the top towards the pure nickel substrate. This is also indicated with the green arrows in Fig. 42. These assumptions are in agreement with the findings of Janssen and Rieck [136]. The majority of the intermetallic phase formed is the strong, and yet leachable, Ni_2Al_3 phase [135].

When heat treated at 610°C, a thermo-chemical diffusion process takes place at the interface between the aluminium and nickel. The aluminium atoms diffuse into the nickel structure and thermodynamically alloys can be formed. The red horizontal line in the phase diagram in Fig. 42 indicates which Ni-Al diffusion couples are thermodynamically stable at 610°C and atmospheric pressure. The thickness of each intermetallic phase formed depends on the diffusion kinetics, the amount of nickel and aluminium available in the diffusion system and the heat treatment parameters.

Fig. 43 shows cross section SEM micrographs of the PVD Al/Ni electrodes after heat treatment followed by the first and second alkaline leaching procedure, PVD Al/Ni 1 and PVD Al/Ni 2, respectively.
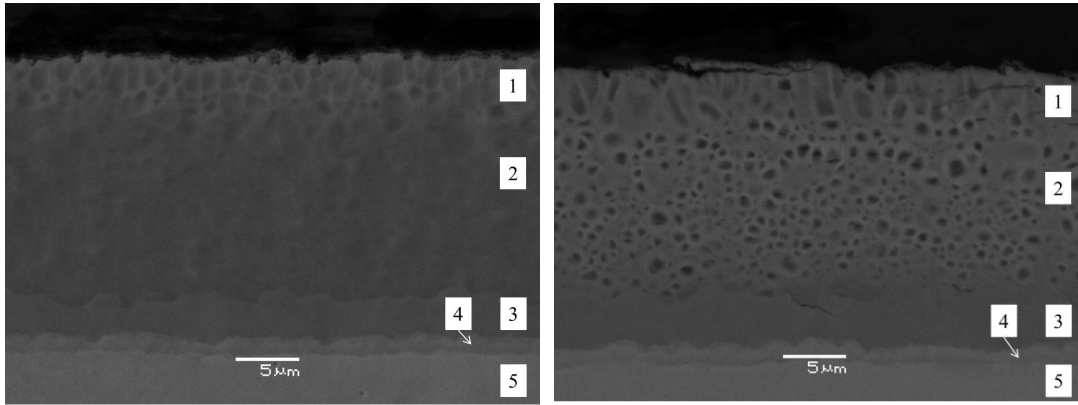
Fig. 43: Cross section SEM micrographs of a PVD Al/Ni electrode after heat treatment at 610°C for 24h, followed by alkaline aluminium leaching. Left: Prepared by the first leaching procedure (PVD Al/Ni 1). Right: Prepared by the second leaching procedure (PVD Al/Ni 2).

For the first leaching procedure, an about 5 μm skeletal Al/Ni residue is formed. When selectively leaching the aluminium with the second leaching procedure the entire Al_3Ni_2 phase is leached, resulting in considerably larger thickness of the porous nickel layer. The difference is due to the slow leaching kinetics of the Ni_2Al_3 phase below 70°C in alkaline media [135]. In addition, some of the aluminium could possibly have been redeposited into the pores during the first leaching method since no KNa-tartrate tetrahydrate was used in that process [138]. The reason for adding KNa-tartrate tetrahydrate to the alkaline leaching solutions is that it works as a complexing agent for the leached aluminium according to [139]:

$$Al(OH)_4^- + n(C_4H_4O_6)^{2-} \rightarrow Al(OH)_3(C_4H_4O_6)_n^{2-} + OH^- \qquad (20)$$
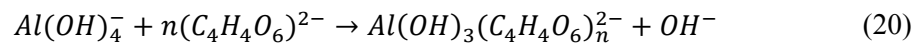
hereby preventing the aluminium hydroxide precipitates to redeposit into the nickel pores [140]:

$$Al(OH)_4^- \rightarrow Al(OH)_3 + OH^- \qquad (21)$$
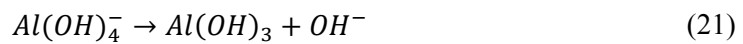
Producing high surface area nickel electrodes by PVD of aluminium onto a nickel plate was found to be successive. Numerous efficiency, durability and metallography investigations have been performed on the structure, see chapter 8, Appended papers I,II and III and the Appendix. After the successful experience of the first generation of electrodes for AWE, other process techniques for producing similar electrodes were assessed. The process techniques were selected with the aim of reducing the production cost associated with the electrode manufacture.

7.2 Hot dip aluminising

7.2.1 Introduction

Hot dip aluminising is a well-known process and widely used in the steel industry for improving the wear and corrosion resistance [141]. Still, only few attempts of hot dip

aluminising of nickel have been reported [142]–[144]. This process technique was chosen because it was expected to give good adhesion between the nickel substrate and the aluminium coating. The technique is, furthermore, inexpensive and relatively simple.

7.2.2   Experimental procedure

Series of nickel coupons (of the same type as in 7.1), measuring approximately 100×20×0.5 mm were immersed into liquid aluminium melt (99,8% Al) at around 700°C for 2 - 600 seconds and subsequently quenched in water at room temperature. The nickel coupons were immersed in a cathodic degreaser for 2 minutes, pickled for 1 minute, rinsed with ethanol and dried prior to each dipping procedure. For minimizing the amount of oxide slag on the specimen surface after dipping, the top layer of the aluminium melt was scraped aside prior to each dipping procedure. Fig. 44 shows the clay crucible used in the experiment as placed in the induction furnace applied, before and after melting of the aluminium.

Fig. 44: The clay crucible used for the hot dip aluminising as placed in the furnace before and after melting of the aluminium.

The hot dip aluminised nickel was subsequently heat treated in an atmospheric furnace at 610°C for 24 hours. The long duration of heat treatment was selected to assure formation of the Al_3Ni_2 phase throughout the whole diffusion layer, as earlier proven successful. The experimental series for the hot dip aluminising procedure are listed in Table 8.

Specimen number	Dipping-time [s]	Heat treatment at 610 ˚C [h]
1	2	-
2	8	-
3	30	24
5	300	-
6	600	-

Table 8: Experimental series for hot dip aluminizing

7.2.3   Results and discussions

The most common challenges when working with hot dip aluminising is degradation of the aluminium melt due to oxidation and hydrogen dissolution [141]. Aluminium has a high affinity to oxygen, thus, the aluminium reacts easily with the oxygen in the atmosphere during melting and an insoluble oxide slag is formed on the surface of the aluminium melt. Liquid aluminium at 700°C has hydrogen solubility of about 1 ml/100 g [145], whereas solid aluminium has hydrogen solubility of maximum 0.034 ml/100g [141]. Therefore, hydrogen

gas entrapped in the aluminium melt will result in voids in the solid aluminium phase. The hydrogen originates from the reaction of liquid aluminium and moisture from the furnace atmosphere according to:

$$2Al + H_2O \rightarrow Al_2O_3 + 3H_2 \tag{22}$$

This reaction has a Gibb's free energy of -787.3 kJ at 700°C, indicating that the reaction is highly thermodynamically favourable at the specific temperature.

As an attempt to reduce the formation of oxygen slag and hydrogen dissolution in the melt, argon gas was purged through the liquid aluminium during dipping. Unfortunately, the purging of argon gas into the melt caused turbulence and agitation in the liquid aluminium leading to significant increase of oxidation of the melt. Specimen B in Fig. 45 characterises a specimen after hot dip aluminising where argon gas has been purged through the melt, whereas specimen A characterises a hot dip aluminised specimen produced without purging of argon gas.

Fig. 45: Two hot dip aluminized nickel coupons. A) Without purging of argon gas and B) with purging of argon gas.

It is clear from the images that more oxide slag is attached to the nickel coupon immersed in the liquid aluminium purged with argon gas. Therefore, it was therefore decided to perform the hot dip aluminising without argon purging.

Fig. 46 shows cross section LOM micrographs of nickel plates after being immersed into molten aluminium for 2 and 8 seconds.
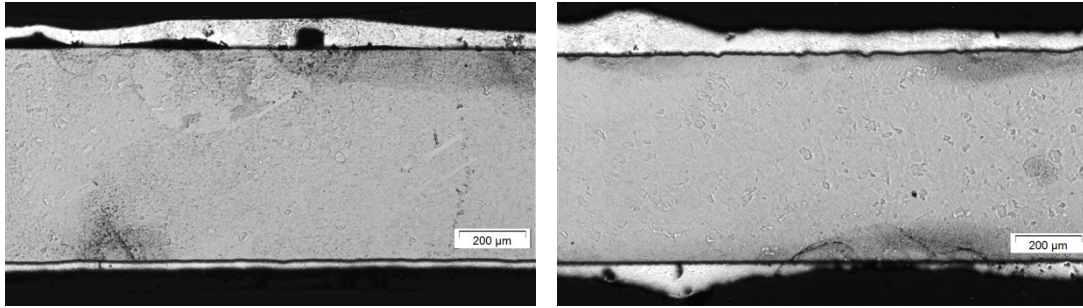
Fig. 46: Cross section LOM image of a nickel plate immersed in molten aluminium. Left: for 2 sec. Right: for 8 sec.

As seen from the LOM micrographs, 2 seconds of dipping time is not enough to achieve proper wetting between the aluminium melt and the nickel surface. When immersing for 8 seconds, considerable better wetting of the nickel surface is attained. There is, however, still some localised unwetted areas to be found on the surface. The inhomogeneous wetting of the surface can be caused by different thickness of nickel oxide to be reduced by metallic aluminium on the coupon surface or by the aluminium oxide formed during the initial reduction of nickel oxide on the surface according to:

$$2Al + 3NiO \rightarrow Al_2O_3 + 3Ni \qquad (23)$$
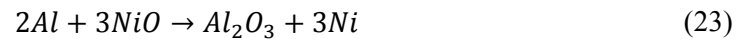
The small pores observed in the aluminium coating are presumably hydrogen pores from the hot dip aluminising process.

When immersing a nickel coupon into the aluminium melt for 30 seconds the entire nickel surface becomes wetted, Fig. 47. The aluminium layer is however, as expected from the inhomogeneous wetting, not uniform.
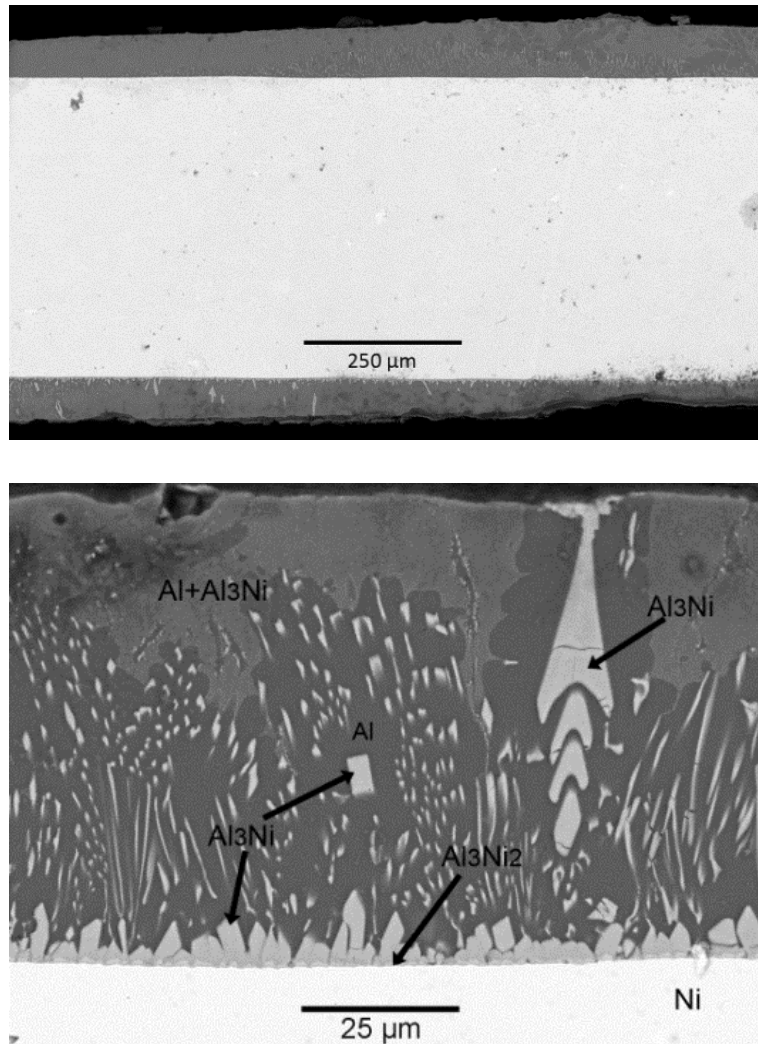
Fig. 47: Cross section BSE SEM micrographs of a nickel coupon after hot dip aluminizing for 30 seconds.

When the nickel plate is immersed into the 700°C aluminium melt, the aluminium starts almost immediately to diffuse into the nickel bulk and the eutectic Al_3Ni phase is formed. According to the Al-Ni binary alloy phase diagram, shown in Fig. 48, the line for the liquid melt at 700°C is in contact with the Al_3Ni phase.
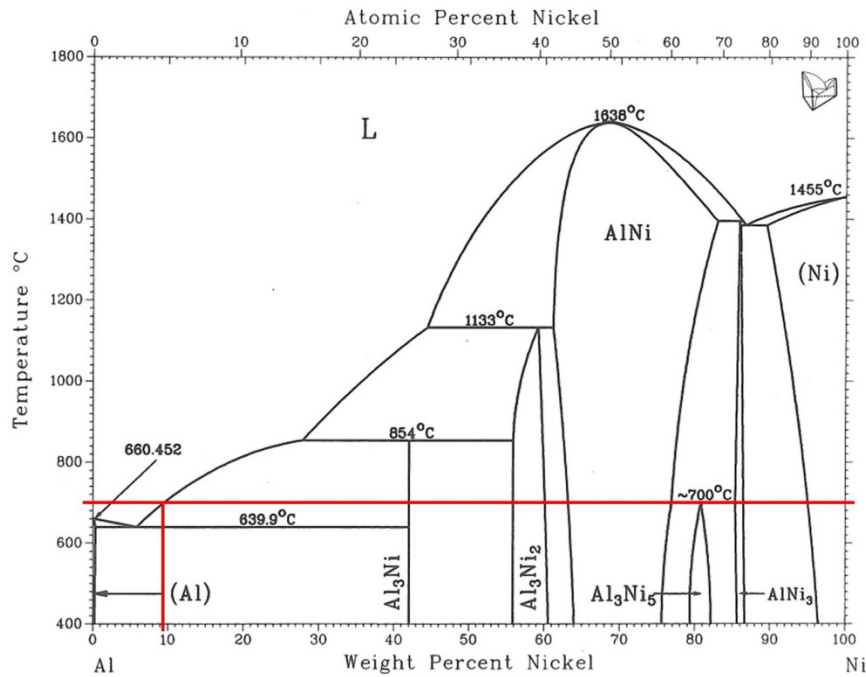
Fig. 48: Al-Ni binary alloy phase diagram [137].

Therefore, some of the Al$_3$Ni phase formed during the hot dip aluminising process will dissolve in the aluminium melt forming Al$_3$Ni precipitates in the aluminium rich melt. This is evident in Fig. 47 where the white areas are Al$_3$Ni precipitates, the grey areas the Al+Al$_3$Ni eutectic phase and the dark areas are aluminium. Solid state diffusion between the Al$_3$Ni and the nickel substrate results in the formation of a thin layer of Al$_3$Ni$_2$ phase. The results from EDS analyses are shown in Table 9.

Name of phase /original phase	Hot dip Al 30 sec.			Hot dip Al 30 sec. + heat @ 610°C for 24h.		
	O [wt.%]	Al [wt.%]	Ni [wt.%]	O [wt.%]	Al [wt.%]	Ni [wt.%]
Ni	-	-	100	-	-	100
Al$_3$Ni$_2$	-	*	*	3	38	59
Al$_3$Ni	-	58	42	-	-	-
Al+Al$_3$Ni	3	87	10	-	-	-
Al	3	92	5	-	-	-

Table 9: Results from EDS analyse on the hot dip aluminised specimen, prior to heat treatment (Fig. 47) and after 24 h. of heat treatment (Fig. 50). All elements from the periodic table except for carbon are analysed.
*The area of the intermetallic phase is too thin to be measured. The name of the phase is predicted from the Al/Ni phase diagram.

Due to the dissolution of the nickel into the aluminium melt during the process it is important not to immerse the specimen into the melt for excessive time periods, as this will destroy the initial surface structure of the nickel coupons, making them very non uniform. The cross section micrograph of a nickel coupon after 5 minutes immersion in the aluminium melt, Fig. 49, shows the dissolution of the nickel coupon after immersion. Hot dip aluminising a nickel coupon for 10 minutes resulted in complete dissolution of the nickel specimen.
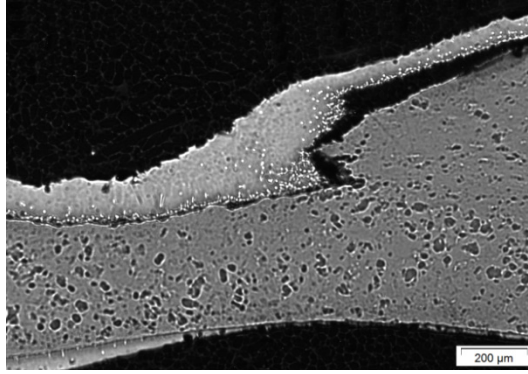
Fig. 49: Cross section LOM micrograph of a nickel coupon after 5 minutes of hot dip aluminising.

In order to facilitate larger amount of the desired Al_3Ni_2 intermetallic phase, a nickel coupon that had been immersed in the aluminium melt for 30 sec. was heat treated at 610°C for 24 hours, see Fig. 50.
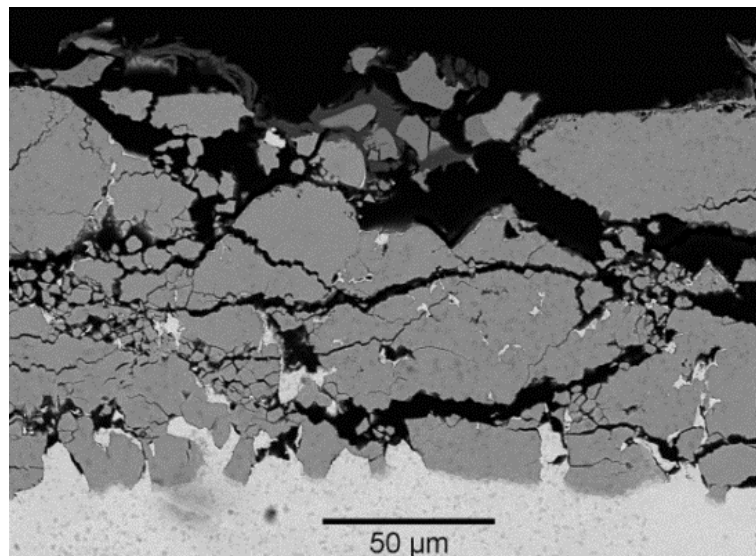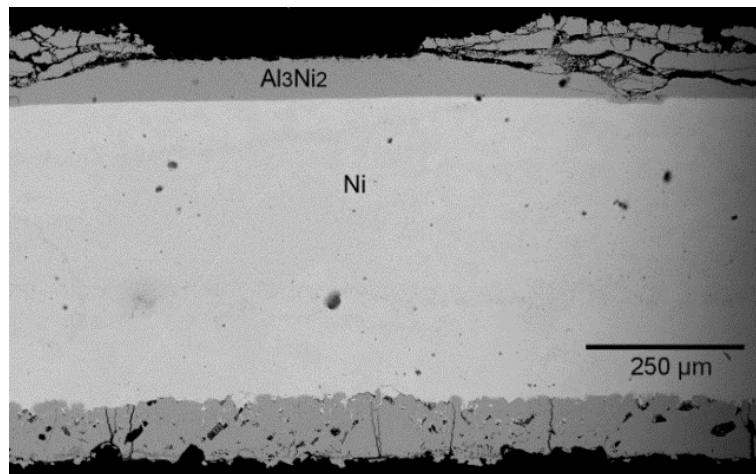
Fig. 50: Cross section SEM micrographs of a nickel coupon hot dip aluminised for 30 sec. and heat treated at 610°C for 24 hours.

EDS analyses of the cross section are listed in Table 9. The analyses indicate that the developed surface solely consists of about 100 μm Al_3Ni_2 phase.

As apparent from the SEM micrographs, the Al_3Ni_2 phase formed contains cracks and voids. The cracks are possibly due to the compressive stress induced in the coating during diffusion and/or due to thermal mismatch stresses generated in the coating as it cools from 610°C to room temperature. The stresses in the coating pile up and increase throughout the thickness of the Al_3Ni_2 layer. The relatively brittle Al_3Ni_2 structure is evidently not able to accommodate for the stresses through the whole structure. This results in lack of space for the developed coating and cracks are formed. The voids in the developed Al_3Ni_2 structure are possibly due to hydrogen and oxides that are formed in the aluminium layer during the hot dip aluminising process as explained earlier.

The next step in the procedure for producing electrodes with large actual surface area for AWE ought to be selective alkaline leaching of the aluminium from the Al_3Ni_2 phase. Due to the brittle features of the coating, the existence of insulating oxides and the difficulties of controlling the layer thickness of the coating, the hot dip aluminising process technique was evaluated to be unsuitable for the AWE electrode development. Further process procedures were, therefore, not prepared for this particular screening.

7.3   Thermo-chemical diffusion of aluminium and nickel sheets

7.3.1   Introduction

In this chapter the screening from the simplest way of diffusing aluminium and nickel together is introduced. The process involves placement of a nickel and aluminium sheet on top of each other and heat treated. This method was actually not expected to give good results due to the oxide layers of the original sheets that could not be sputtered away in-situ as for the PVD process. Due to the surprisingly good results from this trial the results will be reported here.

7.3.2   Experimental procedure

Aluminium sheet (99% Al) measuring 50×50×0.5 mm was placed on top of a nickel sheet (99% Ni, of the same type as previously) of the same size. The sheets were thereafter heat treated in argon atmosphere furnace. The initial temperature was set to be 700°C in order to melt the aluminium. Thereafter the temperature was gradually reduced to 610°C for maintaining thermo-chemical diffusions and preventing nickel dissolution. The overall heat treatment varied for 2 hours. The nickel and aluminium sheets were immersed in a cathodic degreaser for 2 minutes and pickled for 1 minute, rinsed and dried prior to the heat treatment. The specimens were subsequently leached in 30 wt.% KOH and 10 wt.% $KNaC_4H_4O_6{\times}4H_2O$ at 80°C with stirring for 24 hours.

7.3.3   Results and discussions

Similarly to the hot dip aluminising process, Al + Al_3Ni eutectic phase is the first intermetallic phase to be formed during the diffusion process between the aluminium and nickel sheets. This is followed by a solid state diffusion between the Al_3Ni and the nickel resulting in formation of Al_3Ni_2 phase according to [146]:

$$Ni + Al_3Ni \rightarrow Al_3Ni_2 \tag{24}$$

In contrast to the hot dip aluminising process, the direct diffusion process gives the possibility of longer heat treatment without deforming or dissolving the nickel substrate. The two hours of heat treatment results in the formation of about 100 μm of the Al_3Ni_2 phase, see Fig. 51.
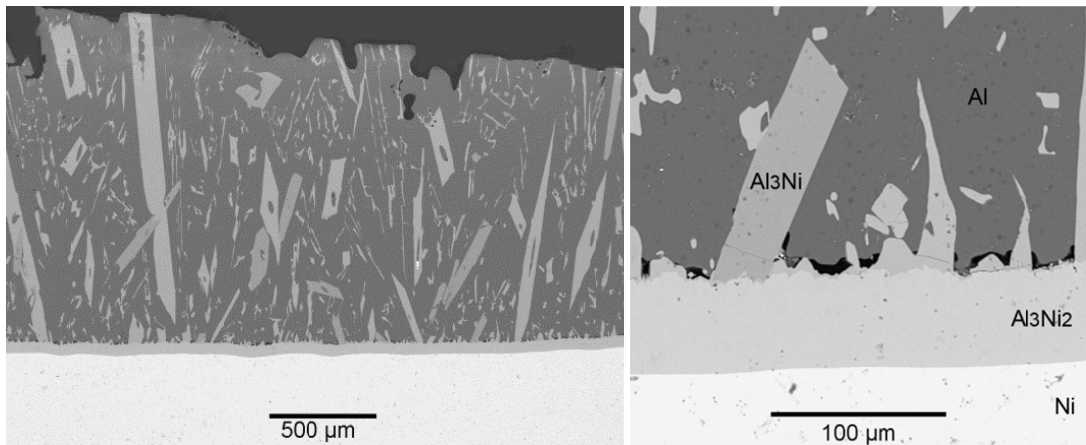
Fig. 51: Cross section BSE SEM micrographs of the thermo-chemical diffused aluminium and nickel sheets.

The direct formation of Al_3Ni_2 takes place because the Al_3Ni eutectic phase is above the lower heat treatment temperature applied, i.e. 610°C, see Al-Ni phase diagram in Fig. 48. As a result, no post heat treatment procedure is needed. The attained Al_3Ni_2 layer is relatively uniform without any cracks or pores. Results from the EDS analyses of the phases in Fig. 51 are reported in Table 10.

Name of phase /original phase	Heat treated		Heat treated and Al leached		
	Al [wt.%]	Ni [wt.%]	O [wt.%]	Al [wt.%]	Ni [wt.%]
Ni	-	100	-	-	100
Al_3Ni_2	43	57	13	8	79
Al_3Ni	73	27	-	-	-
Al	100	-	-	-	-

Table 10: EDS analyses on thermo-chemical diffused aluminium and nickel sheets (Fig. 51 and 52). All elements from the periodic table except for carbon are analysed.

In order to facilitate a porous nickel structure, the heat treated specimen was selectively aluminium leached in 30 wt.% KOH and 10 wt.% $KNaC_4H_4O_6 \times 4H_2O$. During alkaline leaching, the entire aluminium rich top layer of the specimen is etched away. The majority of

the aluminium in the Al_3Ni_2 phase is selectively leached as well. This is evident from the cross section SEM micrograph in Fig. 52 combined with the EDS analyses reported in Table 10.
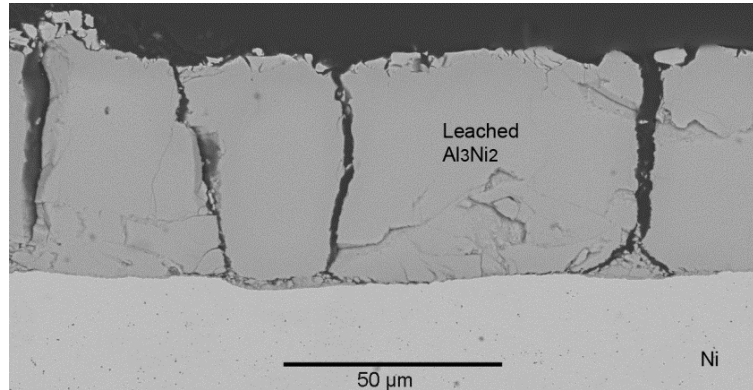
Fig. 52: Cross section BSE SEM micrograph of the thermo-chemical diffused aluminium and nickel sheets after selective leaching of aluminium.

The remaining nickel residue is characterised with large macropores perpendicular to the surface. Smaller cracks can also been seen between the leached layer and the nickel substrate. The cracks are formed due to the tensile stresses that build up in the structure during aluminium leaching. The fact that the etched structure contains only 8 wt.% aluminium and a reasonably large amount of oxygen, 13.wt%, the structure is expected to be porous. This can however not been seen in the SEM micrographs at the possible magnification on the applied SEM.

7.4   Aluminium ionic liquid electroplating

7.4.1   Introduction

Aqueous electroplating is the most common process technique for producing metallic coatings with high purity and god adhesion properties. However, due to the reactive nature of aluminium, i.e. E_0 = -1.66 V vs. SHE [42], hydrogen evolution reaction will take place prior to deposition during electroplating in aqueous media. Electroplating of aluminium can therefore only be prepared in non-aqueous electrolytes. The two main electrolytes used for electroplating of aluminium are non-aqueous organic solvents and molten salts. The non-aqueous organic solvents are generally inflammable, volatile, have low conductivity and narrow electrochemical window. Inorganic molten salts operate at temperatures above 150°C whereas organic molten salts (i.e. ionic liquids) operate at lower temperatures [147]. Several authors have described successful aluminium deposition using a nontoxic ionic liquid bath containing dimethyl sulfone ($DMSO_2$) and aluminium chloride ($AlCl_3$) [147]–[149]. Inspired by the literature aluminium was electroplated in an ionic liquid electroplating bath containing dimethyl sulfone and aluminium chloride with a molar ratio of 10:2 ($DMSO_2/AlCl_3$).

7.4.2 Experimental procedure

Aluminium was electroplated in an ionic liquid electroplating bath containing dimethyl sulfone and aluminium chloride with a molar ratio of 10:2 ($DMSO_2/AlCl_3$). The electroplating procedure was constructed in a sealed glass beaker as illustrated in Fig. 53.
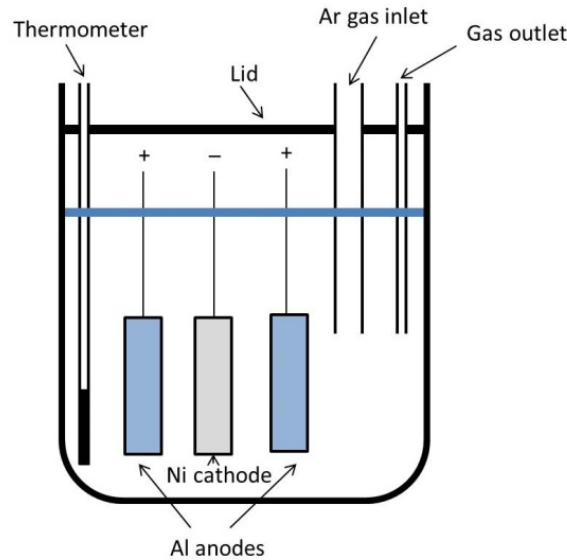
Fig. 53: Schematic illustration of the experimental setup for the aluminium ionic liquid electroplating procedure.

The operation temperature was 120°C and the deposition was prepared at the current density of 10 A/dm^2 for 2 hours in an argon atmosphere. The anode was made of 99% aluminium and the cathode (substrate) consisted of nickel (99 wt.%). The nickel substrates measured approximately 50×10×0.5 mm. Both anode and substrate were cathodically degreased for 2 minutes and pickled for 1 minute prior to the electroplating process. The electroplated specimen was subsequently heat treated in an atmospheric furnace at 610°C for 24 hours.

7.4.3 Results and discussions

According to [150] the plating mechanism is as follows; first blending of the solvent and the reactive aluminium salt according to:

$$4AlCl_3 + 3C_2H_6O_2S \rightarrow Al(C_2H_6O_2S)_3^{+3} + 3AlCl_4^- \tag{25}$$
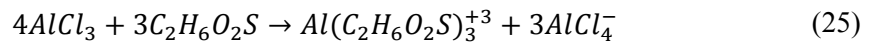
Thereafter reduction of aluminium according to:

$$Al(C_2H_6O_2S)_3^{+3} + 3e^- \rightarrow 3C_2H_6O_2S + Al \tag{26}$$
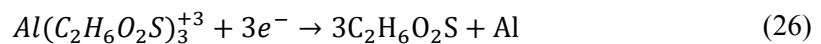
As seen from Fig. 54 (left) at about 100 µm dense aluminium coating is attained from the ionic liquid electroplating process.
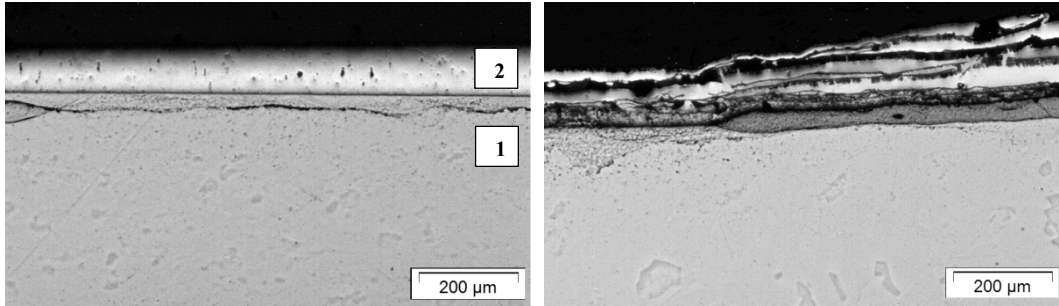
Fig. 54: Cross section LOM micrographs of ionic liquid electroplated Al on a nickel substrate. Left, as plated. Right, heat treated for 24 h. at 610°C.
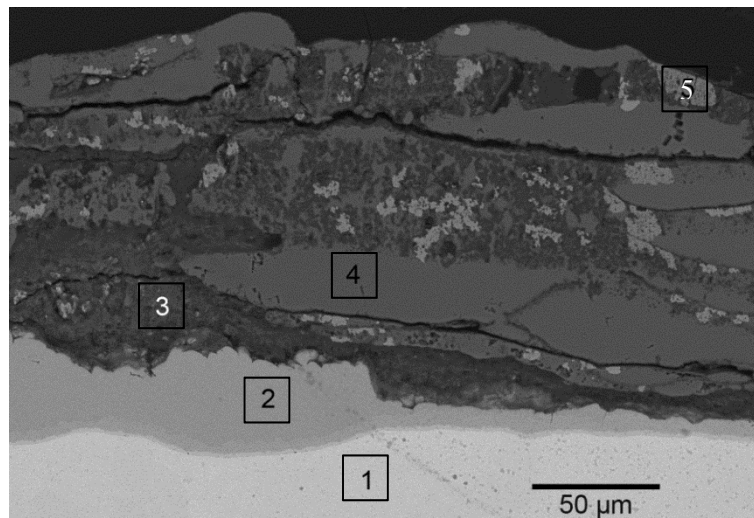
Fig. 55: Cross section SEM micrograph of a ionic liquid electroplated aluminium on a nickel substrate after 24 hours heat treatment at 610 °C.

The aluminium coating is characterised with relatively many pores, similar to those observed with the hot dip aluminising process. The porous structure is possibly due to hydrogen evolution during plating. Although the electroplating process is prepared in argon atmosphere, the hygroscopic nature of the $AlCl_3$ salt makes it difficult to assure that the salt will not react with the water in the atmosphere. As said before, water is not stable at the electroplating potential and will be reduced to hydrogen at the cathode.

EDS analyses of the as plated structure indicates that some sulphur and chlorine is incorporated into the deposited aluminium during plating, see Table 11.

Phase no.	Electroplated					Electroplated + heat @ 610°C for 24 hours				
	O [wt.%]	Al [wt.%]	Ni [wt.%]	S [wt.%]	Cl [wt.%]	O [wt.%]	Al [wt.%]	Ni [wt.%]	S [wt.%]	Cl [wt.%]
1	-	-	100				-	100		
2	4	94	-	1	1	-	37	61		
3						43	48	3	4	2
4							100			
5						8	60	32		

Table 11: EDS analyses on the aluminium ionic liquid electroplated nickel substrate (Fig. 54 and 55). All elements from the periodic table except for carbon are analysed.

Some of the Cl and S content are expected to be from the electrolyte that gets entrapped in the porous structure during plating. However, while electroplating a strong odour of SO_2 was detected from the plating bath, indicating degradation of the $DMSO_2$ solvent. Jiang et al. [150] also reported findings of Cl and S in their coatings. In their study, insufficient cleaning of the electrodes and/or entrapped or codeposited electrolyte was assumed to be the cause of the impurities. Recently Miyake et al. [149] reported thorough investigations of S and Cl impurities in aluminium coatings from $DMSO_2/AlCl_3$ electrolytes at current densities varying from 20–80 A/dm^2 and molar ratio of 10:2 and10:3 ($DMSO_2/AlCl_3$). The produced aluminium coatings were found to contain 0.1–1 at.% of Cl and S. The impurity content was found to decrease with increased current density. Higher molar ration of $AlCl_3$ resulted in a slight rise in the impurity content as well. The authors did, however, not succeed in finding the reason for incorporation of Cl and S impurities in the coating.

Here it is proposed that the S is reduced at the cathode during electrodepositing leading to the formation of Al_2S_3 according to the following half-cell reaction:

$$3C_2H_6O_2S + 2Al^{+3} + 12e^- \rightarrow Al_2S_3 + 3C_2H_2(g) + 6OH^- + 3H_2(g) \qquad (27)$$
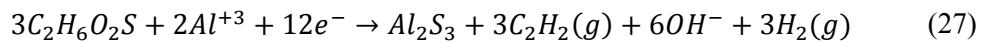
Acetylene (C_2H_2) is proposed as the possible carbon compound formed by the electrochemical reduction of dimethyl sulfone ($DMSO_2$). The half-cell reaction has an equilibrium potential (E_0) of -0.770, which is much lower than the actual equilibrium potential of aluminium. This means that the proposed decomposition mechanism can take place at potentials that are less negative than the cathodic potential needed to deposit aluminium, i.e. less energy is needed to decompose the solvent compared to electroplating of aluminium. Al_2S_3 is, nonetheless, not stable in the atmosphere and when exposing the electroplated coating to air, hydrogen sulphide and aluminium oxide will form according to:

$$Al_2S_3 + 3H_2O \rightarrow 3H_2S(g) + Al_2O_3 \quad (\Delta G = -79.185 \text{ at } 20°C) \qquad (28)$$
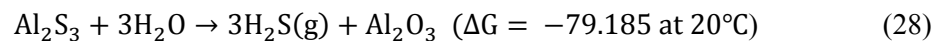
This was verified with an odour of hydrogen sulphide when drying the electrodeposited specimen in air.

Even though H, O, Cl and S contaminants were found in the electroplated aluminium coating, an attempt was made to produce the desired Al_3Ni_2 structure via heat treatment as before. The micrographs in Fig. 54 and Fig. 55 combined with the EDS analyses in Table 11 indicate that only a small amount of aluminium actually diffuses into the structure and forms the Al_3Ni_2 intermetallic structure (phase 2 in Fig. 55). The remaining deposited aluminium coating expands intensively during the heat treatment and a dark layer (with higher Z-contrast) containing large amount of oxygen and traces of S and Cl is formed. These dark layers most likely act as a diffusion barrier between the aluminium and nickel. It is, therefore, evident that the incorporated impurities lead to crack formations and expansion of the structure when heat treated and little or no interdiffusion between the aluminium and nickel takes place. Due to improper Al_3Ni_2 formation from ionic liquid electroplating, no further attempts for producing large surface area nickel structure were done this screening.

7.5 Physical vapour deposition of aluminium onto electroplated sulfamate nickel

7.5.1 Introduction

For the porous nickel electrodes prepared during this project the effort has mainly been concentrated on coating of a commercially pure nickel. For lowering the production cost for large scale production, plating nickel onto an iron or a stainless steel plate would be a better alternative. In this screening, PVD aluminium is deposited onto an electroplated nickel substrate.

7.5.2 Experimental procedure

A sulfamate nickel coating was electroplated onto a 50×50 mm 304 stainless steel substrate in an electrolyte containing ca. 300 g/l $Ni(SO_3NH_2)$, 40 g/l H_3BO_3 and 10 g/l $NiCl_2×6H_2O$. The deposition current density was 4.5 A/dm^2 and the plating duration was 2 hours at 45°C. The pre-treatment of the steel substrate was as follows; cathodic degreaser for 2 min., pickling for 1 min., etching in 20% HCl and 5% H_2O_2 for 1 min. (to remove chromium oxides from the surface), followed by cathodic degreaser for 2 min. and pickling for 1 min. In order to assure good adhesion, a thin layer of woods nickel was electroplated onto the steel substrate according to; anodic at 7 A/dm^2 for 2 min (to remove the last oxides on the surface) and cathodic deposition at 14 A/dm^2 for 2 min.

The nickel plated steel substrates were PVD treated with about 20 μm aluminium as explained in section 7.1.2. The aluminium PVD specimens were subsequently heat treated in an atmospheric furnace for 4 hours at 610°C followed by selective aluminium leaching in 30 wt.% KOH and 10 wt.% $KNaC_4H_4O_6×4H_2O$ at 80°C with stirring for 24 hours.

7.5.3 Results and discussions

Sulfamate nickel coatings are known to have low stress and high ductility. These properties could benefit the durability of the nickel electrodes and therefore sulfamate nickel coating was selected over other nickel coatings. Fig. 56 and Fig. 57 show SEM micrographs of the PVD aluminium nickel structure after 4 hours of heat treatment and after heat treatment followed by selective aluminium leaching. Here shorter heat treatment is selected due to knowledge gained from other thermo-chemical diffusion processes investigated; see Appended papers II and III. The results from the EDS analyses are listed in Table 12.
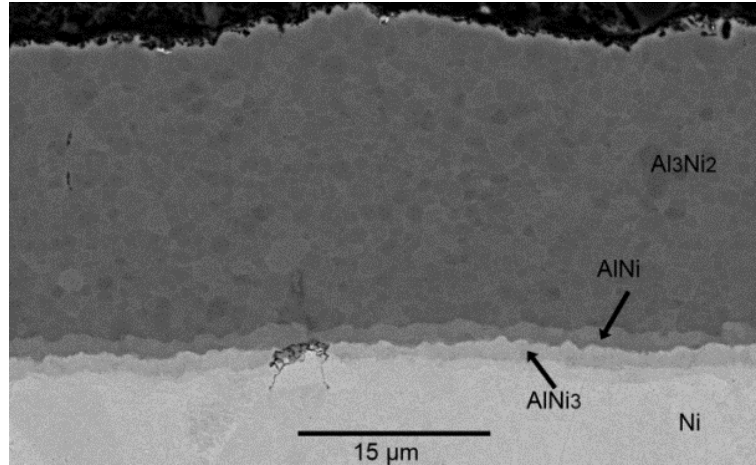
Fig. 56: Cross section SEM micrographs of PVD aluminium on sulfamate nickel substrate heat treated at 610°C for 4 hours.
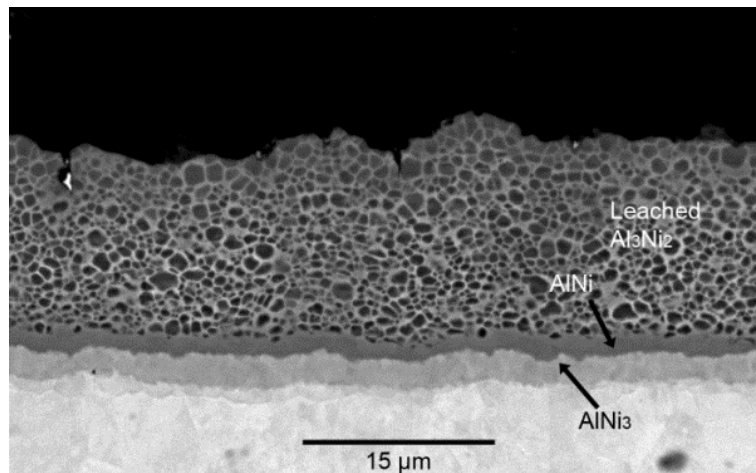
Fig. 57: Cross section SEM micrographs of PVD aluminium on sulfamate Ni substrate heat treated at 610°C for 4 hours and alkaline aluminium leached.

Name of phase /original phase	PVD Al on sulfamate Ni heat treated		PVD Al on sulfamate Ni heat treated and leached		
	Al [wt.%]	Ni [wt.%]	Al [wt.%]	Ni [wt.%]	O [wt.%]
Al_3N_2	39	61	7	71	22
AlNi	29	71	32	68	-
$AlNi_3$	16	84	16	84	-
Ni	-	100	-	100	-

Table 12: EDS analyses on the PVD Al on sulfamate Ni specimens (Fig. 56and Fig. 57). All elements from the periodic table except for carbon are analysed.

It is evident from the SEM micrographs and the EDS analysis that the whole Al_3Ni_2 phase is leached during the leaching process. Porous nickel coating containing 7% aluminium is developed by this process technique. The high oxygen content in the porous layer is most likely due to resin trapped inside the pores, which supports the proposal that the structure is porous. No cracks are visible in the porous structure.

7.6 Conclusions on the manufacturing of a high surface area nickel coating

In the present work an attempt was made to produce dense high surface area nickel structure using five different process techniques. The results together with the advantages, disadvantages are summarised in Table 13. The results show that due to the high affinity of aluminium towards hydrogen and oxygen, production of oxide free Al_3Ni_2 alloy coatings in an inexpensive and simple manner is challenging. The next step in the development process is AWE efficiency and durability testing of the electrodes produced by direct diffusion between aluminium and nickel sheets and the PVD aluminium onto electroplated sulfamate nickel.

Process technique	Advantages	Disadvantages	Results
PVD Al onto Ni	Even and well levelled porous nickel coating is formed.	PVD is a relatively expensive process technique.	Producing high surface area nickel electrodes by PVD of Al onto a Ni plate was found to be successive and numerous efficiency, durability and metallography investigations have been performed, see chapter 8, Appended papers I,I and II.
Hot dip Al of Ni plates	Inexpensive and simple	Hydrogen voids and oxide inclusions are observed. Dissolution of the nickel coupon during immersion. Inhomogeneous wetting of aluminium and difficulties to control the thickness of the aluminium coating.	When heat treated about 100 μm of Al_3Ni_2 was formed. The intermetallic coating contained cracks and insulating oxides making it unsuitable electrocatalytic coating for AWE.
Thermo-chemical diffusion of Al and Ni sheets	Inexpensive and simple. No post heat treatment is needed.	Operating in argon atmosphere is a complication factor for large scale production.	A dense macro- and supposedly nanoporous coating of about 100 μm was formed. Crack formation perpendicular to the surface increase the risk of gas erosion corrosion during AWE operation.
Al ionic liquid electroplating	Inexpensive	Uneven aluminium coating. Contains impurity inclusions such as chlorine, sulphur and oxides.	The impurity inclusions incorporated in the as deposited structure makes it unsuitable as an electrode coating for industrial AWE
PVD Al onto electroplated sulfamate Ni	PVD is a relatively expensive process technique.	Less expensive than using solid nickel plate.	Producing high surface area nickel electrodes by PVD of Al onto a sulfamate Ni was found to be successive.

Table 13: Summary from screening of process techniques for producing high surface nickel electrocatalyst

8 Efficiency and Durability Measurements on the Developed PVD Al/Ni Electrodes

8.1 Introduction

In order to characterise and evaluate the nickel supported PVD Al/Ni electrocatalyst, numerous electrochemical and durability measurements have been performed. Here selected tests will be introduced and discussed in order to evaluate the overall quality of the electrodes. A part of these results have been published or are to be subjected to publication, see Appended papers I and II

8.2 Experimental procedure

The electrodes to be tested were produced by the means of PVD of aluminium onto a nickel substrate as reported in section 7.1. Cathodic measurements of electrodes produced in the same manner, except for reduced heat treatment, are included for comparison. These electrodes were heat treated for 10, 20 and 30 min. instead of the 24 hours. Structural, morphology and composition investigations are given in Appended papers I and II.

The activity and durability of the electrodes was evaluated by means of potentiodynamic measurements, single cell electrolysis measurements and measurements carried out in an electrolysis stack. The potentiodynamic measurements were carried out using the half-cell test setup introduced in section 5.3. The potential of the working electrode was recorded against an Hg/HgO reference electrode from Radiometer (XR440) and a counter electrode made of nickel. The electrolyte was 1 M KOH and the measurements were carried out at 25°C. The half-cell measurements were IR-compensated by means of current interruption. All following half-cell potentials reported are determined versus the Hg/HgO reference electrode.

The cathodic potentiodynamic measurements were carried out as follows: conditioning at -0.8 or -0.9 V for 30 minutes in order to eliminate the amount of hydrates from the surface, open circuit potential (OCP) until 0.01 mV/sec stability followed was reached, followed by a cathodic sweep from -0.615to -1.415 V using scan rate of 1 mV/s. Potentiodynamic measurements on polished nickel was performed in the same manner for comparison. In order to capture potential outputs in the same range as for the developed electrodes the upper limit voltage for the polished nickel measurements was increased to -1.715 V.

In the case of anodic measurements the procedure was initialised by a 30 min. conditioning at 0.815 V, in order to facilitate a stable NiO structure, followed by OCP until 0.01 mV/sec stability was reached. The potentiodynamic measurements were recorded from 0.4 to 0.9 V at a scan rate of 1 mV/s.

Durability and whole cell efficiency investigations were carried out in the electrolysis test setup introduced in section 5.2. The electrolyte contained 50 wt.% KOH and the measurements were operated at 120°C. The electrolyte was pre-electrolysed at 2 V potential for 3 days prior to testing. The high concentration of the electrolyte was in order to achieve high conductivity and to avoid the electrolyte from boiling. The diaphragm used was a Zirfon® Perl 500 UTP. The distance between the anode and cathode was 2.5 mm, 1 mm from the diaphragm on each side plus the thickness of the diaphragm which is approximately 0.5 mm.

Stack measurements were performed in a 17 cell bipolar, non-zero gap electrolysis stack introduced in section 5.4. The stack contained 30 wt.% KOH and was operated under altered conditions, at a maximum temperature of 80°C and a pressure of 22 bar for approximately 9000 hours. Operating data was captured during the first month of operation and the approximately 9000 hours of operation. The data management was carried out at GreenHydrogen.dk

8.3 Results and discussions

8.3.1 Half-cell measurements

8.3.1.1 Cathodes

Results from the potentiodynamic measurements recorded on the developed PVD Al/Ni electrodes produced with different duration of heat treatment are shown in Fig. 58.
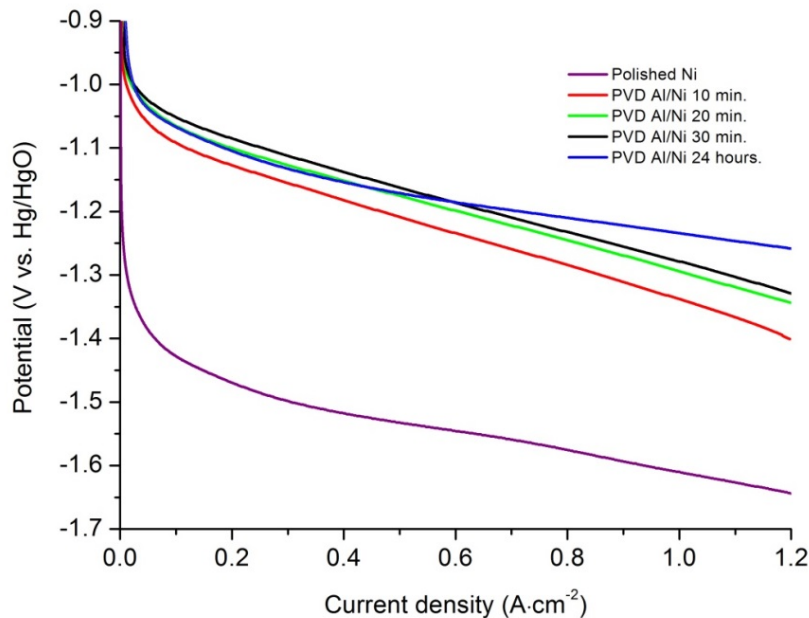
Fig. 58: Cathodic potentiodynamic polarisation curves recorded on the developed electrocatalyst produced with different heat treatments (10, 20, 30 minutes and 24 hours) compared to polished nickel. The electrolyte contains 1 M KOH and the experiments are performed at 25°C.

For the practise of finding the exchange current density and calculating the Tafel slopes for the reactions, the results are re-plotted in logarithmic scale (Fig. 59) where the x-axis intersects the y-axis at the theoretical potential of HER (-0.943 V).
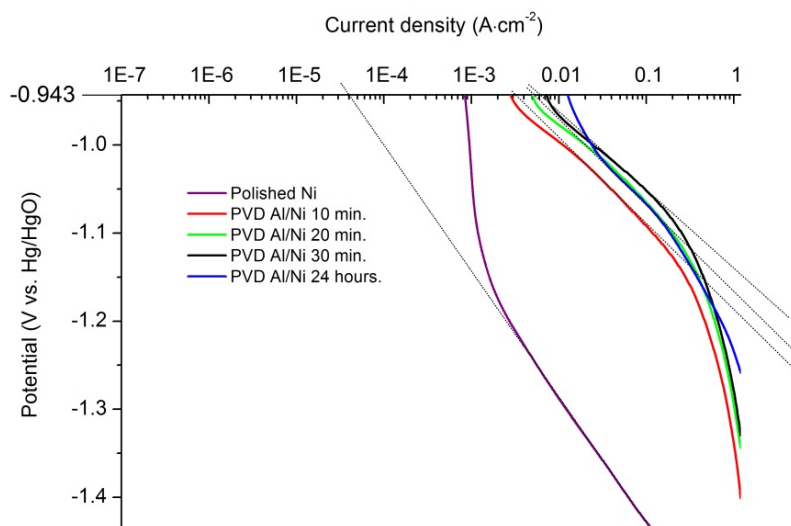
Fig. 59: Re-plot of the cathodic potentiodynamic curves from fig. Fig. 58 in order to find I_0 and Tafel slopes. The grey lines indicate Tafel slope 1 from 0.02 to 0.1 A/cm^{-2}.

Results from the cathodic potentiodynamic measurements are gathered in Table 14.

	Tafel slope 1 [mV/dec.]	Tafel slope 2 [mV/dec.]	I_0 [mA/ cm^2]	η_{HER} @ 200 A/cm^2 [mV]	η_{rev} @ 200 A/cm^2*
Polished Ni	141	171	4e-2	527	64%
PVD Al/Ni 10min.	102	245	3	184	84%
PVD Al/Ni 20min.	94	225	5	157	86%
PVD Al/Ni 30min.	83	228	6	142	87%
PVD Al/Ni 24h.	111	167	5	162	85%

Table 14: Tafel slopes, HER overpotential (η_{HER}) and calculated efficiency (η_{ref}) from the cathodic potentiodynamic measurements recorded on the developed electrode.
*Calculated according to the reversible potential of HER (-943 mV vs. Hg/HgO).

The Tafel slope is calculated from two current density intervals. Tafel slope 1 is calculated from the range of 20-100 mA/cm^2 and Tafel slope 2 from the interval of 100-1000 mA/cm^2. The results from the cathodic potentiodynamic measurements together with efficiency calculations are collected in Table 14.

The HER overpotential at 200 mA/cm^2 is up to 385 mV less for the developed electrocatalyst compared to polished nickel. The electrode showing the best catalytic activity is the PVD Al/Ni heat treated for 30 minutes, comprising a Tafel slope of 83 mV/dec. and exchange

current density for the hydrogen production of 6 mA/cm^2. At higher current density the 24 hours heat treated electrode outpaces the others with a Tafel slope of 167 mV/dec. compared to the 228 mV/dec. for the 30 minutes heat treated electrode. Accordingly, the 24 hours electrode is more applicable to high current density operations. The reason could be that the electrocatalytic structure formed with the 24 hours heat treatment is better to release the hydrogen gas bubbles from the electrode surface. The efficiency of all electrodes range from 84 to 87% compared to the reversible potential of HER.

8.3.1.2   Anodes

The electrodes heat treated for 10, 20 and 30 minutes were not found to be stable as anodes during potentiodynamic measurements, see Appended paper II. Accordingly, results from these will not be analysed.

Two plots, with and without logarithmic scale, are prepared for the anodic potentiodynamic measurements, see Fig. 60 and 61.
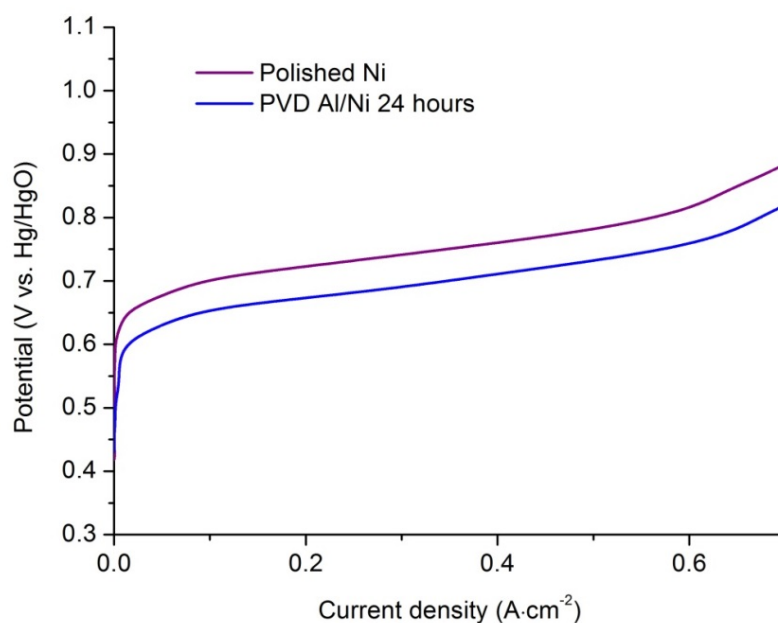
Fig. 60: Anodic potentiodynamic polarisation curves recorded on the developed electrocatalyst compared to polished nickel.
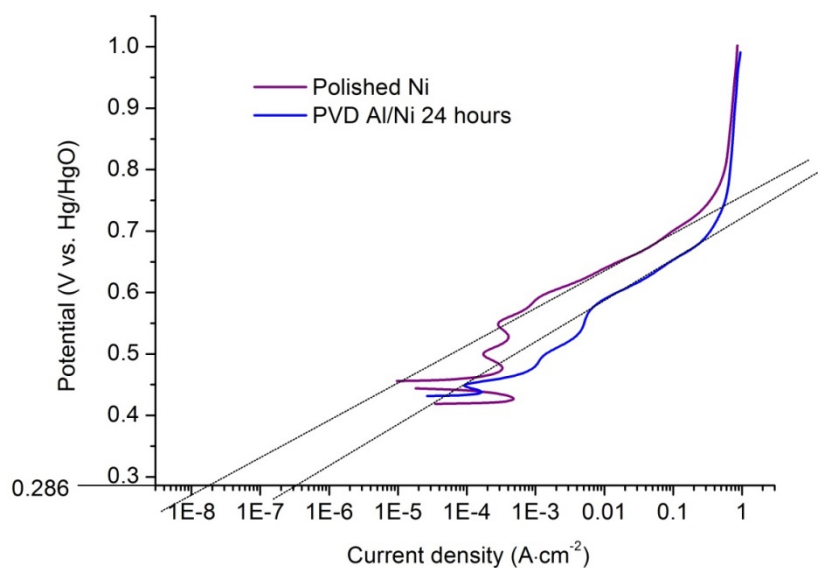
Fig. 61: Re-plot of the anodic potentiodynamic curves from Fig. 60 in order to find I_0 and Tafel slopes. The grey lines indicate Tafel slope 1 from 0.02 to 0.1 A/cm^{-2}.

For the logarithmic plot, the x-axis intersects the y-axis at the theoretical potential for OER (286 mV). The Tafel slopes are calculated from the current density ranging from 0.02-0.1 A/cm^2. Results from the anodic potentiodynamic measurements are listed in Table 15.

	Tafel slope 1 [mV/ dec]	I_0 [mA/cm^2]	η_{OER} @ 200 mA/cm^2 [mV]	η_{rev} @200 mA/cm^2*
Polished Ni	60	2e-5	437	39%
PVD Al/Ni 24h	63	3e-6	387	42%

Table 15: Tafel slopes, OER overpotential (η_{OER}) and calculated efficiency (η_{ref}) from the anodic potentiodynamic measurements recorded on the developed electrode.
 * Calculated according to the theoretical potential of OER is estimated to be 286 mV vs. Hg/HgO.

The developed electrocatalyst is shown to have only 50 mV less OER overpotential compared to polished nickel. Evidently, the developed electrocatalytic structure does not compose superior catalytic behaviour towards OER.

8.3.2   Durability measurements in an electrolysis cell

The electrolysis cell measurements were carried out by applying the PVD Al/Ni electrodes, prepared by 24 hours heat treatment, both as anode and cathode. First the electrolysis cell was operated continuously for over 1500 hours. During the 1500 hours a couple of shutdowns occurred. After each shut-down, the electrolysis measurements were started again without making any changes to the electrolysis setup. Thereafter, the electrolyte was changed out for a new fresh one. The data captured during the durability test compared to durability measurements prepared on polished nickel electrodes are shown in Fig. 62. Efficiency calculations after different time of operation are collected in Table 16.
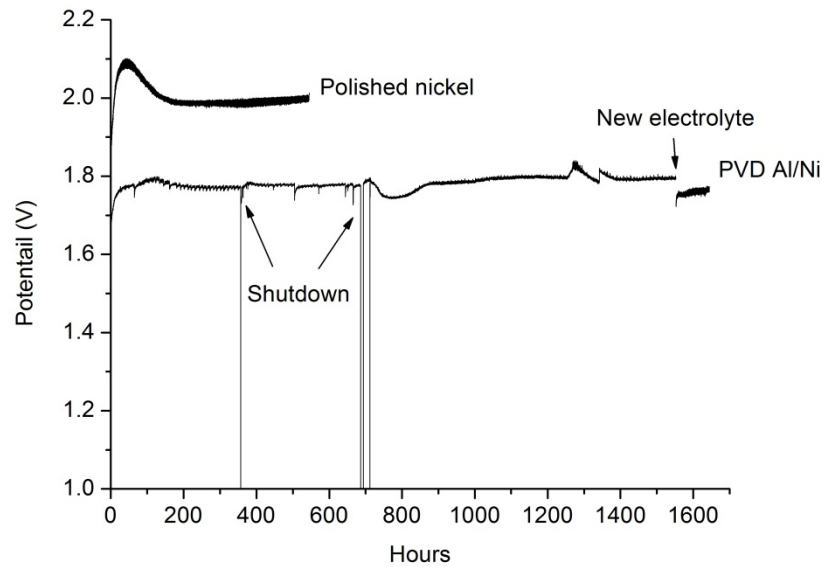
Fig. 62: Electrolysis whole cell measurements, where the developed electrode is applied both as anode and cathode, operated at 200 mA/cm^2, 120°C in 50%KOH. Electrolysis measurements operated under the same conditions, where polished nickel is applied as anode and cathode, is plotted for comparison.

	η_{Cell} @ 5 min.	η_{Cell} @ 2 h.	η_{Cell} @ 200 h.	η_{Cell} @ 500 h.	η_{Cell} @ 1500 h.	η_{Cell} @ 1550 h. new electrolyte*	η_{Cell} @ 1600 h. new electrolyte
Polished Ni	79%	78%	75%	74%	-		-
PVD Al/Ni 24h	91%	88%	84%	83%	83%	86%	84%

Table 16: Efficiency calculations for electrolysis durability test, operated at 200 mA/cm^2, 120°C and 50 wt% KOH, recorded on the developed electrodes compared to polished nickel. The efficiency values are calculated according to the HHV. *Measured immediately after change of electrolyte.

During the first minutes of operation the potential between the electrodes is measured to be about 1.6 V, resulting in efficiency values above 90%. Unfortunately, the potential increases continually until about 100 operating hours, where the cell efficiency has dropped to 83-84%. Thereafter the potential is stable during the rest of the 1500 operating hours. The most obvious reason for the efficiency drop during operation is degradation of the electrodes by gas-erosion. That implies that some of the porous structure is "*blown off*" during operation resulting in less electrocatalytic surface area available for the electrolysis reactions to take place. This assumption can also, to some extend, be verified by the black powder found on the bottom of the electrolysis cell after operation, see Fig. 63. It is noted that such sediments were not observed for any of the potentiodynamic measurements presented above.
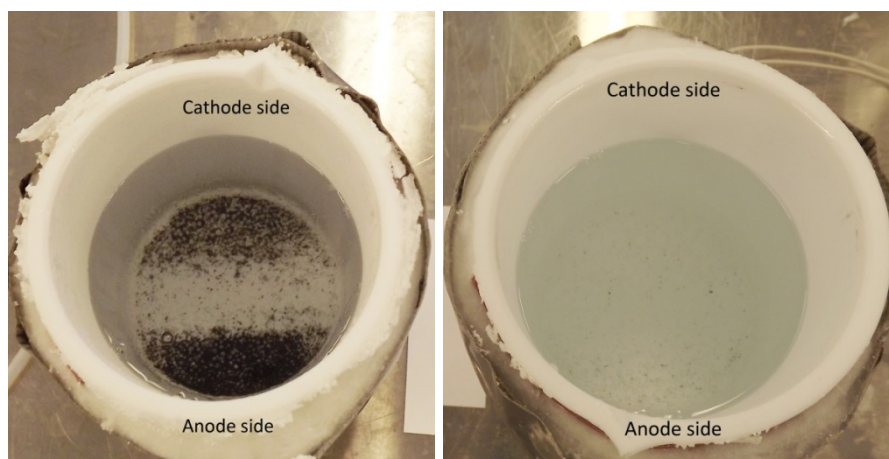
Fig. 63: Left: Black particles found in the electrolyte after over 1600 time of durability testing. Right: the electrolyte in the electrolysis cell after short duration of testing with a new electrolyte.

However, due to the fact that the same degradation trend of deactivation is observed for the polished nickel electrodes there must be an additional explanation of the degradation. Formation of nickel hydrides inside the electrode lattice has been described by various authors [115]–[118]. The formation of nickel hydrides changes the electronic configuration of the electrocatalyst from d-character to sp-character by filling the d-band. This electronic configuration is similar to copper and silver, which are known to have higher hydrogen overpotential compared to nickel [118]. Hence, the 5% efficiency decrease during the 500 hours of operation for polished nickel can most probably be related to the formation of nickel hydrides. Accordingly, some part of the efficiency loss observed for the durability testing of the PVD Al/Ni electrode is supposed to originate from the formation of nickel hydride diminishing the electrocatalytic activity of the catalyst towards the HER.

Another factor that could influence the increased potential is the evaporation of KOH with water resulting in lower ionic conductivity of the electrolyte. Indeed, during operation white KOH crystals are detected on the gas outlet pipes. The evaporation of water was compensated during operation with addition of pure water, but no additional KOH is added during the operating period. Hence, if the KOH evaporates with the water, the ionic conductivity in the electrolyte will obviously decrease leading to higher ohmic drop between the anode and cathode. In order to investigate this, the old electrolyte was changed out for a new fresh 50 wt.% KOH after approximately 1550 hours of operation. Immediately after the changing of the electrolyte the efficiency value increased from 84% to 86%. After less than 10 hours the efficiency reached its initial value of 84%. These results are understood in that way that the evaporation of KOH is not in that large quantity that the factor diminishes the ionic conductivity between the electrodes.

Regarding the ohmic drop between the two electrodes it should be mentioned that no external electrolyte flow is applied to the single cell setup, as usually done in commercial electrolysis stacks to enhance bubble separation from the electrode surfaces during operation. This means that gas bubbles cover the electrode surfaces at all times resulting in less available electrode surface area and higher ohmic drop between the electrodes. Commercial electrolysers are also often pressurised in order to minimise the volume of the gas bubbles in the electrolyte and, thus, lowering the ohmic drop caused by them. It is

therefore expected that the ohmic drop between the electrodes in the single cell electrolysis setup is somewhat larger than for industrial electrolysers.

During the durability testing of the electrodes several shutdowns occurred. The reasons for the shutdowns were of technical kind and will not be emphasised here. What is noteworthy is that no further deactivation of the PVD Al/Ni electrocatalyst was detected after the shutdowns. The resistivity to shutdowns is an important factor in the development of electrocatalysts.

Fig. 64 shows the PVD Al/Ni electrodes after the durability testing. Although evidently some of the electrocatalytic porous nickel structure has scaled off during the procedure, the electrodes still appear black. The anode clearly seems more degraded than the cathode.
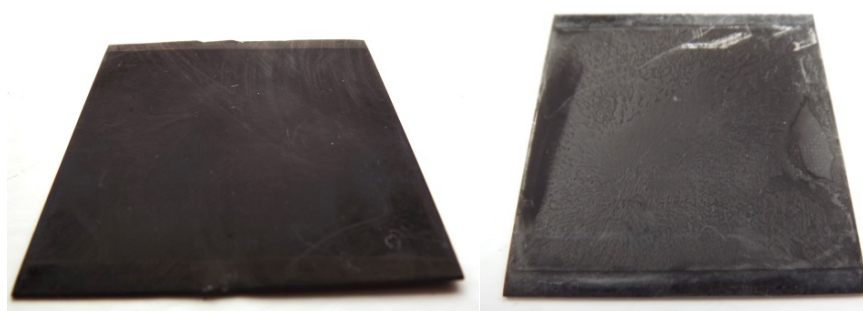
Fig. 64: The PVD Al/Ni electrodes used for single cell electrolysis durability testing after over 1600 hours of operation. Left: Cathode. Right: Anode. The electrode surfaces still appear black indicating that some remaining high surface area skeletal nickel coating.

In order to investigate the influence of the durability testing on the hydrogen electrode, cathodic potentiodynamic polarisation measurements were performed. The result from the potentiodynamic testing on the electrode applied as cathode in the single cell durability test is shown in Fig. 65 and 66. The process parameters for the potentiodynamic measurements are the same as described in the experimental chapter. The Tafel slope is calculated from two current density intervals as before, Tafel slope 1 in the range of 20-100 mA/cm^2 and Tafel slope 2 in the range of 100-1000 mA/cm^2. The results from the cathodic potentiodynamic measurements together with efficiency calculations are gathered in Table 17.
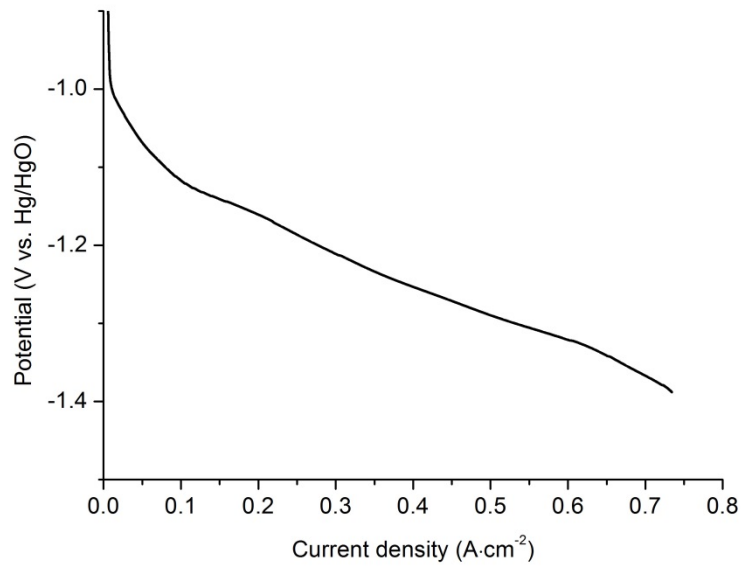
Fig. 65: Cathodic potentiodynamic polarisation curves recorded on the PVD Al/Ni electrode applied as cathode for over 1600 hours durability testing. The electrolyte contains 1 M KOH and the experiments are performed at 25°C.
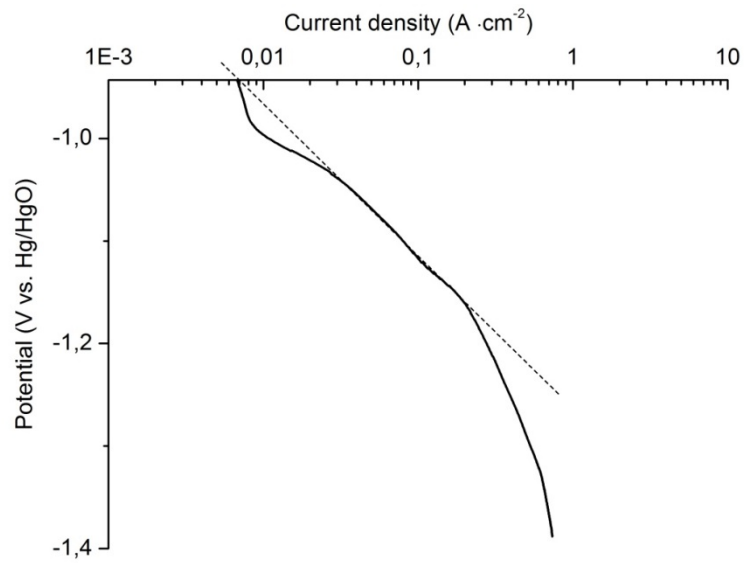
Fig. 66: Re-plot of the cathodic potentiodynamic curves in Fig. 65 in order to find I_0 and the Tafel slope. The dotted line indicate Tafel slope 1 from 0.01 to 0.1 A/cm^{-2}.

	Tafel slope 1 [mV/dec]	Tafel slope 2 [mV/dec]	I_0 [mA/ cm^2]	H_{HER} @ 200 mA/cm^2[mV]	η_{rev} @200 mA/cm^2*
PVD Al/Ni 24h after 1600 h. of operation	140	300	7	218	81%

Table 17: Results and calculated efficiency (η) from the cathodic potentiodynamic measurements recorded on electrode applied as cathode for over 1600 hours single cell electrolysis testing. *Calculated according to the theoretical potential of HER (-943 mV vs. Hg/HgO).

The post potentiodynamic measurement reveal that the PVD Al/Ni has 56 mV higher overpotential towards HER at 200 mA/cm^2 current density compared to a fresh PVD Al/Ni electrode. This results in about 4% reduction in efficiency. An increase of 29 mV/dec. and 133 mV/dec. is observed for Tafel slope 1 and Tafel slope 2, respectively. The great difference between Tafel slope 2 for the fresh and the durability tested electrodes indicate that a reduced surface area has a more significant effect at higher current densities compared to lower current densities. The increased overpotential for the HER originates form a combination of less actual surface area and nickel hydrides that have been formed in the lattice of the electrocatalyst.

8.3.3   Electrolysis stack measurements

16 large electrodes with the developed PVD Al/Ni 24 h. coatings on both sides were produced for testing in a 17 cell bipolar alkaline electrolysis stack. Together with serving as a durability test stack for the PVD Al/Ni electrodes the stack was used for the development and demonstration project called H2-College in Herning. Hence, the electrolysis stack was located on site where the hydrogen was to be produced and not in the laboratory. Continuous potential vs. current measurements were therefore not made on the stack during operation. Instead measurements where prepared occasionally during the operation period.

The alkaline electrolysis stack was at that time in the development stage and for safety reasons, the stack was operated under low temperature and pressure in the beginning of the test period. As it often is for projects in the development stage the biggest focus was on making all the coupled mechanisms to work and function together. Consequently, rather few operation parameters were captured at that time. The limited amount of data recorded during the first month of operation is shown in Fig. 67.
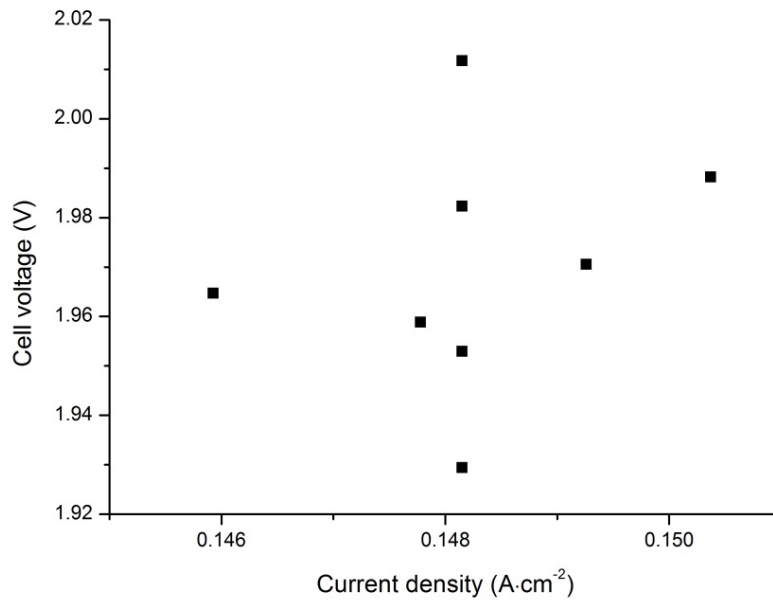
Fig. 67: Current density vs. cell voltage recorded on the 17 cell electrolysis stack during the first month of operation. The operation conditions were 40-45°C and 10 bar.

The electrolysis stack was operated under altering conditions for over 9000 hours. Thereafter plentiful of efficiency measurements were performed on the stack. Both the dependence of the voltage towards the current and the temperature were measured. Fig. 68 and 69 show the current vs. voltage and temp. vs. voltage data captured after 9000 hours of operation. For making the comparison easier between the previous measurements on the PVD Al/Ni electrodes and the stack measurements the measured stack voltage is divided by 17 in order to achieve the average cell voltage.
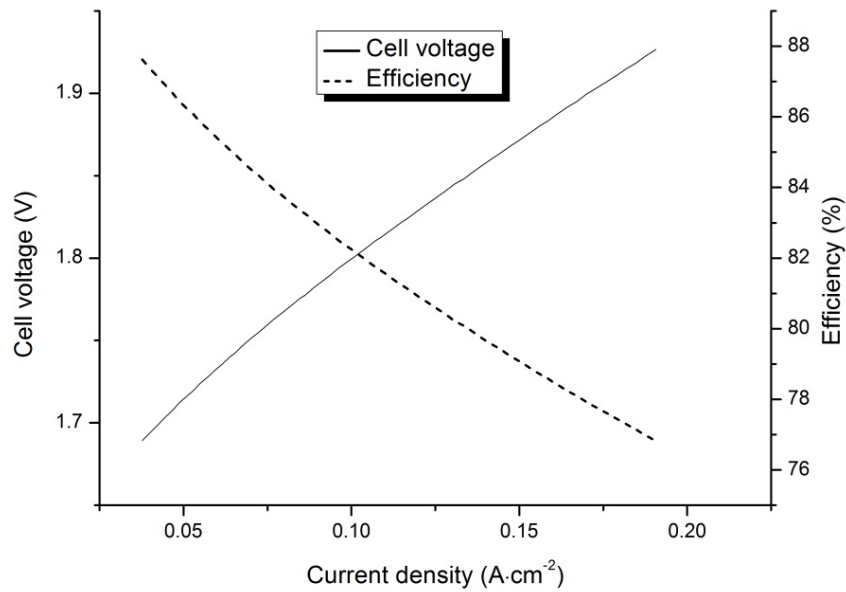
Fig. 68: Current vs. voltage and efficiency data captured on the 17-cell bipolar electrolysis stack after approximately 9000 operating hours. The stack was operated at 60°C and 22 bar. The efficiency calculations are based on the HHV.
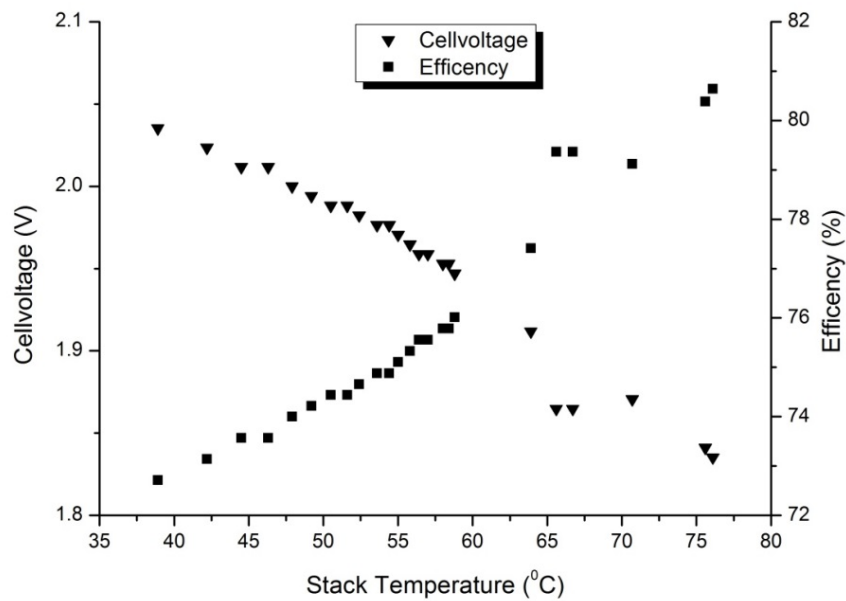
Fig. 69: Temperature vs. voltage plot captured on the 17-cell bipolar electrolysis stack at 22 bar and 200 mA/cm^2 current density, after approximately 9000 operating hours, showing the temperature dependence of the cell voltage. The efficiency calculations are based on the HHV.

A cell efficiency of about 81% is observed at 200 mA/cm^2 at 80°C. This is 3% points less than the efficiency value observed after over 1600 hours of single cell durability test at 120°C and 50 wt.% KOH. The efficiency values from the stack measurements are, however, most likely lower than the actual cell efficiencies due to losses in the stack itself.

The test performed after 9000 hours of operation were focused on measuring the highest operating values. Therefore, the data captured in the start and after the full operating time are not fully comparable. In Table 18 three values from the stack measurements have been chosen for durability assessment, one from the beginning of the test period and two from after 9.000 hours. No serious deactivation during the operation period can be detected from these values.

	Temp. [°C]	Pressure [Bar]	Stack Current [A]	Current density [mA/cm^2]	Stack Voltage [V]	Cell Voltage [V]	Stack efficiency [%]
First month of the operation period	40	10	40	150	33	1.98	75
After 9.000 h. operation	40	22	54	200	35	2.05	73
After 9.000 h. operation	60	22	40	150	32	1.88	79

Table 18: Selected data from Fig. 67, Fig. 68 and Fig. 69 for durability assessment. The efficiency calculations are based on the HHV.

8.4 Conclusions for efficiency and durability testing

The developed electrocatalyst is found to have up to 385 mV less hydrogen overpotential and 50 mV less oxygen overpotential, compared to polished nickel measured at 200 mA/cm^2 and 25°C. Longer heat treatment, 24 hours compared to 30 min., results in more active hydrogen catalyst at higher current densities, resulting in a Tafel slope of 167 mV/dec. for the 24 hours heat treated electrocatalyst compare to 228 mV/dec. for the 30 min. heat treated electrocatalyst

According to the half- cell measurements, the efficiency of an ideal electrolysis cell, where the resistance between the electrodes can be neglected, operated with the PVD Al/Ni 24 h. electrocatalysts, both as anode and cathode, is found to be 83% [HHV], measured at 200 mA/cm^2, 25°C in 1M KOH.

Single cell electrolysis measurements, carried out in 50 wt.% KOH, at 120°C and 200 mA/cm^2, present above 88% cell efficiency during the first two hours of operation. The cell efficiency decreases to 84% after about 100 operating hours and is thereafter constant throughout the remaining 1500 hours of operation. The reason for the drop in efficiency during time is proposed to degradation of the electrodes together with formation of nickel hydrides in the nickel lattice. Operating at such high temperature and strong alkaline electrolyte some efficiency loss must be expected.

In a pressurised electrolysis stack with external convection system, the boiling point of the electrolyte increases, due to the pressure, and less KOH can be applied. Moreover, the volume of the gas bubbles formed will decrease under the pressure and the ohmic loss between the electrodes will become less due to the convection. Consequently, higher efficiency and less degradation might be expected for the developed structure operated in an optimised electrolysis stack.

Durability testing of the developed PVD Al/Ni 24 h. electrocatalyst carried out in a 17 cell bipolar electrolysis stack containing 30 wt.% KOH, operated under altered conditions, at a maximum temperature of 80°C and a pressure of 22 bar, for approximately 9000 hours, indicates no deactivation of the electrodes during the operation period. A stack efficiency of 81% is measured at 200 mA/cm^2 at 80°C. The electrolysis test stack is in the development stage and some losses could be expected in the stack itself.

9   Conclusions

In a world of ever increasing energy demand [4], shortage of fossil fuels [151] and stronger legalisations towards reduction of CO_2 emission [152], new alternative fuels for domestic heat and power as well as for transportation are required. Renewable energy is commonly recognised to be the answer for a more secure, reliable and sustainable future. However, in order to keep production and consumption in balance, more load management is needed. Production of hydrogen by water electrolysis can serve as a balancing load and at the same time act as energy storage.

The water electrolysis technique is not a new invention and, in fact, the technique was developed over two centuries ago [44]. Currently there are two types of commercially available water electrolysis systems. These are: alkaline water electrolysis (AWE) and polymer electrolyte membrane (PEM) electrolysis. The available production rate for AWE is up to 25 times larger than for PEM. Still, PEM electrolysis systems are at least 10 times more expensive than AWE and can offer only half of the life time of AWE. Consequently, alkaline electrolysis is the current standard for large-scale hydrogen production among water decomposition techniques.

Commercial alkaline electrolysers operates in a liquid electrolyte containing 25-30% KOH at a temperature ranging from 80 - 90°C and current density in the range of 100-400 mA/dm^2 [10], [16],[49]. Efficiency values up to 82% have been reported [46]. One of the largest cell efficiency losses for alkaline electrolysis originates from the activation energies for hydrogen and oxygen, generated at the electrodes. The activity of an electrocatalyst depends on the electron configuration of the catalyst material, the structure and geometry and the actual surface area. Among non-noble metals, nickel is one of the most stable in strong alkaline solutions. Nickel is also a relatively good catalyst for hydrogen and oxygen formation. Nickel or nickel plated substrates are therefore typically the core material used in electrodes for AWE systems [6],[10][45].

A great deal of work has been devoted to the development of electrodes for AWE during the past 90 years. The state-of-the-art electrodes have, however, not changed much during the years. Among the newly developed electrocatalysts, durability measurements are usually lacking and few of the published electrocatalysts have actually been tested at current densities applicable for industrial AWE. Hence, finding low cost electrode materials that are both efficient and having long term stability is one of the remaining challenges within the field of AWE.

In the present PhD study the core aim has been to develop high surface area nickel electrodes that are both efficient and durable in large scale alkaline water electrolysis systems. For industrial applications bipolar electrolysers are more commonly applied than monopolar. In bipolar configuration each electrode serves as an anode, on the one side and a cathode, on the other. Hence, having the same electrocatalytic surface on both sides of the electrodes

increases the simplicity and decrease the production cost of the electrodes. Although the main focus was kept on the developing electrodes with high electrocatalytic activity towards the HER, the efficiency of the developed electrodes towards the OER was also investigated. For reliable electrochemical and durability investigations new measurement setup have been developed and constructed during this PhD study.

In the present work, new hydrogen electrodes were developed. The electrodes were produced by physical vapour depositing (PVD) of about 20 μm aluminium coating onto a nickel substrate. The PVD Al-Ni couples were heat treated for 24 hours in order to facilitate large crystalline Al_3Ni_2 alloy formation. Thereafter the electrode coating, consisting primarily of the Al_3Ni_2 phase, was selective aluminium alkaline leached. The developed electrocatalytic surface was characterised with a large actual surface area, uniform structure and with good interlayer adhesion, which is critical for industrial application. IR-compensated polarisation curves prepared in a half-cell setup with 1 M KOH electrolyte at 200 mA/cm^2 at room temperature reveals that 435 mV less potential is needed to decompose water into hydrogen and oxygen with the developed porous PVD Al/Ni electrodes as compared to solid nickel electrodes. The hydrogen electrodes were measured to have 85% efficiency under the same conditions.

By increasing the operating temperature in AWE systems the kinetics of the hydrogen production can be increased. Non-zero gap, single cell electrolysis measurements were carried out where the developed PVD Al/Ni electrodes were applied both as cathode and anode. The operation conditions were; 50 wt.% KOH, 120°C and 200 mA/cm^2. The cell efficiency was measured to be 88% (HHV) during the first two hours of operation. The cell efficiency decreased to 84% after about 100 operating hours and was thereafter constant throughout the remaining 1500 hours of operation. The reason for the efficiency drop over time is proposed to be degradation of the electrodes together with formation of nickel hydrides in the nickel lattice. The material degradation was found to be considerably more severe at the anode compared to the cathode. However, operating at such high temperature and strong alkaline electrolyte some efficiency loss must be expected.

16 full size electrodes with the developed PVD Al/Ni structure were produced for bipolar, non-zero gap, industrial AWE stack. The electrodes were prepared with the developed high surface area Ni structure on both sides. The electrolysis stack was operated with surplus power from wind turbines and the hydrogen produced used to power 66 houses at the campus of Århus University in Herning. The operation conditions of the electrolyser were; 30 wt.% KOH, maximum temperature of 80°C and a pressure of 22 bar. The electrodes were operated in the electrolysis stack for approximately 9000 hours. Comparing operating data captured in first month of operation to data captured after over 9000 hours, indicates no deactivation of the electrodes during the operation period. The stack efficiency after over 9000 hours of operation at 200 mA/cm^2 at 80 °C was measured to be 81% (HHV). It is noted that the electrolysis test stack was in the development stage and some losses were expected in the stack itself.

Microstructure investigations on the PVD Al-Ni diffusion couples at 610°C, for various times of heat treatments, indicate that the initial diffusion mechanism is dominated by grain

boundary diffusion of Ni-rich phases into the PVD Al structure. It is proposed that the first intermetallic phase to form is $AlNi_3$, appearing as small particles in the grain boundaries of the columnar aluminium structure. Due to the high mobility of aluminium at the annealed temperature, finding Ni and Ni-rich containing species to be the most mobile during the heat treatment is highly unexpected and in contrast with other findings in the literature. The diffusion mechanism can be the key to the good properties of the developed PVD Al/Ni electrode.

Both the interdiffusion and the leaching procedures facilitate internal stresses in the electrocatalytic coatings prepared in the present manner. Leaching of PVD Al-Ni structure after a short time of diffusion, 10-30 minutes, results in formation of cracks perpendicular to the Ni substrate. The cracks diminish the mechanical strength of the coating. PVD Al/Ni electrodes heat treated for short times are found not to be stable under OER. Longer heat treatments, up to 24 hours, result in grain growth of the leachable Al_3Ni_2 phase. Selectively aluminium leaching of electrodes heat treated for 24 hours results in dense, crack free and more mechanical stable structure. It is noteworthy that the electrodes heat treated for shorter times are more prone to alkaline leaching. This is verified by the EDS analyses where only 4-5 wt.% aluminium residue is found in the leached structure of the specimens heat treated for 10,20 and 30 minutes, compared to up to 15 wt.% aluminium found in the leached electrode heat treaded for 24 hours. Also from the XRD analyses, some remaining Al_3Ni_2 peaks are observed from the leached structure heat treated for 24 hour where only pure nickel peaks are observed from the leached 10-30 minutes heat treated structures.

Because of the partial penetration of the current into the deeper pores of the structure one could expect that only a limited fraction of the actual surface area, of the highly dispersed Ni structure, contributes to the electrochemical reaction during electrolysis. Potentiodynamic measurements prepared on PVD Al/Ni electrode surfaces heat treated for 10, 20 and 30 minutes, resulting in different thicknesses of porous Ni surface, indicate that the electrocatalytic activity increases in proportion to the porous layer thickens up to the whole 20 μm tested. However, in order to optimise the electrochemical and mechanical properties of the developed electrocatalytic surface, more thorough investigations on the effect of leaching and heat treatment parameters are essential.

After the successful experience of the first generation of electrodes for AWE, four other process techniques, and combinations of these, for producing similar electrodes were assessed. The process techniques were selected with the aim of reducing the production cost associated with the electrode manufacture. The screened processes were; hot dip aluminising of nickel followed by thermo-chemical diffusion, direct thermo-chemical diffusion of aluminium and nickel sheets, aluminium ionic liquid electroplating on a nickel plate followed by thermo-chemical diffusion and physical vapour deposition of aluminium onto electroplated sulfamate nickel substrate followed by thermo-chemical diffusion. Due the high affinity of aluminium towards hydrogen and oxygen, producing oxide free Al_3Ni_2 alloy coatings in an inexpensive and simple manner was found to be challenging. Only the direct diffusion between aluminium and nickel sheets in argon atmosphere and the PVD Al onto electroplated sulfamate nickel were found to give promising coatings. These surfaces have, yet, not been tested electrochemically.

Bibliography

[1] WMO. *Greenhouse Gas Bulletin. The State of Greenhouse Gases in the Atmosphere. Based on Global Observations through 2012,* [Online] November 2013, http://www.wmo.int/pages/prog/arep/gaw/ghg/documents/GHG_Bulletin_No.9_en.pdf (Accessed: 12 November 2013).

[2] United Nations. Framework Convention on Climate Change. *Report of the Conference of the Parties on its sixteenth session, held in Cancun from 29 November to 10 December 2010*, [Online] 15 March 2011, http://unfccc.int/resource/docs/2010/cop16/eng/07a01.pdf#page=2 (Accessed: 12 November 2013).

[3] European Commission. *Energy 2020. A strategy for competitive, sustainable and secure energy,* [Online] November 2012, http://eur-lex.europa.eu/LexUriServ/LexUriServ.do?uri=COM:2010:0639:FIN:EN:PDF (Accessed: 12 November 2013).

[4] OECD, *World Energy Outlook 2013*. Paris: Organisation for Economic Co-operation and Development, 2013

[5] Fuel Cells Today, *Water Electrolysis & Renewable Energy*, [Online] May 2013, http://www.fuelcelltoday.com/media/1871508/water_electrolysis___renewable_energy_systems.pdf (Accessed: 12 November 2013).

[6] T. Smolinka, 'Fuels – Hydrogen Production | Water Electrolysis', in *Encyclopedia of Electrochemical Power Sources*, Jürgen Garche, Ed. Amsterdam: Elsevier, 2009, pp. 394–413.

[7] D. A. J. Rand and R. M. Dell, *Hydrogen Energy : Challenges and Prospects RSC Energy Series v. 1*. Royal Society Of Chemistry.

[8] S. S. Zumdahl, in *Chemical principles*, 4th ed., 2002, pp. 470–471.

[9] H. Wendt, in *Electrochemical hydrogen technologies: electrochemical production and combustion of hydrogen*, Elsevier, 1990, pp. 139–142.

[10] K. Zeng and D. Zhang, 'Recent progress in alkaline water electrolysis for hydrogen production and applications', *Progress in Energy and Combustion Science*, vol. 36, no. 3, pp. 307–326, Jun. 2010.

[11] S. Licht, 'Thermochemical and Thermal/Photo Hybrid Solar Water Splitting', in *Solar Hydrogen Generation*, K. Rajeshwar, R. McConnell, and S. Licht, Eds. Springer New York, 2008, pp. 87–121.

[12] I. Abe, 'Hydrogen Production from Water', in *Energy Carriers and Conversion Systems*, EOLSS Publishers Company Limited, 2009.

[13] E. Bardal, in *Corrosion and Protection*, Springer, 2004, pp. 35–44.

[14] M. Wang, Z. Wang, X. Gong, and Z. Guo, 'The intensification technologies to water electrolysis for hydrogen production – A review', *Renewable and Sustainable Energy Reviews*, vol. 29, pp. 573–588, Jan. 2014.

[15] H. Wendt and G. Imarisio, 'Nine years of research and development on advanced water electrolysis. A review of the research programme of the Commission of the European Communities', *J Appl Electrochem*, vol. 18, no. 1, pp. 1–14, Jan. 1988.

[16] K. Harrison and J. I. Levene, 'Electrolysis of Water', in *Solar Hydrogen Generation*, K. Rajeshwar, R. McConnell, and S. Licht, Eds. Springer New York, 2008, pp. 41–63.

[17] D. Pletcher, in *Instrumental Methods in Electrochemistry*, Ellis Horwood, 2001, pp. 24–25.

[18] S. Trasatti, 'Electrochemical Theory | Hydrogen Evolution', in *Encyclopedia of Electrochemical Power Sources*, J. Garche, Ed. Amsterdam: Elsevier, 2009, pp. 41–48.

[19] D. Pletcher, *Instrumental Methods in Electrochemistry*. Ellis Horwood, 2001.

[20] S. G. Neophytides, S. Zafeiratos, G. D. Papakonstantinou, J. M. Jaksic, F. E. Paloukis, and M. M. Jaksic, 'Extended Brewer hypo–hyper--interionic bonding theory — I. Theoretical considerations and examples for its experimental confirmation', *International Journal of Hydrogen Energy*, vol. 30, no. 2, pp. 131–147, Feb. 2005.

[21] M. M. Jakšić, 'Electrocatalysis of hydrogen evolution in the light of the brewer—engel theory for bonding in metals and intermetallic phases', *Electrochimica Acta*, vol. 29, no. 11, pp. 1539–1550, Nov. 1984.

[22] M. M. Jaksic, 'Hypo–hyper-d-electronic interactive nature of interionic synergism in catalysis and

for hydrogen reactions', *International Journal of Hydrogen Energy*, vol. 26, no. 6, pp. 559–578, Jun. 2001.

[23] J. M. Jaksic, N. V. Krstajic, B. N. Grgur, and M. M. Jaksic, 'Hydridic and electrocatalytic properties of hypo-hyper-d-electronic combinations of transition metal intermetallic phases', *International Journal of Hydrogen Energy*, vol. 23, no. 8, pp. 667–681, Aug. 1998.

[24] M. M. Jaksic, 'Volcano plots along intermetallic hypo-hyper-d-electronic phase diagrams and electrocatalysis for hydrogen electrode reactions', *Journal of New Materials for Electrochemical Systems*, vol. 3, no. 2, pp. 169–182, 2000.

[25] J. M. Jaksic, M. V. Vojnovic, and N. V. Krstajic, 'Kinetic analysis of hydrogen evolution at Ni-Mo alloy electrodes', *Electrochimica Acta*, vol. 45, no. 25–26, pp. 4151–4158, Aug. 2000.

[26] G. S. Tasić, U. Lačnjevac, M. M. Tasić, M. M. Kaninski, V. M. Nikolić, D. L. Žugić, and V. D. Jović, 'Influence of electrodeposition parameters of Ni–W on Ni cathode for alkaline water electrolyser', *International Journal of Hydrogen Energy*, vol. 38, no. 11, pp. 4291–4297, Apr. 2013.

[27] J. R. McKone, B. F. Sadtler, C. A. Werlang, N. S. Lewis, and H. B. Gray, 'Ni–Mo Nanopowders for Efficient Electrochemical Hydrogen Evolution', *ACS Catal.*, vol. 3, no. 2, pp. 166–169, Feb. 2013.

[28] L. Birry and A. Lasia, 'Studies of the hydrogen evolution reaction on Raney nickel-molybdenum electrodes', *J. Appl. Electrochem.*, vol. 34, no. 7, pp. 735–749, Jul. 2004.

[29] J. Greeley, T. F. Jaramillo, J. Bonde, I. Chorkendorff, and J. K. Norskov, 'Computational high-throughput screening of electrocatalytic materials for hydrogen evolution', *Nat Mater*, vol. 5, no. 11, pp. 909–913, Nov. 2006.

[30] S. M. A. Sillitto, N. J. E. Adkins, R. M. Ormerod, E. Paul, and D. R. Hodgson, *Characterisation of advanced Raney nickel electrocatalytic coatings produced by the direct spraying method*. Rugby: Inst Chemical Engineers, 1999.

[31] S. M. A. Sillitto, N. J. E. Adkins, D. R. Hodgson, E. Paul, and R. M. Ormerod, 'Electrochemical testing and structural characterisation of nickel based catalytic coatings produced by direct spraying', in *Advanced Catalytic Materials-1998*, vol. 549, P. W. Lednor, D. A. Nagaki, and L. T. Thompson, Eds. Warrendale: Materials Research Society, 1999, pp. 23–29.

[32] A. Kellenberger, N. Vaszilcsin, W. Brandl, and N. Duteanu, 'Kinetics of hydrogen evolution reaction on skeleton nickel and nickel-titanium electrodes obtained by thermal arc spraying technique', *Int. J. Hydrog. Energy*, vol. 32, no. 15, pp. 3258–3265, Oct. 2007.

[33] A. Kellenberger, N. Vaszilcsin, and W. Brandl, 'Roughness factor evaluation of thermal arc sprayed skeleton nickel electrodes', *J. Solid State Electrochem.*, vol. 11, no. 1, pp. 84–89, Nov. 2007.

[34] A. Kellenberger and N. Vaszilcsin, 'The determination of the roughness factor of skeleton nickel electrodes   by cyclic voltammetry', *Rev. Chim.*, vol. 56, no. 7, pp. 712–715, Jul. 2005.

[35] G. Schiller, R. Henne, and V. Borck, 'Vacuum plasma spraying of high-performance electrodes for alkaline water electrolysis', *JTST*, vol. 4, no. 2, pp. 185–194, 1995.

[36] J. Fournier, D. Miousse, and J. G. Legoux, 'Wire-arc sprayed nickel based coating for hydrogen evolution reaction in   alkaline solutions', *Int. J. Hydrog. Energy*, vol. 24, no. 6, pp. 519–528, Jun. 1999.

[37] T. Boruciński, S. Rausch, and H. Wendt, 'Raney nickel activated H2-cathodes Part II: Correlation of morphology and effective catalytic activity of Raney-nickel coated cathodes', *J Appl Electrochem*, vol. 22, no. 11, pp. 1031–1038, Nov. 1992.

[38] V. S. Bagotsky, in *Fuel Cells: Problems and Solutions*, John Wiley & Sons, 2012, pp. 209–210.

[39] D. Pletcher, in *Instrumental Methods in Electrochemistry*, Ellis Horwood, 2001, pp. 168–171.

[40] P. Møller and L. P. Nielsen, in *Advanced Surface Technology*, 4th ed., Møller & Nielsen, pp. 54–55.

[41] J. C. M. Keith B. Oldham, *Electrochemical Science and Technology: Fundamentals and Applications*. John Wiley & Sons Inc.

[42] P. Møller and L. P. Nielsen, *Advanced Surface Technology*, 4th ed. Møller & Nielsen.

[43] A. J. Bard, *Electrochemical methods : fundamentals and applications*. 2001.

[44] P. Kurzweil, 'History | Electrochemistry', in *Encyclopedia of Electrochemical Power Sources*, Jürgen Garche, Ed. Amsterdam: Elsevier, 2009, pp. 533–554.

[45] G. A. Edited By Luis M. Gandia, *Renewable Hydrogen Technologies : Production, Purification, Storage, Applications and Safety*. Elsevier.

[46] A. Ursua, L. M. Gandia, and P. Sanchis, 'Hydrogen Production From Water Electrolysis: Current Status and Future Trends', *Proceedings of the IEEE*, vol. 100, no. 2, pp. 410 –426, Feb. 2012.

[47] R. L. LeRoy, 'Industrial water electrolysis: Present and future', *International Journal of Hydrogen Energy*, vol. 8, no. 6, pp. 401–417, 1983.

[48] M. Carmo, D. L. Fritz, J. Mergel, and D. Stolten, 'A comprehensive review on PEM water electrolysis', *International Journal of Hydrogen Energy*, vol. 38, no. 12, pp. 4901–4934, Apr. 2013.

[49] C. K. Dyer, P. T. Moseley, Z. Ogumi, D. A. J. Rand, and B. Scrosati, *Encyclopedia of Electrochemical Power Sources*. Newnes, 2013.

[50] K. Scott, 'Ion-exchange and charge driven processes', in *Industrial Membrane Separation Technology*, P. K. Scott and P. R. Hughes, Eds. Springer Netherlands, 1996, pp. 181–257.

[51] P. Vermeiren, W. Adriansens, J. P. Moreels, and R. Leysen, 'Evaluation of the Zirfon® separator for use in alkaline water electrolysis and Ni-H2 batteries', *International Journal of Hydrogen Energy*, vol. 23, no. 5, pp. 321–324, May 1998.

[52] H. Wendt and H. Hofmann, 'Ceramic diaphragms for advanced alkaline water electrolysis', *J Appl Electrochem*, vol. 19, no. 4, pp. 605–610, Jul. 1989.

[53] R. B. Rebak, 'Nickel Alloys for Corrosive Environments', *Advanced materials and processes*, vol. 157, no. PART 2, pp. 37–42, 2000.

[54] 'Corrosion resistance of nickel and nickel-containing alloys in caustic soda and other alkalies.', *INCO (Int Nickel Co, Inc) Corros Man*, 1975.

[55] O. Pfleiderer, 'Electrode', 181857911-Aug-1931.

[56] K. A. Andreassen, H. Harang, J. B. Holte, and K. Widding, 'Method for preparing active cathodes for electrochemical processes', US4171247 A16-Oct-1979.

[57] H. Vandenborre, P. Vermeiren, and R. Leysen, 'Hydrogen evolution at nickel sulphide cathodes in alkaline medium', *Electrochimica Acta*, vol. 29, no. 3, pp. 297–301, Mar. 1984.

[58] G. Hoogers, in *Fuel Cell Technology Handbook*, United States of America: CRC Press, 2002, pp. 20–25.

[59] F. . Crnkovic, S. A. . Machado, and L. . Avaca, 'Electrochemical and morphological studies of electrodeposited Ni–Fe–Mo–Zn alloys tailored for water electrolysis', *International Journal of Hydrogen Energy*, vol. 29, no. 3, pp. 249–254, Mar. 2004.

[60] G. Sheela, 'Zinc-nickel alloy electrodeposits for water electrolysis', *International Journal of Hydrogen Energy*, vol. 27, no. 6, pp. 627–633, 2002.

[61] W. K. Hu, 'Electrocatalytic properties of new electrocatalysts for hydrogen evolution in alkaline water electrolysis', *International Journal of Hydrogen Energy*, vol. 25, no. 2, pp. 111–118, 2000.

[62] P. Los, 'Hydrogen evolution reaction on Ni-Al electrodes', *Journal of Applied Electrochemistry*, vol. 23, no. 2, pp. 135–140, 1993.

[63] I. A. Raj, 'Nickel-based, binary-composite electrocatalysts for the cathodes in the energy-efficient industrial production of hydrogen from alkaline-water electrolytic cells', *J Mater Sci*, vol. 28, no. 16, pp. 4375–4382, Aug. 1993.

[64] Q. Han, S. Cui, N. Pu, J. Chen, K. Liu, and X. Wei, 'A study on pulse plating amorphous Ni–Mo alloy coating used as HER cathode in alkaline medium', *International Journal of Hydrogen Energy*, vol. 35, no. 11, pp. 5194–5201, Jun. 2010.

[65] N. Krstajic, V. Jovic, L. Gajickrstajic, B. Jovic, A. Antozzi, and G. Martelli, 'Electrodeposition of Ni–Mo alloy coatings and their characterization as cathodes for hydrogen evolution in sodium hydroxide solution', *International Journal of Hydrogen Energy*, vol. 33, no. 14, pp. 3676–3687, Jul. 2008.

[66] M. P. Marceta Kaninski, D. P. Saponjic, V. M. Nikolic, D. L. Zugic, and G. S. Tasic, 'Energy consumption and stability of the Ni–Mo electrodes for the alkaline hydrogen production at industrial conditions', *International Journal of Hydrogen Energy*, vol. 36, no. 15, pp. 8864–8868, Jul. 2011.

[67] W. Hu, X. Cao, F. Wang, and Y. Zhang, 'A novel cathode for alkaline water electrolysis', *International Journal of Hydrogen Energy*, vol. 22, no. 6, pp. 621–623, Jun. 1997.

[68] R. N. Singh, L. Bahadur, J. P. Pandey, S. P. Singh, P. Chartier, and G. Poillerat, 'Preparation and characterization of thin films of LaNiO3 for anode application in alkaline water electrolysis', *J Appl Electrochem*, vol. 24, no. 2, Feb. 1994.

[69] S. P. Singh, R. N. Singh, G. Poillearat, and P. Chartier, 'Physicochemical and electrochemical characterization of active films of LaNiO3 for use as anode in alkaline water electrolysis', *International Journal of Hydrogen Energy*, vol. 20, no. 3, pp. 203–210, Mar. 1995.

[70] S. K. Tiwari, J. F. Koenig, G. Poillerat, P. Chartier, and R. N. Singh, 'Electrocatalysis of oxygen evolution/reductionon LaNiO3 prepared by a novel malic acid-aided method', *Journal of Applied Electrochemistry*, vol. 28, no. 1, pp. 114–119, Jan. 1998.

[71] J. O. Bockris and T. Otagawa, 'The Electrocatalysis of Oxygen Evolution on Perovskites', *J. Electrochem. Soc.*, vol. 131, no. 2, pp. 290–302, Feb. 1984.

[72] H. J. Miao and D. L. Piron, 'Electrodeposition of Ni-transition alloys for the oxygen evolution reaction', *J Appl Electrochem*, vol. 21, no. 1, pp. 55–59, Jan. 1991.

[73] J. Balej, 'Electrocatalysts for oxygen evolution in advanced water electrolysis', *International Journal of Hydrogen Energy*, vol. 10, no. 2, pp. 89–99, 1985.

[74] H. Wendt, H. Hofmann, and V. Plzak, 'Materials research and development of electrocatalysts for alkaline water electrolysis', *Materials Chemistry and Physics*, vol. 22, no. 1–2, pp. 27–49, 1989.

[75] S. K. Tiwari, P. Chartier, and R. N. Singh, 'Preparation of Perovskite-Type Oxides of Cobalt by the Malic Acid Aided Process and Their Electrocatalytic Surface Properties in Relation to Oxygen Evolution', *J. Electrochem. Soc.*, vol. 142, no. 1, pp. 148–153, Jan. 1995.

[76]   Q. Han, 'Hydrogen evolution reaction on amorphous Ni-S-Co alloy in alkaline medium', *International Journal of Hydrogen Energy*, vol. 28, no. 12, pp. 1345–1352, 2003.

[77]   W. Hu, 'Electrocatalytic properties of Ti~2Ni Ni Mo composite electrodes for hydrogen evolution reaction', *International Journal of Hydrogen Energy*, vol. 23, no. 4, pp. 253–258, 1998.

[78]   R. Solmaz and G. Kardaş, 'Fabrication and characterization of NiCoZn–M (M: Ag, Pd and Pt) electrocatalysts as cathode materials for electrochemical hydrogen production', *International Journal of Hydrogen Energy*, vol. 36, no. 19, pp. 12079–12087, Sep. 2011.

[79]   A. O. Yüce, A. Döner, and G. Kardaş, 'NiMn composite electrodes as cathode material for hydrogen evolution reaction in alkaline solution', *International Journal of Hydrogen Energy*, vol. 38, no. 11, pp. 4466–4473, Apr. 2013.

[80]   T. Otagawa, 'Lanthanum Nickelate as Electrocatalyst - Oxygen Evolution', *Journal of the Electrochemical Society*, vol. 129, no. 10, pp. 2391–2392, 1982.

[81]   M. Hamdani, M. I. S. Pereira, J. Douch, A. Ait Addi, Y. Berghoute, and M. H. Mendonça, 'Physicochemical and electrocatalytic properties of Li-Co3O4 anodes prepared by chemical spray pyrolysis for application in alkaline water electrolysis', *Electrochimica Acta*, vol. 49, no. 9–10, pp. 1555–1563, Apr. 2004.

[82]   R. N. Singh, D. Mishra, Anindita, A. S. K. Sinha, and A. Singh, 'Novel electrocatalysts for generating oxygen from alkaline water electrolysis', *Electrochemistry Communications*, vol. 9, no. 6, pp. 1369–1373, Jun. 2007.

[83]   M. Eldeab, M. Awad, A. Mohammad, and T. Ohsaka, 'Enhanced water electrolysis: Electrocatalytic generation of oxygen gas at manganese oxide nanorods modified electrodes', *Electrochemistry Communications*, vol. 9, no. 8, pp. 2082–2087, Aug. 2007.

[84]   H.-C. Chien, W.-Y. Cheng, Y.-H. Wang, T.-Y. Wei, and S.-Y. Lu, 'Ultralow overpotentials for oxygen evolution reactions achieved by nickel cobaltite aerogels', *Journal of Materials Chemistry*, vol. 21, no. 45, p. 18180, 2011.

[85]   X. Li, F. C. Walsh, and D. Pletcher, 'Nickel based electrocatalysts for oxygen evolution in high current density, alkaline water electrolysers', *Physical Chemistry Chemical Physics*, vol. 13, no. 3, p. 1162, 2011.

[86]   H. Vandenborre, R. Leysen, H. Nackaerts, and P. Van Asbroeck, 'A survey of five year intensive R&D work in Belgium on advanced alkaline water electrolysis', *International Journal of Hydrogen Energy*, vol. 9, no. 4, pp. 277–284, 1984.

[87]   G. Schiller, R. Henne, P. Mohr, and V. Peinecke, 'High performance electrodes for an advanced intermittently operated 10-kW alkaline water electrolyzer', *Int. J. Hydrog. Energy*, vol. 23, no. 9, pp. 761–765, Sep. 1998.

[88]   D. M. See and R. E. White, 'Temperature and Concentration Dependence of the Specific Conductivity of Concentrated Solutions of Potassium Hydroxide', *J. Chem. Eng. Data*, vol. 42, no. 6, pp. 1266–1268, Nov. 1997.

[89]   R. J. Gilliam, J. W. Graydon, D. W. Kirk, and S. J. Thorpe, 'A review of specific conductivities of potassium hydroxide solutions for various concentrations and temperatures', *International Journal of Hydrogen Energy*, vol. 32, no. 3, pp. 359–364, Mar. 2007.

[90]   F. Allebrod, C. Chatzichristodoulou, P. L. Mollerup, and M. B. Mogensen, 'Electrical conductivity measurements of aqueous and immobilized potassium hydroxide', *International Journal of Hydrogen Energy*, vol. 37, no. 21, pp. 16505–16514, Nov. 2012.

[91]   S. S. Zumdahl, in *Chemical principles*, 4th ed., 2002, pp. 225–244.

[92]   H. Matsushima, D. Kiuchi, Y. Fukunaka, and K. Kuribayashi, 'Single bubble growth during water electrolysis under microgravity', *Electrochemistry Communications*, vol. 11, no. 8, pp. 1721–1723, Aug. 2009.

[93]   H. Matsushima, Y. Fukunaka, and K. Kuribayashi, 'Water electrolysis under microgravity: Part II. Description of gas bubble evolution phenomena', *Electrochimica Acta*, vol. 51, no. 20, pp. 4190–4198, May 2006.

[94]   J. A. Koza, S. Mühlenhoff, P. Zabinski, P. A. Nikrityuk, K. Eckert, M. Uhlemann, A. Gebert, T. Weier, L. Schultz, and S. Odenbach, 'Hydrogen evolution under the influence of a magnetic field', *Electrochimica Acta*, vol. 56, no. 6, pp. 2665–2675, Feb. 2011.

[95]   S. H. Ahn, I. Choi, H.-Y. Park, S. J. Hwang, S. J. Yoo, E. Cho, H.-J. Kim, D. Henkensmeier, S. W. Nam, S.-K. Kim, and J. H. Jang, 'Effect of morphology of electrodeposited Ni catalysts on the behavior of bubbles generated during the oxygen evolution reaction in alkaline water electrolysis', *Chemical Communications*, vol. 49, no. 81, p. 9323, 2013.

[96]   C. W. M. P. Sillen, E. Barendrecht, L. J. J. Janssen, and S. J. D. van Stralen, 'Gas bubble behaviour during water electrolysis', *International Journal of Hydrogen Energy*, vol. 7, no. 7, pp. 577–587, 1982.

[97]   M. Wang, Z. Wang, and Z. Guo, 'Understanding of the intensified effect of super gravity on hydrogen evolution reaction', *International Journal of Hydrogen Energy*, vol. 34, no. 13, pp. 5311–5317, Jul. 2009.

[98]   S.-D. Li, C.-C. Wang, and C.-Y. Chen, 'Water electrolysis in the presence of an ultrasonic field', *Electrochimica Acta*, vol. 54, no. 15, pp. 3877–3883, Jun. 2009.

[99]   T. Iida, H. Matsushima, and Y. Fukunaka, 'Water Electrolysis under a Magnetic Field', *J. Electrochem. Soc.*, vol. 154, no. 8, pp. E112–E115, Jan. 2007.

[100] L. Lao, C. Ramshaw, and H. Yeung, 'Process intensification: water electrolysis in a centrifugal acceleration field', *J Appl Electrochem*, vol. 41, no. 6, pp. 645–656, Jun. 2011.

[101] V. M. Nikolic, G. S. Tasic, A. D. Maksic, D. P. Saponjic, S. M. Miulovic, and M. P. Marceta Kaninski, 'Raising efficiency of hydrogen generation from alkaline water electrolysis – Energy saving', *International Journal of Hydrogen Energy*, vol. 35, no. 22, pp. 12369–12373, Nov. 2010.

[102] M. P. Marčeta Kaninski, A. D. Maksić, D. L. Stojić, and Š. S. Miljanić, 'Ionic activators in the electrolytic production of hydrogen—cost reduction-analysis of the cathode', *Journal of Power Sources*, vol. 131, no. 1–2, pp. 107–111, May 2004.

[103] A. D. Maksic, S. M. Miulovic, V. M. Nikolic, I. M. Perovic, and M. P. Marceta Kaninski, 'Energy consumption of the electrolytic hydrogen production using Ni–W based activators—Part I', *Applied Catalysis A: General*, vol. 405, no. 1–2, pp. 25–28, Oct. 2011.

[104] G. S. Tasic, S. P. Maslovara, D. L. Zugic, A. D. Maksic, and M. P. Marceta Kaninski, 'Characterization of the Ni–Mo catalyst formed in situ during hydrogen generation from alkaline water electrolysis', *International Journal of Hydrogen Energy*, vol. 36, no. 18, pp. 11588–11595, Sep. 2011.

[105] J. Fischer, H. Hofmann, G. Luft, and H. Wendt, 'Fundamental investigations and electrochemical engineering aspects concerning an advanced concept for alkaline water electrolysis', *AIChE Journal*, vol. 26, no. 5, pp. 794–802, 1980.

[106] M. G. Nayar, P. Ragunathan, and S. K. Mitra, 'Development and operation of a high current density high pressure advanced electrolysis cell', *International Journal of Hydrogen Energy*, vol. 5, no. 1, pp. 65–74, 1980.

[107] M. H. Miles, G. Kissel, P. W. T. Lu, and S. Srinivasan, 'Effect of Temperature on Electrode Kinetic Parameters for Hydrogen and Oxygen Evolution Reactions on Nickel Electrodes in Alkaline Solutions', *J. Electrochem. Soc.*, vol. 123, no. 3, pp. 332–336, Jan. 1976.

[108] J. C. Ganley, 'High temperature and pressure alkaline electrolysis', *International Journal of Hydrogen Energy*, vol. 34, no. 9, pp. 3604–3611, May 2009.

[109] A. C. Ferreira, E. R. Gonzalez, E. A. Ticianelli, L. A. Avaca, and B. Matvienko, 'The effect of temperature on the water electrolysis reactions on nickel and nickel-based codeposits', *J Appl Electrochem*, vol. 18, no. 6, pp. 894–898, Nov. 1988.

[110] F. Allebrod, C. Chatzichristodoulou, and M. B. Mogensen, 'Alkaline electrolysis cell at high temperature and pressure of 250 °C and 42 bar', *Journal of Power Sources*, vol. 229, pp. 22–31, May 2013.

[111] J. Larminie and A. Dicks, *Fuel cell systems explained*. J. Wiley, 2003.

[112] H. S. Hong, U.-S. Chae, S.-T. Choo, and K. S. Lee, 'Microstructure and electrical conductivity of Ni/YSZ and NiO/YSZ composites for high-temperature electrolysis prepared by mechanical alloying', *Journal of Power Sources*, vol. 149, pp. 84–89, Sep. 2005.

[113] A. Brisse, J. Schefold, and M. Zahid, 'High temperature water electrolysis in solid oxide cells', *International Journal of Hydrogen Energy*, vol. 33, no. 20, pp. 5375–5382, Oct. 2008.

[114] W. Dönitz and E. Erdle, 'High-temperature electrolysis of water vapor—status of development and perspectives for application', *International Journal of Hydrogen Energy*, vol. 10, no. 5, pp. 291–295, 1985.

[115] D. M. Soares, O. Teschke, and I. Torriani, 'Hydride Effect on the Kinetics of the Hydrogen Evolution Reaction on Nickel Cathodes in Alkaline Media', *J. Electrochem. Soc.*, vol. 139, no. 1, pp. 98–105, Jan. 1992.

[116] J. Y. Huot and L. Brossard, 'Time dependence of the hydrogen discharge at 70°C on nickel cathodes', *International Journal of Hydrogen Energy*, vol. 12, no. 12, pp. 821–830, 1987.

[117] R. M. Abouatallah, D. W. Kirk, and J. W. Graydon, 'Long-term electrolytic hydrogen permeation in nickel and the effect of vanadium species addition', *Electrochimica Acta*, vol. 47, no. 15, pp. 2483–2494, Jun. 2002.

[118] R. . Abouatallah, D. . Kirk, S. . Thorpe, and J. . Graydon, 'Reactivation of nickel cathodes by dissolved vanadium species during hydrogen evolution in alkaline media', *Electrochimica Acta*, vol. 47, no. 4, pp. 613–621, Nov. 2001.

[119] A. E. Mauer, D. W. Kirk, and S. J. Thorpe, 'The role of iron in the prevention of nickel electrode deactivation in alkaline electrolysis', *Electrochimica Acta*, vol. 52, no. 11, pp. 3505–3509, Mar. 2007.

[120] 'http://www.gamry.com/assets/Application-Notes/Check-the-Impedance-of-Your-Reference-Electrode.pdf'. .

[121] 'http://www.burkert.com/media/COM_Chemical_Resistance_Chart.pdf'. .

[122] 'http://greenhydrogen.dk/Default.aspx?ID=551'. [Online]. Available: http://greenhydrogen.dk/Default.aspx?ID=551. [Accessed: 22-Nov-2013].

[123] 'http://www.climatebuildings.dk/h2college.php'. [Online]. Available: http://www.climatebuildings.dk/h2college.php. [Accessed: 22-Nov-2013].

[124] R. Baboian, in *Corrosion tests and standards : application and interpretation*, 2005, p. 26.

[125] H. J. Miao and D. L. Piron, 'Composite-coating electrodes for hydrogen evolution reaction', *Electrochimica Acta*, vol. 38, no. 8, pp. 1079–1085, Jun. 1993.

[126] E. Endoh, H. Otouma, T. Morimoto, and Y. Oda, 'New Raney nickel composite-coated electrode for hydrogen evolution', *International Journal of Hydrogen Energy*, vol. 12, no. 7, pp. 473–479, 1987.

[127] E. Endoh, H. Otouma, and T. Morimoto, 'Advanced low hydrogen overvoltage cathode for chlor-alkali electrolysis cells', *International Journal of Hydrogen Energy*, vol. 13, no. 4, pp. 207–213, 1988.

[128] Y. Choquette, H. Ménard, and L. Brossard, 'Hydrogen discharge on a Raney nickel composite-coated electrode', *International Journal of Hydrogen Energy*, vol. 14, no. 9, pp. 637–642, 1989.

[129] Y. Choquette, L. Brossard, A. Lasia, and H. Menard, 'Study of the Kinetics of Hydrogen Evolution Reaction on Raney Nickel Composite-Coated Electrode by AC Impedance Technique', *J. Electrochem. Soc.*, vol. 137, no. 6, pp. 1723–1730, Jan. 1990.

[130] C. Hitz and A. Lasia, 'Experimental study and modeling of impedance of the her on porous Ni electrodes', *Journal of Electroanalytical Chemistry*, vol. 500, no. 1–2, pp. 213–222, Mar. 2001.

[131] L. Chen and A. Lasia, 'Study of the Kinetics of Hydrogen Evolution Reaction on Nickel-Zinc Alloy Electrodes', *J. Electrochem. Soc.*, vol. 138, no. 11, pp. 3321–3328, Jan. 1991.

[132] J. Balej, J. Divisek, H. Schmitz, and J. Mergel, 'Preparation and properties of raney-nickel electrodes on Ni-Zn base for H2 and O2 evolution from alkaline-solutions. Part I: electrodeposition of Ni-Zn alloys from chloride solutions', *Journal of applied electrochemistry*, vol. 22, no. 8, pp. 705–710, Aug. 1992.

[133] D. Miousse, A. Lasia, and V. Borck, 'Hydrogen evolution reaction on Ni-Al-Mo and Ni-Al electrodes prepared by low pressure plasma spraying', *J Appl Electrochem*, vol. 25, no. 6, pp. 592–602, Jun. 1995.

[134] G. Schiller, R. Henne, and V. Borck, 'Vacuum plasma spraying of high-performance electrodes for alkaline water electrolysis', *Journal of Thermal Spray Technology*, vol. 4, no. 2, pp. 185–194, Jun. 1995.

[135] M. L. Bakker, D. J. Young, and M. S. Wainwright, 'Selective leaching of NiAl3 and Ni2Al3 intermetallics to form Raney nickels', *Journal of Materials Science*, vol. 23, no. 11, pp. 3921–3926, Nov. 1988.

[136] M. Janssen and G. Rieck, 'Reaction diffusion and kirkendall-effect in nickel aluminium system', *Transactions of the metallurgical society of AIME*, vol. 239, no. 9, pp. 1372–1385, 1967.

[137] M. F. Singleton, J. L. Murray, and P. Nash, 'Al-Ni (Aluminium-Nickel)', in *Binary Alloy Phase Diagrams*, 1st. edition., vol. 1, 2 vols., T. B. Massalski, H. Okamoto, P. R. Subramanian, and L. Kacprzak, Eds. American Society for Metals, 1986, p. 142.

[138] R. F. Hunter and P. Hohn, 'Caustic etching of aluminum with matte finish and low waste capability', 509104625-Feb-1992.

[139] H. L. Watts and D. W. Utley, 'Volumetric Analysis of Sodium Aluminate Solutions', *Anal. Chem.*, vol. 25, no. 6, pp. 864–867, Jun. 1953.

[140] Y. Li, Y. Zhang, C. Yang, and Y. Zhang, 'Precipitating sandy aluminium hydroxide from sodium aluminate solution by the neutralization of sodium bicarbonate', *Hydrometallurgy*, vol. 98, no. 1–2, pp. 52–57, Aug. 2009.

[141] J. R. Davies, *Aluminium and Aluminium Alloys*. ASM International, 1993.

[142] A. Kyriakopolous, M. Lynn, and R. Ghomashchi, 'Reactive interaction of molten aluminum and solid nickel', *Journal of Materials Science Letters*, vol. 20, no. 18, pp. 1699–1701, Sep. 2001.

[143] V. I. Dybkov, 'Interaction of iron-nickel alloys with liquid aluminium', *J Mater Sci*, vol. 28, no. 23, pp. 6371–6380, Dec. 1993.

[144] R. Blagoj and M. Jon, 'Interaction of solid nickel with liquid mixture of aluminum and nickel and formation of intermetallic phases', *Metalurgija*, vol. 16, no. 3, pp. 177–185.

[145] H. Liu, M. Bouchard, and L. Zhang, 'An experimental study of hydrogen solubility in liquid aluminium', *Journal of Material Science*, vol. 30, no. 17, pp. 4309–4315, Sep. 1995.

[146] X. R. 任晓, G. Chen, W. Z. 周文龙, C. Wu, and J. Zhang, 'Formation and growth kinetics of intermediate phases in Ni-Al diffusion couples', *J. Wuhan Univ. Technol.-Mat. Sci. Edit.*, vol. 24, no. 5, pp. 787–790, Oct. 2009.

[147] T. Jiang, M. J. C. Brym, G. Dube, A. Lasia, and G. M. Brisard, 'Studies on the AlCl3/dimethylsulfone (DMSO2) electrolytes for the aluminum deposition processes', *Surf. Coat. Technol.*, vol. 201, no. 14, pp. 6309–6317, Apr. 2007.

[148] J. Fransaer, E. Leunis, T. Hirato, and J. P. Celis, 'Aluminium composite coatings containing micrometre and nanometre-sized particles electroplated from a non-aqueous electrolyte', *J. Appl. Electrochem.*, vol. 32, no. 2, pp. 123–128, Feb. 2002.

[149] M. Miyake, H. Motonami, S. Shiomi, and T. Hirato, 'Electrodeposition of purified aluminum coatings from dimethylsulfone–AlCl3 electrolytes with trimethylamine hydrochloride', *Surface and Coatings Technology*, vol. 206, no. 19–20, pp. 4225–4229, May 2012.

[150] T. Jiang, M. J. C. Brym, G. Dube, A. Lasia, and G. M. Brisard, 'Studies on the AlCl3/dimethylsulfone (DMSO2) electrolytes for the aluminum deposition processes', *Surf. Coat. Technol.*, vol. 201, no. 14, pp. 6309–6317, Apr. 2007.

[151] European Hydrogen Association. *Where will the energy for hydrogen production come from? - Status and Alternatives-*. [Online] 2006 http://www.lbst.de/ressources/docs2007/EHA_WhereWillH2ComeFrom_2007.pdf (Accessed: 21 November 2013)

[152] EUR-Lex. Communication from the commission to the European Parliament, the council, the European Economic and social committee and the Regions. *Energy 2020 A strategy for competitive, sustainable and secure energy* [Online] November 2010 http://eur-lex.europa.eu/LexUriServ/LexUriServ.do?uri=COM:2010:0639:FIN:EN:HTML (Accessed: 2 August 2012)

[153] F. Mohseni, M. Magnusson, M. Görling, and P. Alvfors, 'Biogas from renewable electricity – Increasing a climate neutral fuel supply', Appl. Energy, vol. 90, no. 1, pp. 11–16, Feb. 2012.

[154] C. A. Floudas, J. A. Elia, and R. C. Baliban, 'Hybrid and single feedstock energy processes for liquid transportation fuels: A critical review', Comput. Chem. Eng., vol. 41, pp. 24–51, Jun. 2012.

[155] M. F. Hordeski, Alternative Fuels: The Future of Hydrogen, Second Edition, 2nd ed. The Fairmont Press, Inc., 2008.

Appended Papers

Development of durable and efficient electrodes for large-scale alkaline water electrolysis

Cecilía Kristín Kjartansdóttir [a,*], *Lars Pleth Nielsen* [b], *Per Møller* [a]

[a] *Department of Mechanical Engineering, Technical University of Denmark, Produktionstorvet, Building 425, 2800 Kgs. Lyngby, Denmark*
[b] *Danish Technological Institute, Kongsvang Allé 29, 8000 Aarhus C, Denmark*

ARTICLE INFO

ABSTRACT

A new type of electrodes for alkaline water electrolysis is produced by physical vapour depositing (PVD) of aluminium onto a nickel substrate. The PVD Al/Ni is heat-treated to facilitate alloy formation followed by a selective aluminium alkaline leaching. The obtained porous Ni surface is uniform and characterized by a unique interlayer adhesion, which is critical for industrial application. IR-compensated polarisation curves prepared in a half-cell setup with 1 M KOH electrolyte at room temperature reveals that at least 400 mV less potential is needed to decompose water into hydrogen and oxygen with the developed porous PVD Al/Ni electrodes as compared to solid nickel electrodes. High-resolution scanning electron microscope (HR-SEM) micrographs reveal Ni-electrode surfaces characterized by a large surface area with pores down to a few nanometre sizes. Durability tests were carried out in a commercially produced bipolar electrolyser stack. The developed electrodes showed stable behaviour under intermittent operation for over 9000 h indicating no serious deactivation in the density of active sites.

1. Introduction

According to *the World of Energy Outlook 2010*, made by the International Energy Agency, renewable energy is the answer for a more secure, reliable and sustainable future. This implies that a higher percentage of the energy will have to come from fluctuating renewable energy sources such as wind, sun and water. Simultaneously, the ever increasing demand and stronger legalisations towards reducing the CO_2 emission worldwide [1] makes it necessary to develop new efficient alternatives for energy conversion, energy storage and load management. Using the excess electrical power from renewable energy sources, e.g. wind, solar and wave technologies, to produce hydrogen via water electrolysis, offers the possibility of increased production capacity and load management with no greenhouse emissions. The hydrogen can subsequently be stored and used for producing electricity via fuel cells, combustion engines or gas turbines, whenever needed. New ideas for using hydrogen as a raw material for production of synthetic fuels, such as methane by the Sabatier process [2], liquid fuels by the Fischer–Tropsch synthesis [3] or simply pumping the hydrogen gas into the existing natural gas infrastructure, the "power-to-gas" idea will suddenly be a reality when hydrogen becomes available in large quantities [4].

A variety of water electrolysis systems have been proposed and constructed over the years. Alkaline electrolysis is the most mature commercial water electrolysis technology and offers the advantages of simplicity and is the current standard

for large-scale water electrolysis systems [5] [6]. However, finding low cost electrode materials that are both efficient and durable is one of the remaining challenges for alkaline water electrolysis (AWE) techniques.

Traditionally, the cathode material for AWE systems was made of steel and the anode material from nickel or nickel-coated steel [7]. The pioneer work of Paul Sabatier (1912) and Murray Raney (1925) on hydrogenation catalysts [8] enabled Justi and Winsel to discover the highly porous Raney nickel as an efficient hydrogen electrocatalyst in an alkaline media already in 1961 [9].

Raney nickel catalysts are generally prepared by rapidly cooling a molten solution of nickel and aluminium. The cooling procedure controls which Al–Ni phases are formed in the solid. After solidification, the product is crushed into a fine powder. The catalyst powder is subsequently activated by selectively leaching aluminium from the Al–Ni alloy [10]. Lattice vacancies formed when leaching causes large surface areas and high density of active sites due to a high density of reactive lattice defects [11]. The activated catalyst therefore provides superior performance compared to unactivated non-porous nickel cathodes.

Plasma spraying leachable precursor alloys (Al_3Ni and/or Al_3Ni_2) onto a nickel or steel support is an alternative and common technique applied when producing supported Raney nickel electrocatalysts for alkaline electrolysis [12–19]. Cold rolling and hot dipping of aluminium combined with a thermo-chemical diffusion process have also been proposed [8] [20]. However, the reproducibility and durability of the Raney nickel electrodes are often deficient [7].

When utilizing atmospheric plasma spraying (APS) to form supported Raney nickel electrodes, formation of the electrical resistive and brittle Al_2O_3 phase cannot be avoided. During vacuum plasma spraying (VPS), no oxygen is available to react with the aluminium, and the initial Raney nickel structure appears to be highly active towards the hydrogen evolution reaction (HER) [18]. Producing a VPS Raney nickel structure with interlayer adhesion that can withstand the harsh gas erosion during AWE is however challenging.

In this paper, we report studies on large-scale production of electrodes suitable for commercially available alkaline water electrolysis stacks. The electrodes are produced by plasma vapour deposition (PVD) followed by a thermo-chemical diffusion process and alkaline leaching. Structural characterisation of the electrodes is performed by high-resolution scanning electron microscope (HR-SEM). The electrocatalytic activity of the developed electrodes is studied with steady-state electrochemical measurements and cyclic voltammetry. Durability tests are carried out in an industrial scale-electrolysis stack.

2. Experimental

2.1. Preparation of electrodes

Commercially available nickel plates with a thickness of 0.5 mm were used as an electrode substrate. The purity of the nickel plates were determined by optical emission spectroscopy, detecting 99% Ni, 0.25% Mn, 0.14% Fe and 0.11% Al. Other residual elements were determined to be below 0.1%. The nickel plates were cut to form circular specimens with a diameter of 3 cm, intended for small-scale electrochemical measurements and scanning electron microscope investigations. 16 nickel plates, designed for a commercial bi-polar electrolysis stack, were prepared from the same type of nickel. All nickel specimens to be Al PVD treated were cathodically degreased for 2 min prior to the PVD process. The Al PVD was done in a non-reactive DC-magnetron sputtering mode using a CC800/9 SinOx coating unit from CemeCon AG. The Ni substrates were heated and etched in situ by Ar sputtering prior to sputter-depositing aluminium to remove nickel oxide (NiO) from the surface. The circular specimens were coated on one side, whereas the specimens for the electrolysis stack were coated on both sides. The thickness of the aluminium coating ranged from 20 to 40 μm. The Al PVD plated specimens were subsequently heat treated in an atmospheric furnace for 24 h at 610 °C followed by a selective aluminium leaching.

Two circular specimen were leached according to the following procedure; 2 h in 1% NaOH at room temperature, 20 h in 10% NaOH at room temperature and 4 h in 30% NaOH at 100 °C, respectively. These specimens will be referred to as PVD Al/Ni 1. Two circular specimens were leached in 30% KOH and 10% $KNaC_4H_4O_6$*$4H_2O$ at 80 °C with stirring for 24 h. These specimens will be referred to as PVD Al/Ni 2. The aluminium leaching procedure for the 16 large electrodes was identical to the leaching procedure for the PVD Al/Ni 2 specimens.

2.2. Structural characterisation and composition

For cross section characterisation and composition analyses, four PVD Al/Ni specimens, one as plated, one from each leaching method and one unleached, were cut into 1×1.5 cm^2. Each specimen was hot-mounted in CloroFast resin and grinded down to 4000 grit, subsequently polished with 3 μm diamond and 0.04 μm SiO_2 particles. JEOL JSM 5900 scanning electron microscope (SEM) was used for the cross section investigations and an integrated energy-dispersive X-ray spectroscopy from Oxford Instruments was used for elemental analysis. The surface structure and morphology of the PVD Al/Ni 2 electrodes were characterized by means of a FEI Quanta 200 ESEM FEG scanning electron microscope.

2.3. Electrochemical measurements

The catalytic activity of the developed electrodes was evaluated by means of potentiodynamic polarisation curves. The electrocatalytic active surface area of the electrodes was determined by the amount of Ni hydroxide formed during cyclic voltammetry. The measurements were carried out using Gamry Reference 3000 potentiostat/galvanostat and a three-electrode electrochemical cell made of teflon. The reference electrode was a Hg/HgO electrode from Radiometer and the counter electrode was made of pure nickel. The electrolyte contained 1 M KOH and the measurements were operated at 25 °C. All the electrochemical measurements were IR-compensation by means of current interruption technique. All following potentials are specified against the standard hydrogen electrode (SHE) potential.

Prior to the cathodic polarisation measurements, the electrodes were conditioned at −0.8 V for 30 min. Thereafter the electrodes were kept at open circuit potential (OCP) for 5 min or until 0.01 mV/s stability was reached. Subsequently cathodic sweep from −0.5 V up to 0.6 A current, at scan rate of 1 mV/s, was performed. The experimental procedure for the anodic polarisation curves was as follows; conditioning at 0.7 V for 30 min, OCP for 5 min, or until stability of 0.01 mV/s was reached and anodic sweep from 0.5 V up to 0.6 A current density at 1 mV/s scan rate.

The cyclic voltammetry measurements were performed from −0.9 to −1.1 V with upper limit of −0.1 V at the scan rate of 50 mV/s. Prior the measurement the electrodes were conditioned at −1.5 V for 30 min and −0.9 V for 5 min.

2.4. Adhesion and durability test

The 16 large PVD Al/Ni electrodes were mounted in a 17 cell bipolar, non-zero gap electrolysis stack produced by Green-Hydrogen.dk. The stack contained 30% KOH and was operated under altered conditions, at a maximum temperature of 80 °C and a pressure of 22 bars for more than 9000 h. As the electrodes were treated with the alkaline-etched PVD Al/Ni on both sides, the developed surface functioned both as an anode and as a cathode in the electrolysis stack.

The mechanical strength and adhesion properties of the developed electrodes were evaluated via a bending test comparable to ASTM B571, 1997 (2008) e1.

3. Results and discussions

3.1. Structural characterisation and composition

When heat-treated at 610 °C, a thermo-chemical diffusion process takes place at the contact area between the aluminium and nickel phase. The aluminium atoms diffuse into the nickel structure and thermodynamically stable

Fig. 2 — Cross section SEM micrograph of a PVD Al/Ni electrode as plated.

diffusion couples at that temperature can be formed. The diffusion coefficient for the Al—Ni system is used for selecting appropriate heat treatment parameters, they have been calculated elsewhere [21]. The red horizontal line in the phase diagram in Fig. 1 indicates which Al—Ni diffusion couples are thermodynamically stable at 610 °C and atmospheric pressure. The thickness of each intermetallic phase formed depends on the amount of Ni and Al available in the diffusion system and the heat treatment parameters.

The SEM micrographs in Figs. 2 and 3 show cross section micrographs of a PVD Al/Ni electrode prior and after the heat treatment. Comparing the energy-dispersive X-ray spectroscopy (EDS) data, Table 1, with the Al—Ni phase diagram, it is supposed that the three following Al—Ni intermetallic phases are formed during heat treatment; Al_3Ni_2, AlNi and $AlNi_3$, seen from the top towards the pure Ni substrate. This is in agreement with the findings of Janssen and Rieck [21]. The lowermost phase in Fig. 3 is the unaffected nickel substrate. The majority of the intermetallic phases formed is the strong, and yet leachable, Al_3Ni_2 phase [22].
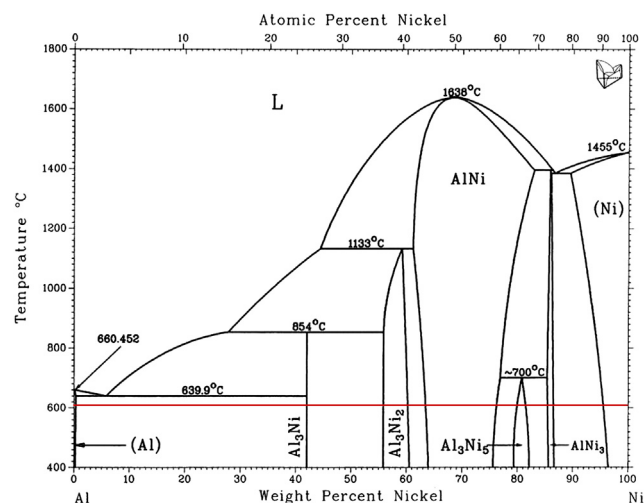

Fig. 1 — Phase diagram for the Al—Ni diffusion couples adopted from [23]. The horizontal line indicates the thermo-chemical diffusion temperature (610 °C) selected for the electrode development.
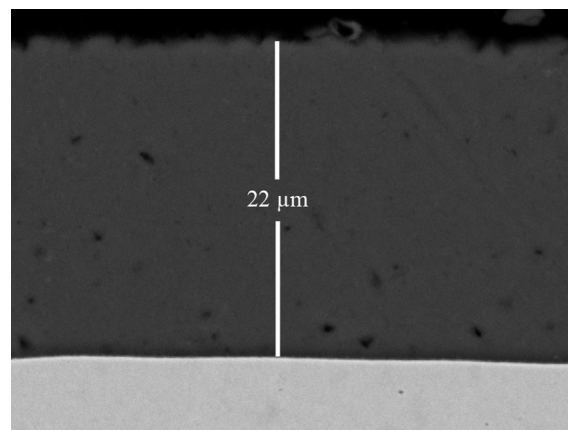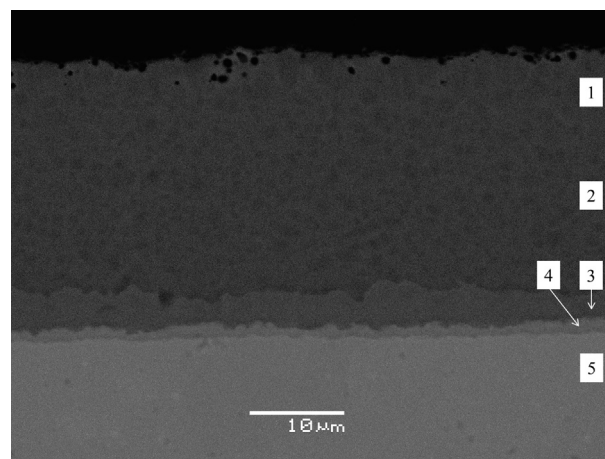

Fig. 3 — Cross section SEM micrograph of a PVD Al/Ni electrode after heat treatment at 610 °C for 24 h, prior to leaching. The numbers refer to the EDS analysis in Table 1.

Table 1 – Results from the cross section EDS analysis on PVD Al/Ni electrodes before and after the first and the second leaching procedure. The phase numbers refer to the numbers in Figs. 3–5. All elements from the periodic table are analysed.

Phase nr.	Name of phase	Before leaching		After the 1. leaching procedure			After the 2. leaching procedure		
		Al wt.%	Ni wt.%	O wt%	Al wt.%	Ni wt.%	O wt%	Al wt.%	Ni wt.%
1	Al_3Ni_2	37	63	4	21	75	7	13	80
2	Al_3Ni_2	37	63		36	64	4	15	81
3	AlNi	30	70		30	70		29	71
4	$AlNi_3$	13	87		13	87		14	86
5	Ni		100			100			100

Fig. 4 and Fig. 5 show cross section SEM micrographs of the PVD Al/Ni electrodes after heat treatment followed by the first and second alkaline leaching procedure, PVD Al/Ni 1 and PVD Al/Ni 2, respectively. Using the first leaching procedure, about 5 μm skeletal Al/Ni residue is formed. However, when selectively leaching the Al with the second leaching procedure, the

Fig. 4 – Cross section SEM micrograph of a PVD Al/Ni 1 electrode after heat treatment at 610 °C for 24 h and aluminium leaching for 2 h in 1% NaOH at room temperature, 20 h in 10% NaOH at room temperature and 4 h in 30% NaOH at 100 °C, respectively.

a

b
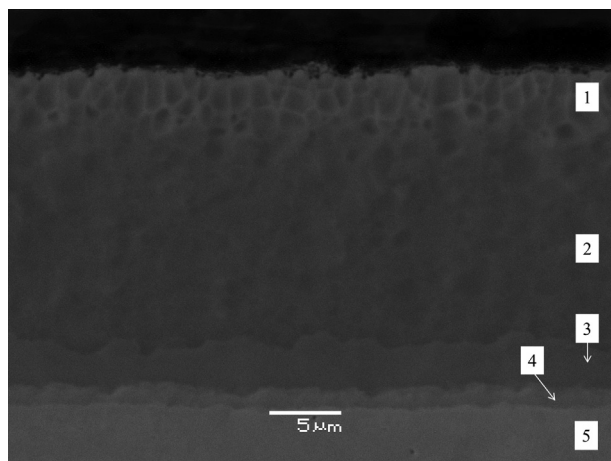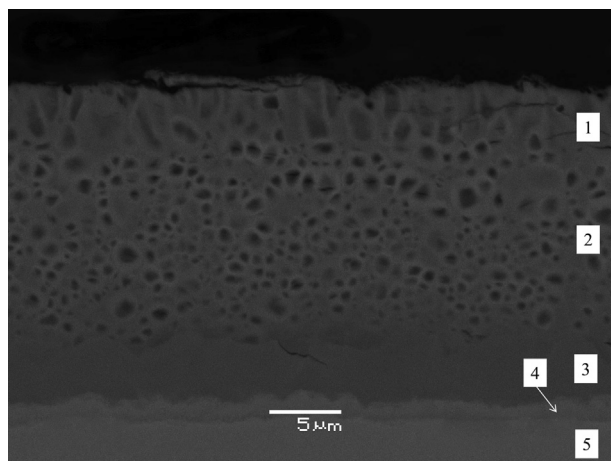

Fig. 5 – Cross section SEM micrograph of a PVD Al/Ni 2 electrode after heat treatment at 610 °C for 24 h and selective leaching of aluminium in 30% KOH and 10% $KNaC_4H_4O_6 \cdot 4H_2O$ at 80 °C for 24 h, respectively.

Fig. 6 – HR-SEM micrographs of a PVD Al/Ni 2 surface after heat treatment and complete alkaline leaching.
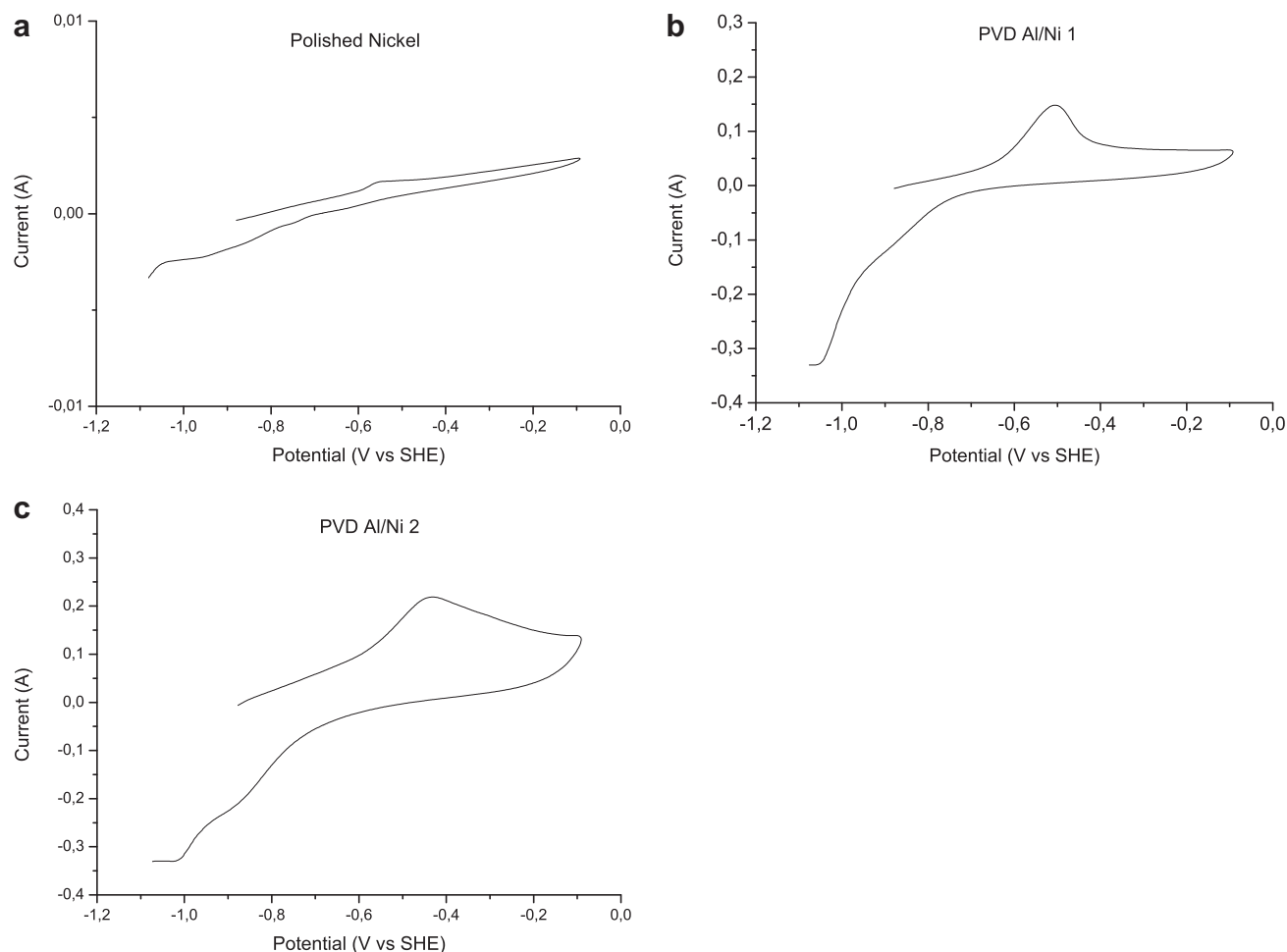
Fig. 7 – Voltammograms recorded on polished Ni, PVD Al/Ni 1 and PVD Al/NI 2 electrodes from −0.9 to −1.1 V with upper limit of −0.1 V at the scan rate of 50 mV/s, in 1 M KOH at 25 °C the anodic peek represents the oxidation of the Ni surface to α-Ni(OH)$_2$.

entire Al$_3$Ni$_2$ phase is leached, resulting in considerably larger thickness of the porous nickel layer. The PVD Al/Ni 1 electrodes also have larger amount of aluminium remaining in the leached structure, or 21 wt% compared to 13–15 wt% for the PVD Al/Ni 2 electrodes. The difference can be due to the slow leaching kinetics of the Al$_3$Ni$_2$ phase below 70 °C in alkaline media [22]. For the first leaching procedure, the leaching steps at room temperature were selected for thorough leaching of the Al$_3$Ni phase, which, according to the Al–Ni phase diagram,

was expected to be formed during the heat treatment. However, after the heat treatment, no Al$_3$Ni phase was formed in the inter-diffusion structure. Therefore, the leaching procedures at room temperature do not contribute to the leaching process. The 4 h of leaching at 100 °C in NaOH is evidently not enough for complete leaching of the Al$_3$Ni$_2$ structure. In addition, some of the Al could possibly have been redeposited into the pores during the first leaching method since no KNa-tartrate tetrahydrate was used in that process [24]. The reason

Specimen	Geometrical surface area (cm^2)	Charge associating with the formation of α-Ni(OH)$_2$ (mC)	The active electrochemical surface area (cm^2)[a]	Roughness factor[b]
Polished Nickel	2	1.1	2.1	1,05
PVD Al/Ni 1	2	246.3	479.2	239.6
PVD Al/Ni$_2$	2	558.2	1086.0	543.0

Table 2 – Results from cyclic voltammetry investigations at 1 M KOH and 25 °C.

a The charge associating with formation of α-Ni(OH)$_2$ recorded divided by the charge associating with the formation and reduction of a monolayer of α-Ni(OH)$_2$ (514 C cm^{-2}) for nickel electrode according to [28].
b The active electrochemical surface area divided by the geometrical surface area.

for adding KNa-tartrate tetrahydrate to the alkaline leaching solutions is that it works as a complexing agent for the leached aluminium according to [25]:

$$Al(OH)_4^- + n(C_4H_4O_6)^{2-} \rightarrow Al(OH)_3(C_4H_4O_6)_n^{2-} + OH^-$$
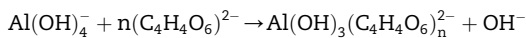
hereby preventing aluminium hydroxide precipitates to redeposit into the nickel pores [26]:

$$Al(OH)_4^- \rightarrow Al(OH)_3 + OH^-$$
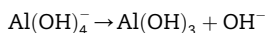
The cross section images reveal a highly porous nickel microstructure with pores in the range of approximately 0.5–1.5 μm. For nanostructure investigations, high-resolution SEM studies are required. HR-SEM micrographs of the surface of a PVD Al/Ni 2 specimen at different magnifications are shown in Fig. 6. When looking at the HR-SEM micrographs, nanopores down to at least 20 nm are revealed.

3.2. Electrochemical measurements

The anodic peaks in the voltammograms in Fig. 7 represents the oxidation of the Ni surface to α-Ni(OH)$_2$ [27]. The charge associating with the formation and reduction of a mono-layer of α-Ni(OH)$_2$ on plain nickel is known to be 514 μC cm^{-2} [28]. The ratio between the charge associated with the formation of α-Ni(OH)$_2$ on the tested surfaces and the known charge value for nickel can be used to estimate the actual electrochemical surface area. The roughness factor of the surfaces can then be estimated by dividing the actual electrochemical surface area by the geometrical surface area. The charge associating with the formation of a monolayer of α-Ni(OH)$_2$ on polished Ni, PVD Al/Ni 1 and PVD Al/Ni 2 are found to be 1.1 mC, 246.3 mC and 558.2 mC, respectively. Due to irreversible aging of α-Ni(OH)$_2$ to β-Ni(OH)$_2$ under the voltammetry conditions the first cycle from the cycle sweeps was chosen for peek estimation. The results from the vol-tammogram measurements are collected in Table 2. From the roughness factors it is evident that the electrodes leached with the first leaching method (PVD Al/Ni 1) have about 230 times larger electrochemical active surface area compared to the polished nickel electrode. The electrodes leached with the second leaching method (PVD Al/Ni 2) have about 517 times larger electrochemical active surface area compared to polished nickel and 2 times larger electro-chemical active surface area compared to PVD Al/Ni 1. The cyclic voltammetry analysis support that the developed electrodes are highly porous as indicated by the SEM mi-crographs. The cyclic voltammograms do however not say anything about how deep porous layer contributes to the electrochemical active surface. It is indeed expected that only few micrometres of the porous layer contributes to the actual electrochemical surface area. The large difference in active surface area between the electrodes produced with the two different etching methods is supposed to be due to the large amount of aluminium that is remaining in the top structure of the PVD Al/Ni 1 electrodes compare to the PVD Al/Ni 2 electrodes. That results in less pores and smaller surface area at the surface.

Fig. 8 shows cathodic polarisation curves recorded on a PVD Al/Ni 1, PVD Al/Ni 2 and polished nickel repeated three

Fig. 8 – Cathodic polarisation curves recorded on PVD Al/Ni 1, a PVD Al/Ni 2 and a polished nickel (99%), repeated three times, in 1 M KOH electrolyte at 25 °C.

times in a row. As seen from the figure, the measurements are consistent. From the polarisation curves it is evident that the PVD Al/Ni 1 is more active towards the HER compared to the polished nickel but less active compared to the PVD Al/Ni 2 electrodes. At 200 mA/cm^2 (which is a typical operation cur-rent density for commercial electrolysers) the PVD Al/Ni 1 electrode has about 280 mV less hydrogen overpotential compared to polished Ni. The PVD Al/Ni 2 electrode has however about 360 mV less overpotential, compared to the nickel. At higher current density values the overpotential of the PVD Al/Ni 1 structure degreases more rapidly than for the other two structures. This difference can be due to the large amount of aluminium (about 21 wt%) that is remaining in the top layer of the electrode.

In order to minimize the complexity and cost for the bi-polar electrode production, developing one type of

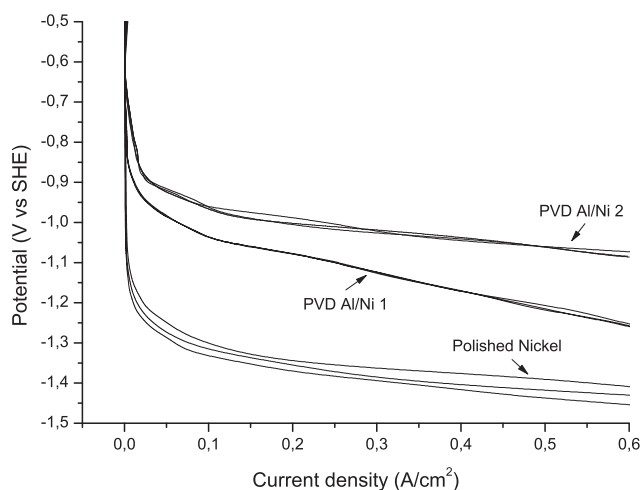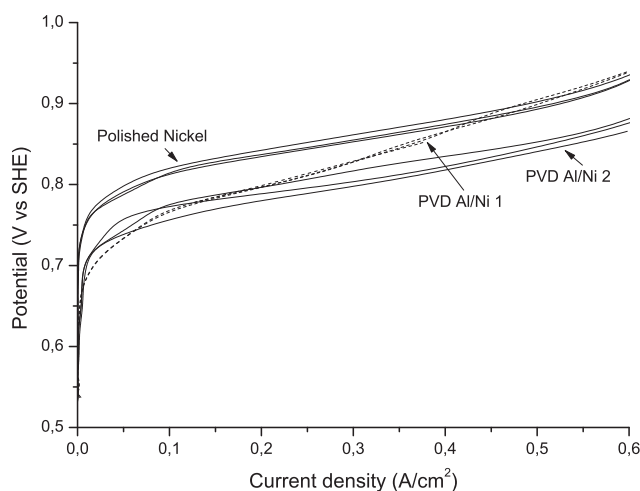Fig. 9 – Anodic polarisation curves recorded on PVD Al/Ni 1, a PVD Al/Ni 2 and a polished nickel (99%), repeated three times, in 1 M KOH electrolyte at 25 °C.
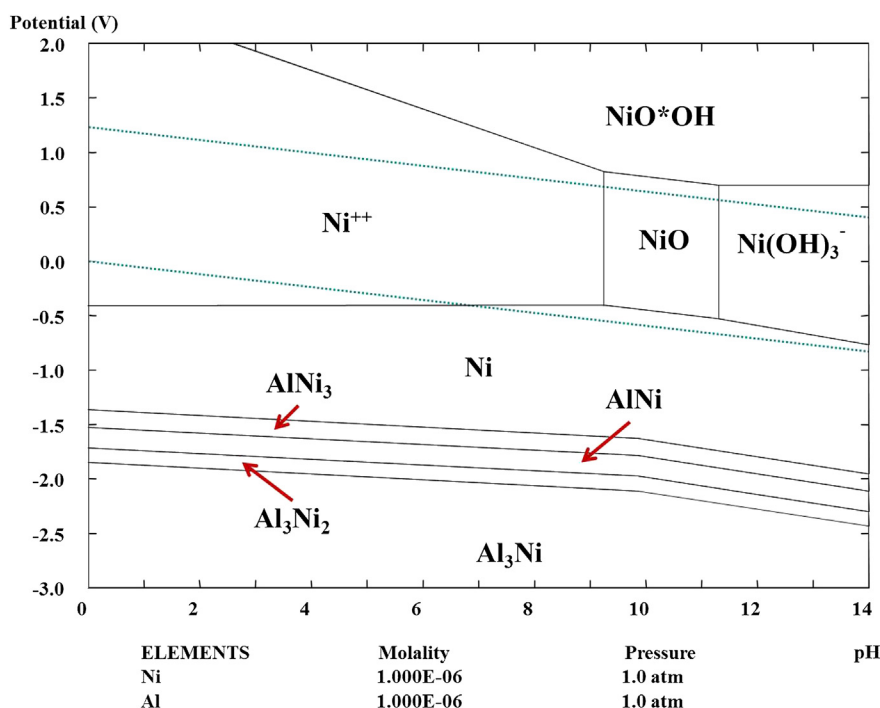
Fig. 10 – Pourbiax diagram for the Al–Ni–H₂O system at 25 °C.

electrocatalytic surface that is efficient and durable for both the anodic and cathodic reaction will be of major advantage. Although, the developed electrocatalyst was mainly designed for the HER process, testing of its performance for the oxygen evolution reaction (OER) is also of interest.

Fig. 9 shows anodic polarisation curves recorded on a PVD Al/Ni 1, PVD Al/Ni 2 and a polished nickel surfaces. As seen from the figure, PVD Al/Ni 1 and PVD Al/Ni 2 are similarly active towards OER at current densities up to 300 mA/cm². Only 50 mV is gained by using PVD Al/Ni 2 for the OER compared to polished nickel. As seen from the cyclic voltammetry measurements and SEM images, the surface area of the developed electrocatalysts are much larger than the surface area of the smooth electrode, thus more difference in efficiency would be expected. However, according to the Pourbaix-diagram in Fig. 9, nickel oxides are formed during the OER at the electrode surfaces. It is therefore probable that the skeletal nickel structure will be transformed into nickel oxide or corrode. The result of this might be blockage of some

of the nanopores with oxides already after a short time of operation. This will decrease the actual surface area of the electrode, decaying the performance towards that of a smooth nickel surface. The following anodic half-cell reactions and dissolution processes are suggested to describe the mentioned decomposition reactions of the anode in a strong alkaline solution:

$$Ni + 3OH^- \rightarrow Ni(OH)_3^- + 2e^-$$

$$Ni + 2OH^- \rightarrow NiO + H_2O + 2e^-$$

$$NiO + H_2O + OH^- \rightarrow Ni(OH)_3^-$$
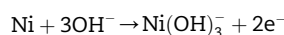
It is noteworthy that the slopes for the PVD Al/Ni 2 electrodes and the nickel electrodes are parallel for both HER and OER, see Figs. 8 and 9. This indicates that the same reaction

Table 3 – The chemical reactions and corresponding Gibbs free energy for alkaline aluminium leaching of the Al–Ni intermetallic phases in the Pourbaix diagram in Fig. 10. The energy values are calculated at 20 °C.

Chemical reaction	Gibbs free energy [ΔG⁰]
$Al_3Ni + 3OH^- + 9H_2O \rightarrow 3Al(OH)_4^- + 4.5H_2 + Ni$	−1157.3 kJ
$Al_3Ni_2 + 3OH^- + 9H_2O \rightarrow 3Al(OH)_4^- + 4.5H_2 + 2Ni$	−1026.7 kJ
$AlNi_3 + OH^- + 3H_2O \rightarrow Al(OH)_4^- + 1.5H_2 + 3Ni$	−284.4 kJ
$AlNi + OH^- + 3H_2O \rightarrow Al(OH)_4^- + 1.5H_2 + Ni$	−318.4 kJ

Fig. 11 – Single bend test on a heat-treated and leached PVD Al/Ni 2 electrode.
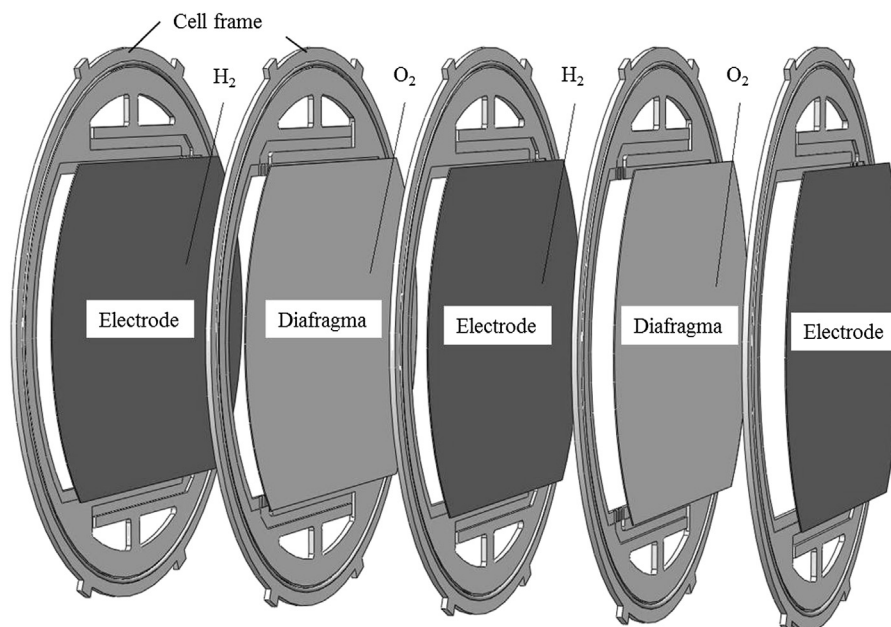
Fig. 12 – The bipolar construction of the electrolysis stack used for durability testing.

mechanism is taking place and the difference in activity comes from the difference in the actual surface area and the increase in the electrochemical active sides. That is, the intrinsic electrocatalytic properties are evidently the same or similar for the developed electrodes and pure nickel. For the PVD Al/Ni 1 structure where there is more aluminium remaining in the structure this is not the chase. The polarisation curves therefore show clearly that proper etching of the developed electrodes is crucial for attaining the optimal efficiency, especially at higher current densities.

3.3. Adhesion and durability

The durability of electrodes for AWE depends on the corrosion resistivity of the material in the operating media and the mechanical stability of the electrodes during operation. Fig. 10 shows a Pourbaix diagram calculated for the Al–Ni–H_2O system. The two dotted lines indicate the area where water is thermodynamically stable. Thus, the HER reaction can only take place below these lines, whereas the OER can only take place above the lines. The diagram shows that none of the Al–Ni intermetallic phases produced during the heat treatment is thermodynamically stable in strong alkali at the operating potentials. The chemical reactions and Gibbs free energy for aluminium leaching of the intermetallic phases in the Pourbaix diagram are shown in Table 3

Fig. 13 – Current vs. voltage data captured on the 17-cell bipolar electrolysis stack during the first month of operation. The operation conditions were 40–45 °C and at 10 bars.

Fig. 14 – Current vs. voltage and efficiency data captured on the 17-cell bipolar electrolysis stack after more than 9000 operating hours. The stak was operated at 60 °C and 22 bars. The efficiency calculations are based upon the value of the thermal neutral voltage (E = 1.48 V).
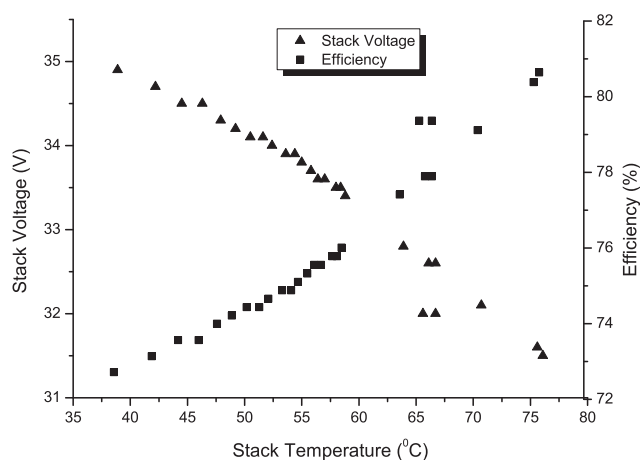
Fig. 15 – Efficiency measurement captured on the 17-cell bipolar electrolysis stack at 22 bars and 200 mA/cm² current density, after more than 9000 operating hours. The efficiency calculations are based upon the value of the thermal neutral voltage (E = 1.48 V).

Although the thermodynamics indicate otherwise, it is evident from the EDS analyses on the leached structures in Table 1 that the AlNi and AlNi₃ phases are stable in strong alkali. It can therefore be assumed that the leaching kinetics of AlNi and AlNi₃ at elevated temperatures are too slow for the mechanism to take place. In addition, according to the thermodynamics, nickel is not stable in strong alkali inside the water-stable area. If this was the case, the Ni electrocatalysts would decompose when the electrolysis stack was switched-off. However, due to the use of nickel as an anode in AWE for many years, it is evident that the dissolution of Ni in alkaline media is slow, making nickel one of the most corrosion-resistant metals of non-noble metals in that media.

During commercial alkaline water electrolysis, the high pH of the electrolyte, intermediate temperatures, and gas evolution all contribute in making the electrode environment extremely harsh. The knowledge of the chemical resistivity of nickel in strong alkaline solution has made nickel the material of choice when developing electrodes for AWE. However, the large mechanical stresses caused by gas evolution during the process are often neglected. Adhesion between the electrocatalyst and the substrate is crucial for the mechanical resistivity of the electrode. If the adhesion is not

sufficient, the electrolyte will eventually penetrate in-between the two layers and electrochemical reactions will take place leading to gas formation in the interphase. When this happens, the gas bubbles apply mechanical forces on the relatively brittle porous microstructure leading to gas erosion corrosion. The catalytic active surface will in that case scale off and the electrodes will lose their high active catalytic behaviour and the efficiency of the electrolysis stack will decrease.

For testing the adhesion between the developed electrocatalyst and the nickel substrate, bending tests were constructed on the leached PVD Al/Ni 2 electrodes produced. Fig. 11 shows a reproducible image of a tested electrode after bending. As seen from the figure, the PVD Al/Ni 2 coating does not peel off during the bending. This is an indication of good adhesion between the substrate and the electrocatalyst.

Durability test on sixteen large electrodes containing the developed electrocatalytic surface was carried out in a 17 cell bipolar electrolyser stack produced by the company Green-Hydrogen.dk. The end electrodes in the stack were made of pure nickel. Fig. 12 shows the bipolar constructions of the stack.

As mentioned before, the stack was operated under altered conditions, maximum temperature of 80 °C and a pressure of 22 bars, for more than 9000 h. For safety reasons the stack was operated under low temperature and pressure in the beginning of the testing period.

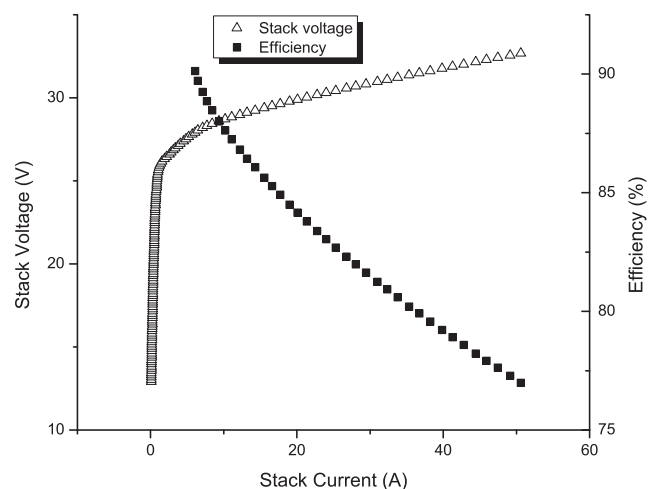Figs. 13–15 show the current vs. voltage and temperature vs. voltage data from the 17-cell bipolar electrolysis stack from the first month of the operating period and after over 9000 h operation. The fact that the test electrolysis stack was operated under different conditions in the beginning and the end of the testing period makes durability comparison challenging but not impossible. In Table 4 three values from the stack measurements showed in Figs. 13 and 15 have been chosen for durability assessment, one from the beginning of the test period and two from after 9000 h. These values indicate that no serious deactivation have taken place on the electrodes during the 9000 h testing period. It should be mentioned that these efficiency values are lower than the actual cell efficiencies. Designing an electrolysis stack with low energy losses is a complex matter. Large losses can come from stray current between cells and piling op of gases due to improper stack design [29]. This is however out of the scope of the present work.

Table 4 – Selected data from Figs. 11–13 for durability assessment.							
	Temperature (°C)	Pressure (Bar)	Stack current (A)	Cell current density (A/cm²)	Stack voltage (V)	Cell voltage (V)	Stack efficiency[a] (%)
First month of the operation period	40	10	40	0.15	33	1.94	76
After more than 9000 h operation	40	22	54	0.2	35	2.05	73
After more than 9000 h operation	60	22	40	0.15	32	1.88	79
a The efficiency calculations is based upon the value of the thermal neutral voltage (E = 1.48 V).							

4. Conclusions

The development of the present electrodes has been caried out with the focus on durability, stability and potential large-scale production. The electrocatalytical activity of an electrode depends on the electron configuration and the structure and geometry of the catalyst. In the well-known volcano plot, where the metal-hydrogen bond strength of a material is plotted against the exchange current density of the HER [30], it is shown that Ni is the most active pure metal among the non-noble candidates. Finding electrocatalytic material with good intrinsic properties and increasing the efficiency of the catalyst by enlarging the actual surface area have been described by various authors [31—35]. However, information about the mechanical stability and durability of the modified electro-catalysts is often lacking.

The present electrodes show good potentials as electrodes for large-scale alkaline water electrolysis systems. The developed electrodes have shown to be highly efficient for the hydrogen evolutions reaction, however, more efficiency is desired for the oxygen evolutions reaction. One of the major drawbacks of using nickel for the anodic process is that a low electrical conductive oxide layer is formed during electrolysis. Furthermore, the nanopores in the developed structure will presumably be filled up with oxides and will therefore not contribute to the actual surface area of the electrode. The next step in the development process is to optimize the anode material and carry out further durability testing.

Acknowledgement

REFERENCES

[1] Energy 2020-Strategy of the European Commission for a Competitive, sustainable and secure power Engineering. Energetika Prague 2011;61(Part 2):159—67.

[2]. Mohseni F, Magnusson M, Görling M, Alvfors P. Biogas from renewable electricity — increasing a climate neutral fuel supply. Applied Energy 2012;90(1):11—6.

[3] Floudas CA, Elia JA, Baliban RC. Hybrid and single feedstock energy processes for liquid transportation fuels: a critical review. Computers & Chemical Engineering 2012;41:24—51.

[4] Hordeski MF. Alternative fuels: the future of hydrogen. 2nd ed. Lilburn: The Fairmont Press, Inc; 2008.

[5] Wendt H, Imarisio G. Nine years of research and development on advanced water electrolysis. A review of the research programme of the Commission of the European Communities. Journal of Applied Electrochemistry 1988;18(1):1—14.

[6] Zeng K, Zhang D. Recent progress in alkaline water electrolysis for hydrogen production and applications. Progress in Energy and Combustion Science 2010;36(3):307—26.

[7] Lessing PA. Materials for water electrolysis cells. In: Jones RH, Thomas GJ, editors. Materials for the hydrogen economy. 1st ed. Boca Raton: CRC Press; 2007. p. 38—41.

[8] Method of producing finely-divided nickel. U.S. Patent 162819010-May-1927.

[9] Chen E. History. In: Hoogers G, editor. Fuel cell technology Handbook. USA: CRC Press; 2002.

[10] Wainwright MS. Skeletal metal catalysts. In: Ertl G, Knözinger H, Weitkamp J, editors. Preparation of solid catalysts. Wiley-VCH Verlag GmbH; 1999. p. 28—43.

[11] Bagotsky VS. Fuel cells: problems and solutions. John Wiley & Sons; 2012209—10.

[12] Sillitto SMA, Adkins NJE, Ormerod RM, Paul E, Hodgson DR. Wragg AA, editor. Characterisation of advanced Raney nickel electrocatalytic coatings produced by the direct spraying method. Rugby: Inst Chemical Engineers; 1999.

[13] Sillitto SMA, Adkins NJE, Hodgson DR, Paul E, Ormerod RM. Electrochemical testing and structural characterisation of nickel based catalytic coatings produced by direct spraying. In: Lednor PW, Nagaki DA, Thompson LT, editors. Advanced catalytic materials-1998. Warrendale: Materials Research Society; 1999. p. 23—9.

[14] Kellenberger A, Vaszilcsin N, Brandl W, Duteanu N. Kinetics of hydrogen evolution reaction on skeleton nickel and nickel-titanium electrodes obtained by thermal arc spraying technique. International Journal of Hydrogen Energy 2007;32(15):3258—65.

[15] Kellenberger A, Vaszilcsin N, Brandl W. Roughness factor evaluation of thermal arc sprayed skeleton nickel electrodes. Journal of Solid State Electrochemistry 2007;11(1):84—9.

[16] Birry L, Lasia A. Studies of the hydrogen evolution reaction on Raney nickel-molybdenum electrodes. Journal of Applied Electrochemistry 2004;34(7):735—49.

[17] Kellenberger A, Vaszilcsin N. The determination of the roughness factor of skeleton nickel electrodes by cyclic voltammetry. International Journal of Hydrogen Energy 2007;32(15):3258—65.

[18] Schiller G, Henne R, Borck V. Vacuum plasma spraying of high-performance electrodes for alkaline water electrolysis. Journal of Thermal Spray Technology 1995;4(2):185—94.

[19] Fournier J, Miousse D, Legoux JG. Wire-arc sprayed nickel based coating for hydrogen evolution reaction in alkaline solutions. International Journal of Hydrogen Energy 1999;24(6):519—28.

[20] Boruciński T, Rausch S, Wendt H. Raney nickel activated H2-cathodes part II: correlation of morphology and effective catalytic activity of Raney-nickel coated cathodes. Journal of Applied Electrochemistry 1992;22(11):1031—8.

[21] Janssen M, Rieck G. Reaction diffusion and kirkendal-effect in nickel aluminium system. Transactions of the Metallurgical Society of AIME 1967;239(9):1372—85.

[22] Bakker ML, Young DJ, Wainwright MS. Selective leaching of NiAl3 and Ni2Al3 intermetallics to form Raney nickels. Journal of Materials Science 1988;23(11):3921—6.

[23] Singleton MF, Murray JL, Nash P. Al-Ni (Aluminium-Nickel). In: Massalski TB, Okamoto H, Subramanian PR, Kacprzak L,

editors. Binary alloy phase diagrams. 1st. ed. Ohio: American Society for Metals; 1986. p. 142.

[24] Hunter RF, Hohn P. Caustic etching of aluminum with matte finish and low waste capability. U.S. Patent 509104625-Feb-1992.

[25] Watts HL, Utley DW. Volumetric analysis of sodium aluminate solutions. Analytical Chemistry 1953;25(6):864—7.

[26] Li Y, Zhang Y, Yang C, Zhang Y. Precipitating sandy aluminium hydroxide from sodium aluminate solution by the neutralization of sodium bicarbonate. Hydrometallurgy 2009;98(1—2):52—7.

[27] Correia AN, Machado SAS. Hydrogen evolution on electrodeposited Ni and Hg ultramicroelectrodes. Electrochimica Acta 1998;43(3—4):367—73.

[28] Brown IJ, Sotiris S. Electrodeposition of Ni from a high internal phase emulsion (HIPE) template. Electrochimica Acta 2001;46(17):2711—20.

[29] Caspersen M, Kirkegaard JB. Modelling electrolyte conductivity in a water electrolyzer cell. International Journal of Hydrogen Energy 2012;37(9):7436—41.

[30] Trasatti S. Electrochemical theory | hydrogen evolution. In: Garche J, editor. Encyclopedia of electrochemical power sources. Amsterdam: Elsevier; 2009. p. 41—8.

[31] Eldeab M, Awad M, Mohammad A, Ohsaka T. Enhanced water electrolysis: electrocatalytic generation of oxygen gas at manganese oxide nanorods modified electrodes. Electrochemistry Communications 2007;9(8):2082—7.

[32] Brennecke PW, Ewe HH. Hydrogen evolution of highly porous Raney nickel cathodes in alkaline electrolyte. Energy Conversion and Management 1991;31(6):585—94.

[33] Dyer CK. Improved nickel anodes for industrial water electrolyzers. Journal of the Electrochemical Society 1985;132(1):64—7.

[34] Martínez WM, Fernández AM, Cano U, Sandoval JA. Synthesis of nickel-based skeletal catalyst for an alkaline electrolyzer. International Journal of Hydrogen Energy 2010;35(16):8457—62.

[35] Herraiz-Cardona I, Ortega E, Pérez-Herranz V. Impedance study of hydrogen evolution on Ni/Zn and Ni—Co/Zn stainless steel based electrodeposits. Electrochimica Acta 2011;56(3):1308—15.

Electrochemical investigation of surface area effects on PVD Al-Ni as electrocatalyst for alkaline water electrolysis

Cecilía Kjartansdóttir[a], Michael Caspersen[b], Sune Egelund[b] and Per Møller[a].

[a] Department of Mechanical Engineering, The Technical University of Denmark
[b] Siemens A/S

Abstract

A thermo-chemical diffusion process on about 20 μm physical vapour deposited aluminium onto a nickel substrate, leads to a rapid formation of Al/Ni intermetallic layer that is particularly acceptable for dissolution of aluminium in strong alkali. The geometry and the structure of the final skeletal nickel coatings can be manipulated by altering the time interval of the diffusion. In that way the actual electrochemical surface area and, thus, the electrocatalytic activity of the coatings towards HER and OER can be influenced. Cyclic voltammetry (CV) and electrochemical impedance spectroscopy (EIS) investigations, display that the electrocatalytic surface area increases in proportion to the thickness of the developed porous nickel structure.

In the case of the HER an increase in roughness factor (R_f) from 1 (for polished Ni) to 800, results in reduction of the hydrogen overpotential of 337 mV. When further increasing R_f up to above 2000, additional 40 mV are gained. For the OER, smaller roughness values were detected with the same activity trend as for the HER. The electrocatalyst are however found not to be stable in the anodic environment during electrolysis. The corrosion mechanism of a skeletal nickel electrocatalyst during the OER in an alkaline environment is briefly discussed.

The structure and composition of the electrocatalysts are characterised by scanning electron microscopy and X-ray diffraction. The actual electrocatalytic surface area and the electrocatalytic behaviour are studied with potentiodynamic polarisation, CVs and EISs.

1   Introduction

Nickel is known for its good corrosion resistivity in strong alkali [1][2] and its relatively good oxygen and hydrogen electrocatalytic properties [3]. Nickel is therefore typically the core material used in bipolar electrodes for alkaline water electrolysis systems [4]. In 1961 Justi and Winsel [5] discovered that Raney nickel (originally developed as a catalyst for hydrogenation of vegetable oils) was an effective hydrogen electrocatalyst for alkaline electrolysis. The principle behind the Raney nickel catalysts is that Al or Zn is selectively leached from NiAl or NiZn alloys [6–8]. Lattice vacancies formed when leaching result in large surface area and high density of lattice defects, which again leads to formation of additional active sides for the electrocatalytic reaction to take place [9]. Later, many authors have published an increase in electrocatalytic activity towards the hydrogen evolution reaction (HER) by selectively leaching one or more elements from metal alloys [10–18]. One recent example is the work of Birry and Lasia [14] where Al-Ni and Al-Ni-Mo alloys were prepared by the means of pressing and heating and by vacuum plasma spraying. They reported HER overpotentials for alkaline leached Al_3Ni and Al_3Ni_2 alloys measured in 1 M KOH at 25°C to be 136 and 280 mV, respectively. They also showed that drastic reduction in overpotential could be reached by adding Mo to high aluminium containing alloys. HER overpotential of only 67 mV was measured for a plasma sprayed and alkaline leached $NiAl_{5.95}Mo_{0.66}$ alloy.

Raney nickel has also, occasionally, been proposed as a suitable electrocatalyst for the oxygen evolution reaction (OER). In almost all cases it has, independently of preparation procedure, proved to be superior to elemental nickel [19,20]. In [16] Raney nickel electrodes were prepared by plasma spraying with a mixture of Ni-Al alloy powder and Co_3O_4 particles. This procedure provided a catalyst with an oxygen overpotential reduction of approximately 150 mV when compared to plain nickel. The stability of this catalyst was later found to be acceptable when the electrodes were subjected to test in a full scale electrolyser [21]. Maunowski and Jtilich [22] reported results where Raney nickel was shown to be superior as anode catalyst when compared to other well-known and active catalysts such as $NiCo_2O_4$, Co_3O_4, $LaNiO_3$ and $La_{0.5}Sr_{0.5}CoO_3$.

In a previous study [23], porous nickel electrodes were produced by physical vapour deposition (PVD) of Al onto a nickel substrate followed by thermo-chemical diffusion and alkaline aluminium leaching. The electrodes were shown to be durable and have good cell potentials as bipolar electrodes for industrial scale alkaline water electrolysers. However, the optimal thickness of the electrocatalyst had not been studied. When producing porous nickel electrocatalyst in that manner, there is a trade-off between the thickness of the electrocatalyst and the build-up of internal stresses in the coating. During manufacturing, both the interdiffusion and the leaching procedures facilitate internal stresses which escalate in proportion to the thickness of the catalyst. If the internal stresses in the coating become excessively large, the relatively brittle Al/Ni intermetallic structure and the fragile nickel residue fail to accommodate for the stresses during heat treatment and leaching. This will lead to formation of cracks in the developed structure, diminishing the mechanical strength of the final electrocatalyst. Conversely, by increasing the thickness of the electrocatalyst a larger actual surface area can be produced. Wendt and Plzak [20] pointed out that only a limited fraction of the actual surface area of a highly dispersed structure contributes to the electrochemical reaction during electrolysis. This is because of the limited penetration of the current into the deeper pores of the structure. It is therefore important to identify the minimum thickness of a porous electrocatalyst without diminishing the electrocatalytic activity of the final product.

In the present work we investigate how the geometry and structure of a PVD Al/Ni electrocatalyst influences the actual surface area and the electrocatalytic activity towards the HER and the OER. The structure and composition of the developed electrodes is characterised by the means of a scanning electron microscope (SEM) and X-ray diffraction (XRD). The electrocatalytic activity and actual surface area are studied with potentiodynamic polarisation, cyclic voltammetry (CV) and electrochemical impedance spectroscopy (EIS).

2   Experimental

2.1 Preparation of electrodes

The electrodes were produced by PVD of aluminium onto a 0.5 mm thick nickel plate (99 wt.%). The nickel plate was cathodically degreased for two minutes prior to the PVD process. The Al PVD was prepared in a non-reactive DC-magnetron sputtering mode using a CC800/9 SinOx coating unit from CemeCon AG. In order to remove nickel oxide from the surface, the nickel was heated and etched in situ by argon sputtering prior to the sputtering process. The thickness of the aluminium coating was about 20 μm. The aluminium deposited nickel plates where cut to form three 25×25 mm coupons, suitable for XRD measurements and electrochemical measurements, and seven 15×10 mm coupons, suitable for microscopy investigations. The coupons were then heat treated and selectively aluminium leached as outlined in table 1.

Treatment	Ref. Name	25×25 mm coupons	15×10 mm coupons
No treatment	AlNi	-	x
10 min at 610 °C	AlNiHT10	-	x
10 min at 610 °C + leaching	AlNIHT10+L	x	x
20 min at 610 °C	AlNIHT20	-	x
20 min at 610 °C + leaching	AlNIHT20+L	x	x
30 min at 610 °C	AlNIHT30	-	x
30 min at 610 °C + leaching	AlNIHT30+L	x	x

Table 1: Outline of the heat and leaching treatments for the PVD aluminium deposited nickel coupons.

The heat treatments were prepared in an atmospheric furnace. The selective aluminium leaching procedure was performed in 30% KOH and 10% $KNaC_4H_4O_6*4H_2O$ at 80 °C with stirring for 24 hours.

2.2 Structural characterisation and composition

The un-leached 15×10 mm coupons, listed in table 1, were hot-mounted in PolyFast from Struers, ground down to 4000 grit and subsequently polished with 3 and 1 μm diamonds. In order not to damage the porous surface of the leached coupons during mounting, more delicate mounting process was selected. The leached 15x10 mm coupons were cold mounted in epoxy from Struers via vacuum impregnation. The cold mounted specimens were grinded down to 4000 grit, subsequently polished with 3 and 1 μm diamonds and mechanical/chemical polished with 0.04 μm colloidal silica.

All the prepared specimens listed in table 1 were investigated in TM 3000 Tabletop scanning electron microscope from Hitachi. An integrated energy-dispersive X-ray spectroscopy (EDS) was utilised for elemental analyses. Phase analyses were performed via grazing incidence (GI) XRD on a Bruker AXS, D8-Discover with Cu K_α radiation. The GI angel was selected to be 6 degrees for all the specimens.

2.3 Electrochemical measurements

The electrocatalytic activity of the developed electrodes was evaluated by means of anodic and cathodic potentiodynamic polarisation, CV and EIS. The measurements were carried out using a Gamry Reference 3000 potentiostat. A typical three-electrode electrochemical cell made of Teflon and was used for the electrochemical measurements. The cell contained an Hg/HgO reference electrode from Radiometer Analytical and a counter electrode of pure nickel. The electrolyte consisted of 1 M KOH and the measurements were carried out at 25 °C. The potentiodynamic and cyclic voltammetry measurements were IR-compensated by the means of current interruption. All following half-cell potentials are reported vs. Hg/HgO.

The experimental procedure for the cathodic polarisation curve was as follows: conditioning at -1.015 V for 30 minutes, open circuit potential (OCP) until 0.01 mV/sec stability followed by a cathodic sweep from -0.615 V to -1.415 V at a scan rate of 1 mV/s.

The electrocatalytic active surface area of the electrodes was determined by the amount of nickel hydroxide formed during cyclic voltammetry. For the cathodic reaction, CV measurements were performed from -1.0 V to -0.2 V at a scan rate of 50 mV/s. In order to eliminate the amount of hydrates from the surface, the electrodes were conditioned at -1.015 V for 5 minutes prior to the measurements. Following the CV, EIS was used for determination of double layer capacitance as a measure for the electrochemical active surface area.

The measurements were conducted between 100 mHz and 100 kHz at a potential of -1.1 V with an AC amplitude of 3 mV.

In the case of anodic measurements the procedure was initialised by a 30 min. polarisation at -0.943 V, in order to facilitate a stable NiO structure. Thereafter, a CV between -0.943 and 0.68 V at the scan rate of 50 mV/s was recorded. Each CV measurement was cycled 10 times in order to obtain reproducibility. The CV measurements on the samples was designated CV_{before}. The CV_{before} was followed by a 5 min conditioning at 0.285 V, being approximately the theoretical OER potential. A steady state measurement was then recorded from 0.285 V to 0.80 V at a scan rate of 1 mV/s in order to measure the OER activity. In order to look for structural changes this measurement was followed by a second 5 min conditioning and CV, designated CV_{after} using the same parameters as previously.

For comparison, anodic and cathodic potentiodynamic polarisation, CV and EIS investigations were prepared on a 25×25 mm, 3 μm diamonds polished, nickel plate (99 wt.%).

3 Results and discussions

3.1 Structural characterisation and composition

The as-deposited stage

The aluminium deposit obtained from the PVD process is characterised with columnar crystal structure. The columnar grains are small in width, < 1μm, close to the substrate and become larger as the deposited layer grows, further away from the substrate. This is verified with a cross section micrograph of a broken Al PVD coated silicon wafer deposited simultaneously with the nickel substrate in the present work, see fig. 1.
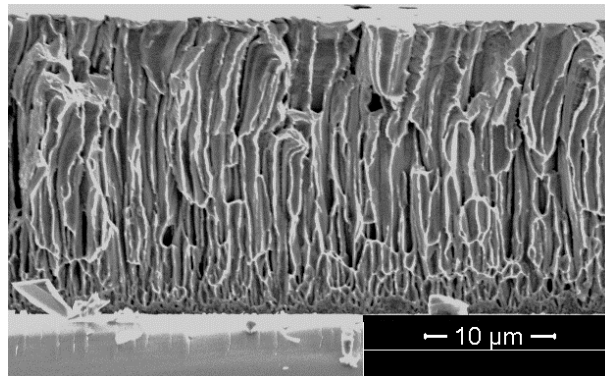
Fig 1: Cross section micrographs of a physical vapour deposited aluminium on top of a silicon wafer. The silicon wafer is broken mechanically. The micrograph reveals the columnar structure of the deposit. Courtesy of the Technological Institute of Denmark.

Thermo-chemical diffusion

Fig. 2 shows cross section back scatter electron (BSE) micrographs of the PVD Al deposited nickel substrates, as-deposited and after 10, 20 and 30 minutes of heat treatment. The EDS analyses from the cross section micrographs are listed in table 2.
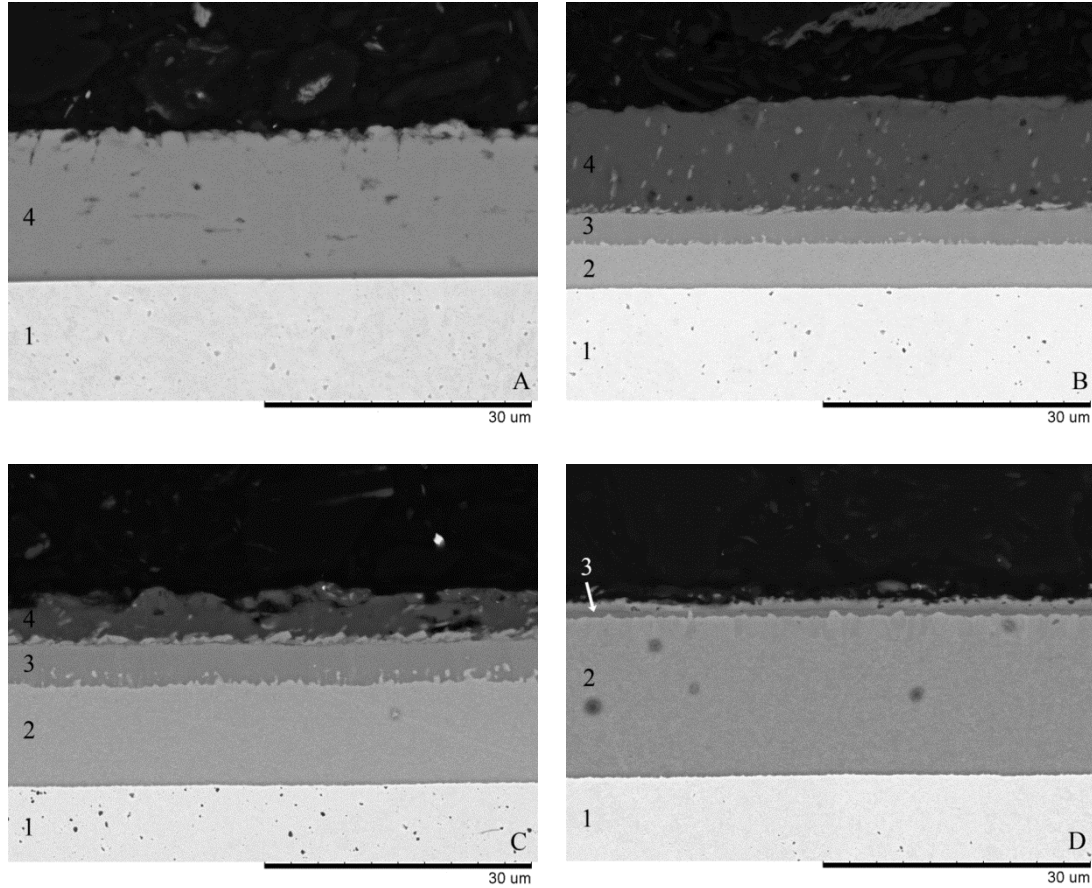
Fig 2: Cross section BSE micrographs of the PVD Al/Ni coatings before and after 10, 20 and 30 min. heat treatments A) as deposited [AlNi], B) 10 min. heat treatment [AlNiHT10], C) 20 min. heat treatment [AlNiHT20] and D) 30 min. heat treatment [AlNiHT30]. The numbers refer to the EDS analyses reported in table 2.

(EDS no) Phase	AlNi		10 min. heat treatment					20 min. heat treatment					30 min. heat treatment				
			AlNiHT10		AlNiHT10+L			AlNiHT20		AlNiHT20+L			AlNiHT30		AlNiHT30+L		
	Al wt.%	Ni wt.%	Al wt.%	Ni wt.%	O wt.%	Al wt.%	Ni wt.%	Al wt.%	Ni wt.%	O wt.%	Al wt.%	Ni wt.%	Al wt.%	Ni wt.%	O wt.%	Al wt.%	Ni wt.%
(1)Ni	-	100	-	100	-	-	100	-	-	-	-	100		100	-	-	100
(2)Al$_3$Ni$_2$	-	-	41	59	17	4	79	38	61	12	5	83	37	62	18	4	78
(3)Al$_3$Ni	-	-	55	45	12	-	88	57	42	9	2	89	59	41	11	3	86
(4)Al	100	-	98	2	-	-	-	97	3	-	-	-	-	-	-	-	-

Table 2: Results from the cross section EDS analysis on the specimens in fig. 2 and fig. 5. All elements from the periodic table are analysed.

Relating the EDS results with the Al-Ni binary alloy phase diagram, the diffusion layer no. 2 is predicted to mainly consist of the Al_3Ni_2 phase and layer no. 3 of the Al_3Ni phase. The XRD analyses on the heat treated samples (fig. 3) verify the existence of the Al_3Ni and Al_3Ni_2 phases in the PVD Al-Ni diffusion couples.

Fig. 3: GI X-ray diffractograms for the PVD Al-Ni couples after various times of heat treatments. (•) Al, (∆)Ni, (∗) Al_2O_3 , (◊) Al_3Ni (∇) Al_3Ni_2. JCPDS card-numbers 4-787, 4-850, 46-1212, 3-1052 and 2-416. The incident angel is 6 degrees for all the tested specimens.

A part from the two intermetallic phases, pure nickel and aluminium peaks are detected. The intensities of the aluminium peaks are the largest for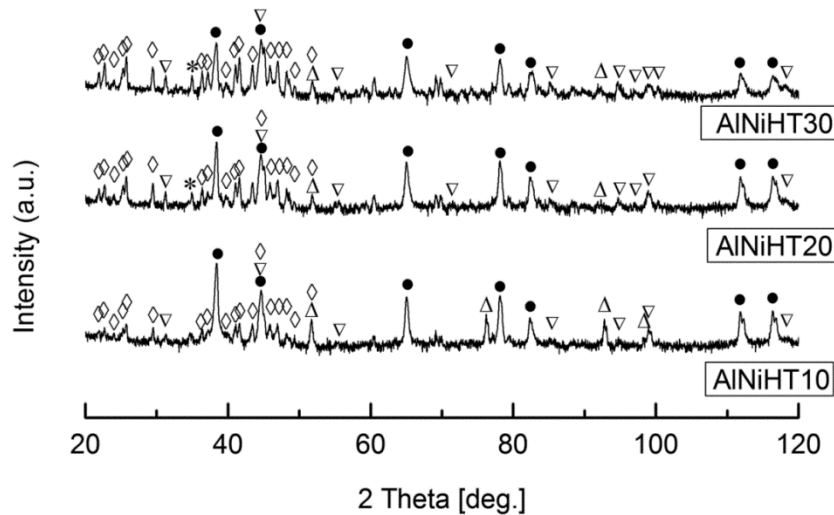 the shortest diffusion time, as expected. The Al_3Ni and Al_3Ni_2 signals get more pronounced in proportion to diffusion time. The only non-overlapping pure nickel peak is to be found at about 93 degrees 2θ. The highest intensity is for 10 min. of diffusion, where nickel has had the least time to diffuse into the structure. This is presumably scattering signals from the nickel substrate due to the high penetration depth of x-rays in pure aluminium, resulting in larger amount of scattering from the substrate. Hence, no assumptions can be made about the amount elemental nickel in the diffusion layers from the XRD analyses alone.

When the existence of the Al_3Ni_2 and Al_3Ni phases in the interdiffused layers has been verified, the following can be identified from the micrographs in fig. 2. After 10 min. of heat treatment about 5 μm Al_3Ni_2 and 4 μm of the Al_3Ni intermetallic phases are formed. In the remaining aluminium, closest to the top surface, particles with higher Z contrast (larger atomic number) compared to the surrounding aluminium are observed. This indicates diffusion of nickel containing particles into the PVD aluminium coating. Moreover, the ragged interface of layer 2 into layer 3, and layer 3 into layer 4, seen fig. 2b and c, indicate that the diffusion mechanism is mainly controlled by the movement of nickel-rich phases into the aluminium and aluminium-rich phases. These findings are in contrast with the observations of M. Jansssen and G. Rieck [24], where only aluminium was found to take part in the diffusion mechanism for Ni-Al couples at temperatures at about 600 degrees. It is however well known that grain boundaries provide high diffusivity paths in metals and that diffusion along grain boundaries is in order of magnitude faster than bulk diffusion [25].

According to Harrison's classification of the diffusion kinetics [26], diffusion may be considered to take place only within the grain boundaries at short diffusion times/and or when the volume diffusion coefficient is much smaller than the grain boundary diffusion coefficient. Due to the large columnar structure of the aluminium deposits, one or both of this mechanism do evidentially take place during heat treatments of the PVD aluminium deposited nickel specimens. One could moreover imagine that as the concentration of the nickel builds up in the grain boundaries, nickel atoms start to diffuse from the boundary into the aluminium bulk contributing to the formation of the Al_3Ni and later the Al_3Ni_2 phase. Over time the diffusion characteristic changes from being grain boundary diffusion controlled into being volume diffusion controlled and competition between the formation of Al_3Ni and Al_3Ni_2 takes place. From the experiments of Castleman and Seigle [27] the diffusion coefficient of Al_3Ni and Al_3Ni_2 are found to be 1.8×10^{-11} and 9.1×10^{-10} cm^2/sec, respectively. Hence, the Al_3Ni_2 phase grows faster than the Al_3Ni phase and therefore, for structures with limited aluminium sources, when heat treated for long enough time the Al-Ni diffusion film will consist solely of the Al_3Ni_2 phase. This is in agreement with the results shown in fig. 2 where the Al_3Ni_2 phase increases with extended time of heat treatment. For 20 minutes of heat treatment about 5 µm of Al_3Ni and 11 µm Al_3Ni_2 is formed. When heat treated for 30 min. no aluminium is left on the top surface and almost all the diffused layer is transformed into the Al_3Ni_2 phase, resulting in about 18 µm Al_3Ni_2 and 2 µm of Ni_3Al.

Selective leaching of aluminium

Fig. 4 and 5 show surface and cross section BSE micrographs of the heat treated specimen after selectively alkaline leaching of the aluminium. The EDS analyses on the leached cross sections in fig. 5 are listed in table 2.
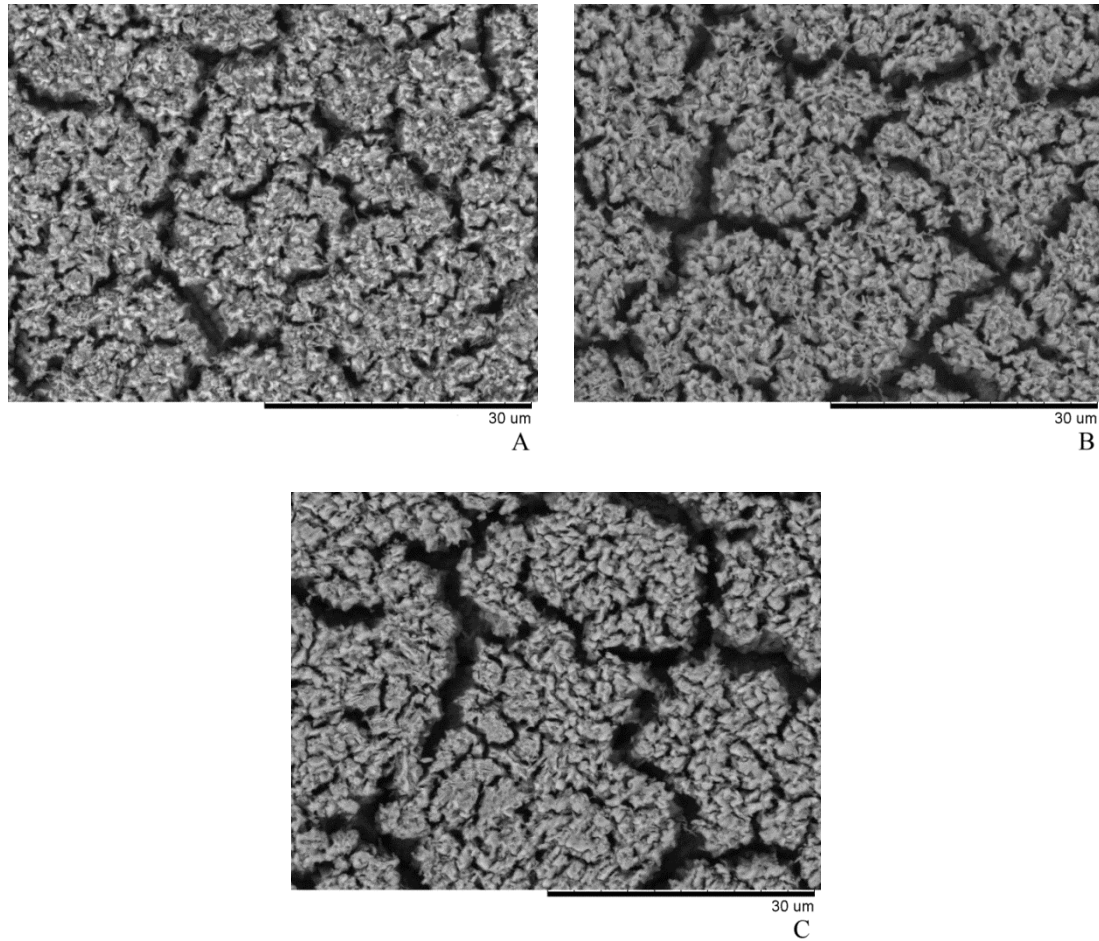

Fig. 4: Surface BSE micrographs of the PVD Al/Ni coatings after 10, 20 and 30 min. heat treatment and leaching. A) AlNiHT10+L, B) AlNiHT20+L and C) AlNiHT30+L.
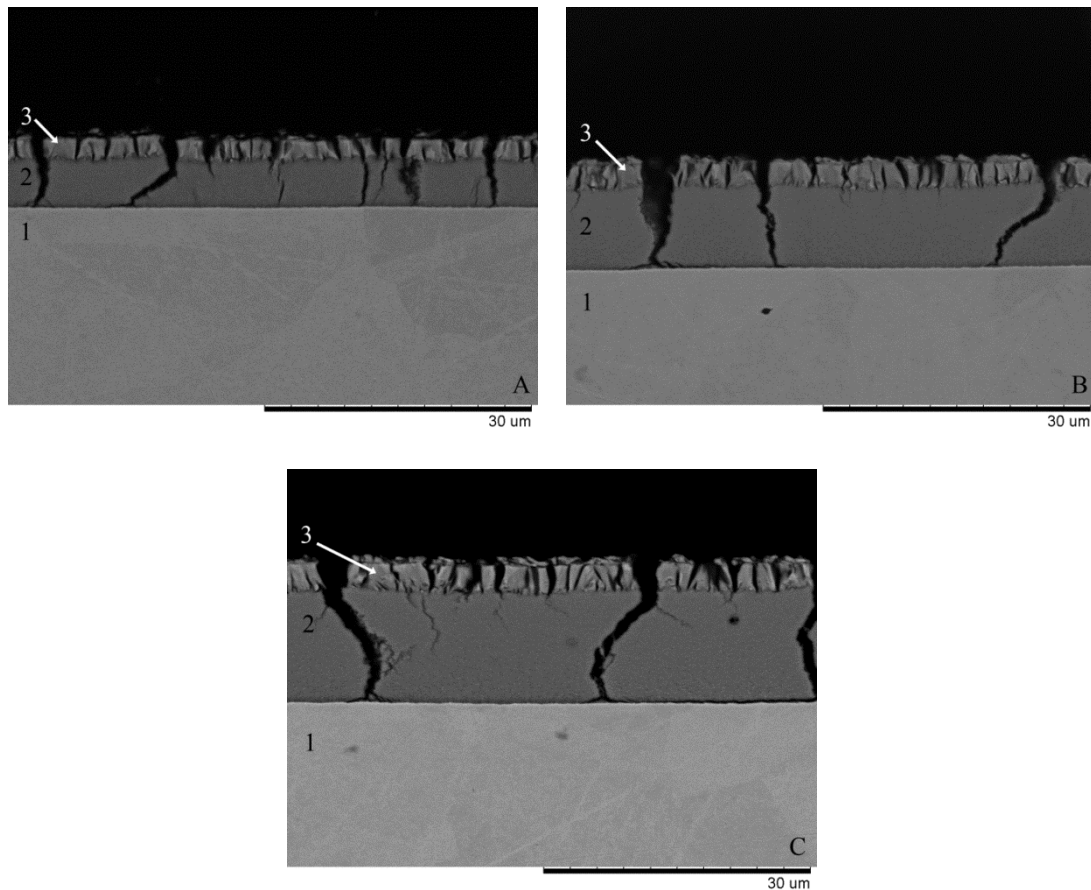
Fig. 5: Cross section BSE micrographs of the PVD Al/Ni coatings after 10, 20 and 30 min. heat treatment and leaching. A) AlNiHT10+L, B) AlNiHT20+L and C) AlNiHT30+L. The numbers refer to the EDS analyses reported in Table 2.

The surface micrographs indicate that the top structure is highly porous. It is evident, from the surface and cross section micrographs, that the cracks perpendicular to the surface become larger for extended heat treatments, the cracks are seen as macro pores in the surface micrographs. As there are no cracks in the structure after heat treatment, the cracks are obviously formed during leaching. The cracks are presumably due to shrinkage of the lattice during leaching resulting in tensile stresses in the structure. The internal stresses in the Al_3Ni_2 layer evidently increase in proportion to the layer thickness.

At the available magnification, for the cross section images in fig. 5, no pores in the leached Al_3Ni_2 structure are visible. However, the finding of oxygen and the reduction of aluminium, from about 40 wt.% aluminium for the un-leached sample to only 5 wt.% for the leached sample, indicate that the leached Al_3Ni_2 phase is porous as well. Due to the larger amount of aluminium in the initial Al_3Ni structure, the leached nickel residue becomes considerably more macro porous, compared to the leached Al_3Ni_2 structure. It is noteworthy that the residue aluminium after leaching is significantly less in the present specimens compared to the previous published study [23], where the PVD Al/Ni electrodes were heat treated for 24 hours. In that study, 15 wt.% aluminium residue was observed in the skeletal nickel structure. The deviation in aluminium content is, thus, probably due to grain growth of the Al_3Ni_2 crystallites during longer annealing time. The larger Al_3Ni_2 crystal structure is evidently not as prone to alkaline leaching as the present one.

XRD diffractograms from the heat treated and leached samples are shown in fig. 6.
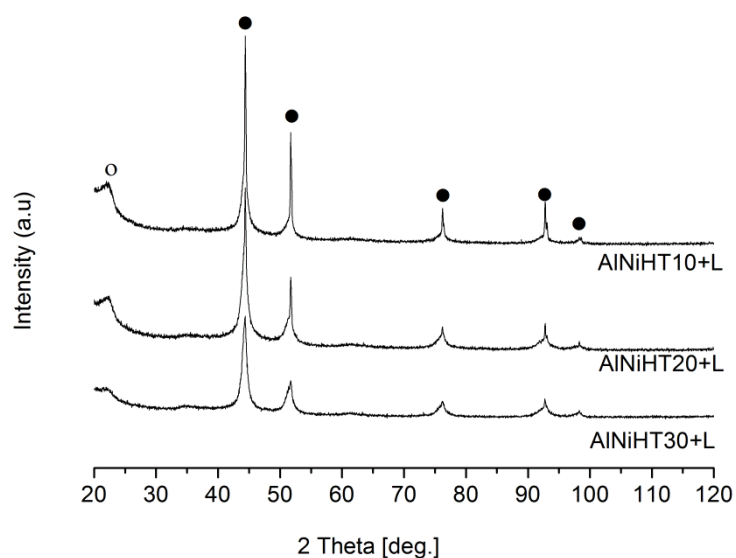
Fig. 6: GI X-ray diffractograms for PVD Al/Ni coatings after 10, 20 and 30 min. heat treatment and selective aluminium leaching. The incident angel is 6 degrees for all the specimens. (●) Ni, (o) K. JCPDS card-numbers 4-850 and 40-994.

After the leaching procedure, only nickel peaks and potassium peaks, from the leaching procedure, are identified in the diffractograms. This confirming that most of the aluminium has been leached from the intermetallic structures as indicated in the EDS analyses. The intensity of the nickel peaks is the largest for the thinnest sample, 10 min. heat treatment, indicating some scattering from the nickel substrate.

3.2 Electrochemical Measurements

3.2.1. Cathode

Cyclic Voltammetry

The initial cyclic voltammograms for polished nickel and the heat treated and leached coatings are shown in fig. 7 and fig. 8.
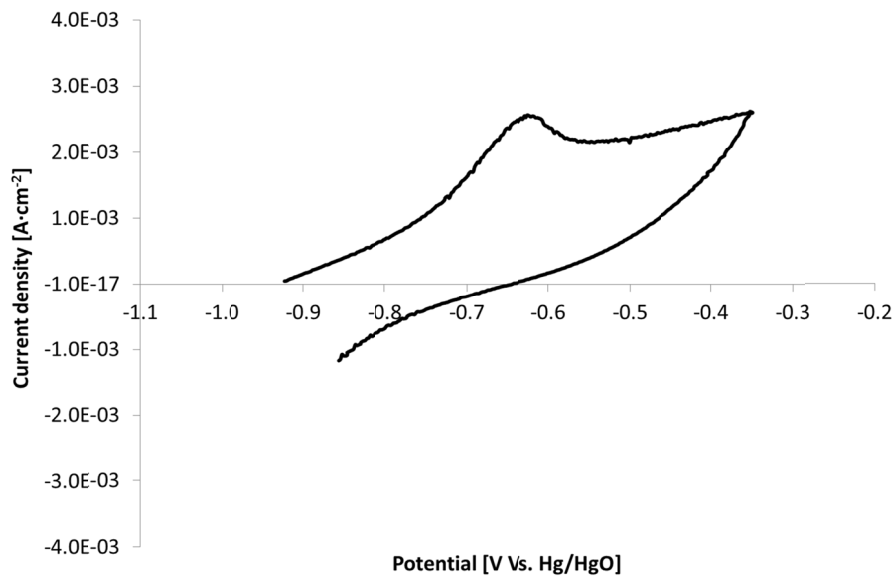
Fig. 7: Cyclic voltammogram recorded on polished Ni. The anodic peak represents the oxidation of Ni to α-Ni(OH)$_2$.
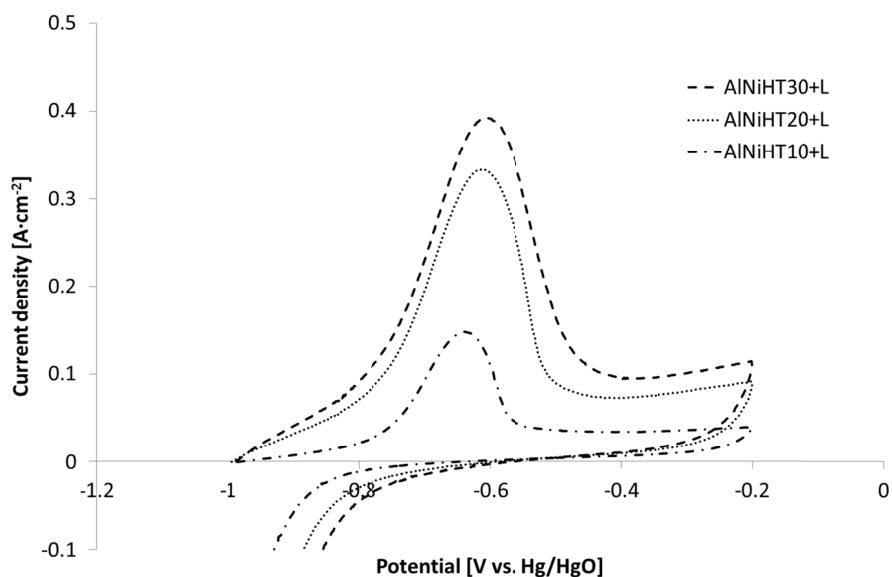
Fig. 8: Cyclic voltammograms recorded on the PVD Al/Ni coatings after heat treatment for 10, 20 and 30 min. and selective aluminium leaching. The anodic peak represents the oxidation of Ni to α-Ni(OH)$_2$.

A characteristic of evaluating the roughness factor using CV is that the electrochemically active surface area is measured, that is the surface that can exchange electrons with the electrolyte. Unlike the Brunauer-Emmett –Teller theory (BET), where the physical absorption of gas on the surface is measured. Accordingly, the CV method seems more appropriate considering the application of the electrocatalytic coating. The peak for formation of Ni → α-Ni(OH)$_2$ is used for the evaluation and area under the curve, i.e. the charge associated with the formation of α-Ni(OH)$_2$, was integrated by the means of Gamry Echem Analyst software. In order to calculate the roughness factor the values for each electrode, shown in table 3, were compared to the measured charge of 514 µC·cm^{-2} for a polished nickel electrode established elsewhere [28]. The fact that the

area under the curve in fig. 7 does not equal 514 $\mu C \cdot cm^{-2}$ is due to small residue roughness after polishing and uncertainties from measurements.

Electrode	Charge [$C \cdot cm^{-2}$]	R_f [$cm^2 \cdot cm^{-2}$]	Tafel slope [$mV\ dec^{-1}$]	$\eta_{HER\ @}\ 100$ [$mA\ cm^{-2}$]
Polished Ni	574E-6	~1	150	508
AlNiHT10+L	492E-3	~800	95	171
AlNiHT20+L	955E-3	~1900	82	131
AlNiHT30+L	1156E-3	~2200	76	123

Table 3: Results from the cathodic CVs and potentiodynamic polarisations recorded on the PVD Al/Ni coatings compared to polished Ni. The theoretical potential of HER is estimated to be -943 mV vs. Hg/HgO.

The values state the trend from SEM images in fig. 5, that a significant leachable diffusion zone can be obtained from very short thermal treatments and that the formed intermetallic phases increase rapidly due to the fast diffusion properties of the PVD coating. What is not clear though from the BSE micrographs is how the surface area increases according to longer soaking time – the fast diffusion kinetics thus gives an effect within only 10 min, but as seen from AlNiHT20+L and AlNiHT30+L longer diffusion time further maximizes the surface area.

Steady-State Potential Dynamic Sweep

Steady-state voltammetry was applied for measuring the electrochemical activity of the developed electrodes. The potential was swept over a range comprising the current densities traditionally used in industrial alkaline electrolysers [4]. The observed trend from cyclic voltammetry is manifested in fig. 9.
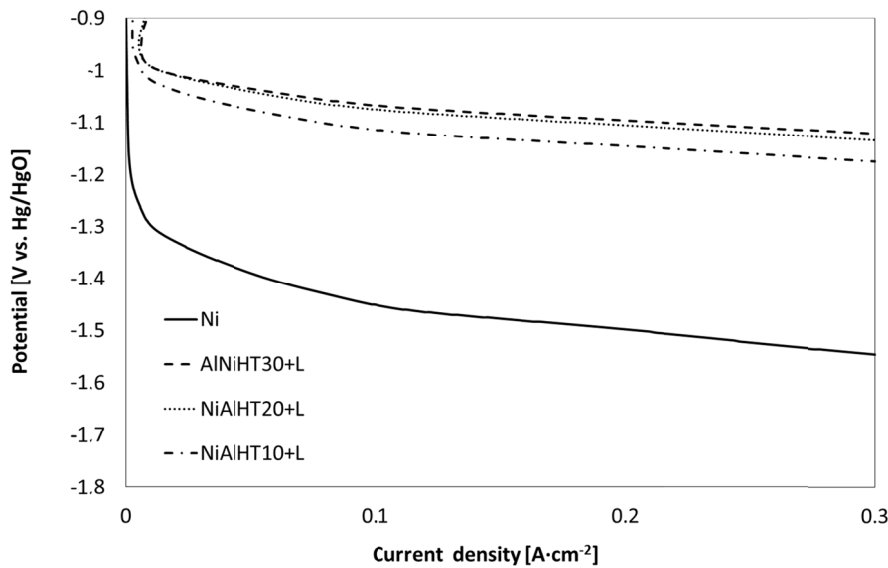
Fig. 9: Cathodic potentiodynamic polarisations recorded on the PVD Al/Ni coatings and polished Ni in 1 M KOH at 25°C.

All three electrodes show much improved catalytic activity for the HER, as compared to polished nickel, showing a reduction in overpotential of 337 mV for AlNiHT10+L to 385 mV for AlNiHT30+L. In between lays AlNiHT20+L closer to the AlNiHT30+L results, as could be expected from R_f values. Hence, there seems to be an agreement between measured surface area and electrochemical activity.

From fig. 9 it is noteworthy that the decline of the Tafel slope, associated with the reaction mechanisms for the HER [3,29], is significantly altered when comparing the three samples to polished nickel, i.e. the intrinsic properties of the coatings seem to differ from pure nickel. It is evident, however, that the number of available reaction sites is the predominant factor for the increase in catalytic activity. The Tafel slopes for the cathodic potential sweeps as well as overpotentials for HER are shown in table 3.

Electrochemical Impedance Spectroscopy measurements

In order to assess the electrocatalytic properties of the electrodes, impedance spectra were analysed for all the electrodes. Electrochemical impedance spectroscopy conducted at -1.1V (Vs. Hg/HgO) revealed electrocatalytic differences between the processed electrodes. In fig. 10 a Nyquist plot for polished nickel is seen while plots for NiAlHT10+L, NiAlHT20+L and NiAlHT30+L are collected in fig. 11.

Fig. 10: Nyquist plot from impedance spectra recorded on polished nickel at a potential of -1.1 V.
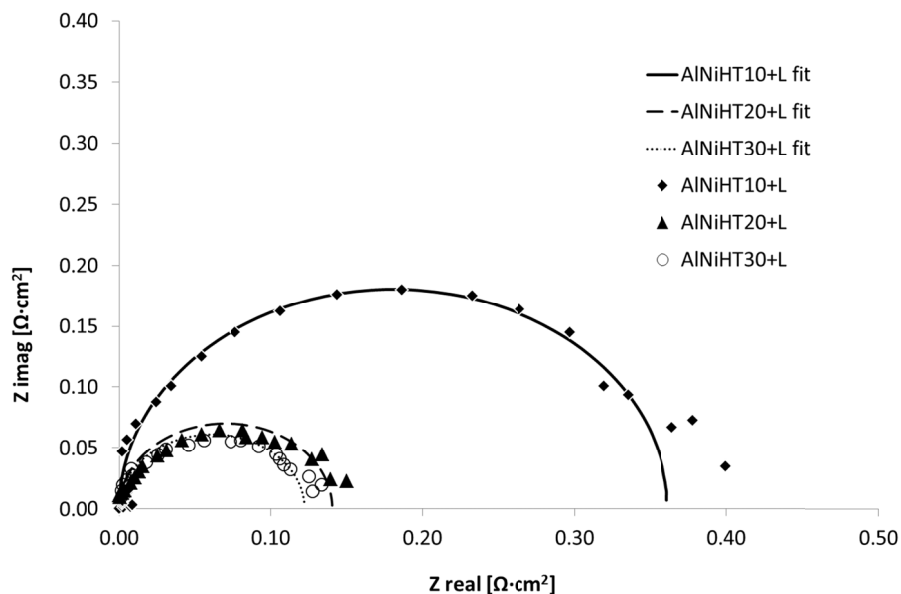
Fig. 11: Nyquist plots from impedance spectrum recorded on the PVD Al/Ni coatings at a potential of -1.1 V.

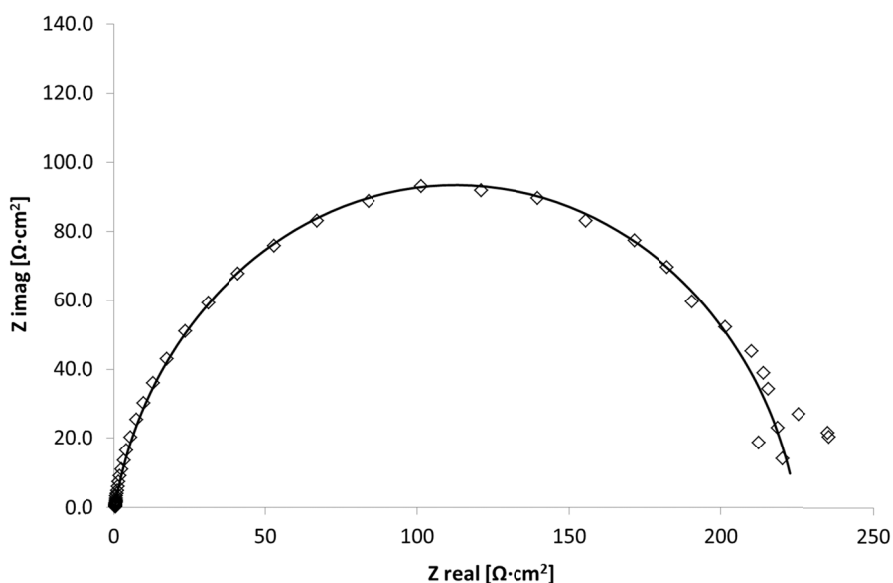All three impedance spectra produced arcs which could be satisfactorily fitted to the electric equivalent circuit (EEC). At higher frequencies a slight distortion seems noticeable, without any indications of a second arc, though. Observing and fitting of multiple arcs at higher frequencies has been made by other authors [30] and is normally associated with characteristics of the coating itself from one arc, while the second is related to the HER (or OER). As for the purpose of this study it is not found relevant to increment to higher frequencies.

Since only a single arc appears in the complex-impedance-plot the characteristics of each electrode were described by an EEC based on a single time constant model used for fitting parameters, i.e. the classic Randles EEC seen in fig. 12. Here, R_{CT} is the charge transfer resistance associated with the working electrode, R_e is the (ohmic) resistance of the electrolyte and C_{dl} is the double layer capacitance of the electrocatalyst.
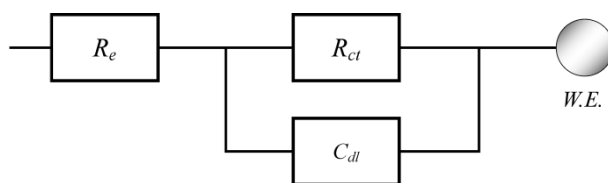
Fig. 12: Randles EEC used for fitting EIS parameters

The choice and fitting procedure of EEC is of course critical in order to correctly describe the non-ideal situation at hand. The single time-constant model is a widely used empirical model to account for the non-ideal behaviour of the capacitive elements due to different physical phenomena such as surface heterogeneity resulting from surface roughness, impurities, dislocations etc. [31]. The roughness factor has been calculated from a comparison with the capacitance measured from a plane nickel surface [32] showing a value of $25\mu F \cdot cm^{-2}$. The catalytic parameters obtained from the Randles EEC from the developed electrocatalysts are summarized in table 4.

Electrode	R_e [Ohm·cm^2]	R_{ct} [Ohm·cm^2]	C_{dl} [F cm^{-2}]	R_f
Polished Ni	565e-3	220	1.490e-4	6
AlNiHT10+L	368e-3	362e-3	4.409e-2	~900
AlNiHT20+L	478e-3	140-3	9.847e-2	~2000
AlNiHT30+L	457e-3	122e-3	11.34e-2	~2300

Table 4: EIS fitting parameters from Randles EEC data recorded on the PVD Al/Ni coatings and polished Ni.

Again, the deviance from 1 for polished nickel is ascribed to measurement uncertainties and small residue roughness after polishing. The roughness values for the developed electrodes attained from the EIS measurements are evidently in agreement with the results from the CV investigations.

3.2.2. Anode

Cyclic Voltammetry

Fig. 13 and fig. 14 show a comparison of the cyclic voltammograms for the heat treated and leached coatings, recorded prior and after a steady state measurement.
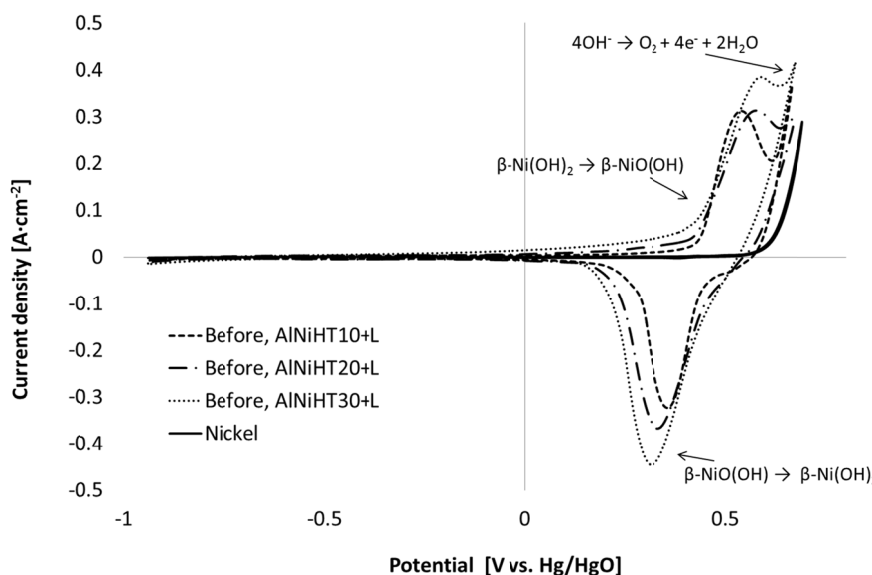
Fig. 13: Cyclic voltammograms recorded on the developed electrocatalytic coatings prior the anodic potentiodynamic measurements compared with polished Ni.
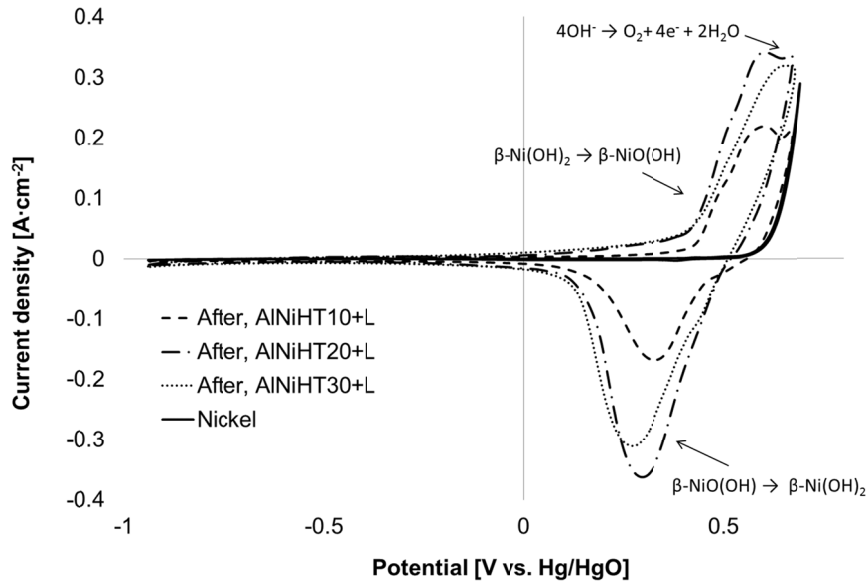
Fig. 14: Cyclic voltammograms recorded on the developed electrocatalytic coatings after the anodic steady state potential dynamic sweeps recorded compared with polished Ni.

All three tested electrodes show well defined and symmetrical peaks for the reduction of oxy-hydroxide, β-NiOOH $\rightarrow$ β-Ni(OH)$_2$ [33]. For all three samples an individual peak was also observed on the scan towards more positive potentials indicating reversibility of the reaction.

A pronounced anodic peak was found. This is accepted as the reversible Ni(II) $\rightarrow$ Ni(III) transformation, generally written as [34]:

β-Ni(OH)$_2$ + OH$^-$ $\leftrightarrow$ β-NiO(OH) + H$_2$O + e$^-$
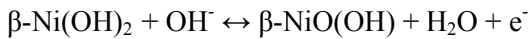
The reaction is followed by O$_2$ evolution which in the case of alkaline media is [35,36];

4OH$^-$ $\rightarrow$ O$_2$+4e$^-$ + 2H$_2$O.
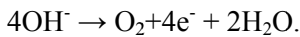
Fig. 13 shows the before CVs for all three samples compared with nickel. When comparing the before CVs with the non-porous nickel, an increase in β-NiO(OH) $\rightarrow$ β-Ni(OH)$_2$ charge were observed. By integration an increase of the charge associated with the reduction was found to be in the following order; polished nickel > 10 min > 20 min > 30 min, see table 5.

Electrode	Charge [C·cm^{-2}]	R_f [cm^2·cm^{-2}]	$\eta_{OER \, @ \, 100}$ [mA cm^{-2}]
Polished Ni	1.3E-3	~1	412
AlNiHT10+L	643E-3	~500	338
AlNiHT20+L	983E-3	~750	347
AlNiHT30+L	1429E-3	~1100	340

Table 5: Results from the anodic CV$_{before}$ and potentiodynamic polarisations recorded on the PVD Al/Ni coatings compared to polished Ni. The theoretical potential of OER is estimated to be 286 mV vs. Hg/HgO

This was found to be in agreement with visual inspections of the coatings thicknesses as discussed earlier. The porous electrodes have active surface areas in the order of 500 – 1100 times polished nickel. Other authors state that peak charge for the Ni(OH)$_2$ $\rightarrow$ NiOOH transition is in the order of 0.7 – 1.0 mC cm^{-2} which corresponds to oxidation of a monolayer on a smooth nickel surface [37],[38].

The proposed explanation for finding lower roughness factor values by looking at β-NiO(OH) $\leftrightarrow$ β-Ni(OH)$_2$ peak charges, compared to what was found via Ni $\leftrightarrow$ α-Ni(OH)$_2$, is either poor utilization of the inner branched structure of the high surface coating or a blockage with hydrated oxides of the in-depth nanostructure. The formation of hydroxide takes place as a consequence of the initial hydration of NiO upon un-polarized immersion in the electrolyte [38,39].

From the CVs recorded after the steady state experiment the charge tendency changed and the following order of anodic charge was observed; Ni > 10 min >30 min >20 min (fig. 14). It is believed that this inconsistency was caused by partial delamination of the coating which also was found on post-SEM images as illustrated in fig. 15.
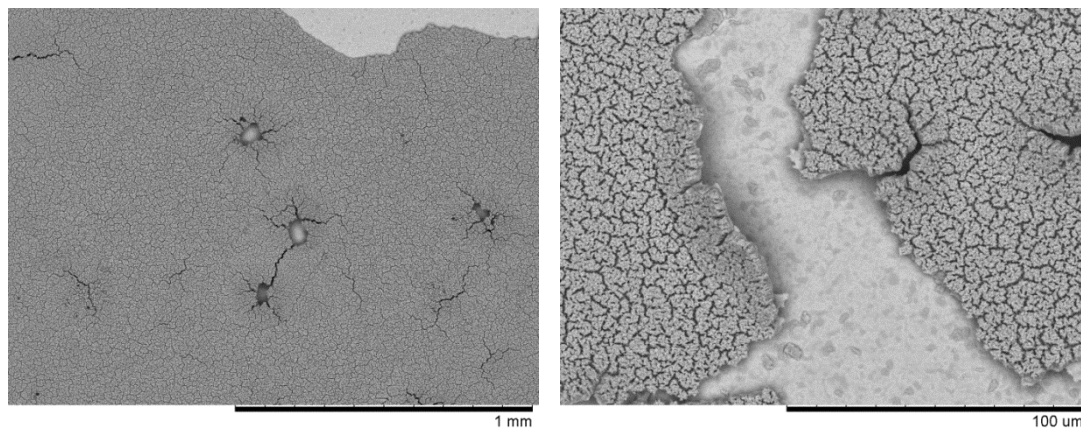
Fig. 15: AlNiHT20+L to the left, AlNiHT10+L to the right, subsequent to the OER characterization. Illustration of separation of phases.

Even after the steady state experiments all samples indicated a significantly higher charge associated with the direct oxidation of β-NiOOH, compared to non-porous nickel. This could be caused by at least two things; the first being that the coating is only partially delaminated and the second being that the underlying NiAl phase has some beneficial electrocatalytic properties compared to polished Nickel. The delamination for the 10 min sample is shown in fig. 15.

Steady-State Potential Dynamic Sweep

The anodic catalytic activity measurements are shown in fig. 16 where the steady state characterization for the electrodes is presented in comparison with polished nickel. The order of activity corresponds to what was observed by the evaluation of the charge associated with the anodic peak from the after-CVs.
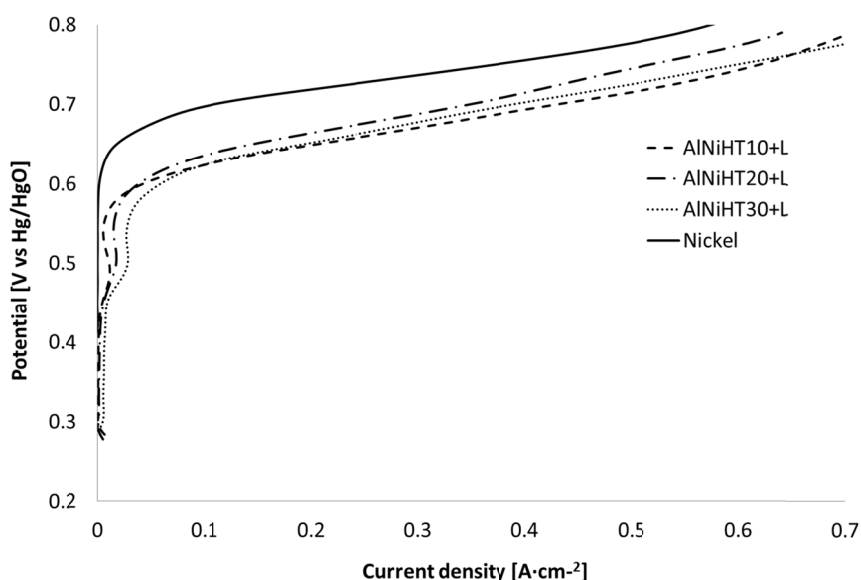
Fig. 16: Anodic potentiodynamic polarisations recorded on the PVD Al/Ni coatings in 1 M KOH at 25 °C.

The overpotential for these coatings was found to be 340 mV, at 100 mA/cm^2, compared to 412 mV for polished nickel. The order of magnitude for the found overpotentials does seem reasonable low compared to what is found in literature. A list of overpotentials for well-known OER catalysts can be found in i.e. [3,40]. The recorded overpotentials are listed in Table 5.

Corrosion mechanism during the OER

With basis in the observed delamination a mechanism involving the initial corrosion of the coating interface is proposed. We believe that the phase transition interface is a weak skeletal zone which upon anodic polarisation corrodes because of one or both of the following corrosion mechanisms:

a) Initial dissolution of nickel due to low Ni-ion concentrations in the electrolyte.

b) Localised acid formation inside the porous structure during oxygen evolution.

The former mechanism (a) the corrosion could take place as follows. Initially, when the anode is placed in the electrolysis cell no nickel ions are present in the electrolyte. Under these conditions, nickel is not thermodynamically stable at zero potential and during the OER and the electrode corrodes according to:

$Ni + 3OH^- \rightarrow Ni(OH)_3^- + 2e^-$

This can be seen from the E-pH diagram in fig. 17 for nickel ionic concentration at $1e^{-6}$ m.
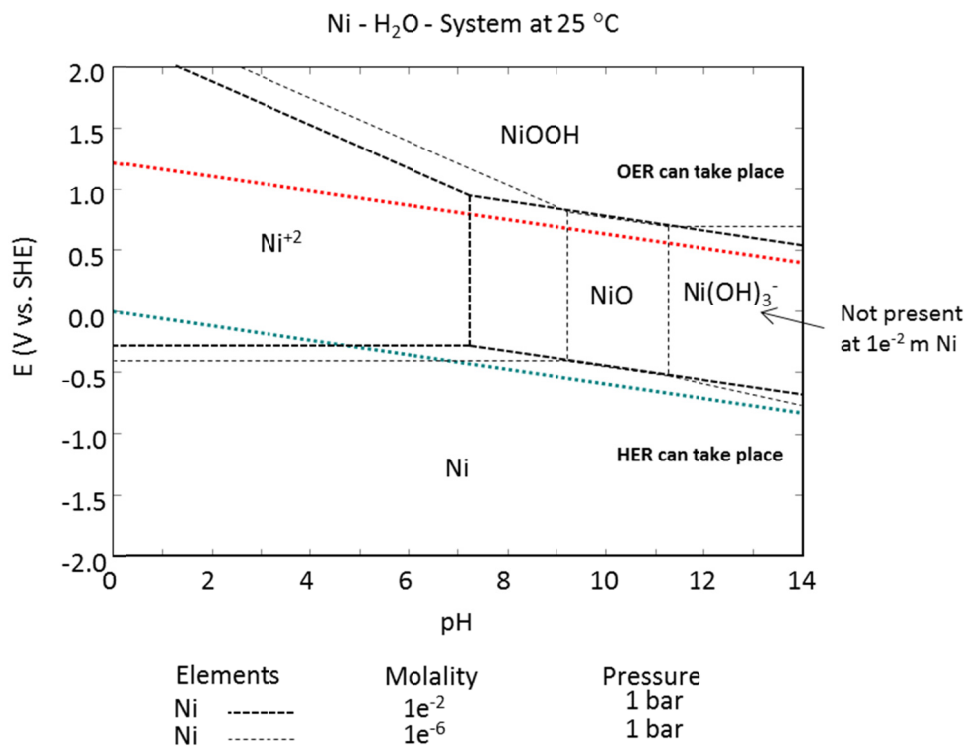
Fig 17: E-pH diagram showing thermodynamics of Ni in an aqueous solution, calculated for 1 atm., 25°C with Ni molality of $1e^{-6}$. and of $1e^{-2}$.

However, the kinetics of the nickel dissolution is most likely not fast close to zero potential. Nevertheless as the current is raised to more positive values, current is applied between the electrodes, the corrosion mechanism gets accelerated by the OER. Thus, the concentration of nickel ions within the boundary region increases and corrosion is slowed down and eventually stopped. This is evident by looking at the E-pH diagram for nickel ionic consecration at $1e^{-2}$ m where $Ni(OH)_3^-$ cannot be formed. Hence, only NiO is present in the region between Ni and NiOOH.

For the latter mentioned corrosion mechanism (b) it is supposed that when protons are formed during OER according to:

$2H_2O \rightarrow O_2 + 4H^+ + 4e^-$
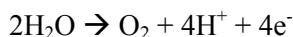
This reaction, which corresponds to the OER reaction in acidic water electrolysis, is a consequence of disturbance from oxygen bubbles on OH⁻ migration into the inner active sites of the catalyst. As a result the

pH is locally decreased. As this happens the skeletal zone is further weakened and corrosion will ultimately lead to delamination.

The proposed result is that the electrolyte in the pores becomes locally acidic and the Al_3Ni structure corrodes according to:

$$Al_3Ni + 11H^+ + 2.75O_2(g) = 3Al^{+3} + Ni^{+2} + 5.5H_2O \quad \Delta G_0 = -2641 \text{ kJ}$$
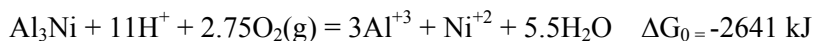
The gips free energy for the reaction above is highly negative which means that the corrosion mechanism is highly thermodynamically favourable.

Due to the small nickel versus volume ration for the leached Al_3Ni structure, it is particularly vulnerable to corrosion. That is, only small amount of nickel dissolution results in dramatic weakening of the structure. The delamination of the leached Al_3Ni structure is proposed to be further accelerated by the subsequent oxygen evolution which causes a coating blow-off as shown in fig 15.

4 Conclusions

Microscopic investigations indicate that nickel and nickel-rich phases are the main moving species during interdiffusion of PVD deposited aluminium and nickel substrate at 610 °C and not vice versa as might be expected. This diffusion mechanism leads to formation of fine grained Al/Ni intermetallic structures that are very susceptible to alkaline leaching of aluminium in strong alkali. By altering the diffusion time, from 10 to 30 min, different thicknesses of intermetallic structures can be tailored. By alkaline aluminium leaching of the intermetallic structure, a porous nickel electrode, with max 5% aluminium residue, is produced.

The roughness factor of the porous nickel coatings rises in proportion to the thickness of the intermetallic layer formed, which in addition is in line with the diffusion time. In that way one can obtain high electrocatalytic surface areas with a roughness factor close to 1000, using the shortest diffusion time, i.e. 10 min. Increasing the diffusion time to 20 minutes will again dramatically increase the roughness factor and lower the charge transfer resistance associated with the electrode. As the diffusion time is further prolonged (30 min.) still the electrode characteristics are improved, although to a minor degree. All in all, time and energy consumption can be lowered in the processing of the electrodes leading to the feasibility of industrial implementation. What is more, since the material characteristics of the three binary alloys are the same, these observations clearly emphasize how the electrochemically active surface area plays a dominant role when designing electro catalytic electrodes.

The leached Al_3Ni structure was not stable and became delaminated during the OER. Two corrosion mechanism accelerated by the O_2 gas erosion where presented for the observed delamination. A more detailed study of this delamination is most certainly needed if these coatings are to be used as anodes for bipolar electrodes in industrial alkaline water electrolysis. From the OER measurement, it was found that all coatings comprise higher activity compared to polished nickel. This finding is a reality, even though the coatings are highly damaged by the polarization, and suggests that the underlying phase provides some increased activity for the OER. A more detailed study of this underlying phase should therefore be initiated.

Acknowledgement

References

[1]   Corrosion resistance of nickel and nickel-containing alloys in caustic soda and other alkalies. INCO (Int Nickel Co, Inc) Corros Man 1975.

[2]   Rebak RB. Nickel Alloys for Corrosive Environments. Advanced Materials and Processes 2000;157:37–42.

[3]   Zeng K, Zhang D. Recent progress in alkaline water electrolysis for hydrogen production and applications. Progress in Energy and Combustion Science 2010;36:307–26.

[4]   Ursua A, Gandia LM, Sanchis P. Hydrogen Production From Water Electrolysis: Current Status and Future Trends. Proceedings of the IEEE 2012;100:410 –426.

[5]   Hoogers G. Fuel Cell Technology Handbook, United States of America: CRC Press; 2002, p. 20–5.

[6]   Balej J, Divisek J, Schmitz H, Mergel J. Preparation and properties of raney-nickel electrodes on Ni-Zn base for H2 and O2 evolution from alkaline-solutions. Part I: electrodeposition of Ni-Zn alloys from chloride solutions. Journal of Applied Electrochemistry 1992;22:705–10.

[7]   Oden LL, Russell JH, Sanker PE. Method for producing supported Raney nickel catalyst. United States patent US4049580. 1976

[8]   Raney M. Method of producing finely-divided nickel. . United States patent US1628190. 1927.

[9]   Bagotsky VS. Fuel Cells: Problems and Solutions, John Wiley & Sons; 2012, p. 209–10.

[10]   Sillitto SMA, Adkins NJE, Ormerod RM, Paul E, Hodgson DR. Characterisation of advanced Raney nickel electrocatalytic coatings   produced by the direct spraying method. Rugby: Inst Chemical Engineers; 1999.

[11]   Sillitto SMA, Adkins NJE, Hodgson DR, Paul E, Ormerod RM. Electrochemical testing and structural characterisation of nickel based   catalytic coatings produced by direct spraying. In: Lednor PW, Nagaki DA, Thompson LT, editors. Advanced Catalytic Materials-1998, vol. 549, Warrendale: Materials Research Society; 1999, p. 23–9.

[12]   Kellenberger A, Vaszilcsin N, Brandl W, Duteanu N. Kinetics of hydrogen evolution reaction on skeleton nickel and   nickel-titanium electrodes obtained by thermal arc spraying technique. Int J Hydrog Energy 2007;32:3258–65.

[13]   Kellenberger A, Vaszilcsin N, Brandl W. Roughness factor evaluation of thermal arc sprayed skeleton nickel   electrodes. J Solid State Electrochem 2007;11:84–9.

[14]   Birry L, Lasia A. Studies of the hydrogen evolution reaction on Raney nickel-molybdenum electrodes. J Appl Electrochem 2004;34:735–49.

[15]   Kellenberger A, Vaszilcsin N. The determination of the roughness factor of skeleton nickel electrodes by cyclic voltammetry. Rev Chim 2005;56:712–5.

[16]   Schiller G, Henne R, Borck V. Vacuum plasma spraying of high-performance electrodes for alkaline water electrolysis. JTST 1995;4:185–94.

[17]   Fournier J, Miousse D, Legoux JG. Wire-arc sprayed nickel based coating for hydrogen evolution reaction in   alkaline solutions. Int J Hydrog Energy 1999;24:519–28.

[18]   Boruciński T, Rausch S, Wendt H. Raney nickel activated H2-cathodes Part II: Correlation of morphology and effective catalytic activity of Raney-nickel coated cathodes. J Appl Electrochem 1992;22:1031–8.

[19] Wendt H, Hofmann H, Plzak V. Anode and cathode-activation, diaphragm-construction and electrolyzer configuration in advanced alkaline water electrolysis. Int J Hydrog Energy 1984;9:297–302.

[20] Wendt H, Plzak V. Electrocatalytic and thermal activation of anodic oxygen- and cathodic hydrogen-evolution in alkaline water electrolysis. Electrochimica Acta 1983;28:27–34.

[21] Schiller G. High performance electrodes for an advanced intermittently operated 10-kW alkaline water electrolyzer. Int J Hydrog Energy 1998;23:761–5.

[22] Maunowski P, Jtilich C. Improved components for advanced alkaline water electrolysis. Int J Hydrog Energy 1988;13:141–50.

[23] Kjartansdóttir CK, Nielsen LP, Møller P. Development of durable and efficient electrodes for large-scale alkaline water electrolysis. Int J Hydrog Energy 2013;38:8221–31.

[24] Jansssen M, Rieck G. Reaction diffusion and kirkendal-effect in nickel aluminium system. Transactions of the Metallurgical Society of AIME 1967;239:1372–85.

[25] Inderjeet Kaur, Mishin Y, Gust W. Fundamentals of grain and interphase boundary diffusion. Chichester; New York: John Wiley; 1995.

[26] Harrison LG. Influence of dislocations on diffusion kinetics in solids with particular reference to the alkali halides. Trans Faraday Soc 1961;57:1191–9.

[27] Castleman LS, Seigle LL. Layer growth during interdiffusion in aluminum-nickel alloy system. Met Soc AIME -- Trans 1958;212:589–96.

[28] Machado SAS, Avaca LA. The hydrogen evolution reaction on nickel surfaces stabilized by H-absorption. Electrochimica Acta 1994;39:1385–91.

[29] Guerrini E, Trasatti S. Recent developments in understanding factors of electrocatalysis. Russ J Electrochem 2006;42:1017–25.

[30] Herraiz-Cardona I, Ortega E, Pérez-Herranz V. Impedance study of hydrogen evolution on Ni/Zn and Ni–Co/Zn stainless steel based electrodeposits. Electrochimica Acta 2011;56:1308–15.

[31] Marceta Kaninski MP, Miulovic SM, Tasic GS, Maksic AD, Nikolic VM. A study on the Co–W activated Ni electrodes for the hydrogen production from alkaline water electrolysis – Energy saving. Int J Hydrog Energy 2011;36:5227–35.

[32] Šimpraga RP, Conway BE. The real-area scaling factor in electrocatalysis and in charge storage by supercapacitors. Electrochimica Acta 1998;43:3045–58.

[33] Kumar M, Awasthi R, Sinha a. SK, Singh RN. New ternary Fe, Co, and Mo mixed oxide electrocatalysts for oxygen evolution. Int J Hydrog Energy 2011;36:8831–8.

[34] Weininger JL, Breiter MW. Effect of Crystal Structure on the Anodic Oxidation of Nickel. Journal of The Electrochemical Society 1963;110:484.

[35] Sanchis P, Ieee M. Water Electrolysis : Current Status and Future Trends. Proceedings of the IEEE 2012;100.

[36] Pletcher D, Li X. Prospects for alkaline zero gap water electrolysers for hydrogen production. Int J Hydrog Energy 2011;36:15089–104.

[37] Nelson PA, Elliott JM, Attard GS, Owen JR. Mesoporous Nickel / Nickel Oxidesa Nanoarchitectured Electrode. Chem Mater 2002:524–9.

[38] Li X, Walsh FC, Pletcher D. Nickel based electrocatalysts for oxygen evolution in high current density, alkaline water electrolysers. Physical Chemistry Chemical Physics 2011;13:1162.

[39] Rebouillat S. Paving the Way to The Integration of Smart Nanostructures: Part II: Nanostructured Microdispersed Hydrated Metal Oxides for Electrochemical Energy Conversion and Storage Applications. International Journal of Electrochemical Science 2011;6:5830–917.

[40] Hamdani M. Co3O4 and Co- Based Spinel Oxides Bifunctional Oxygen Electrodes. International Journal of Electrochemical Science 2010;5:556–77.

Investigations of the diffusion mechanism of PVD Al and Ni couples at 610°C

Cecilía Kjartansdóttir[a], Hossein Alimadadi[b], Takeshi Kasama[b] and Per Møller[a].

[a] Department of Mechanical Engineering, The Technical University of Denmark
[b] Center for Electron Nanoscopy, The Technical University of Denmark

Abstract

PVD Al-Ni diffusion couples are heat treated at 610°C for few minutes up to 24 hours. Initially, the dominant diffusion mechanism is found to be grain boundary diffusion of Ni-rich phases into the high containing Al structure. It is proposed that the first intermetallic phase to form is $AlNi_3$, appearing as small crystallites in the grain boundaries of the columnar aluminium structure. Together with the $AlNi_3$ particles in the aluminium residue, only Al_3Ni and Al_3Ni_2 phases are formed in the diffusion zone for up to 30 minutes of heat treatment. 2 hours of heat treatment results in depletion of the Al and the Al_3Ni and thin layers of AlNi and $AlNi_3$ are formed closest to the Ni substrate. Also, highly porous γ-Al_2O_3 has formed on the top surface of the Al_2Ni_3 phase. No remaining $AlNi_3$ are found in the Al_3Ni_2 structure after 2 hours of diffusion. Longer annealing time, results in slow enlargement of the AlNi, $AlNi_3$ and γ-Al_2O_3 layers and grain growth in the Al_2Ni_3 phase.

1   Introduction

Increasing the surface area and altering the electrocatalytic configuration of an electrocatalyst by selectively leaching one or more element from metal alloys, has widely been used to promote the activity of hydrogen electrocatalysts [1–11]. Various techniques for producing the leachable NiZn or NiAl alloys, such as electrodepositiont, powder pressing and thermal spraying have been proposed [3],[9],[7], [12–22].

In a previous study [1], efficient hydrogen electrodes were produced by physical vapour deposition (PVD) of Al onto a nickel substrate, followed by heat treatment for 24 hours at 610 °C and selective aluminium leaching. The final electrocatalytic behaviour of the electrode depends on the electrode composition and structure. In order to facilitate the optimal electrocatalysts produced in this, manner understanding the diffusion mechanism of the PVD Al-Ni couples is essential.

According to the Ni-Al binary alloy phase diagram [23] four thermodynamically stable alloys, namely Al_3Ni, Al_3Ni_2, NiAl, and Al Ni_3, can be formed at temperatures below 854 °C. Formation of the Al_3Ni_5 phase is also proposed at temperatures below 700 °C. The existence of that phase is, however, still not well established. Several work on Ni-Al couples at temperatures around 600 °C have been published [24-27] where only Al_3Ni and Al_3Ni_2 phases were found to be formed. In one publication [28] thin layers of NiAl and $AlNi_3$ were formed after 340 hours of heat treatment. Janssen and Rieck [24] reported that only aluminium was found to take part in the diffusion mechanism for Ni-Al couples at temperatures at about 600°C. Here, $AlNi_3$ is proposed to be the initial phase to form at 610 °C and thin layers of NiAl and $AlNi_3$ are detected after only 2 hours of diffusion. Furthermore, Ni and Ni-rich phases appear to be the main moving species at 610 °C in PVD Al-Ni couples.

In this paper we report studies on PVD Al-Ni diffusion couples, heat treated at 610 °C for few minutes up to 24 hours, investigated by the means of, high resolution scanning electron microscope (HR-SEM), energy dispersive X-ray spectroscopy (EDS), X-ray diffractometry (XRD), electron backscatter diffraction (EBSD), ion channelling contrast imaging (ICCI) and transmission electron microscopy (TEM).

2 Experimental

2.1 Material

Commercially available, rolled and annealed, nickel plate is served as substrate for aluminium physical vapour deposition (PVD). Using optical emission spectroscopy, the purity of the plate is measured to be 99%. An approximately 20 μm thick layer of aluminium is physical vapour deposited onto the Ni substrate by the means of non-reactive DC-magnetron sputtering process, using a CC800/9 SinOx coating unit from CemeCon AG. The aluminium source is an Al 1050 alloy target run at 750 W, the RF bias on the substrate is set to 800 W and the start pressure in the chamber is 1 mPa. Before placing the nickel plate inside the PVD chamber the plate is cathodically decreased and dried. Nickel oxides are removed from the surface in situ by means of Ar sputtering. The Al deposited Ni plate is cut to form 25×25 mm^2 coupons, suitable for X-ray diffraction measurements and 10×15 mm^2 and 5×10 mm^2 coupons suitable for microscopy investigations. The prepared coupons are heat treated in an atmospheric furnace at 610˚C for various times: 0, 3, 10, 20, 30, 120, 240, 360, 480, and 1440 min. The coupons are removed from the furnace directly after heat treatment and cooled at ambient temperature.

2.2 Sample preparation

For cross section investigations the 10×15mm^2 coupons are hot-mounted in PolyFast from Struers grinded down to 4000 grit and subsequently polished with 3 and 1 μm diamond. For detailed microscopic characterisation the 5×10 mm^2 coupons are mounted in a custom made sample holder specially prepared for cross section polishing. The coupons are grinded down to 4000 grid followed by 3, 1 and 0.25 μm diamond polishing and mechanical/chemical polishing with 0.04 μm colloidal silica (OPS from Struers).

2.3 Grazing incidence X-ray diffraction

The grazing incident X-ray diffraction (GI-XRD) method is applied for phase analyses. The analyses are performed using a Bruker axs, D8-Discover instrument with Cu Kα radiation. The GI angel is selected to be 6 degrees for all the XRD investigations.

2.4 Electron / Ion microscopy

For general microstructural and elemental investigations a Hitachi TM 3000 Tabletop SEM is applied for all samples. For detailed investigations of the as-deposited sample and samples heat treated for 10 and 120 minutes, electron backscatter diffraction (EBSD) and ion channelling contrast imaging (ICCI) are performed

in a FEI Helios NanoLab^{TM} 600, equipped with an EDAX-TSL EBSD system and a Hikari camera. The ICCI investigation is performed using Ga+ ions with energy of 30 keV.

The sample heat-treated for 120 minutes is studied in an FEI Titan 80–300 filed-emission-gun TEM, equipped with an energy dispersive X-ray spectroscopy (Oxford Instruments, X-Max^{N} 80 mm^2 silicon drift detector) and a spherical aberration probe corrector. The microscope is operated in scanning TEM mode at 300 kV and the images are acquired using either a bright-field or a high-angle annular dark-field detector. STEM-EDS is carried out with an interval of 10 nm from a region of 100×200 nm^2.

The EBSD measurement is performed in a hexagonal grid with an electron probe current of 5.5 nA at an acceleration voltage of 15 kV. The cleaning procedure of the measured data is applied using OIM 6^{TM} as follows: (i) grain confidence index standardization, (ii) single iteration grain dilation (in both cases, a grain is defined as a region consisting of at least four connected points with misorientations of less than 5˚), (iii) all the data points with confidence index below 0.1 are disregarded.

3 Results

3.1 General investigations

Backscatter electron imaging

Fig.1 shows backscatter electron (BSE) micrographs of the cross section of PVD aluminium nickel coupons as- deposited and after various times of heat treatments at 610˚C. The micrographs clearly show the general trend of microstructural change as a function of time. In the as-deposited state the large difference in the BSE intensity between aluminium and nickel is evident. This owes to higher atomic number of nickel which appears brighter compared to aluminium with lower atomic number (Z contrast). Z contrast is beneficial for general investigation of the change in microstructure upon heat treatment.

As can be easily seen in Fig.1, after only 3 minutes of heat treatment, particles with higher atomic number than Al appear within the Al layer. For the coupon heat treated for 10 minutes, a larger amount of bright particles are detected in the Al top layer. Furthermore, two sharply defined layers, referred hereafter as W and Z, are formed between the nickel substrate and the Al layer. With further increase of the diffusion time, an increase in the formation of Z layer on the detriment of the W phase is observed. After 30 minutes of the heat treatment, no pure Al layer is left and only the diffusion zone and the intermetallic structure, consisting primarily of the Z phase, remains.
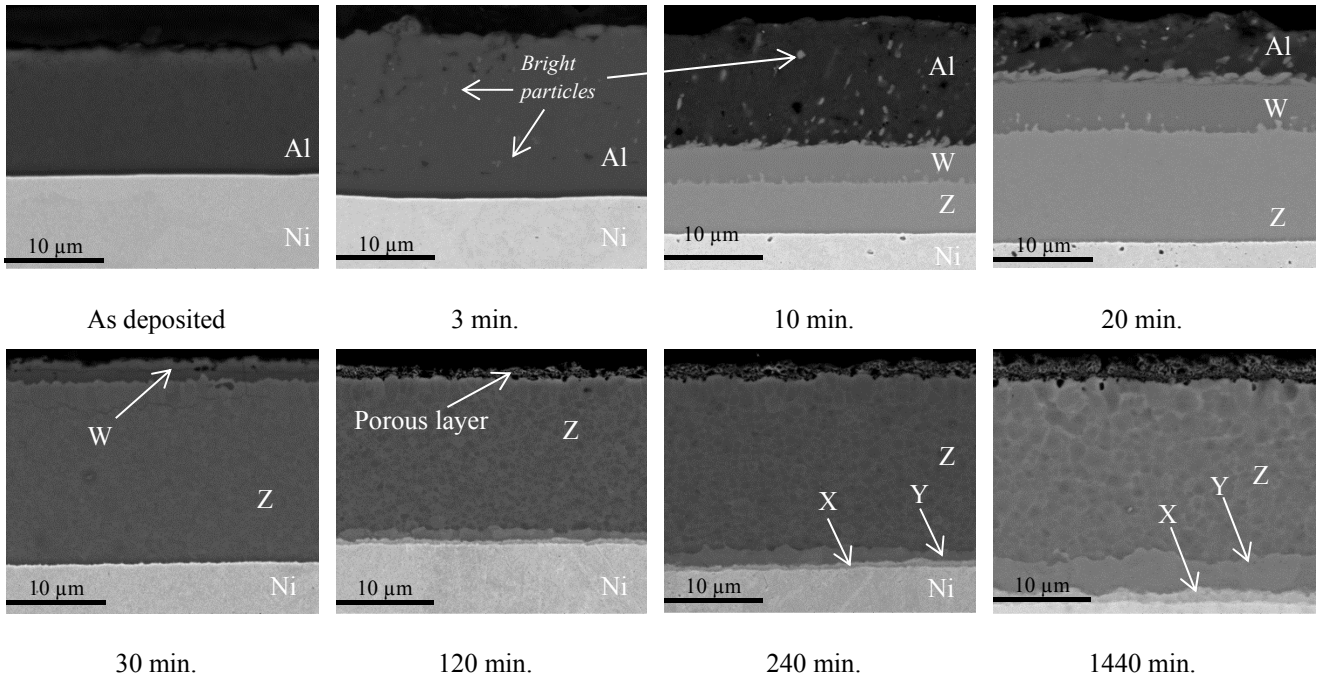
| As deposited | 3 min. | 10 min. | 20 min. |

| 30 min. | 120 min. | 240 min. | 1440 min. |

Fig.1: Backscatter electron images on the cross section of the PVD Al/Ni coupons after various times of heat treatment at 610˚C.

Heat treatment for 120 minutes brings about formation of a porous layer at the very top surface and two newly formed layers close to the nickel substrate, hereafter entitled X and Y. It is noted that BSE micrographs vaguely reveals presence of equi-axed grains in the Z layer.

Heat treatment for longer times, i.e. 360, 480 and 1440 results in a slow growth of X and Y layers as well as growth of equi-axed grains in the Z layer. It is noted that micrographs for the 360 and 480 minutes coupons do not contribute with any new microstructural information. Investigations of these are therefore considered superfluous and results thereof will not be included here. In order to investigate the chemical composition in the diffusion layers of the Al-Ni couples, EDS and GI-XRD are applied.

Energy dispersive X-ray spectroscopy

To characterize different diffusion layers revealed by backscatter electron imaging, EDS is applied on the cross-section of the samples shown in Fig. 1. The chemical compositions of Ni in the detected diffusion layers are listed in Table 1.

Time of diffusion (Min.)	W [Al$_3$Ni] (wt.% Ni)	Z [Al$_3$Ni$_2$] (wt.% Ni)	Y [AlNi] (wt.% Ni)	X [AlNi$_3$] (wt.% Ni)
10	45	59	-	-
20	42	61	-	-
30	41	62	-	-
120	-	63	x	x
240	-	64	71	87
1440	-	64	71	88

Table 1: The chemical composition of Ni in the PVD Al-Ni diffusion layers shown in Fig 1. The possible binary alloy is indicated in square brackets.(¯ The phase is not present. ^{x} The interaction volume of electron beam is larger than the width of the layer.)

It is noted that the chemical composition of all the cases is balanced to 100 by Al. Relating the EDS results with the Al-Ni binary alloy phase diagram the diffusion layers are predicted to mainly consist of the following intermetallic phases: W, Z, Y and X are Al$_3$Ni, Al$_3$Ni$_2$, AlNi and AlNi$_3$ respectively.

Grazing incidence X-ray diffraction

In order to supplement the EDS information, GI-XRD is applied. The results from the XRD measurements are shown in Fig. 2.
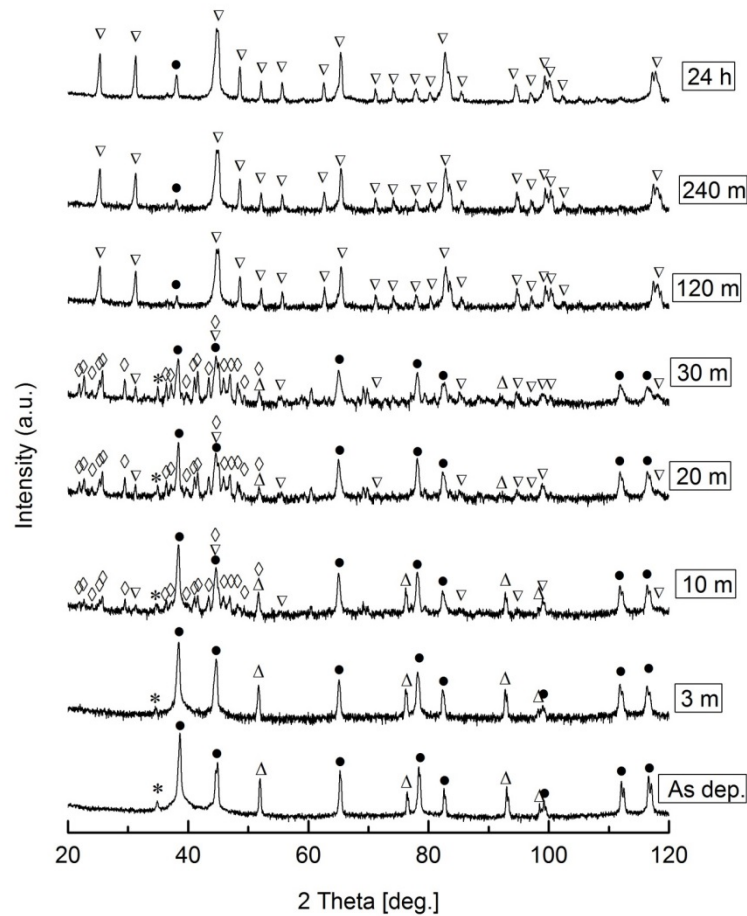
Fig. 2: GI X-ray diffractograms for the PVD Al-Ni couples after various times of heat treatments. (•) Al, Δ Ni, (*) Al_2O_3 (Corundum), (◊) Al_3Ni (∇) Al_3Ni_2. JCPDS card-numbers 4-787, 4-850, 46-1212, 3-1052 and 2-416. The incident angel is 6 degrees for all the tested specimens.

From the diffraction patterns for the as plated and 3 min. coupons aluminium, aluminium oxide and nickel diffraction peaks are detected. On grounds of that the as plated PVD Al structure does not contain any Ni, the Ni signals in the XRD result must stem from the Ni substrate. Therefore, although only 6 degrees GI angle is applied, X-ray diffraction from the Ni substrate can be expected due to the large penetration depth of X-ray in Al. Consequently, no interpretations can be made about the presence of pure Ni in the diffusion layer of the heat treated coupon from the XRD results alone. While it is evident, from the SEM image, that some diffusion has taken place into the PVD Al layer after only 3 minutes of heat treatment, no intermetallic phase is detected from the corresponding diffractogram.

For the coupon heat treated for 10 min. Al_3Ni and weak Al_3Ni_2 diffraction peaks are detected in addition to those previously found. For the 20 and 30 min. coupons the Al_3Ni and Al_3Ni_2 peaks get more pronounced. Also, the Ni diffractions at ~76° 2θ and ~98° 2θ disappear. This is most likely due to a smaller amount of X-ray signals from the Ni substrate because of less X-ray penetration in the intermetallic phases formed, compared to pure Al. After 120, 240 and 1440 minutes of heat treatment, higher intensities from the Al_3Ni_2 phase are detected and all the Al_3Ni and Al_2O_3 peaks disappear.

As seen in Fig. 2, a number of low intensity diffractions, for the coupons heat treated for 10 min. and longer, have not been assigned to any phases. Due to many overlapping peaks, distinguishing between different Al-Ni binary alloys and oxides thereof from the XRD results is challenging. When making phase analyses on the data some of the reaming peaks could correspond to Al_4Ni_3, $NiAl_2O_4$, Al_2O_3, AlNi and $AlNi_3$. Another limitation of the XRD analyses is that small crystallites have less diffraction volume compared to larger ones; therefore, the corresponding peaks have low intensities. Also, small crystals results in a broad diffraction peak whereas large crystals give sharp diffraction peaks. Therefore, when identifying small crystallites among diffractions from larger crystallites some diffraction peaks can be overlooked. Accordingly local microscopic characterisation is carried out on selected samples.

3.2 Detailed investigations

Based on the backscatter electron imaging results from the EDS and XRD investigations, three samples are chosen for detailed microscopic characterization (as-deposited, 10 min. and 120 min. heat treated). As-deposited microstructure is selected to identify the crystal structure of the PVD Al before heat treatment. The 10 min. treated coupon is selected to analyse the initial diffusion behaviour and the two firstly detected diffusion layers i.e. W and Z. Lastly the 120 min. treated coupon is selected to investigate the changes of the crystal structures in the Z layer together with the latter developed diffusion layers, Y, X and the porous one. These three samples encompass all the different layers and phases which are formed in the as-deposited state and after heat treatment for various times.

As-deposited PVD Al

Fig.3 shows the microstructure of the as-deposited Al on Ni.
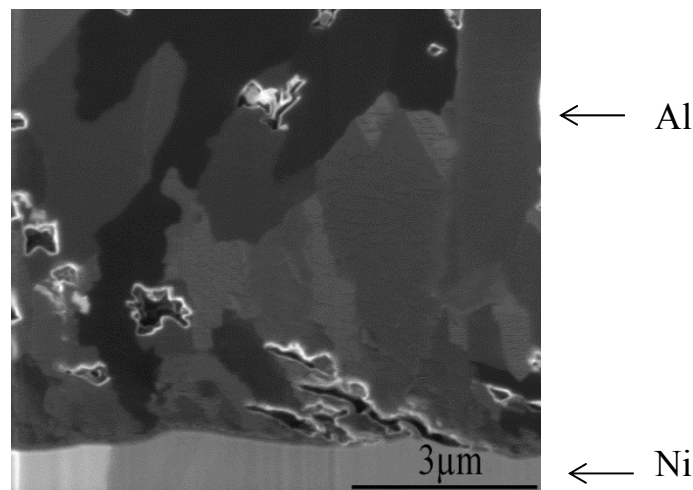
Fig. 3: ICCI micrograph of an as deposited PVD Al on Ni, showing the columnar structure of the aluminium.

The Al layer has a columnar microstructure in which the microstructure consists of fine grains at the vicinity of the substrate and by increase of distance from the substrate, some grains outgrow the rest. Notably, the microstructure of Al is not fully dense and no epitaxial relation between Ni substrate and Al deposit is observed.

10 min. heat treatment

The cross section forward scatter detector (FSD) micrograph of the PVD Al-Ni diffusion couples after 10 min. of heat treatment is shown in Fig. 4. The micrograph reveals the especially small crystallites in the W and X layers, compared to the Al and Ni structures.
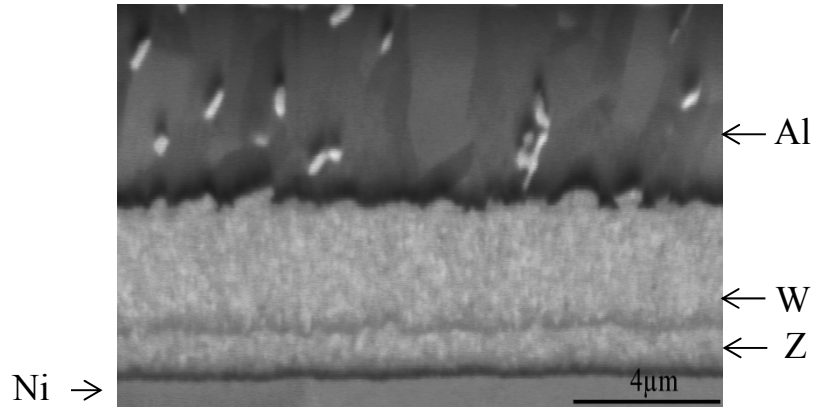

Fig.4: FSD micrograph of the PVD Al-Ni diffusion couples after 10 min. of heat treatment at 610 °C showing the small crystallites in the W and X layers and the high z-contrast particles in the grain boundaries of the Al.

Image capture from ICCI investigations on the microstructure of the 10 min. sample is shown in Fig. 5. No additional information could be obtained on Ni and Z layer from the imaging, hence, only the W and the Al layer are shown in Fig 5. Very fine crystallites are present in the W layer and are marked by arrows in Fig. 5. Observing the interface between the W layer and the Al, the W layer has an outward curvature whilst the Al has inward curvature. This strongly suggests that diffusion is from the W layer into the Al layer. In addition, a nickel rich phase is formed on the grain boundaries and triple lines of the Al columnar grains.
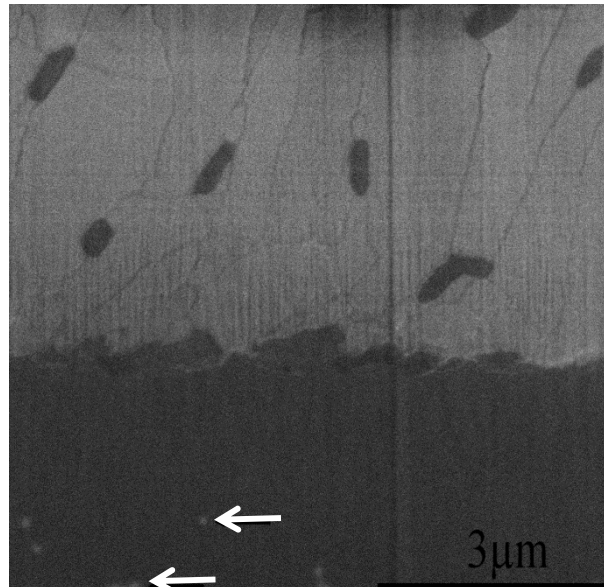

Fig. 5: ICCI micrograph of PVD Al-Ni diffusion couples after 10 min. of heat treatment at 610°C.

To characterize the nickel rich phase at the grain boundaries EBSD is applied. Fig. 6a shows the electron backscatter pattern (EBSP) of one of the nickel rich crystallites detected and Fig. 6b shows the same pattern after background subtraction. The high quality pattern shown in Fig. 6b is used for phase identification in which various phases i.e. Al, Al_3Ni, Al_3Ni_2, Al_4Ni_3, AlNi, Al_3Ni_5, $AlNi_3$, and Ni are indexed. Indexing the pattern using $AlNi_3$ provides the highest similarity to the measured pattern as shown in Fig.6c. It is also attempted to identify the fine crystallites present in the W layer. However, due to the limited diffracting volume, it is not possible to obtain high quality patterns that can be used for reliable phase identification.
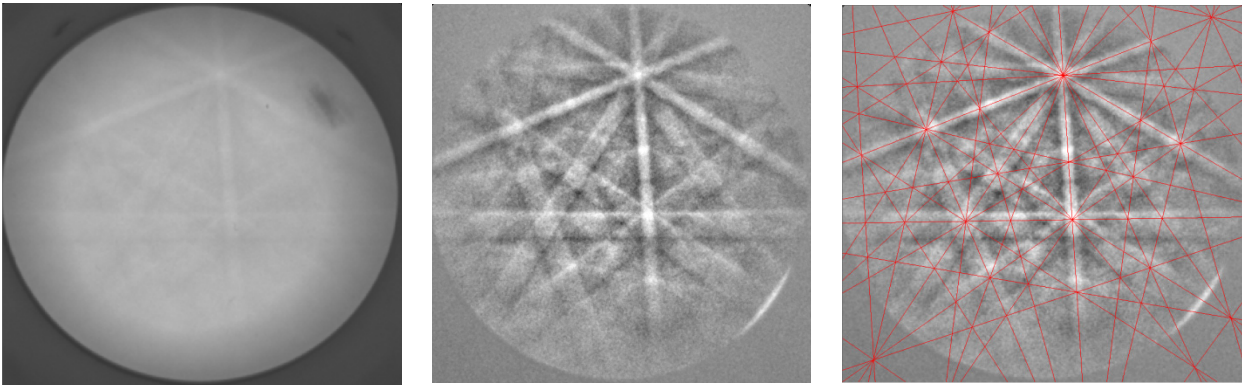

Fig. 6: a) EBSP from one nickel rich crystallite detected in Fig. 4. b) The EBSP after background subtraction. c) Indexing of the pattern with $AlNi_3$.

Simultaneously to the EBSD, EDS and orientation microscopy are applied. The results are shown in Fig 7.

a) EDS map of the diffsuion sone.

— Ni, —Z, —W, — Al

b) EBSD orientation map showing the columnar Al structure.
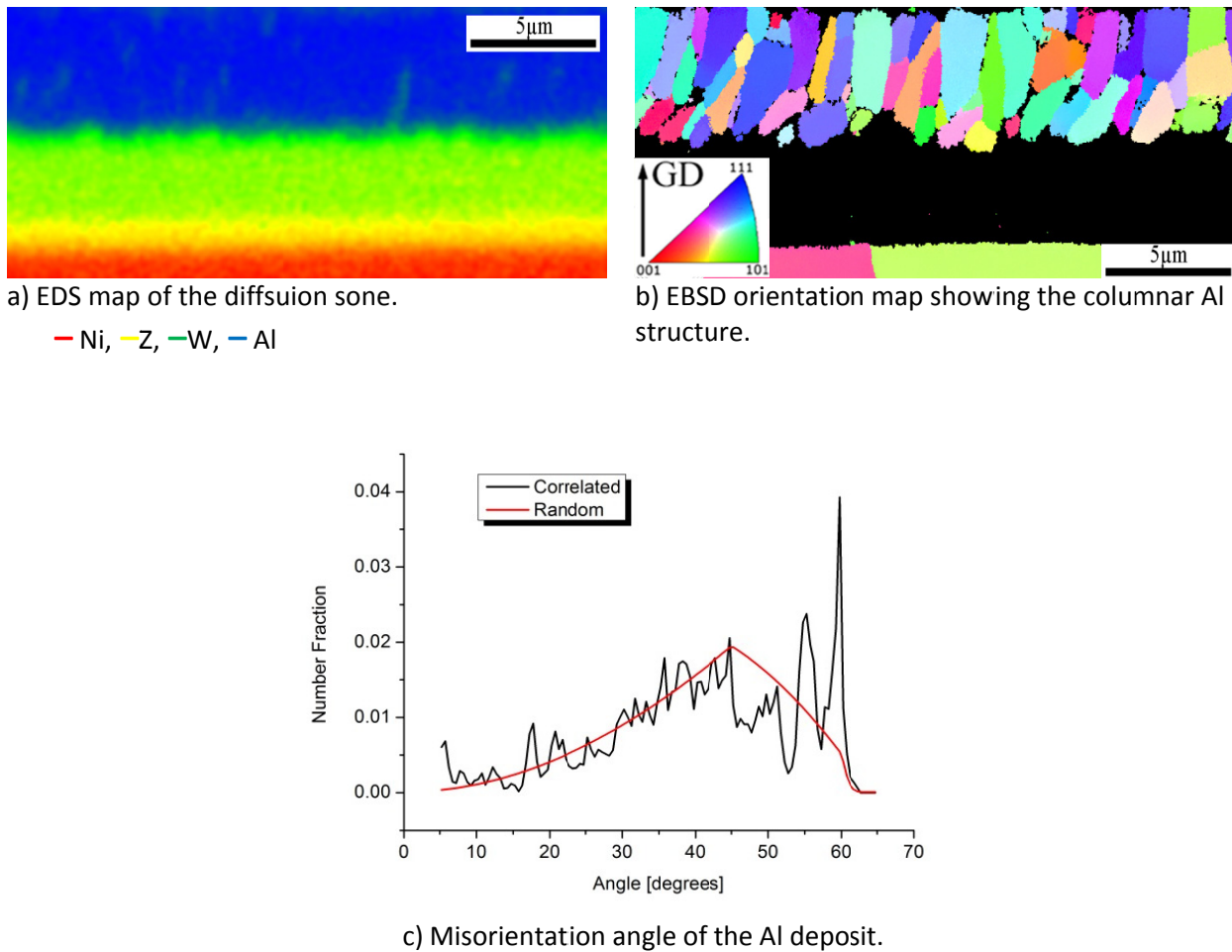

c) Misorientation angle of the Al deposit.

Fig. 7: EDS, EBSD and orientation microscopy of the PVD Al-Ni diffusion couples after 10 min.

Fig. 7a shows the EDS map of nickel covering Ni, Z, W and Al layers and Fig. 7b shows the orientation map of the sample at the same location. The Ni, Z, W and Al layer are clearly visible in the EDS map and appear as red, yellow, green and blue respectively in the used colour coding scheme. No reliable pattern is obtained in layers Z and W (very fine crystallites or amorphous) for phase identification, consequently orientation microscopy (Fig.7b) yields no results. However, the Al microstructure is clearly visible in which the columnar nature of as-deposited Al is preserved. Most of the grains are close to blue colour indicating a rather weak <111> texture in the Al deposition growth direction. The misorientation angle distribution is also calculated (Fig.7c). The distribution is close to random distribution of FCC material [29], however, there is a significantly higher population than random close to 60° which corresponds to misorientation of Σ3 boundaries in FCC material.

120 min. heat treatment

Using ICCI, Ni substrate and the diffusion layers X, Y and Z can clearly be seen in the sample heat treated for 120 minutes, see Fig. 8a.
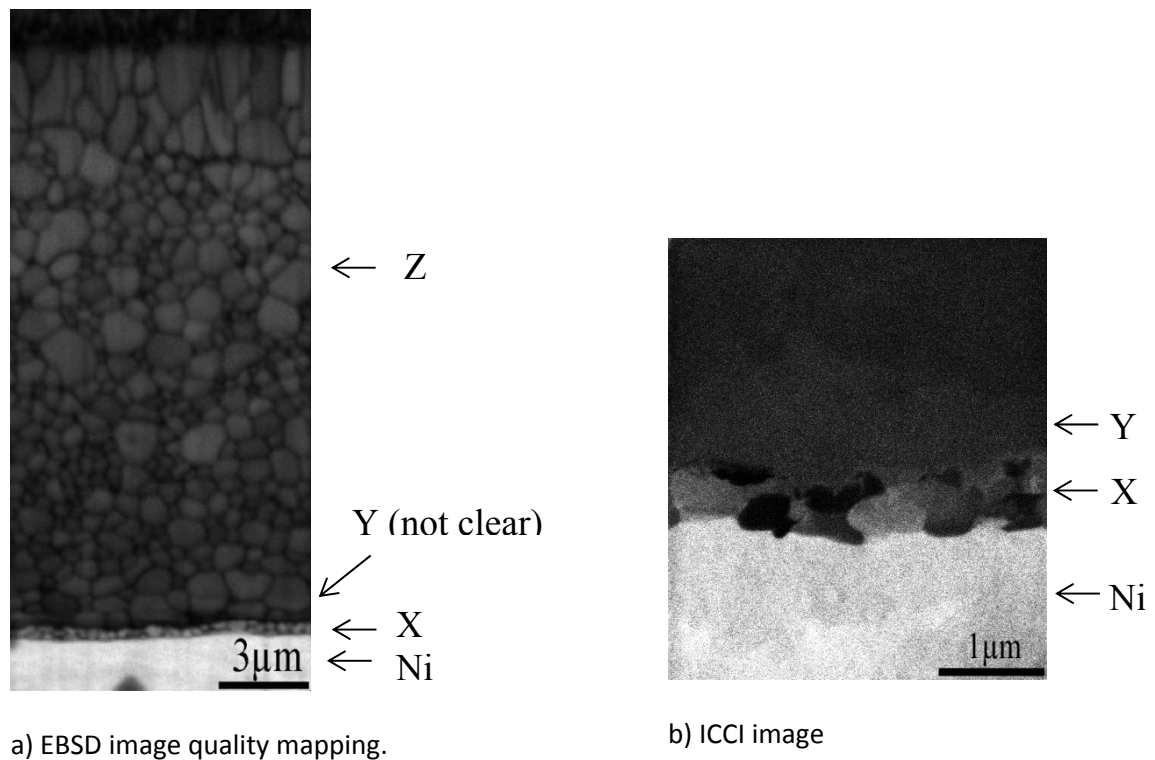
a) EBSD image quality mapping.

b) ICCI image

Figure 8: Images of PVD Al-Ni diffusion couples after 120 min.

The mean grain size in the X layer is about 300 nm. The microstructure of Y and Z layer are, however, not visible in the ICCI micrograph. Fig. 8b shows the image quality map of EBSD data in which the microstructure of Y and Z layers can be easily seen. The average grain size in layer Z is 812 nm. There is a very limited number of grains in the Y layer in the analysed map, nevertheless the grain size is of the same order as the grains in layer Z. It is noted that the grains at the top of Z layer, are elongated whilst the rest of microstructure of the Z layer is composed of equi-axed grains. EBSD (Fig. 8a) and TEM (not shown) analyses of elongated grains and equi-axed grains in Z layer show that both of their grains are trigonal Al_3Ni_2.

A high-resolution STEM image shown in Fig. 9, which corresponds to Al_3Ni_2 [211], indicates that there are generally no detectable defects or $AlNi_3$ crystallites in the Z layer (Fig.9a) although several dislocations in a few grains are observed as shown in Fig. 9a.

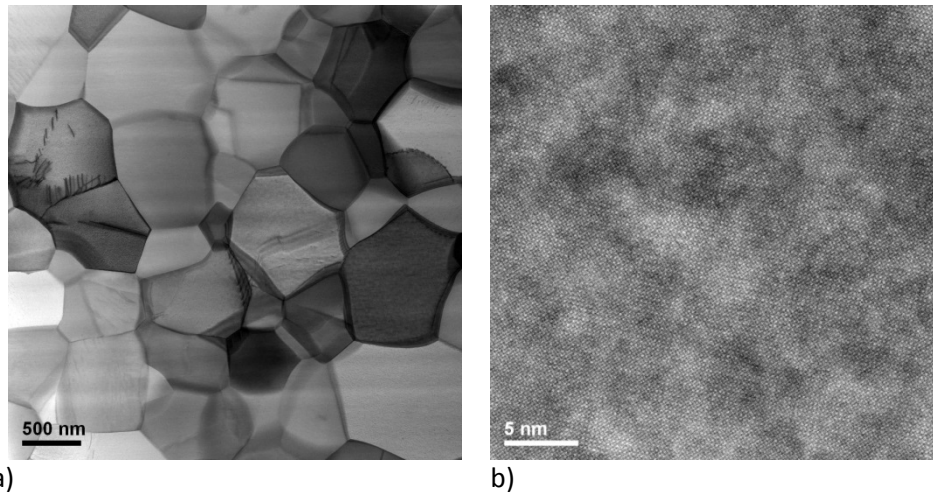a)   b)

Fig. 9: TEM micrographs of the Z layer for PVD Al-Ni diffusion couples heat treated for 120 minutes. (a) Low-magnification STEM BF image. Most of the grains do not contain defects or inclusions. (b) High-resolution STEM BF image. The contrast variation originates mainly from milling damage during FIB preparation.

The porous layer on the top of the sample after 120 min treatment is also investigated with TEM. As shown in Fig.10a, two different types of the pores are observed. Smaller pores (i.e. voids) have sharp planar interfaces, while larger pores (>50 nm) have irregular shapes with a rim of ~15 nm showing darker contrast. STEM-EDS measurements of a pore of about 100 nm in diameter (Fig. 10b) shows that the rim of the pore is rich in Al and O and is lacking in Ni. A high-resolution TEM image of the rim shown in Fig. 11 suggests the phase to be gamma-Al_2O_3.
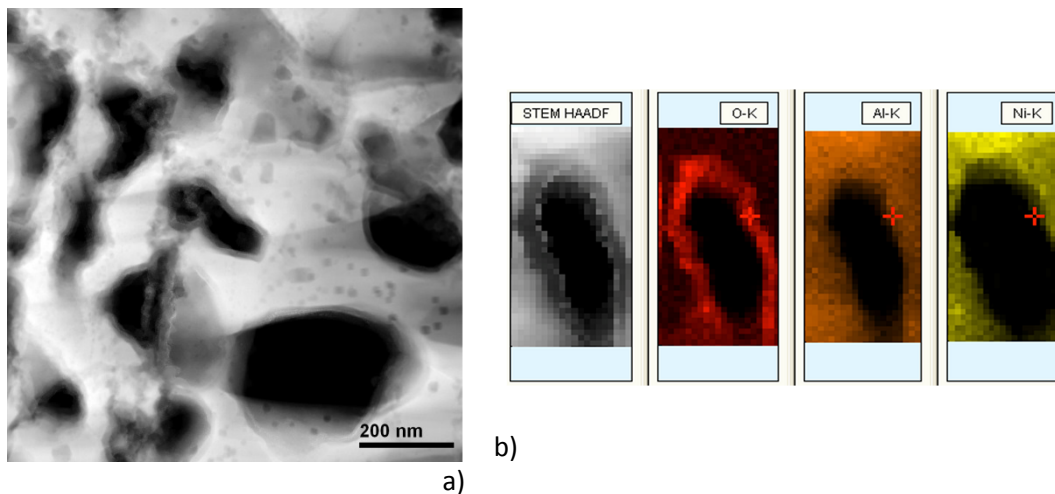

b)

a)

Fig. 10: a) STEM HAADF image of a porous layer located on the top of the specimen. b) STEM HAADF image and STEM-EDS elemental maps of a rim of a pore with ~100 nm in size. The elemental mapping shows a composition of 38 at% Al and 62 at% O (assumed the density to be 4.0 g/cm^3 and the thickness to be 50 nm).
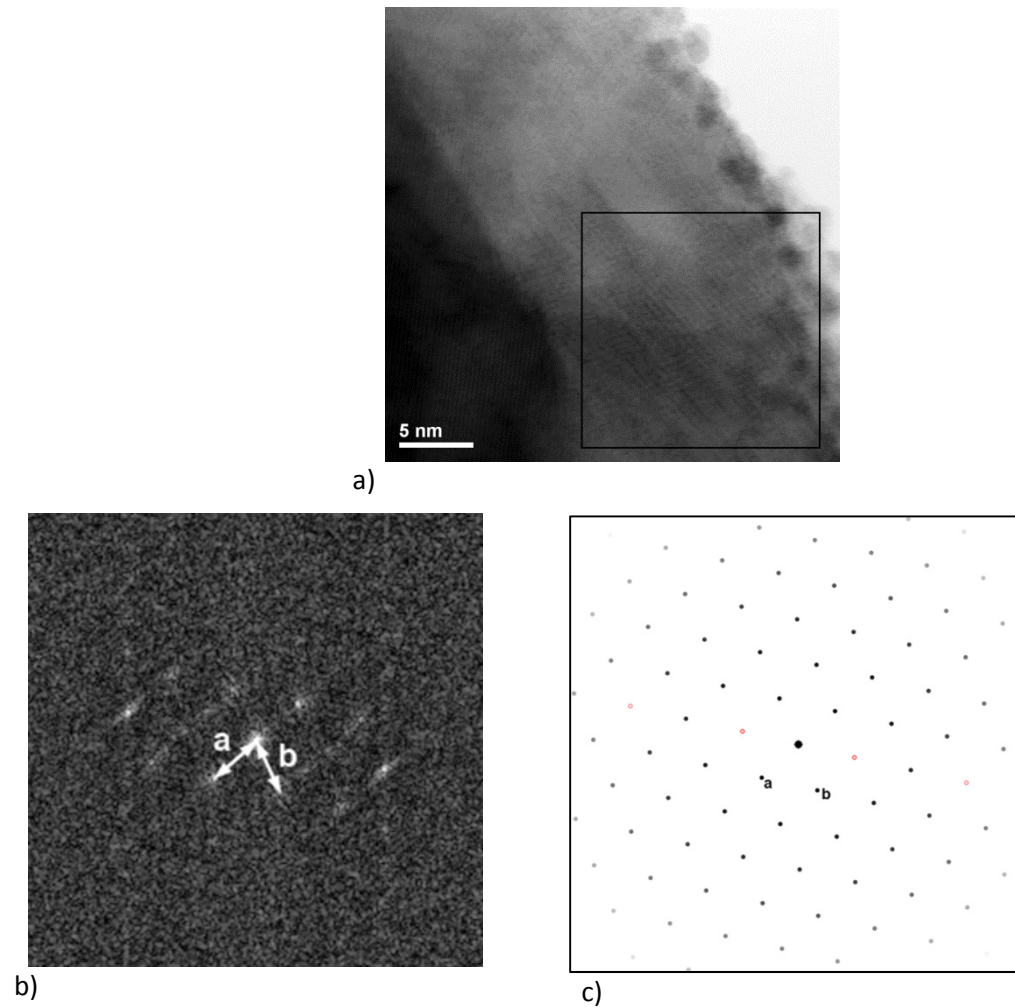
Fig.11: a) High resolution STEM BF image of a rim of a pore of ~100 nm in size. The lattice spacing of 0.29 nm at the bottom-left corner corresponds to {101} planes of Al_3Ni_2. Pt particles on the surface of the rim appear to be transferred from a Pt protection layer by FIB milling. Wide lattice fringes observed at the rim are in good agreement with those of gamma-Al_2O_3 [011]. (b) Fast Fourier transform of an area marked with a box in Fig11a, (c) Simulated electron diffraction pattern of gamma-Al2O3 [011].

4   Discussion

As evident from the ICCI micrograph in Fig. 3, the as-received PVD aluminium coating is characterised by a not fully dense, void open boundaries, columnar microstructure. This type of coating are typically formed with vapour deposition where the substrate temperature is relatively low compared to the melting temperature of the coating [30],[31] and may indicate tensile intrinsic stresses in the coating [32].

From the BSE cross section micrographs investigations shown in Fig. 1 nickel rich particles are observed to diffuse in to the PVD aluminium coating after only 3 minutes of heat treatment. EBSD investigations on the 10 minutes heat treatment sample, Fig. 5, indicate the nickel rich phase to be $AlNi_3$ (Fig. 6). The formation of high nickel containing phase instead of a high Al containing phase inside the aluminium coating is not expected. The outward curvature of the Al_3Ni towards the Al phase detected, furthermore, suggests diffusion direction mainly from nickel or nickel rich phases towards aluminium [25]. The same phenomena can be seen between the Al_2Ni_3 and the Al_3Ni phases in Fig. 1. Because of a higher mobility of Al at 610°C,

opposite diffusion direction would be expected. In the work made by Jansssen and Rieck [24] only aluminium was found to take part in the diffusion mechanism for Ni-Al couples at temperatures at about 600°C. Wang et al. investigated Ni-Al couples prepared by rolling and annealing of Ni and Al sheets. After 5 and 15 minutes heat treatments at 650 °C only Al_3Ni and Al_3Ni_2 intermetallic phases were found. Both Ni and Al were determined to be active diffusants at the annealing temperature.

Grain boundaries are known to provide high diffusivity paths in metals and diffusion along grain boundaries is in an order of magnitude faster than bulk diffusion [33]. Identifying diffusion only or mainly in the grain boundaries after short time of heat treatment, before the volume diffusion and leakage of diffusant through the walls of the boundary into the adjoining crystals takes place, is therefore not surprising. The fact that it is nickel atoms that diffuse into the grain boundaries of aluminium, instead of the opposite, is however unexpected.

Harrison´s classification of diffusion kinetics [34] is the first and still the most common method applied to explain the possible diffusion behaviour along grain boundaries. Harrison divided the diffusion mechanism into three regimes called A, B and C kinetics, see Fig 12.
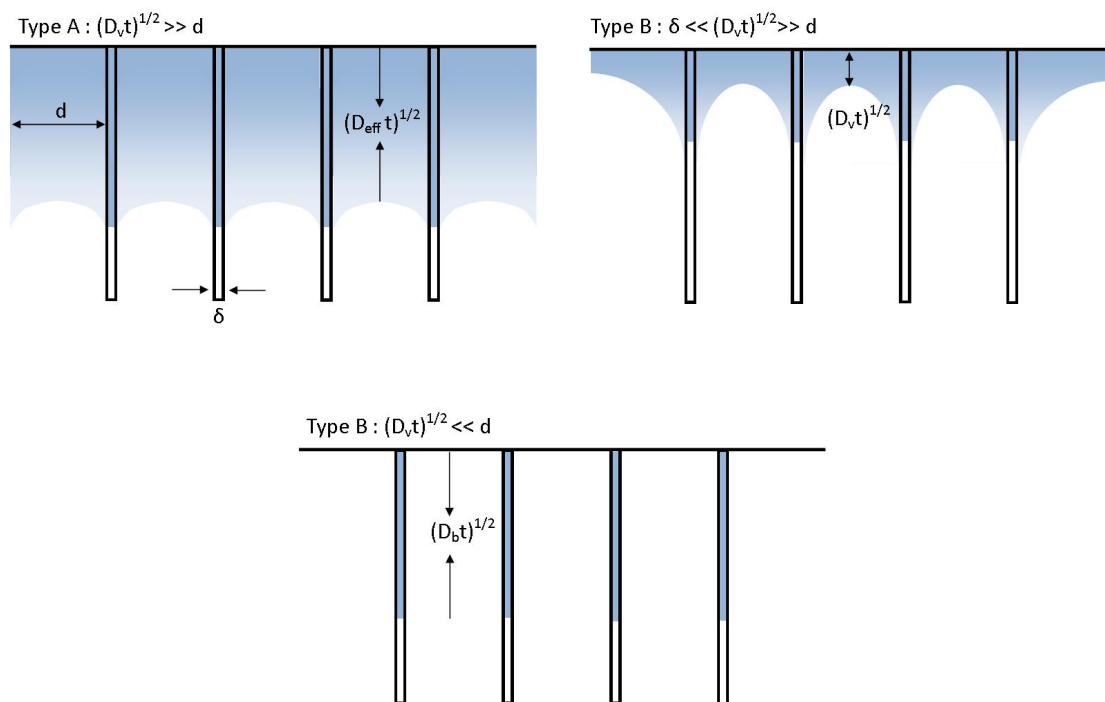
Fig. 12: Schematic illustration of Harrison´s three regime classification of diffusion kinetics. Where D_v is the volume diffusion coefficient, D_b is the grain boundary coefficient, t is the diffusion time, d is the spacing between the grain boundaries and δ is the grain boundary width.

Regime A takes place under the conditions of high temperature and/or very long heat treatment and/or small grain sizes. Under these conditions the volume diffusion length $(D_v t)^{1/2}$, where D_v is the volume diffusion coefficient and t is the diffusion time, is much larger than the spacing between the grain boundaries (d). Under these conditions leakage fields from each grain boundary overlap each other. Hence, the system appears to obey Fick´s law of diffusion where the whole system has the same diffusion coefficient D_{eff}. At lower temperatures, and/or shorter diffusion time, and/or for polycrystals with larger grain size the diffusion

can be characterised under the B type regime. Still the grain boundary diffusion takes place simultaneously with the volume diffusion. The difference is, that here the overlapping between leakage fields of each grain is not actual. For regime C, diffusion may be considered to take place only within the grain boundaries. Here the conditions are a lower temperature and/or shorter diffusion time and or when the volume diffusion coefficient is much smaller than the grain boundary diffusion coefficient.

The diffusion kinetics during the first minutes of heat treatment for the PVD Al-Ni diffusion couples can be described by Type C regime in Harrison´s diffusion system. After formation of the relatively small crystalline Al_3Ni phase, Type B and A become more and more dominant as recognized by the 10 and 20 min. heat treatments. For longer heat treatments the diffusion kinetics obey primarily the Type A regime. During the heat treatment a competition between the formation of Al_3Ni and Al_3Ni_2 take place. From the experiments of Castleman and Seigle [28] the diffusion coefficient of Al_3Ni and Al_3Ni_2 are 1.8 x 10^{-11} and 9.1 x 10^{-10} cm^2/sec, respectively. Hence, the Al_3Ni_2 phase grows faster than the Al_3Ni phase and therefore, for structures with limited Al sources, when heat treated for long enough time the Al-Ni diffusion film will consist solely of the Al_3Ni_2 phase as evident from Fig. 1.

When the entire Al layer is consumed, somewhere in-between 30 min. and 2, hours AlNi and $AlNi_3$ phases start to form in between the Al_3Ni_2 phase and the Ni substrate. Further heat treatment results in slow growth of these two phases and crystal growth of the Al_3Ni_2 phase. Simultaneously, a porous γ-Al_2O_3 phase is formed on the top surface of the Al_3Ni_2. Local TEM analyses on a relatively large cross section area of 2 hours heat treated sample (Fig. 9) indicate no traces of $AlNi_3$ in the Al_3Ni_2 intermetallic phase. From the EBSD IQ map in Fig. 8, elongated grains of the Al_3Ni_2 structure are detected closest to the γ-Al_2O_3 phase. The reason for the elongated grains can be slow diffusion kinetics due to a shortage of Ni reactants.

Correlating the present findings to the literature, the following can be found: Janssen´s and Rieck´s [24] annealing experiments on Ni-Al couples for up to 66 hours resulted in formation of no other phases except Al_3Ni and Al_3Ni_2. Castleman and Seigle [28], however, showed that after all heat treatment at 600°C for 340 hours $AlNi_3$ and AlNi formed in between the Al_3Ni_2 and Ni phase. Tarento and Blaise [35] studied interdiffusion between single crystal Ni substrate and evaporated 200 nm thick Al heat treated at 220 °C for up to 11 hours. They observed the $AlNi_3$ phase to be the first to be formed after only a few minutes of heat treatment. They explain the formation to be due to a lowering of stoichiometry of 2% of aluminium concentration resulting in easy nucleation. In this study it is propose that the initial diffusion mechanism is through movement of Al into Ni which results in formation of $AlNi_3$. The overall diffusion mechanism was, however, explained by manly being in the form of grain boundary diffusion. According to a review of thin film aluminide formation by Colcan (1990) [36], predicting what phase will form initially during thin film reaction is not yet possible. In another publication [37] the same author together with Mayer suggests that it is the most aluminium rich phase in the phase diagram that forms first and that aluminium is the dominant diffusion species during the initial phase formation.

Venezia et al. [38] reported formation of only γ-Al_2O_3 on the top of $AlNi_3$ alloy exposed to 2.5e^{-7} oxygen pressure and 700°C temperature. It has also been shown that γ-Al_2O_3 can be formed by the annealing of boehmite and pseudoboehmite at temperatures from 500-700°C [39,40].

5   Conclusions

In the present study it has been shown that diffusion coupling of columnar structured PVD Al and large crystalline Ni plate at 610°C, the dominant diffusion mechanism is grain boundary diffusion of high Ni containing phases into Al and Al-rich phases. The initial phase formed during the diffusion process is proposed to be the AlNi$_3$ phase. In addition to the formation of Al-Ni intermetallic alloys, γ-Al$_2$O$_3$ is detected on the top surface of the samples after 2 hours of heat treatment. In Fig. 13 the composition of the PVD Al-Ni diffusion couples as deposited, heat treated for 10, and heat treated for 120 minutes are schematically illustrated.
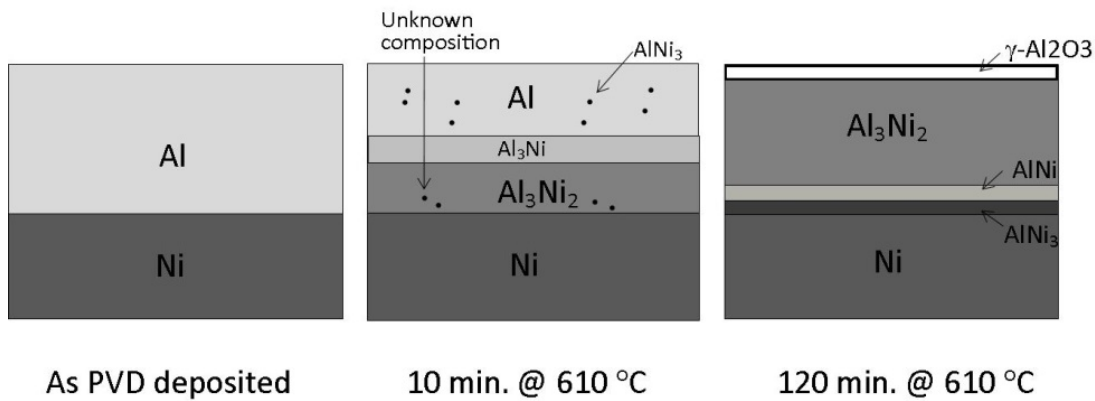

Fig: 13: Schematic diagrams showing the metallic and intermetallic phases found in the as deposited, 10 min. and 120 min. heat treated samples.

The main findings in this study are as follows:

As deposited stage
- The as deposited PVD Al layer has a columnar structure
- No epitaxial relation between Ni substrate and Al deposit is detected

10 min. of heat treatment at 610 °C
- Very fine crystallites with unknown chemical composition are present in the Al$_3$Ni$_2$ layer
- The Al$_3$Ni and Al$_3$Ni$_2$ diffusion layers have outward curvature towards the Al has inward curvature strongly suggesting that the main diffusion is from higher Ni containing species to the lower Ni containing species
- AlNi$_3$ phase is formed on the grain boundaries and triple lines of Al columnar grains
- The grain size of the interdiffused layers, Al$_3$Ni and Al$_3$Ni$_2$, are too small for EBSD analyses to be prepared

120 min. heat treatment

- The average grain size of the AlNi3 layer closest to the Ni substrate is about 300 nm.
- The average grain size of the AlNi and Al$_3$Ni$_2$ is 812 nm.
- The Al3Ni2 microstructure is characterised with equi-axed grains and slightly elongated grains closest to the top

- Relatively large area of the Al_3Ni_2 layer is investigated with high resolution TEM and only Al_3Ni_2 is found
- Highly porous γ-Al_2O_3 is formed on the top surface of the diffusion layer.

Acknowledgement

References

[1]   Kjartansdóttir CK, Nielsen LP, Møller P. Development of durable and efficient electrodes for large-scale alkaline water electrolysis. Int J Hydrog Energy 2013;38:8221–31.

[2]   Kellenberger A, Vaszilcsin N, Brandl W, Duteanu N. Kinetics of hydrogen evolution reaction on skeleton nickel and   nickel-titanium electrodes obtained by thermal arc spraying technique. Int J Hydrog Energy 2007;32:3258–65.

[3]   Birry L, Lasia A. Studies of the hydrogen evolution reaction on Raney nickel-molybdenum electrodes. J Appl Electrochem 2004;34:735–49.

[4]   Kellenberger A, Vaszilcsin N. The determination of the roughness factor of skeleton nickel electrodes by cyclic voltammetry. Rev Chim 2005;56:712–5.

[5]   Boruciński T, Rausch S, Wendt H. Raney nickel activated H2-cathodes Part II: Correlation of morphology and effective catalytic activity of Raney-nickel coated cathodes. J Appl Electrochem 1992;22:1031–8.

[6]   Crnkovic F., Machado SA., Avaca L. Electrochemical and morphological studies of electrodeposited Ni–Fe–Mo–Zn alloys tailored for water electrolysis. Int J Hydrog Energy 2004;29:249–54.

[7]   Sheela G. Zinc-nickel alloy electrodeposits for water electrolysis. Int J Hydrog Energy 2002;27:627–33.

[8]   Hu WK. Electrocatalytic properties of new electrocatalysts for hydrogen evolution in alkaline water electrolysis. Int J Hydrog Energy 2000;25:111–8.

[9]   Los P. Hydrogen evolution reaction on Ni-Al electrodes. J Appl Electrochem 1993;23:135–40.

[10]   Raj IA. Nickel-based, binary-composite electrocatalysts for the cathodes in the energy-efficient industrial production of hydrogen from alkaline-water electrolytic cells. J Mater Sci 1993;28:4375–82.

[11]   Wendt H, Imarisio G. Nine years of research and development on advanced water electrolysis. A review of the research programme of the Commission of the European Communities. J Appl Electrochem 1988;18:1–14.

[12]   Miao HJ, Piron DL. Composite-coating electrodes for hydrogen evolution reaction. Electrochimica Acta 1993;38:1079–85.

[13] Endoh E, Otouma H, Morimoto T, Oda Y. New Raney nickel composite-coated electrode for hydrogen evolution. Int J Hydrog Energy 1987;12:473–9.

[14] Endoh E, Otouma H, Morimoto T. Advanced low hydrogen overvoltage cathode for chlor-alkali electrolysis cells. Int J Hydrog Energy 1988;13:207–13.

[15] Choquette Y, Ménard H, Brossard L. Hydrogen discharge on a Raney nickel composite-coated electrode. Int J Hydrog Energy 1989;14:637–42.

[16] Choquette Y, Brossard L, Lasia A, Menard H. Study of the Kinetics of Hydrogen Evolution Reaction on Raney Nickel Composite-Coated Electrode by AC Impedance Technique. J Electrochem Soc 1990;137:1723–30.

[17] Hitz C, Lasia A. Experimental study and modeling of impedance of the her on porous Ni electrodes. J Electroanal Chem 2001;500:213–22.

[18] Chen L, Lasia A. Study of the Kinetics of Hydrogen Evolution Reaction on Nickel-Zinc Alloy Electrodes. J Electrochem Soc 1991;138:3321–8.

[19] Balej J, Divisek J, Schmitz H, Mergel J. Preparation and properties of raney-nickel electrodes on Ni-Zn base for H2 and O2 evolution from alkaline-solutions. Part I: electrodeposition of Ni-Zn alloys from chloride solutions. J Appl Electrochem 1992;22:705–10.

[20] Schiller G, Henne R, Borck V. Vacuum plasma spraying of high-performance electrodes for alkaline water electrolysis. J Therm Spray Technol 1995;4:185–94.

[21] Miousse D, Lasia A, Borck V. Hydrogen evolution reaction on Ni-Al-Mo and Ni-Al electrodes prepared by low pressure plasma spraying. J Appl Electrochem 1995;25:592–602.

[22] Fournier J, Miousse D, Legoux JG. Wire-arc sprayed nickel based coating for hydrogen evolution reaction in   alkaline solutions. Int J Hydrog Energy 1999;24:519–28.

[23] Singleton MF, Murray JL, Nash P. Al-Ni (Aluminium-Nickel). In: Massalski TB, Okamoto H, Subramanian PR, Kacprzak L, editors. Bin. Alloy Phase Diagr., vol. 1, American Society for Metals; 1986, p. 142.

[24] Janssen M, Rieck G. Reaction diffusion and kirkendall-effect in nickel aluminium system. Trans Metall Soc AIME 1967;239:1372–85.

[25] Konieczny M, Mola R, Thomas P, Kopciał M. Processing, Microstructure and Properties of Laminated Ni-Intermetallic Composites Synthesised Using Ni Sheets and Al Foils. Arch Metall Mater 2011;56:693–702.

[26] Wang QW, Fan GH, Geng L, Zhang J, Zhang YZ, Cui XP. Formation of intermetallic compound layer in multi-laminated Ni–(TiB2/Al) composite sheets during annealing treatment. Micron 2013;45:150–4.

[27] Tsao C-L, Chen S-W. Interfacial reactions in the liquid diffusion couples of Mg/Ni, Al/Ni and Al/(Ni)-Al2O3 systems. J Mater Sci 1995;30:5215–22.

[28] Castleman LS, Seigle LL. Layer growth during interdiffusion in aluminum-nickel alloy system. Metall Soc Am Inst Min Metall Pet Eng -- Trans 1958;212:589–96.

[29] Mackenzie JK. Second Paper on Statistics Associated with the Random Disorientation of Cubes. Biometrika 1958;45:229–40.

[30] Thornton JA. The microstructure of sputter-deposited coatings. J Vac Sci Technol A 1986;4:3059–65.

[31] Kelly P., Arnell R. Magnetron sputtering: a review of recent developments and applications. Vacuum 2000;56:159–72.

[32] Pauleau Y. Generation and evolution of residual stresses in physical vapour-deposited thin films. Vacuum 2001;61:175–81.

[33] Inderjeet Kaur, Mishin Y, Gust W. Fundamentals of grain and interphase boundary diffusion. Chichester; New York: John Wiley; 1995.

[34] Harrison LG. Influence of dislocations on diffusion kinetics in solids with particular reference to the alkali halides. Trans Faraday Soc 1961;57:1191–9.

[35] Tarento RJ, Blaise G. Studies of the first steps of thin film interdiffusion in the Al-Ni system. Acta Metall 1989;37:2305–12.

[36] Colgan EG. A review of thin-film aluminide formation. Mater Sci Rep 1990;5:1–44.

[37] Colgan EG, Mayer JW. Aluminium-Transition Metal Thin-Film Reactions. MRS Online Proc Libr 1988;119:null–null.

[38]   Venezia AM, Loxton CM. Low pressure oxidation of Ni3Al alloys at elevated temperatures as studied by x-ray photoelectron spectroscopy and Auger spectroscopy. Surf Sci 1988;194:136–48.

[39]   Han L, Jun-Qiao W, Ji-Zhou C. Structure imperfection of γ-Al2O3. Polyhedron 1995;14:445–9.

[40]   Lee M-H, Cheng C-F, Heine V, Klinowski J. Distribution of tetrahedral and octahedral A1 sites in gamma alumina. Chem Phys Lett 1997;265:673–6.

Unveiling the secrets of the Standard Hydrogen Electrode - An inspiration for the on-going development of hydrogen electrocatalysts

Martin Flyvbjerg(a), Cecilía K. Kjartansdóttir(a), Per Møller(a) & Michael Caspersen(a,b)

a)   Department of Mechanical Engineering, Technical University of Denmark (DTU), Materials and Surface Engineering Section (MTU), Produktionstorvet Building 425, 2800 Kgs. Lyngby Denmark.

b)   Siemens A/S, Borupvang 9, 2750 Ballerup

ABSTRACT: New aspects in the on-going discussion of what contributes to the electrode potential during hydrogen evolution reaction (HER) are put forward. The focus is on available number of active sites vs. intrinsic material properties, unveiling for the first time the nano-scale topography of the electrode. The Platinum Black electrode has always be known to have a very well defined potential used as reference for the electrochemical scale, and the particular surface topography is basis for inspiration for electrochemical catalysis and other processes like hydrogenation where other catalysts are used, such as Raney nickel. A new perspective on electrode design and electrodeposition of the platinum black electrode are presented.

Background

The platinum black electrode is accepted worldwide as the Standard Hydrogen Electrode (SHE) and in electrochemistry it is defined the reference electrode for the absolute zero potential. Platinum is known for good corrosive resistance, extremely good catalytic properties, preferred electrocatalysis in fuel cell and environmental industry[1-3], and may serve as solution as energy storage for sustainable energy sources, known as the "hydrogen economy"[4,5].

Smooth platinum comprises greater hydrogen overvoltage, than platinized platinum (platinum black) 150mV vs. 0 at 1 mA/cm² [6]. Therefore one would assume that platinum black electrode is the ideal electrode for water electrolysis as well as other reactions that depend upon low hydrogen overpotential. A very important question arises what actually contributes to the very low hydrogen overvoltage? Is overvoltage a material constant or does the microstructure influence the catalytic behaviour?

The historical origins

The history of platinum black goes as far back as 1890 where O.R. Lummer and F. Kurlbaum [7] started searching for a black substrate to replace the current method for measuring radiation, by creating a reproducible bolometer for measuring the black body radiation.

Blackbody radiation was at that time measuring the resistance though metal strip connected to a Wheatstone bridge; radiation hitting the strip will cause a rise in temperature and thereby electrical resistance. Prior to the platinum black experiments, a metallic strip blackened by soot from a burning petroleum flame was used, however the exact layer of soot was not easy to reproduce.

It was acknowledged that a layer of completely black platinum could be electrodeposited from a (platinum chlorid) "platinchlorid" bath by adding copper or lead to the bath. The actual composition based on hexachloroplatinic acid or platinum(IV) chloride. Kohlrausch pointed out that this term is commonly applied to hexachloroplatinic acid. Adding copper sulphate to the plating bath was found to give larger, smoother and less brittle platinum black coating. However, adding a very small amount of lead acetate instead yielded even better results. Later on other additives have been added to improve the adhesion between the platinum layer and the substrate. Inspired by Arrhenius' dissociation theory, Nobel laureate Walter Nernst[89] developed his theories of thermodynamic aspects of an electrochemical cell in 1889, presently known as the Nernst equation. The theory provides a relation between the hydrogen and hydroxyl ion concentration.

In 1893 Max Le Blanc [10] made a practical discovery in an attempt to measure the hydrogen ion concentration in a given solution, today described as pH, by letting a stream of hydrogen gas flow around a platinum electrode, electroplated with platinum (platinized platinum/platinum

black) the electrode will behave like a hydrogen electrode i.e. absolute potential.

Thereby he established a basis for the electromotive force measurement in a cell, by the known hydrogen half-cell redox reaction:

$$2H^+_{(aq)} + 2e^- \rightarrow H_{2(g)}$$
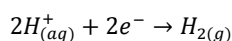
According to Trasatti [11] the SHE is a scale for obtaining the absolute electrode potential, defined as the difference in electronic energy between an electrolyte and the Fermi energy of a metal electrode. Fermi level is defined as the energy level between a point in a solid crystalline and an electron at rest in vacuum.

In order to match the physical scale to the electrochemical scale the SHE is defined by IUPAC [11] via following relation at 298.15 K:

$$\frac{E^M_{(abs)}}{V} = \frac{E^M_{(SHE)}}{V} + 4.44$$

Where E^M(abs) is the absolute potential for the metal M and SHE the hydrogen electrode. The origin of the electrochemical scale predates the physical scale, and is determined by a redox half-cell reaction.

$$2H^+_{(aq)} + 2e^- \rightarrow H_{2(g)}$$
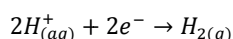
This reaction occurs at a platinized platinum electrode, submerged in an acidic solution with hydrogen bubbling thought it. The relation and theory between electrode and electrochemical potential is fully described in [12,13]. The SHE is occasionally confused with the Normal Hydrogen Electrode (NHE). The NHE is defined as the potential of platinum in a 1N acid solution [13] and was used as reference electrode in the early days of electrochemistry. The SHE is on the other hand defined by the concentration of H+ in the electrode/solution interface. For the SHE the activity of the hydrogen half-cell reaction must be of aH+ = 1, as derived from Nernst equation, under standard conditions.

The electrocatalytic effect of a hydrogen electrode

The ability to adsorb hydrogen atoms plays a key role in the mechanism and kinetics of hydrogen electrodes. Several transition metals have such a strong M – H bond that they are able to dissociate hydrogen molecules in a solution, this is particularly the case for Pt. Hence the Pt – H bond is stronger than the H – H bond [14].

The hydrogen adsorption mechanism on a metal (M) surface is commonly written as
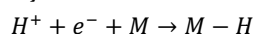
$$H^+ + e^- + M \rightarrow M - H$$

Most theories state that the adsorbed hydrogen atoms combine into hydrogen molecules either by reacting with further discharging H$^+$ or by recombining with another adsorbed hydrogen atom. The first discharge step where hydrogen is adsorbed at the electrode surface is known as the Volmer reaction, and the second step where hydrogen molecules are formed is known as the Heyrovsky reaction. The recombination of two adsorbed hydrogen atoms is known as Tafel reactions. Both Volmer and Heyrovsky reactions are electrochemical reactions whereas the Tafel reaction is solely a chemical reaction. The table below shows the Volmer, Heyrovsky and Tafel reactions as they take place in acidic and alkaline solutions.

Volmer, Heyrovsky reactions:

	Acidic	Alkaline
Volmer reaction	$H^+ + e^- \rightarrow H_{ads}$	$H_2O + e^- \rightarrow H_{ads} + OH^-$
Heyrovsky reaction	$H_{ads} + H^+ + e^- \rightarrow H_2$	$H_{ads} + H_2O + e^- \rightarrow H_2 + OH^-$
Tafel	$H_{ads} + H_{ads} \rightarrow H_2$	$H_{ads} + H_{ads} \rightarrow H_2$

During hydrogen evolution the two discharging steps occur simultaneously, the slower step determines the HER rate. From the previous it is clear the activation energy decreases with increased adsorption energy (M–H bond strength), while increased adsorption energy means increase in terms of H_{ads} coverage on the electrode surface. Therefore if they M—H bond energy is too strong the H_{ads} will occupy the available surface sites and inhibit the second step of the total reaction. Thus the best hydrogen electrode should be the one having intermediate M–H bond energy (or free energy of hydrogen adsorption (ΔG_{ads})), as stated in the Sabatier principle [15]. When plotting the electrocatalytic activity (exchange current density for HER) vs. the M–H bond strength for different metals a so called volcano plot is formed. The volcano plot in Figure 1 supports Sabatier's theory and shows clearly that platinum should be the most active metal for hydrogen evolution.
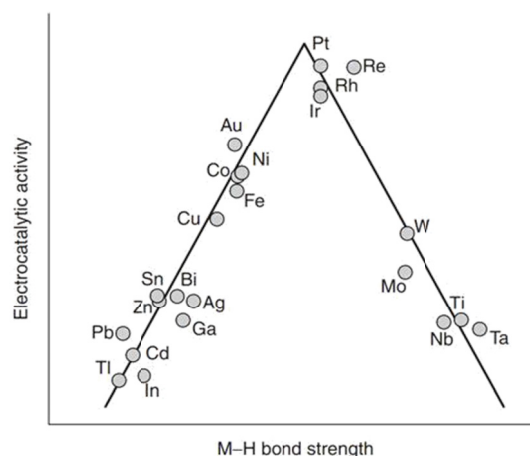

Figure 1: The dependence of the electrocatalytic activity for HER on the metal – hydrogen bond formed [14].

A more recent way to define the volcano curves principle is based on the electronic configuration of the atoms within the lattice of the catalyst material [16–19] or the so called hypo- hyper-d theory. Here metals on the left side

of the volcano plot are called hypo-d-electronic metals because they have empty or half-filled vacant d-orbitals and the metals on the right side of the volcano plot is called hyper-d- electronic elements because they have internally pared d-electrons which are not available for bonding in pure metals. The optimum (best catalyst, the catalyst at the top of the volcano plot) is either defined[20] to be at d^8 or d^5.

From the volcano plot one can imagine that the electrocatalytic activity towards hydrogen evolution could be tailored by combining metals from the left-hand side of the volcano plot (hypo-d-electron metals) with metals from the right-hand side of the volcano plot (hyper-d-electron metals). This seems to be the case and it has been shown that the activity of intermetallic phases and alloys of transition metals towards the HER obey the same sort of volcano plots as pure metals[21].

Recently, J. Greeley et al.[22] used the density function theory (DFT) to calculate the free energy of hydrogen adsorption for over 700 binary transition-metal surface alloys. Their calculations showed that the electrocatalytic activity of BiPt towards HER is comparable, or better, than for pure Pt. Electrochemical testing on a synthesized BiPt alloy was showed to support the theoretical evaluation.

Although illuminating some interesting trends there are some uncertainties to whether DFT calculations by their own are viable for actual electrocatalytic surfaces. In its nature DFT is considering only the ground state of a material in order to evaluate its pure intrinsic properties. This approach will though, in spite of delivering interesting theoretical predictions, not necessarily give the right indication for actual electrocatalytic surfaces where crystallographic defects and lattice distortion will alter the system away from its ground state. Furthermore, often limited number of atoms constitutes the idealized single crystal considered in the calculations due to the available computer power. Hence, other bulk phenomena occurring in a solid polycrystalline specimen such as interactions from grain boundaries, segregation and atomic impurities are neither taken into consideration. As a consequence, consistency with actual observations is not always obtainable, and indeed the practical usage of DFT has yet to be further evaluated and documented, until it can potentially be used as an impactful argument. For genuine optimization of electrocatalytic surfaces the above mentioned phenomena has to be emphasized as well as how they will affect the final electrocatalyst.

The actual electrocatalytic effect does not only depend on the electron configuration. The structure and topography of the catalyst also has a great influence of the apparent electrocatalytic efficiency.

Previous studies have shown that improved efficiency, lower cell potential, in e.g. PEM fuel cells or electrolysis cells can be obtained by modifying the electrode morphology with various techniques. Depositing active layers on highly porous carbon supports[23,24] or creating highly porous electrodes prepared by selectively leaching of one or more elements from metal alloys are good examples of this[25,26].

In the latter case the conclusion has been made that higher activity stems from creation of new lattice vacancies along with an increase in surface area is obtained during leaching [27]. In fact, several authors have ascribed increased efficiencies of alloys compared to plain substances, often nickel, to gain in surface area rather than intrinsic factors[28,29]. A larger surface area per unit mass will all things being equal increase the amount of active surface sites thus lowering the local current density and reduce the required potential for the reaction to proceed, but this does not directly prove or disprove the d-electron theory. Indeed, it has been shown[29-31] how surface area effects can be combined with electronic effects from various noble metals to reach higher catalytic efficiency for the HER.

This can be supported by work done on particular favourable crystallographic orientations of platinum in neighbouring studies[32], implying that higher order index facets are more active in nature due to higher number of steps and missing atomic bonds (high surface energy). Equivalence back to the high activity of leached alloys seems reasonable. Here we argue that a complex correlation must exist between the various contributions and that all contributions should be tailored in order to maximize electrocatalytic activity.

Experimental procedure

Hexachloroplatinic acid H_2PtCl_6 for the plating bath was prepared by dissolving a wire of pure platinum in aqua regia, (1 part of concentrated nitric acid, and 3 parts of concentrated hydrochloric acid). In order to denox the solution, additional HCl 20 mL was added three times and boiled off, to ensure the solution was free of any additional HNO_3 and NO_2. The solution was boiled down and DI-water was added to reach the desired concentration of 0.072M (3.5 %) H_2PtCl_6 with pH of 0.8.

According to the original recipe for platinum black a piece of platinum foil is desired for the platinization process. However due to the current price of Pt a gold plated substrate is used as replacement. The Au is selected to ensure good adhesion. Several authors have reported adhesion problems in the production of platinized platinum when using additive free plating solutions [33-36]. The lattice constant of Au is relatively close to the lattice constant of Pt, as the original recipe of platinized platinum requires. For the electrode substrate, a piece of stainless steel AISI 304 10 x 10 x 1 mm was selected, initially plated with strike nickel from Wood's electrolyte followed by a layer of sulphamate Ni (~15μm). The substrate was thereafter plated with 1.5 μm gold layer.

The platinum was deposited, with current density of 3 A/dm², from the hexachloroplatinic acid with 1.3 * 10⁻⁴ M (0.005 %) Pb-acetate trihydrate added to the electrolyte. The Pb is addet in order to achieve the deep black surface as described in literature [37]. The developed electrode was cleaned by gentle dipping in DI-water and dried prior to any investigations. However, it should be mentioned that the original recipe states the electrode must be kept wet and stored in DI-water for maximum catalytic properties.

In order to estimate the surface area of the Pb-black electrode Brunauer-Emmett-Teller (BET) method was employed. The Pt-black electrode for the BET analyses was prepared on a copper wire followed by a nickel and gold layer as described earlier. The analysis was carried out on a Micromeritics ASAP 2020, using N_2 at liquid nitrogen temperature. Prior to the measurements the sample was degassed at 200°C in vacuum for 6 hours. A commercial nickel foam sample was also investigated using same procedure for comparison.

The structure and morphology of the Pt electrode was investigated using a FEI Helios Nanolab 600i, a Field Emission Gun-Scanning Electron Microscope (FEG-SEM) at DTU-Cen (Center for Electron Nanoscopy). The maximum resolution of the SEM is listed to be better than 1.5 nm at 1kV.
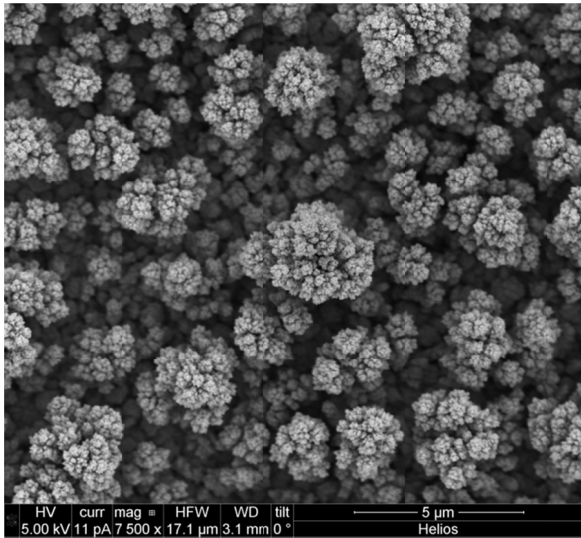
Figure 2 FEG-SEM micrograph of Pt-black electrode as deposited, showing a flower-like morphology (full window magnification x15.000).
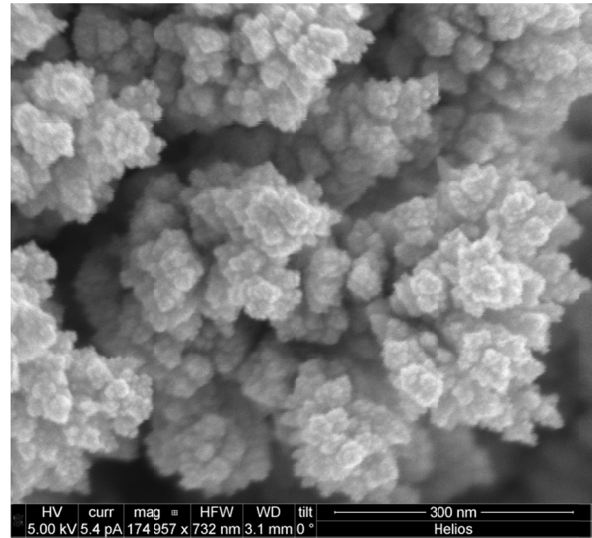

Figure 4 FEG-SEM micrograph of Pt Black electrode, with increased magnification (x 350.000).
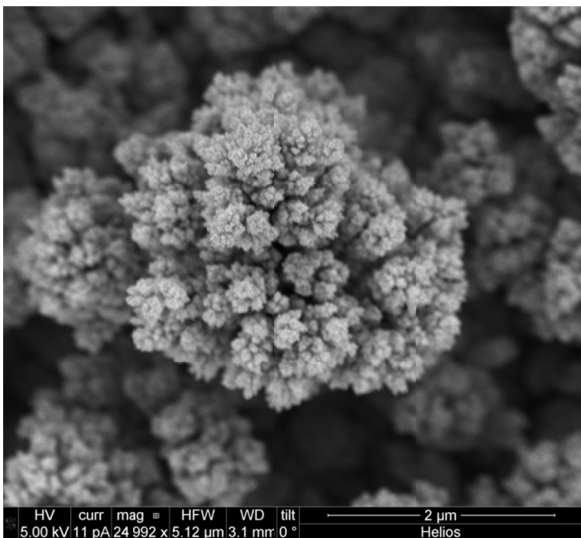

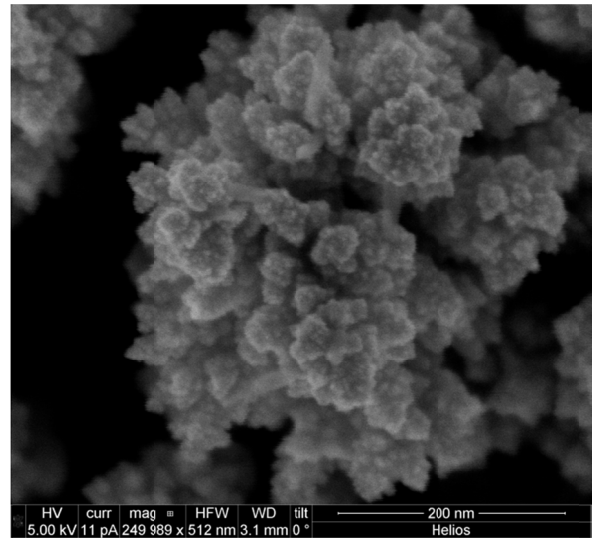Figure 3 FEG-SEM micrograph of Pt-Black electrode, with increased magnification (x 50.000).

Figure 5 FEG-SEM micrograph of Pt Black electrode, with the highest reached magnification. Small white dots appear possibly being new nucleations. (x 500.000).

Tailoring the optimal surface morphology

For any electro deposited materials the structure of the layer depends upon two crucial factors - the current density and the inhibition of deposition. There are in general two theories we can apply to the electrodepostion of Pt black, either Pb can act as an accelerator for the plating process or it can inhibit the formation of hydrogen at the cathode thereby allowing Pt to be deposited at greater rate.

René Winand created a diagram, Figure 7 showing the structure of layers made with electro deposition as a tool for classifying deposited layers. By using the Winand and the Pourbaix diagrams for platinum and lead as tools it might be possible to work out the theories of platinum black plating.
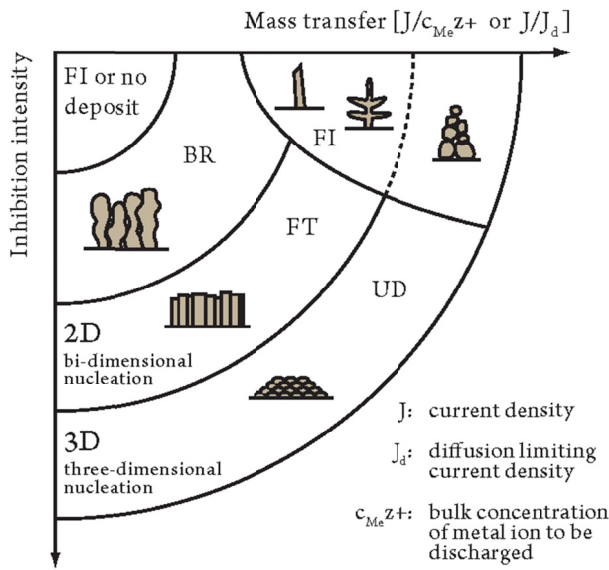

Figure 7 A simplified version of the diagram of R. Winand, showing different types of polycrystalline electrodeposits as a function of J /$C_{Me}z^+$ (or J / J_d) and inhibition intensity[38]. FI: Field oriented isolated crystals, BR: Basis oriented reproduction, Field oriented texture type, UD: Unoriented dispersion type, 2D: bidimesional nucleation, 3D: tridimesional nucleation.

By comparing the structure of the electrode with the Winand diagram the structure is likely to be of BR or FI type rather than UD or FT. Both BR and FI indicate low current density and lack of inhibition. By adding Pb to the plating bath the surface structure will change dramatically and therefore the chemistry of the plating bath would also been altered. By once again consulting the Winand diagram the typical structure is likely to be unoriented dispersive growth or the unnamed region just above. In order to match the diagram a plausible theory is that Pb slightly inhibits the deposition of Pt resulting in forced new nucleation, causing the dendrite-like structure to constantly spawn new branches but only allowing them to grow to a specific size before a new branch is spawned and the process is repeated.
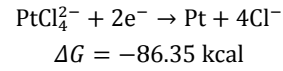
There have been multiple theories for how the plating process takes place, the most popular is likely described by [39,40] where couples of platinum chloride (Pt(IV)Cl_6^{2-}

and Pt(II)Cl_4^{2-}) is reduced to pure Pt. However this theory does not explain the role of lead or the chemistry involved.

One of the claimed reaction couples in the electrodeposition of platinum from chloroplatinic acid is:

$$Pt(IV)Cl_6^{2-} + 2e^- \rightleftarrows PtCl_4^{2-} + 2Cl^-$$
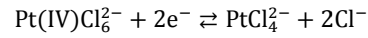
Thereafter platinum is deposited according to:

$$PtCl_4^{2-} + 2e^- \rightarrow Pt + 4Cl^-$$
$$\Delta G = -86.35 \text{ kcal}$$

The Gibbs free energy (ΔG) for deposition is negative indicating that the reaction is thermodynamically favourable.

One theory [40] states possible adsorption of lead where, the adsorbed Pb ions act as sites for electron transfer between the surface and the $PtCl_6^{2-}$ ions. These Pb ions could be considered "pseudo-defects" acting as nucleation
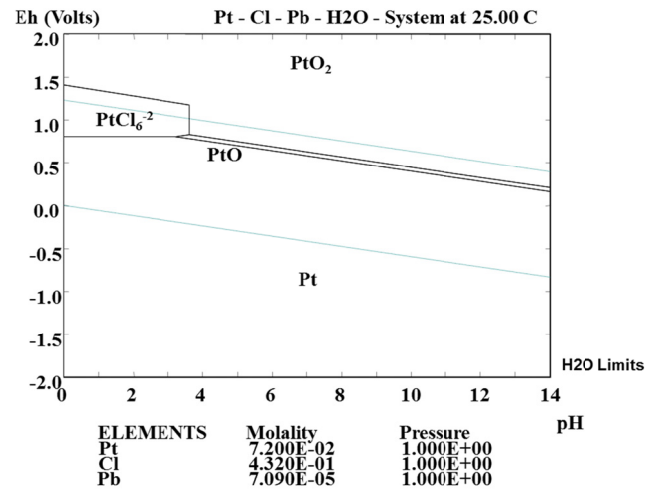

Figure 6 Pourbaix diagram for Pt – Cl and Pb with respective plating bath concentration.

centres for Pt islands on the flat areas. Other experimental results [41] indicate that "Pb-acetate significantly enhances the electrode reactions in platinum black coating by mainly lowering the energy barrier for the reduction of Pt (IV) to Pt and by suppressing the reduction of Pt (IV) to Pt (II)".

However no single element has the ability to suppress change in oxidation states. These theories simply cannot be supported by any of the following chemistry, or the Pourbaix diagrams.

The Pourbaix diagram is a powerful tool to show thermodynamic stable complexes at various pH and potential. As shown in Figure 6, Pt and the $PtCl_6^{2-}$ ion appears in the diagram. More interesting are the diagram for Pb Figure 8, keeping in mind the pH of the plating electrolyte was around 0.8 two ions are noticeable $PbCl^-$ and $PbCl_4^-$.
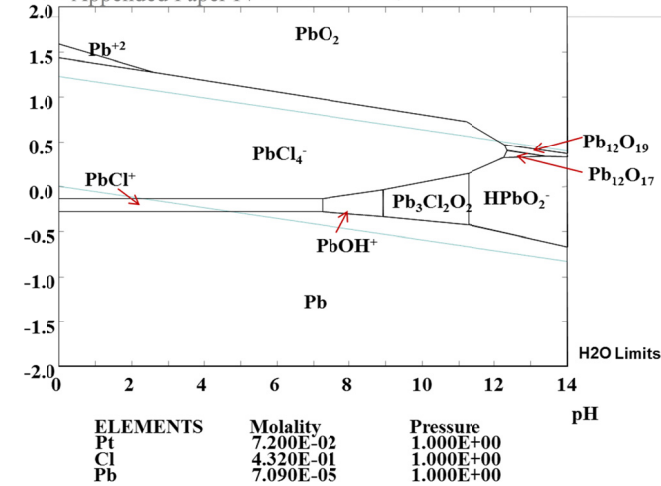
Eh (Volts) Pb - Cl - Pt - H2O - System at 25.00 C

ELEMENTS	Molality	Pressure
Pt	7.200E-02	1.000E+00
Cl	4.320E-01	1.000E+00
Pb	7.090E-05	1.000E+00

Figure 8 Pourbaix diagram for Pb -Cl PbCl+ is especially notice-able species likely to influence the plating of Pt-Black.

One could imagine that $Pb(III)Cl_4^-$ could be reduced to $Pb(II)Cl^+$, and thereby changing the oxidation state of Pb and creates an initiation step for the platinum plating. During the process Pb is reduced from oxidation state +3, to +2. As seen in following reaction the lead ion can be oxidized by the platinum acid, leaving behind pure plati-num. Calculated at 20ºC.

$$4PbCl^+ + PtCl_6^{2-} + 6Cl^- \rightarrow Pt + 4PbCl_4^-$$

$$\Delta G = -381.6 \text{ kcal}$$
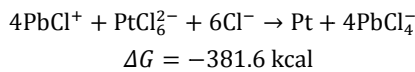
This makes the $PbCl^+$ a reduction agent for the $PtCl_6^{2-}$ ion, oxidizing $PbCl^+$ to $4PbCl_4^-$. As mentioned earlier according to [40] the platinum plating relies only on reduc-tion of platinum chloride, when calculating the ΔG of both reactions the reaction involving PbCl is much more plausible to happened rather than simple $PtCl_2$ or $PtCl_4$ complex reduced to Pt. This could explain the require-ment for Pb to be present in order to be able to electro-deposit the platinum-black electrodes, since $PtCl6_2^-$ is instantaneously reduced and creates the very delicate nanocrystals.

If any Pb was to be found in the electrodeposited layer of the electrode the overvoltage of the electrode is not likely to be as low, since , lead have an exchange current[6] of $2 \cdot 10^{-13}$ A/cm².

An alternative plausible theory of a Pb free layer states, one could argue lead could possibly as pure Pb, after-wards be able to reduce the $PtCl_6^{2-}$ to Pt via the following reactions.

$$4Pb + 3PtCl_6^{2-} \rightarrow 3Pt + 4PbCl_4^- + 2Cl^-$$

or

$$2Pb + PtCl_6^{2-} \rightarrow Pt + PbCl^+ + 4Cl^-$$
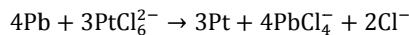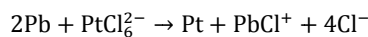
Results and Discussion

When looking at the deposited Pt-black electrode with the bare eye the electrode appears completely black and does not reflect any incident light, i.e. acts like a perfect black body, as original intended as described earlier.

FEG-SEM micrographs of the Pt-black electrode surface, as deposited, are shown in Fig. 2 to 5. The micrographs reveal very distinct features that remarkable resampling the flowerhead of a Chrysanthemum flower at a nano-scale. With increased magnification it becomes clear that the pattern of growth repeats itself down towards nano-scale level.

The surface of the electrode is very fragile and black material flakes of if touched. This delicate surface topography explains the pitch black appearance of the electrode. Hence all incident and diffuse light are trapped unable to escape the surface.

Various theories for plating platinum black have been discussed earlier in this article. Clearly lead plays an important role when depositing Pt-black. In order to detect if the supposed lead chloride complex reactions will take place an in-situ ultraviolet analysis of the plating process is required. From a theoretical point of view this reaction could explain the requirement for lead to be present in the solution in order to achieve the pitch black surface.

The pitch black platinum electrode proves to hide a very unique crystal structure as revealed in the SEM micrographs, a morphology with extremely large surface area, which holds immense amount of intrinsic sites along the crystal edges where reactions such as the HER is likely to occur. The combination of a large area with lots of intrinsic sites is likely to result in good possibilities for electrocatalytic reactions. Hence the morphology of this ideal electrode evidently plays a crucial role for the overvoltage.

Deposition trials without the addition of Pb resulted in flaking of the Au and Pt layer, a possible explanation for debonding is likely stress in the Pt layer peeling off both layers. This was not investigated further the focus was pointed towards electrolyte with lead.

From the BET analysis the surface area of the Pt-black is estimated to have a "roughness factor" of approximately 5900 times compared to a geometric smooth surface. The roughness factors of the Pt-black electrode have been reported in the range of 3900-20000 [42]. However in this case helium was used for the measurement instead of nitrogen as in the present study. Helium molecules are far smaller than nitrogen and possibly able to enter smaller cavities. By comparison to commercial available nickel foam sample with a roughness factor in the range of 300 times greater.

It must be kept in mind the BET analysis is sensitive towards the weight of the sample and the thickness of different layers applied during the plating process. The recipe for Pt-black does not state how thick a layer will be applied or the efficiency of the plating bath, so the final Pt layer was estimated by subtracting the inner layers (determined by SEM), so that only the Pt layer density was evaluated in the BET measurement

In spite of uncertainties connected to the use of this method the magnitude of the found roughness factor clearly renders the uncertainties insignificant, and there can be no doubt that the Pt black electrode possesses a natural huge surface area.

The Pt-black electrode can serve as inspiration for fabricating of HER catalysts. By mimicking the morphology of the Pt-black electrode with a cheaper material the electrocatalytic properties can be altered to more positive direction. Here the importance of large amount of active sites in the development of catalysts has been emphasised. By combining the knowledge of how the electronic configuration of a catalyst influences catalytic properties (as explained with the Volcano plot) to the importance of high active surface area less expensive and more active HER catalysts can be produced.

Another well-known catalyst metal with a similar structure, Raney-Nickel shares some of the properties with the Pt-black electrode. Both materials have a large surface area with numerous intrinsic sites for reaction. It is no secret within the catalyst industry [30,31,43], that morphologies with high surface area increase the activity of a heterogeneous reaction.

The volcano plot based upon the Sabatier principle is often calculated using the density functional theory (DFT), a quantum mechanical mathematic model based upon energy levels. Then calculating these models often a single crystal is considered or a system with very limited configuration limiting the use of the model. Since reactions occur at the intrinsic sites along the edges of a crystal it is necessary to consider different spacious configurations and consider all the intermetallic compounds between the elements. This does not consider where or not the intermetallic is thermodynamically stable or possible to produce.

This increases the difficulties related with create a workable mathematical model for electrocatalytic design and one should question the usefulness of already existing models.

The plating process of Pt-black electrodes occurs at such low potentials that hydrogen formation is impossible to avoid, despite the electrode is unable to function as cathode for electrolysis of water. The electrode is purely designed for measureing the reversible reaction of hydrogen, measuring the potential where hydrogen gas is aerated around the electrode in an acidic solution. If used as cathode for making hydrogen the fine structure and topography of the electrode is likely to be destroyed due to gas erosion.

When designing electrocatalysts the mechanical and thermodynamic stability must be taken into consideration.

REFERENCES

(1)   GRIGORIEV, S.; POREMBSKY, V.; FATEEV, V. *Int. J. Hydrogen Energy* **2006**, *31*, 171–175.

(2)   Granovskii, M.; Dincer, I.; Rosen, M. a. *J. Power Sources* **2006**, *157*, 411–421.

(3)   KREUTER, W. *Int. J. Hydrogen Energy* **1998**, *23*, 661–666.

(4)   Bockris, J. O. *PROCEEDINGS- Electrochem. Soc. PV* **2000**, *2000-20*, 1 – 24.

(5)   Bockris, J. O.; Veziroglu, T. N. *Int. J. Hydrogen Energy* **2007**, *32*, 1605–1610.

(6)   Baboian, R. *Corrosion tests and standards : application and interpretation*; 2005.

(7)   Lummer, O.; Kurlbaum, F. *Ann. Phys.* **1892**, *282*, 204–224.

(8)   Von Ettingshausen, A.; Nernst, W. *Ann. Phys.* **1888**, *269*, 474–492.

(9)   Nernst, W. *Ann. Phys.* **1887**, *267*, 760–789.

(10)   Le Blanc, M. *Zeitschrift für Phys. Chemie* **1893**, *12*, 333.

(11)   Trasatti, S.; of Pure, I. U.; Division, A. C. P. C. *The Absolute Electrode Potential: An Explanatory Note (recommendations 1986)*; Blackwell Scientific, 1986.

(12)   Biegler, T.; Woods, R. *J. Chem. Educ.* **1973**, *50*, 604.

(13)   Ramette, R. W. *J. Chem. Educ.* **1987**, *64*, 885.

(14)   Trasatti, S. In *Encyclopedia of Electrochemical Power Sources*; Jürgen Garche, Ed.; Amsterdam, 2009; pp. 41–18.

(15)   Sabatier, P. *Berichte der Dtsch. Chem. Gesellschaft* **1911**, *44*, 1984–2001.

(16)   Jaksic, J. M.; Krstajic, N. V.; Grgur, B. N.; Jaksic, M. M. *Int. J. Hydrogen Energy* *23*, 667–681.

(17)   Jaksic, M. M. *Int. J. Hydrogen Energy* **2001**, *26*, 559–578.

(18)   Neophytides, S. G.; Zafeiratos, S.; Papakonstantinou, G. D.; Jaksic, J. M.; Paloukis, F. E.; Jaksic, M. M. Extended Brewer hypo-hyper-d-interionic bonding theory - I. Theoretical considerations and examples for its experimental confirmation. *INTERNATIONAL JOURNAL OF HYDROGEN ENERGY*, 2005, *30*, 131–147.

(19)   Jaksic, M. M. ELECTROCATALYSIS OF HYDROGEN EVOLUTION IN THE LIGHT OF THE BREWER-ENGEL THEORY FOR BONDING IN METALS AND INTERMETALLIC PHASES. *ELECTROCHIMICA ACTA*, 1984, *29*, 1539–1550.

(20)   Jaksic, M. M.; Lacnjevac, C. M.; Grgur, B. N.; Krstajic, N. V. Volcano plots along intermetallic hypo-hyper-d-electronic phase diagrams and electrocatalysis for hydrogen electrode reactions. *JOURNAL OF NEW MATERIALS FOR ELECTROCHEMICAL SYSTEMS*, 2000, *3*, 169–182.

(21)   JAKI, J. *Int. J. Hydrogen Energy* **1998**, *23*, 667–681.

(22)   Greeley, J.; Jaramillo, T. F.; Bonde, J.; Chorkendorff, I. B.; Nørskov, J. K. *Nat. Mater.* **2006**, *5*, 909–13.

(23)   Popovski, O. *NEW TRENDS Res. Energ. Mater.* **2006**, 416 – 422.

(24)   Paunovic, P. *Maced. J. Chem. Chem. Eng.* **2007**, *26*, 87 – 93.

(25)   Brennecke, P. W.; Ewe, H. H. *Energy Convers. Manag.* **1991**, *31*, 585–594.

(26)   Choudhary, V. R. *J. Chem. Technol. Biotechnol. Chem. Technol.* **1983**, *33A*, 339 – 349.

(27)   Bagotsky, V. S. *Fuel cells : problems and solutions*; Wiley, 2012; p. 1 vol. (XVIII–385 p.).

(28)   Birry, L.; Lasia, A. *NEW Mater. Electrochem. Syst.* **2001**, 69–72.

(29)   Herraiz-Cardona, I.; Ortega, E.; Vazquez-Gomez, L.; Perez-Herranz, V. Electrochemical characterization of a NiCo/Zn cathode for hydrogen generation. *INTERNATIONAL JOURNAL OF HYDROGEN ENERGY*, 2011, *36*, 11578–11587.

(30)   Solmaz, R.; Kardas, G. Fabrication and characterization of NiCoZn-M (M: Ag, Pd and Pt) electrocatalysts as cathode materials for electrochemical hydrogen production. *INTERNATIONAL JOURNAL OF HYDROGEN ENERGY*, 2011, *36*, 12079–12087.

(31)   Dominguez-Crespo, M. A.; Torres-Huerta, A. M.; Brachetti-Sibaja, B.; Flores-Vela, A. Electrochemical performance of Ni-RE (RE = rare earth) as electrode material for hydrogen evolution reaction in alkaline medium. *INTERNATIONAL JOURNAL OF HYDROGEN ENERGY*, 2011, *36*, 135–151.

(32)   Tian, N.; Zhou, Z.-Y.; Sun, S.-G.; Ding, Y.; Wang, Z. L. *Sci.* **2007**, *316* , 732–735.

(33)   Jones, G.; Bollinger, D. M. *J. Am. Chem. Soc.* **1935**, *57*, 280–284.

(34)   Von Hevesy, G.; Somiya, T. Platinum black. *ZEITSCHRIFT FUR PHYSIKALISCHE CHEMIE-ABTEILUNG A-CHEMISCHE THERMODYNAMIK KINETIK ELEKTROCHEMIE EIGENSCHAFTSLEHRE*, 1934, *171*, 41–48.

(35)   Popoff, S.; Kunz, A. H.; Snow, R. D. *J. Phys. Chem.* **1928**, *32*, 1056–1060.

(36)   Joncich, M. J.; Hackerman, N. PREPARATION AND SURFACE AREA MEASUREMENTS OF PLATINIZED-PLATINUM ELECTRODES. *JOURNAL OF THE ELECTROCHEMICAL SOCIETY*, 1964, *111*, 1286–1289.

(37)   Kohlrausch, F. *Ann. der Phys. und Chemie* **1897**.

(38)   Winand, R. ELECTRODEPOSITION OF METALS AND ALLOYS - NEW RESULTS AND PERSPECTIVES. *ELECTROCHIMICA ACTA*, 1994, *39*, 1091–1105.

(39)   Feltham, A. M.; Spiro, M. PLATINIZED PLATINUM ELECTRODES. *CHEMICAL REVIEWS*, 1971, *71*.

(40)   Layson, A. R.; Columbia, M. R. The morphology of platinum black electrodeposited on highly oriented pyrolytic graphite studied with scanning electron microscopy and scanning tunneling microscopy. *MICROCHEMICAL JOURNAL*, 1997, *56*, 103–113.

(41)   Saitou, M. Electrochemical characterization of platinum black electrodeposited from electrolyte including lead acetate trihydrate. *Surface and Coatings Technology*, 2007, *201*.

(42)   Brodd, R. J.; Hackerman, N. POLARIZATION CAPACITY AT SOLID ELECTRODES AND TRUE SURFACE AREA VALUES. *JOURNAL OF THE ELECTROCHEMICAL SOCIETY*, 1957, *104*, 704–709.

(43)   Rosalbino, F.; Maccio, D.; Angelini, E.; Saccone, A.; Delfino, S. Characterization of Fe-Zn-R (R = rare earth metal) crystalline alloys as electrocatalysts for hydrogen evolution. *INTERNATIONAL JOURNAL OF HYDROGEN ENERGY*, 2008, *33*, 2660–2667.

Appendix
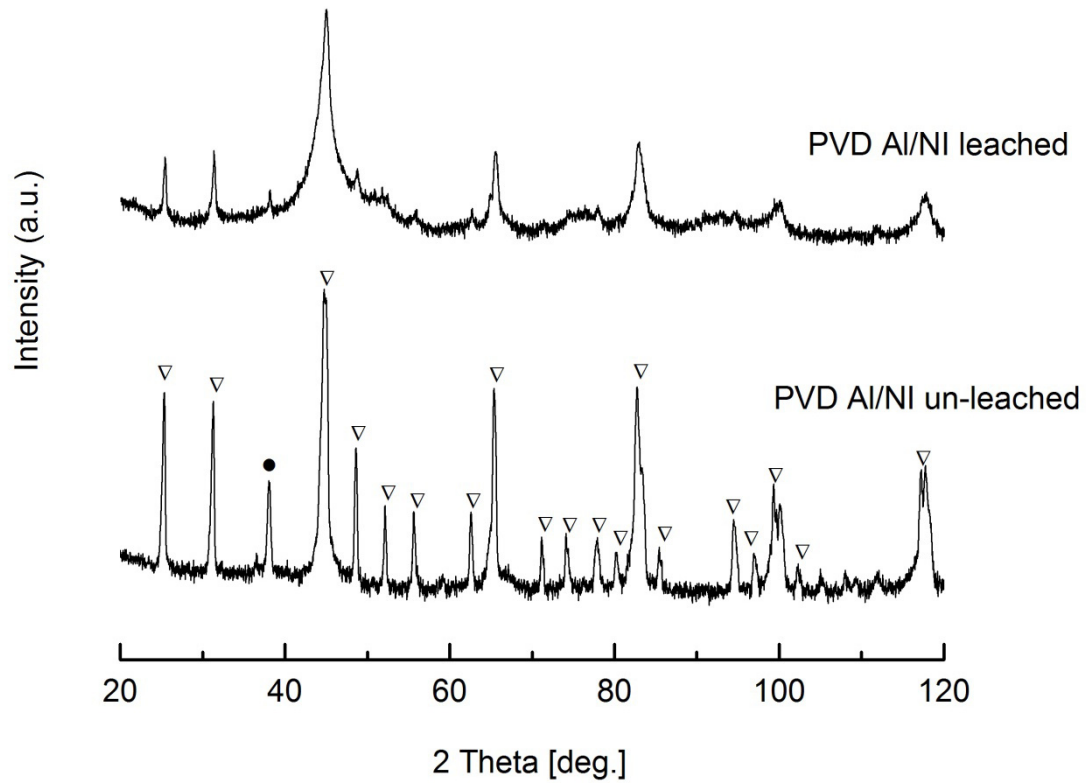
GI-X-ray diffractograms for the PVD Al-Ni couples after 24 hours of heat treatments, before and after leaching.(•) Al, (∇) Al_3Ni_2. The incident angel is 6 degrees for both specimens.